University of Alberta

Preparation of Platinum/Yttria-Stabilized Zirconia and Platinum/Ceria Fuel Cell Anodes

by

Christine Mary Volohatuke

A thesis submitted to the Faculty of Graduate Studies and Research in partial fulfillment of the requirements for the degree of Master of Science

in

Materials Engineering

Department of Chemical and Materials Engineering

Edmonton, Alberta

Fall 2005

Library and Archives Canada

Published Heritage Branch

395 Wellington Street
Ottawa ON K1A 0N4
Canada

Bibliothèque et Archives Canada

Direction du Patrimoine de l'édition

395, rue Wellington
Ottawa ON K1A 0N4
Canada

Your file Votre référence
ISBN: 0-494-09307-2
Our file Notre référence
ISBN: 0-494-09307-2

NOTICE:
The author has granted a non-exclusive license allowing Library and Archives Canada to reproduce, publish, archive, preserve, conserve, communicate to the public by telecommunication or on the Internet, loan, distribute and sell theses worldwide, for commercial or non-commercial purposes, in microform, paper, electronic and/or any other formats.

The author retains copyright ownership and moral rights in this thesis. Neither the thesis nor substantial extracts from it may be printed or otherwise reproduced without the author's permission.

AVIS:
L'auteur a accordé une licence non exclusive permettant à la Bibliothèque et Archives Canada de reproduire, publier, archiver, sauvegarder, conserver, transmettre au public par télécommunication ou par l'Internet, prêter, distribuer et vendre des thèses partout dans le monde, à des fins commerciales ou autres, sur support microforme, papier, électronique et/ou autres formats.

L'auteur conserve la propriété du droit d'auteur et des droits moraux qui protège cette thèse. Ni la thèse ni des extraits substantiels de celle-ci ne doivent être imprimés ou autrement reproduits sans son autorisation.

In compliance with the Canadian Privacy Act some supporting forms may have been removed from this thesis.

While these forms may be included in the document page count, their removal does not represent any loss of content from the thesis.

Conformément à la loi canadienne sur la protection de la vie privée, quelques formulaires secondaires ont été enlevés de cette thèse.

Bien que ces formulaires aient inclus dans la pagination, il n'y aura aucun contenu manquant.

Canada

To Dan,

for his unwavering confidence in me

and for his love

Abstract

Research into solid oxide fuel cell (SOFC) anodes has concentrated on the selection of appropriate materials but anode microstructure is also important to anode performance. Polarized electrochemical vapour deposition (PEVD) is a technique that allows a thin, ionically conducting ceramic layer to be deposited over a complex metal surface. The coating protects the metal surface from the harsh operating environment and reduces sintering. The ionic conductivity of the coating will expand the triple phase boundary area without interfering with the metal's electrical conductivity.

Yttria-stabilized zirconia (YSZ) deposition using PEVD was studied under various deposition conditions using yttrium chloride (YCl_3) and zirconium chloride ($ZrCl_4$) precursors. Preliminary research of cerium (III) chloride ($CeCl_3$) as a precursor for ceria (CeO_2) deposition by this method was also completed. The cells were examined and their anode structures characterized by SEM. Electrochemical performance of the cells was analyzed both before and after the depositions.

Acknowledgements

I would like to extend my gratitude to Dr. Thomas H. Etsell for the continual support, enthusiasm and valuable advice he has offered me during the course of this degree.

Many thanks also go out to the wonderful staff of the Department of Chemical and Materials Engineering. Thank you to Ms. Tina Barker for all of her help with the SEM, to Mr. Shiraz Merali for his help with laboratory equipment and supplies and to Mr. Walter Boddez for his help with all things electrical. To Mr. Mark Haldane, thank you for the many helpful conversations and your aid in the laboratory. I would also like to extend my thanks to my fellow graduate students who became friends.

Last, but certainly not least, I would like to thank my parents, Mary and Walter, and my siblings, Tammy and Michael, for their unfailing support of my goals and their constant encouragement. To Angela and Vicky, thank you for being the friends I can always count on to be my cheerleaders.

Table of Contents

1.0 Introduction.....1

1.1 Types of Fuel Cells.....3

1.1.1 Alkaline Fuel Cell.....3

1.1.2 Polymer Electrolyte Membrane Fuel Cell.....3

1.1.3 Phosphoric Acid Fuel Cell.....4

1.1.4 Molten Carbonate Fuel Cell.....4

1.2 Fuel Cell Applications.....5

2.0 Solid Oxide Fuel Cell.....7

2.1 The Basics.....7

2.2 Electrolyte.....8

2.2.1 Zirconia.....8

2.2.2 Ceria.....10

2.2.3 Bismuth Oxide.....11

2.2.4 Oxygen-Deficient Perovskites.....11

2.2.5 Pyrochlores, BIMEVOX and Others.....12

2.2.6 Composites.....13

2.3 Anode.....14

2.3.1 Metal.....14

2.3.2 Nickel/Yttria-Stabilized Zirconia.....14

2.3.3 Doped Ceria.....15

2.3.4 Perovskite Oxides.....16

2.3.5 Tetragonal Tungsten Bronzes.....17

2.4 Cathode.....18

2.4.1 Lanthanum Oxide Based.....19

2.4.1.1 Lanthanum Manganite.....19

2.4.1.2 Lanthanum Cobaltite.....20

2.4.1.3 Lanthanum Iron Oxide.....20

2.4.1.4 Lanthanum Copper Oxide.....20

2.4.2 Other.....21

2.4.3 Composites.....21

2.5 Interconnect.....21
2.5.1 Ceramic Interconnects.....22
2.5.2 Metallic Interconnects.....23
2.5.2.1 Chromium-Based Interconnects.....23
2.5.2.2 Ferritic Stainless Steel Interconnects.....23
2.5.2.3 Other.....24
2.6 Solid Oxide Fuel Cell Configuration.....24
2.7 Advantages of the Solid Oxide Fuel Cell.....25
2.8 Solid Oxide Fuel Cell Applications.....26

3.0 Vapour Deposition Methods.....27
3.1 Chemical Vapour Deposition (CVD).....27
3.2 Electrochemical Vapour Deposition (EVD).....30
3.3 Polarized Electrochemical Vapour Deposition (PEVD).....32

4.0 Effect of Anode Microstructure on Electrical Performance of Solid Oxide Fuel Cells.....36
4.1 Nickel/Yttria-Stabilized Zirconia.....36
4.1.1 Cermet Preparation.....36
4.1.2 Particle Size and Composition.....40
4.1.3 Sintering Temperature.....43
4.2 Doped Ceria.....45
4.2.1 Samaria-Doped Ceria.....45
4.2.1.1 Metal Electrocatalysts.....45
4.2.1.2 Nickel/Samaria-Doped Ceria.....46
4.2.2 Gadolinia-Doped Ceria.....47
4.3 Nickel/Titanium Dioxide.....48

5.0 Experimental Procedure.....50
5.1 Polarized Electrochemical Vapour Deposition.....50
5.2 Electrochemical Analysis.....53
5.3 Microstructural Examination.....54
5.4 Materials.....54

6.0 Results and Discussion – Yttria-Stabilized Zirconia Depositions.....56
6.1 Effect of Deposition Time.....56
6.1.1 Summary.....79
6.2 Effect of Deposition Bias Voltage and Equilibrium Vapour Pressure Ratio.....80
6.2.1 Experimental Difficulties.....81
6.2.2 750°C Experiments.....82
6.2.2.1 Equilibrium Vapour Pressure Ratio 8:1.....82
6.2.2.2 Equilibrium Vapour Pressure Ratio 5.25:1.....99
6.2.3 800°C Experiments.....107
6.2.3.1 Equilibrium Vapour Pressure Ratio 8:1.....107
6.2.3.2 Equilibrium Vapour Pressure Ratio 5.25:1.....120
6.2.4 Summary.....130

7.0 Results and Discussion – Ceria Depositions.....134
7.1 Effect of Deposition Time.....134
7.2 Effect of $CeCl_3$ Temperature.....148
7.3 Summary.....158

8.0 Conclusions.....160
8.1 Yttria-Stabilized Zirconia Depositions.....160
8.2 Ceria Depositions.....160
8.3 Suggestions for Future Work.....161

References.....162

List of Tables

5-1 Electrolyte disc specifications....54

5-2 Yttrium chloride (YCl_3) analysis....54

5-3 Zirconium chloride ($ZrCl_4$) analysis....55

5-4 Cerium (III) chloride ($CeCl_3$) analysis....55

6-1 Fuel cell samples for YSZ deposition at 900°C and -400 mV....57

6-2 Maximum power density for deposition time increment samples....64

6-3 Elemental analysis from overall EDX analysis for 900°C and -400 mV samples viewed in the SEM....78

6-4 Elemental analysis from EDX point analysis of crystal-like layer....79

6-5 Fuel cell samples for YSZ deposition at 750°C and vapour pressure ratio 8:1....82

6-6 Maximum power density for 750°C and 8:1 samples....89

6-7 Elemental analysis from overall EDX analysis for 750°C and vapour pressure ratio 8:1 samples viewed in the SEM....96

6-8 Fuel cell samples for YSZ deposition at 750°C and vapour pressure ratio 5.25:1....99

6-9 Maximum power density for 750°C and 5.25:1 samples....105

6-10 Fuel cell samples for YSZ deposition at 800°C and vapour pressure ratio 8:1....107

6-11 Maximum power density for 800 °C and 8:1 samples....116

6-12 Elemental analysis from overall EDX analysis for 800°C and vapour pressure ratio 8:1 samples viewed in the SEM....119

6-13 Fuel cell samples for YSZ deposition at 800°C and vapour pressure ratio 5.25:1....120

6-14 Maximum power density for 800°C and 5.25:1 samples....127

6-15 Elemental analysis from overall EDX analysis for 800°C and vapour pressure ratio 5.25:1 samples viewed in the SEM....129

7-1 Fuel cell samples for ceria deposition at 900°C and -100 mV....134

7-2 Maximum power density for 900°C and -100 mV samples....144

7-3 Elemental analysis from overall EDX analysis for 900°C and -100 mV samples viewed in the SEM....147

7-4 Fuel cell samples for ceria deposition at 1000°C and -100 mV....148

7-5 Maximum power density for 1000°C and -100 mV samples....151

7-6 Elemental analysis from overall EDX analysis for 1000°C and -100 mV samples viewed in the SEM....155

List of Figures

2-1 Comparison of the cubic perovskite and tetragonal tungsten bronze structures (a) $SrTiO_3$ and (b) $Sr_{0.6}Ti_{0.2}Nb_{0.8}O_3$ viewed down the [001] axis[35].....18

2-2 Solid oxide fuel cell configurations[18].....25

3-1 Chemical vapour deposition structures (a) domed columnar grains, (b) faceted columnar grains, (c) fine accost grains[55].....29

3-2 Diagrams of the (a) chemical vapour deposition and (b) scale growth steps of electrochemical vapour deposition[64].....31

3-3 SEM micrographs of the platinum anode before (a, c) and after (b, d) deposition of 5.5YSZ by PEVD[70].....35

4-1 Comparison of the microstructure of Ni-YSZ anodes prepared by spray pyrolysis (a) NiO-YSZ composite powder, (b) Ni-YSZ anode after reduction[74].....38

4-2 Comparison of the final anode microstructure for the two Ni-YSZ anode cermets (a) first type, (b) second type[85].....41

4-3 Cracking of NiO-YSZ cermets sintered to YSZ electrolytes at temperatures of (a) 1100°C and (b) 1300°C[92].....44

4-4 SEM micrographs of the cross sections of the Ni-GDC anodes fabricated from (a) commercial NiO and commercial GDC, (b) GNP NiO and commercial GDC, (c) commercial NiO and GNP GDC, (d) GNP NiO and GNP GDC[104].....49

5-1 Diagram of solid oxide fuel cell (a) side view of cell with no reference electrodes, (b) downward view of cell with reference anode.....50

5-2 Diagram of closed end of alumina tube (downward view).....51

5-3 Diagram of alumina tube/fuel cell assembly (a) side view of assembly, (b) cut-away view showing position of lead wires within tube.....52

5-4 Cut-away side view of PEVD reactor set-up.....52

6-1 Corrected polarization curves for YSZ deposition at 900°C and -400 mV by number of depositions.....57

6-2 Corrected polarization curves for YSZ deposition at 900°C and -400 mV by sample.....60

6-3 Effect of overvoltage on polarization and power curves[6].....62

6-4 Corrected power curves for YSZ deposition at 900°C and -400 mV by number of depositions.....65

6-5 Corrected power curves for YSZ deposition at 900°C and -400 mV by sample.....67

6-6 SEM secondary electron images of solid oxide fuel cell anode after preparation (plan view)....71
6-7 SEM secondary electron images of solid oxide fuel cell anode after preparation (cross section view)....72
6-8 SEM secondary electron images of sample 03-08 (plan view)....73
6-9 SEM secondary electron images of sample 03-10 (plan view)....74
6-10 SEM secondary electron images of sample 03-10 (cross section view)....75
6-11 SEM secondary electron images of sample 03-01 (plan view)....76
6-12 EDX overall spectra for sample 03-10....78
6-13 EDX point analysis spectra for sample 03-10....80
6-14 SEM secondary electron images of 0.508 mm platinum wire (a) appearance before failure, (b) appearance after failure....83
6-15 Corrected polarization curves for YSZ deposition at 750°C and vapour pressure ratio 8:1 by number of depositions....84
6-16 Corrected polarization curves for YSZ deposition at 750°C and vapour pressure ratio 8:1 by sample....86
6-17 Corrected power curves for YSZ deposition at 750°C and vapour pressure ratio 8:1 by number of depositions....90
6-18 Corrected power curves for YSZ deposition at 750°C and vapour pressure ratio 8:1 by sample....92
6-19 SEM secondary electron image of sample 04-02 (plan view)....94
6-20 SEM secondary electron image of sample 04-03 (plan view)....95
6-21 SEM secondary electron image of sample 04-06 (plan view)....95
6-22 EDX overall spectra for sample 04-02....97
6-23 Corrected polarization and power curves for operating temperature cycling testing for sample 04-06....98
6-24 Corrected polarization curves for YSZ deposition at 750°C and vapour pressure ratio 5.25:1 by number of depositions....100
6-25 Corrected power curves for YSZ deposition at 750°C and vapour pressure ratio 5.25:1 by number of depositions....102
6-26 SEM secondary electron image of sample 05-09 (plan view)....106
6-27 EDX overall spectra for sample 05-09....106
6-28 Corrected polarization and power curves for operating temperature cycling testing for sample 05-09....108

6-29 Corrected polarization curves for YSZ deposition at 800°C and vapour pressure ratio 8:1 by number of depositions.....109
6-30 Corrected polarization curves for YSZ deposition at 800°C and vapour pressure ratio 8:1 by sample.....111
6-31 Corrected power curves for YSZ deposition at 800°C and vapour pressure ratio 8:1 by number of depositions.....113
6-32 Corrected power curves for YSZ deposition at 800°C and vapour pressure ratio 8:1 by sample.....115
6-33 SEM secondary electron image of sample 04-07.....117
6-34 SEM secondary electron image of sample 05-05 (plan view).....118
6-35 EDX overall spectra for sample 05-05.....119
6-36 Corrected polarization and power curves for operating temperature cycling testing for sample 05-05.....121
6-37 Corrected polarization curves for YSZ deposition at 800°C and vapour pressure ratio 5.25:1 by number of depositions.....122
6-38 Corrected power curves for YSZ deposition at 800°C and vapour pressure ratio 5.25:1 by number of depositions.....124
6-39 SEM secondary electron image of sample 05-06 (plan view).....128
6-40 SEM secondary electron image of sample 05-07 (plan view).....128
6-41 EDX overall spectra for sample 05-07.....129
6-42 Corrected polarization and power curves for operating temperature cycling testing for sample 05-06.....131
6-43 Corrected polarization and power curves for operating temperature cycling testing for sample 05-07.....132
7-1 Cerium (III) chloride equilibrium vapour pressure from various sources[104-108].....135
7-2 Corrected polarization curves for ceria deposition at 900°C and -100 mV by number of depositions.....135
7-3 Corrected polarization curves for ceria deposition at 900°C and -100 mV by Sample.....138
7-4 Corrected power curves for ceria deposition at 900°C and -100 mV by number of depositions.....140
7-5 Corrected power curves for ceria deposition at 900°C and -100 mV by sample.....142
7-6 SEM secondary electron image of sample 05-10 (plan view).....145
7-7 SEM secondary electron image of sample 05-13 (plan view).....145

7-8 SEM secondary electron image of sample 05-11.....146
7-9 EDX overall spectra for sample 05-10.....147
7-10 Corrected polarization curves for ceria deposition at 1000°C and -100 mV by number of depositions.....149
7-11 Corrected polarization curves for ceria deposition at 1000°C and -100 mV by Sample.....150
7-12 Corrected power curves for ceria deposition at 1000°C and -100 mV by number of depositions.....152
7-13 Corrected power curves for ceria deposition at 1000°C and -100 mV by sample.....153
7-14 Impedance analysis for ceria deposition at 1000°C and -100 mV by sample.....154
7-15 SEM secondary electron image of sample 05-14.....156
7-16 SEM secondary electron image of sample 05-15 (plan view).....157
7-17 EDX overall spectra for sample 05-14.....158

1.0 Introduction

Today's society is very dependent on the use of hydrocarbon fuels to provide power. These fuels (such as natural gas, coal, methane, etc) need to undergo combustion in order to release the energy stored within. The products of hydrocarbon combustion, carbon dioxide (CO_2) and water vapour, accumulate in the earth's atmosphere along with other "greenhouse" gases, such as nitrous oxide (NO) and methane (CH_4).[1] These gases trap energy from the sun and warm the earth to a livable temperature by the "greenhouse effect".[1] However, greater amounts of greenhouse gases than ever before are accumulating in the atmosphere and are believed to be causing an increase in the temperature of the earth.[1] Concerns over the effect of a rising global temperature on the world's ecosystems have prompted research into alternative methods of generating power that would be less destructive to the planet.

One possible solution lies in the use of fuel cells. Fuel cells were first discovered by Sir William Robert Grove in the mid-1800s.[2] Through the understanding that electricity was required to separate water into its constituent elements of hydrogen and water, Grove theorized that their combination would generate electricity.[2] His theory was proven when he constructed the first fuel cell, made of platinum electrodes and a sulphuric acid electrolyte, with the end of one electrode sealed in hydrogen and the other in oxygen.[2] While research into fuel cells continued for the next 100 years, significant efforts did not arise again until the 1960s with the development of the alkaline fuel cell by Francis Thomas Bacon, which was licensed by Pratt & Whitney for use in the Apollo spacecraft.[3]

While there is more than one type of fuel cell available, each type performs the same basic function: the generation of electricity via an electrochemical reaction. However, fuel cells do not require that the fuel undergo combustion prior to the reaction.[4] The main components of a fuel cell are the electrolyte and the electrodes (anode and cathode). The role of the electrolyte is to be selectively permeable to a particular ion, which is dependent on the type of electrolyte used.[5] The anode, or fuel electrode, is the site of oxidation in the fuel cell. Fuel, typically hydrogen, is provided to the anode, where the H_2 molecules are dissociated and electrons are stripped from the hydrogen atoms, forming hydrogen ions (H^+).[6] These electrons are released to the electric circuit and thus are the source of the electricity provided by the fuel cell.[5] The cathode is the site of reduction in the fuel cell. Oxygen, usually from air, is provided to the cathode where it picks up two electrons from the electric circuit to become O^{2-}, and it may then either pass through the electrolyte to join with hydrogen ions, or join with hydrogen ions that have passed through the

electrolyte.[5] In either case, water is the product of the electrochemical reactions occurring in the fuel cell.

Since an individual fuel cell does not provide enough power by itself, cells are "stacked". This stacking combines the power output of more than one cell, much like a typical battery. In order to accomplish this, an additional component, called an interconnect, is required. The function of this component is two-fold: to provide an electrical connection between the anode of one fuel cell and the cathode of the next, and to physically separate and protect the anode from the oxidizing atmosphere of the cathode and the cathode from the reducing atmosphere of the anode.[7]

This thesis focuses on the optimization of the SOFC anode through the deposition of a ceramic layer onto a metallic anode by polarized electrochemical vapour deposition (PEVD). By depositing a thin, ionically conducting layer over a continuous metallic phase, the three-phase region will be expanded to the entirety of the anode (rather than just the anode-electrolyte interface) while resistance losses should be decreased by having continuous phases.[8] It is also hoped that the operating temperature of the SOFC can be reduced by this anode optimization, since the lowering of resistance losses will make up for the increased overpotential at lower temperatures. Additionally, thermal expansion coefficients of the electrolyte and anode will be more inline, reducing thermal stresses that may be induced at operating temperature.[8] The metallic phase will be protected from sintering, evaporation and poisoning (due to impurities in the fuel stream).[8]

The remainder of this chapter gives a brief overview of the types of fuel cells and some of their applications. The literature survey, chapters 2 through 4, focuses on the solid oxide fuel cell, vapour deposition methods and the effect of anode microstructure on electrical performance. Experimental results for the deposition of yttria-stabilized zirconia (YSZ) and ceria (CeO_2) by PEVD are presented and discussed in chapters 6 and 7, respectively. The study of YSZ deposition focuses on the effect of various experimental parameters on the resulting deposit and is a continuation of the work carried out by Tang[9], Young[10] and Haldane[11]. The study of ceria deposition presents preliminary results of the use of cerium (III) chloride ($CeCl_3$) to deposit a ceria layer by the PEVD method. The final chapter presents conclusions and suggestions for future work.

1.1 Types of Fuel Cells

1.1.1 Alkaline Fuel Cell

The different types of fuel cells available are named according to the type of electrolyte used. The alkaline fuel cell (AFC) uses an aqueous potassium hydroxide (KOH) electrolyte with carbon electrodes supporting a platinum catalyst.[6] Depending on the concentration of the electrolyte, AFCs have an operating temperature of 60-90°C (35-50 wt% KOH) or ~260°C (85 wt% KOH).[8] The cells require that very pure hydrogen and oxygen be used as fuel and oxidant, respectively, as the reaction pathways can be easily blocked by acidic impurities present in either stream.[6] This type of electrolyte allows for the transport of hydroxide ions (OH^-) from the cathode side to the anode side, thereby producing water at the anode. The anode and cathode reactions are:

$$\text{Anode: } H_2 + 2(OH^-) \rightarrow 2H_2O + 2e^- \qquad \text{Cathode: } \tfrac{1}{2}O_2 + H_2O + 2e^- \rightarrow 2(OH^-)$$

Electrodeposited magnesium is the common choice for interconnects for AFCs, although carbon can be used for cells operating at temperatures around 65°C.[2]

1.1.2 Polymer Electrolyte Membrane Fuel Cell

The polymer electrolyte membrane fuel cell (PEMFC) uses a polymer membrane that conducts hydrogen ions as the electrolyte.[6] The polymer most commonly used for this type of fuel cell is Nafion® 117 manufactured by Dow Chemical.[12] The electrodes used are gas-diffusion electrodes made up of carbon and platinum catalyst particles.[6] The PEMFC has a similar operating temperature as the AFC, at about 80°C. The electrolyte is better able to handle carbon dioxide, thus allowing the hydrogen used as fuel to be derived from hydrocarbon fuels, with oxygen being fed to the cathode side.[13] However, carbon monoxide levels should be kept below 10pmm[13] due to deactivation of the platinum catalyst when CO is adsorbed.[12] Since the electrolyte allows for the transport of hydrogen ions, water is formed at the cathode side of the fuel cell. The anode and cathode reactions are:

$$\text{Anode: } H_2 \rightarrow 2H^+ + 2e^- \qquad \text{Cathode: } \tfrac{1}{2}O_2 + 2H^+ + 2e^- \rightarrow H_2O$$

PEMFCs require close attention to the water content of the polymer membrane, as its dehydration decreases its ionic conductivity.[6] The current material choice for the interconnects of PEMFCs is machined graphite.[12]

1.1.3 Phosphoric Acid Fuel Cell

The phosphoric acid fuel cell (PAFC) uses 100 wt% phosphoric acid (H_3PO_4) immobilized in a matrix as an electrolyte.[6] As with the AFC and PEMFC, carbon substrates with platinum catalysts are used as electrodes.[6] The operating temperature of this cell is somewhat higher than the AFC and PEMFC at ~200°C.[4] The PAFC can use reformed fuels or clean coal gas as fuel, as long as impurities such as carbon monoxide and sulphur-containing compounds are kept at low levels, since they deactivate the platinum catalyst.[6] Ammonia (NH_3) is an impurity that acts as a fuel, but its reaction with the electrolyte produces monoammonium phosphate, $(NH_4)H_2PO_4$, a phosphate salt which decreases the oxygen reduction rate.[6] As with the PEMFC, the PAFC electrolyte conducts hydrogen ions from the anode side to the cathode side, thus forming water at the cathode side of the fuel cell. The anode and cathode reactions are:

- Anode: $H_2 \rightarrow 2H^+ + 2e^-$ Cathode: $\frac{1}{2}O_2 + 2H^+ + 2e^- \rightarrow H_2O$

Also similar to the PEMFC, interconnect materials for the PAFC are based on graphite. The material commonly used is based on graphite resin mixtures that are carbonized and then heat treated to improve corrosion resistance.[12]

1.1.4 Molten Carbonate Fuel Cell

The molten carbonate fuel cell (MCFC), one of the newer additions to the types of fuel cells available, uses carbonate salts immobilized in a ceramic matrix as its electrolyte.[6] The carbonate salts commonly used are either a mixture of 62 mol% Li_2CO_3 and 38 mol% K_2CO_3, or a mixture of 50 mol% Li_2CO_3 and 50 mol% Na_2CO_3.[6] The electrodes consist of nickel for the anode and nickel oxide for the cathode (typically formed by the oxidation of nickel at startup).[14] As a result of the use of carbonate salts as the electrolyte, this type of fuel cell requires a significantly higher operating temperature than the three cells previously discussed in order to achieve the required conductivity (along with the requirement that the salt be in a molten state), and is usually in the range of 650°C.[6] This higher operating temperature lessens the concern of impurities in the fuel streams as noble-metal catalysts are not required since the reaction kinetics are much higher at this operating temperature. In the case of the MCFC, carbon trioxide ions (CO_3^{2-}) are the mobile carrier, and are formed from the reaction of oxygen and carbon dioxide with electrons from the hydrogen supplied to the anode; their removal results in the production of water and carbon dioxide at the anode.[6] However, it should be taken into consideration that CO_3^{2-} ions are large ions and smaller ions, such as Li^+, Na^+ and K^+ ions, move more easily through the molten salt,

and will more likely act as the mobile carrier. Proceeding with normal convention though, the anode and cathode reactions are:

Anode: $H_2 + CO_3^{2-} \rightarrow H_2O + CO_2 + 2e^-$ Cathode: $\frac{1}{2} O_2 + CO_2 + 2e^- \rightarrow CO_3^{2-}$

The electrolyte material and its operating temperature for this type of fuel cell makes the material choice for the interconnect more of a challenge. Interconnects for the MCFC are usually fabricated from 310S or 316L austenitic stainless steel, with a nickel coating on the anode side of the interconnect.[14]

In addition to these four types of fuel cells, the solid oxide fuel cell (SOFC) is also a current focus of fuel cell research. The next chapter provides a more detailed description of the operation of the SOFC and materials used for its major components.

1.2 Fuel Cell Applications

The applications for fuel cells are as varied as the types of fuel cells currently available. The AFC requires very pure hydrogen and oxygen as fuel, which makes it difficult for use in everyday, common applications. This type of cell has been used in both underwater and space applications. It is particularly well suited for space applications as its by-product of water can by used by the astronauts. Recently, it has been considered as a replacement for the traditional automobile battery.

However, the PEMFC has been more successful as a potential replacement for the automobile battery due to its low operating temperature. Companies such as Ballard Power Systems, as well as automakers Ford and Volkswagen, are continuing research in this area.[15] These cells are also being considered for both stationary and portable power systems.

The PAFC is currently the most commercially used fuel cell today, in applications similar to the PEMFC. Due to their higher operating temperature, they take more time to warm up compared to the PEMFC[16], but run at a higher overall efficiency when their waste heat is used in cogeneration applications.[4] In cogeneration applications, the efficiency of the PAFC may reach up to 80%.[16]

Also excellent for cogeneration applications is the MCFC. With an operating temperature even

higher than that of the PAFC, even more waste heat is available to do work on other processes. These cells are commonly used for stationary power plants and have been tested in Japan and the United States.[17] The efficiency of these cells may reach up to 85% when used in cogeneration applications.[4]

2.0 Solid Oxide Fuel Cell

2.1 The Basics

The Solid Oxide Fuel Cell (SOFC) is composed of a ceramic electrolyte, anode, cathode and interconnect. There are two types of SOFCs, based on the kind of electrolyte is used: the proton-conductor SOFC and the oxygen-ion-conductor SOFC.[18] The proton-conductor SOFC operates by conducting hydrogen ions (H^+) through the electrolyte from the anode to the cathode. The hydrogen is supplied to the anode, where the molecules are dissociated and the individual atoms are oxidized. The electrons then travel through the external circuit to the cathode side of the fuel cell, while the hydrogen ions travel through the electrolyte to the cathode. Oxygen is supplied to the cathode, and there the hydrogen ions react with the oxygen molecules that have been reduced by the electrons from the external circuit to produce water.

In contrast, the oxygen-ion-conductor SOFC conducts oxygen ions (O^{2-}) through the electrolyte from the cathode to the anode. As for the proton-conductor SOFC, hydrogen is supplied to the anode side of the fuel cell, where it is oxidized and the electrons are released to the external circuit. At the cathode, oxygen molecules (either from pure oxygen or air) undergo reduction by the electrons from the external circuit and then travel through the electrolyte to the anode. At the anode, the oxidized hydrogen reacts with the oxygen ions to form water. If carbon monoxide is present in the fuel, carbon dioxide will also be produced at the anode.[18] Oxygen-ion-conductor SOFCs are the more commonly researched type of solid oxide fuel cell for commercial applications.

As with the molten carbonate fuel cell, the solid oxide fuel operates at a high temperature, usually in the range of 1000°C.[6] This is beneficial to the cell, as it does not require expensive catalysts to be used to speed up the anode and cathode reactions; reaction kinetics are sufficient at this temperature. Another benefit of this high operating temperature, along with the oxygen ion conductivity of the electrolyte, is that pure hydrogen is not necessary to fuel the cell, but rather hydrocarbon fuels such as methane, diesel oils and coal gas can be processed directly.[6] However, sulphur impurity levels should be closely monitored and should be less than 10 ppm, or cell performance degradation will occur.[19] The SOFC typically operates at an efficiency of 55-65%[6], though higher efficiencies have been achieved when the waste heat is used for cogeneration applications.

While cell operating temperature has typically hovered in the 1000°C range, recent efforts have

been made to reduce this operating temperature to as low as 600°C.[6,18] The goal of this temperature reduction is to simplify the materials requirements for the cell components, thus reducing the fabrication cost and making the cells more commercially viable. A lower operating temperature will also increase the chances for long-term stability of the cells.

A brief review of the materials commonly used as the electrolyte, anode, cathode and interconnect for the solid oxide fuel cell follows. Also included is information on new materials currently being researched for these components.

2.2 Electrolyte

The material chosen as the solid oxide fuel cell electrolyte must meet several criteria before it can be considered as an option. Since most SOFCs researched are oxygen-ion-conductors, it is necessary that the material have a high oxygen-ion conductivity, σ_o, and a low electronic conductivity, σ_e, at the fuel cell operating temperature.[20-22] Goodenough specifies that the oxygen-ion conductivity should be greater than 10^{-2} S/cm.[20] Another factor that is highly important in the selection of an electrolyte material is its thermal expansion coefficient (TEC). It is necessary that this coefficient be very close to that of the other cell components[23], though quite often the other fuel cell components are selected to have a thermal expansion coefficient matching that of the electrolyte. In addition to these two important criteria, the fuel cell electrolyte must be both chemically and mechanically stable.[20,22] The electrolyte must not form reaction products with the other cell components that will reduce the performance of the SOFC, and it must have strength and toughness to structurally support the fuel cell stack.[20,22] The chemical and mechanical stability must extend through a range of temperatures, not just at the operating temperature, because of the various fabrication steps the cell goes through.[22] The electrolyte must have good gas tightness to prevent the diffusion of oxygen or fuel from the cathode and anode, respectively, to the other side of the cell.[21]

2.2.1 Zirconia

Zirconia (ZrO_2) is the most commonly used material for the solid oxide fuel cell electrolyte. While pure zirconia has a low ionic conductivity (it is mainly an electronic conductor), doping of the material significantly increases its conductivity.[22] At room temperature, zirconia is a monoclinic phase and undergoes a displacive transformation to the tetragonal phase at 1170°C, then to the cubic phase at 2370°C before melting at 2680°C.[24] Though the tetragonal phase has a higher strength and toughness than the cubic phase, the latter is more commonly used due to the

instability of the tetragonal phase in a moist environment and its primarily electronic conduction.[20]

The high-temperature phases of zirconia, namely the tetragonal and cubic phases, can be stabilized to room temperature with the addition of one or more dopants.[20,22] These dopants include Y_2O_3, Yb_2O_3, Sc_2O_3, Gd_2O_3, Dy_2O_3, Nd_2O_3, Sm_2O_3, CaO and MgO.[22] When these dopants are added to zirconia, they substitute for the Zr^{4+} cation in the lattice structure.[20,22] These cations are larger and have a lower valency state than the Zr^{4+} cation, which stabilizes the high temperature phases and introduces oxygen vacancies into the lattice, thus increasing the ionic conductivity of the zirconia.[20,22] In order to achieve maximum ionic conductivity, the amount of trivalent dopant used should give an oxygen vacancy concentration of 3.5-4% and the amount of divalent dopant used should give an oxygen vacancy concentration of 6-7%.[22]

In addition to having sufficient ionic conductivity to act as an SOFC electrolyte material, zirconia materials show good chemical stability. They are inert to both the reactants used in the SOFC, as well as the usual electrode materials.[20]

Yttria-stabilized zirconia (YSZ) is the most commonly used electrolyte for solid oxide fuel cells. The use of yttria (Y_2O_3) as dopant to stabilize zirconia allows for either the tetragonal or cubic phase to be stabilized.[20,22] In general, 8-9 mol% of yttria is required to stabilize the cubic phase, while only 2-3 mol% is required to stabilize the tetragonal phase.[20,22] Yttria-stabilized zirconia will provide sufficient ionic conductivity for its role as the SOFC electrolyte as long as it is fabricated to be thin and dense, with little to no grain boundary impurities.[20] However, one disadvantage of using YSZ as an electrolyte is that an operating temperature in the range of 1000°C is required for the material to have sufficient ionic conductivity.[21]

An alternative to yttria-stabilized zirconia is scandia-stabilized zirconia (SSZ). The typical requirement is 8-9 mol% of scandia (Sc_2O_3) to fully stabilize zirconia in its cubic phase.[20,22] While scandia gives the highest ionic conductivity of the stabilized zirconias (0.32 S/cm for 7.8 mol% Sc_2O_3 at 1000°C)[7], it is an expensive dopant and thus not regularly used.[20,22] The ionic conductivity can be attributed to the fact that the Sc^{3+} cation is most closely matched in size to the Zr^{4+} cation.[20] However, the advantage of SSZ having the highest ionic conductivity is diminished by the fact that the performance of cells using this electrolyte deteriorates over time when operated at 1000°C.[22]

Along with the use of yttria and scandia as dopants to stabilize zirconia, rare earth oxides are used. These generally require a dopant level of 8-12 mol% to stabilize zirconia in its cubic phase.[20]

2.2.2 Ceria

A material that has seen a significant amount of research in recent years as a potential SOFC electrolyte material is ceria (CeO_2). The appeal of ceria is that the fuel cell could be operated at a lower temperature than with yttria-stabilized zirconia as the electrolyte because ceria-based oxides achieve sufficient ionic conductivity at temperatures approximately 200°C lower than YSZ.[23]

Ceria has a fluorite structure, which contains cations in an face-centered cubic (FCC) structure with anions in the tetrahedral interstices.[24] As in the case of zirconia, ceria is doped with various compounds in order to increase its ionic conductivity. The principle is the same: doping with a lower valence cation increases the oxygen vacancies, improving the diffusion of oxygen ions.[21,25] The mechanism by which the doping increases the ionic conductivity of ceria may not only be due to the trapping of isolated oxygen vacancies.[20] Goodenough postulates that the dopant ions may act "...as nucleating centers for the formation of ordered-vacancy clusters."[20] The typical ionic conductivity of undoped ceria at a temperature of 800°C is in the range of 3.0×10^{-4} S/cm, but with doping it jumps by over two orders of magnitude to the range of 10.0×10^{-2} S/cm.[25] As with the doping of zirconia, the highest ionic conductivity is achieved when the size of the doping ion is as close as possible to the size of the ion being replaced.[21] Since the samarium ion (Sm^{3+}) and gadolinium ion (Gd^{3+}) have the closest matching ionic radius to the cerium ion, their use as dopants results in doped-ceria oxides with the highest ionic conductivity.[20-22]

Ceria-based oxides have been found to be chemically inert to the materials used as SOFC electrodes.[20] However, at low oxygen partial pressures, doped ceria can undergo reduction from Ce^{4+} to Ce^{3+}, which leads to an increase in electronic conduction by the material.[21-23] With the electrolyte a partial electronic conductor, the cell potential is decreased, thus giving poor performance.

As mentioned, the use of samaria (Sm_2O_3) and gadolinia (Gd_2O_3) as dopants results in ceria-based oxides with the highest ionic conductivity. Which of the two dopants results in the highest ionic

conductivity is not certain, as Goodenough states $Sm_{0.2}Ce_{0.8}O_2$ (SDC) gives the highest[16], while Ball and Stevens state Gd-doped ceria (GDC) does.[26] It has been reported that GDC has a low fracture strength and toughness, as well as being less stable at the oxygen partial pressures experienced by the fuel cell.[21,26] Another consideration in the use of samaria and gadolinia dopants is their cost. They are relatively expensive materials, so an alternate option is to use calcium oxide (CaO) instead.[23] Calcium-doped ceria (CDC) has been found to give a higher ionic conductivity at intermediate temperatures when compared to GDC.[23,27]

2.2.3 Bismuth Oxide

The δ-phase of bismuth oxide (Bi_2O_3), which is stable at temperatures between 730°C and 804°C, shows the highest ionic conductivity at 800°C, with a value of 2.3 S/cm.[20] The structure of δ-Bi_2O_3 is "...fluorite-related with oxide ions randomly occupying ¾ of the tetrahedral interstices of the face-centered cubic Bi^{3+}-ion sublattice."[20] In order to stabilize this material to room temperature, dopants such as WO_3, Y_2O_3, Gd_2O_3, Dy_2O_3, Er_2O_3, Nb_2O_5 and Ta_2O_5 are used.[20,22] However, as the Bi^{3+} ions are substituted by other cations, the conductivity of δ-Bi_2O_3 decreases, so it is necessary to use the least dopant possible to stabilize the δ-phase.[20] This is achieved in $Bi_{0.8}Er_{0.2}O_{1.5}$.[20] Doped Bi_2O_3 yields an order of magnitude increase in conductivity at 700-800°C.[22] However, the use of doped-bismuth oxides as SOFC electrolytes is limited by their poor stability in a reducing environment and interactions with other fuel cell components.[20,22] In addition, these materials show low strength and toughness.[22]

2.2.4 Oxygen-Deficient Perovskites

The possibility of using oxygen-deficient perovskites as SOFC electrolyte materials has also been investigated. The perovskite structure, of the general formula ABO_3, has large cations at the corners and a small cation at the center of the cube, with anions in the faces of the cube.[24] Materials with this type of structure are of interest as SOFC electrolytes because the structure can accommodate a large concentration of oxygen vacancies.[20]

One of the most common perovskites studied as a potential SOFC electrolyte is lanthanum gallate, $LaGaO_3$. Several different cations can be used to substitute for the La^{3+} (A-site) ion and the Ga^{3+} (B-site) ion, with Sr^{2+} or Ba^{2+} as common dopants on the A-site, and Mg^{2+} or Mn^{2+} as common dopants on the B-site.[20,22,28] The cations used most often are Sr^{2+} and Mg^{2+} in amounts of 10-20 mol% each.[22,29] It has been found that substituting Mn^{2+} for Mg^{2+} on the B-site can raise the ionic conductivity and lower the activation energy.[29] The optimum composition found

to date is $La_{0.8}Sr_{0.2}Ga_{0.83}Mg_{0.17}O_{2.815}$, which is commonly known as LSGM.[20]

An attractive feature of these materials is their pure oxygen-ion conductivity.[20] $LaGaO_3$-based materials show an ionic conductivity at 800°C that is comparable to that shown by YSZ at temperatures around 1000°C.[28] This is attributed to the high oxygen ion mobility and oxygen vacancy concentration the $LaGaO_3$-based oxides have compared to YSZ.[28] In many cases, the conductivity of $LaGaO_3$-based materials show a conductivity two times greater than that achievable by 8 mol% YSZ at the same operating temperature.[22,29]

While $LaGaO_3$-based oxides have been shown to be stable when hydrocarbon fuels are used, problems can be encountered. Oxygen-ion transport can be blocked if ceria-based materials are used as a layer between composite nickel anodes and the LSGM electrolyte, as the La^{3+} ions can form phases at the ceria-LSGM interface.[20] Also, the cost of gallium compounds is high and these materials show low mechanical strength at the fuel cell operating temperature.[22]

2.2.5 Pyrochlores, BIMEVOX and Others

Pyrochlores, of the chemical formula $A_2B_2O_7$, may have the potential to be SOFC electrolytes. The pyrochlore structure is similar to the fluorite structure, with the exception that there are two types of cations (A and B) and one less anion. It is the missing anion that may give this material the required property of high oxygen-ion conductivity for SOFC electrolyte applications.[20] More research still needs to be conducted.

The γ-phase of $Bi_2VO_{5.5}$, present at temperatures greater than 570°C, has a very high oxygen-ion conductivity.[20] Stabilizing this phase by the substitution of vanadium by other elements may lead to the possibility of a high ionic conductivity electrolyte for the solid oxide fuel cell.[20] These materials have been dubbed "BIMEVOX", where "ME" is replaced by the dopant metal atom.[20] To date, BICUVOX-10 ($Bi_2V_{0.9}Cu_{0.1}O_{5.35}$) has shown the highest ionic conductivity, similar to that of $Bi_2V_{0.85}Ti_{0.15}O_{5.425}$.[20] However, BICUVOX has the disadvantage of undergoing reduction when oxygen partial pressures are less than 10^{-2} atm, which may form irreversible phases at the anode.[20] The desired properties of chemical stability, sufficient mechanical strength and a TEC close to that of other commonly used SOFC components are not present in this material.[20]

Thoria (ThO_2) and hafnia (HfO_2) doped with aliovalent metal oxides have also been investigated

as possible SOFC electrolytes. Unfortunately, while stable in a reducing atmosphere, these materials show an ionic conductivity lower than that of zirconia-based systems.[22]

2.2.6 Composites

Instead of depending on a single material to satisfy the requirements of an electrolyte for the solid oxide fuel cell, research has been undertaken to consider composite materials that would serve the purpose. In theory, the composite would have the desired properties from two or more individual materials. The composite materials are especially of interest in designing low operating temperature SOFCs.

Doped cerias, particularly gadolinia-doped ceria (GDC) and samaria-doped ceria (SDC), have been investigated for use as composite electrolyte materials. Luo et al[21] have studied the effect of combining various ratios of GDC and 3% YSZ. Samples containing 3YSZ had a lower thermal expansion coefficient than 100 wt% GDC (lowest for the sample with 30 wt% GDC), though the conductivity of the material gradually decreased with GDC additions.[21] However, the conductivity of the samples did increase with increasing temperature, as would be expected.[21] In the low temperature range, 200-500°C, pure GDC had higher conductivity than either the pure 3YSZ or composite samples.[21] Ball and Stevens[26] have also investigated the composite material formed from 20% GDC and 3YSZ. Their work found that a decrease in the fracture strength of the material occurred as the amount of 3YSZ was increased from 1-5 wt%, then stabilized.[26] No evidence of a correlation between activation energy and weight fraction of 3YSZ particles was found.[26]

Zhu et al[28] have studied the effect of adding alkaline carbonates to SDC, and found that a conductivity of greater than 10^{-2} S/cm was achievable at temperatures greater than 300°C. These composites were also found to be chemically stable with respect to each other, since no reaction products or change in phase structure was observed between the components.[28]

Zhu et al[23] have also considered the possibility of combining ceria with oxyacid salts, as well as halides, carbonates and hydroxides. Ceria-salt composites have both ionic and protonic conduction, and may suppress electronic conduction while enhancing material stability, thus improving the performance of the fuel cell.[23,26] Additionally, the interfaces between these materials can improve performance with greater ionic conductivity and diffusivity.[29]

2.3 Anode

The anode is the site of fuel oxidation in the solid oxide fuel cell. This component has several duties it must fulfill, the most important being that it provide sites for the electrochemical reaction (oxidation) to occur.[30] The microstructure must allow for the fuel to reach the reaction sites, as well as allow the by-products of the reaction to be removed from these sites, and it must also provide a path for electron transport to the interconnect.[30]

Some requirements for the anode material are similar to requirements for other fuel cell components. It must be chemically stable with any components it comes in contact with (typically the electrolyte and interconnect) and have a similar thermal expansion coefficient.[30] Also, it must have a high electrocatalytic activity for the oxidation of fuel gases, and ideally be a mixed electronic and ionic conductor (MEIC) with predominant electronic conduction.[22,30] Sufficient porosity is necessary to enable the transport of fuel to the reaction sites.[30] Carburization and sulphidation resistance of the material are important if hydrocarbon fuels are being used, and as with all SOFC components, low cost and ease of fabrication are highly desirable.[30]

The most commonly used anode material to date with hydrogen as fuel is a cermet composed of nickel and 8 mol% yttria-stabilized zirconia (Ni-8YSZ). However, current research into SOFCs is quite focused on the use of hydrocarbon fuels such as methane (CH_4) at the anode.

2.3.1 Metal

Nickel, cobalt and ruthenium metals are all stable in the reducing environment of the SOFC anode and may be used as anode materials.[22] However, pure metal anodes are seldom used for solid oxide fuel cells because several problems are associated with them that lead to poor cell performance. These problems include a high sintering rate, which leads to grain growth and shrinkage, as well having thermal expansion coefficients that are quite a bit higher than that of the electrolyte.[22]

2.3.2 Nickel /Yttria-Stabilized Zirconia

As mentioned previously, a nickel-8YSZ cermet is the most commonly used solid oxide fuel cell anode at present. The two components are chosen for their desirable properties. Nickel is an electrocatalyst for the oxidation of hydrogen.[30] Ytrria-stabilized zirconia is chosen as the second component of the cermet because it helps to bring the TEC of the material closer to that of the

electrolyte, as well as acting as a framework for the nickel particles.[22,30] It also provides the benefit of preventing the nickel particles from coarsening too much, thus improving the long-term stability of the anode.[22,30] Since the YSZ is an ionic conductor, the cermet is more of a mixed electronic and ionic conductor material, so the YSZ increases the triple-phase boundary area of the cell.[22,30] The materials are low-cost and chemically stable in the fuel environment.[30] Thus the combination of the two materials creates a cermet that strongly fulfills the requirements for an SOFC anode.

In order to have suitable performance from this anode material, the nickel content in the cermet must be at least 30 vol%, with typical amounts usually in the 40-45 vol% range.[22,30] The specification of 30 vol% arises from percolation theory, since it is at this point where a strong increase in cermet conductivity occurs.[18] Percolation theory is important since the total conductivity of the cermet is most dependent on electronic conduction through the metallic phase.[22] In addition, a porosity of 30 vol% or greater is also required.[30]

Unfortunately, there are problems associated with the use of Ni-8YSZ as an anode material. The most significant of these is the tendency of nickel particles to agglomerate as operating time increases, which results in a decrease in the triple-phase boundary area and conductivity, and thus cell performance.[30] The oxidation of nickel (when hydrogen is used as fuel) over long-term operation, as well as low carburization and sulphidation resistance also reduce cell performance.[30] In addition, nickel forms Ni-Cr spinels when it reacts with chromia formed from interconnect materials.[30] It has been found that additions of MgO, TiO_2, Mn_3O_4 and Cr_2O_3 to the anode cermet are effective in reducing the degree of coarsening that occurs in the nickel particles while at the same time improving the sintering of YSZ.[30] Doping the cermet with molybdenum or gold helps resist deactivation of the cell by carbon deposition, while the addition of CeO_2 or TiO_2 to the YSZ increases its electrical conductivity.[22,30]

2.3.3 Doped Ceria

In the search for a material that can provide mixed electronic and ionic conductivity in order to expand the electrochemically active area of the fuel cell anode, doped ceria has found some success. Both doped and undoped ceria provide MEIC at low oxygen partial pressures, with the doped ceria having an ionic conductivity an order of magnitude greater than that of YSZ at the same temperature.[30] The electronic conductivity of doped ceria is also significant, and results in a decrease in the anode polarization.[30] The addition of a small amount of nickel to these

materials has also been found to improve anode performance, with Ni-CGO anodes showing better performance than a Ni-YSZ anode when hydrogen is used as fuel.[30]

One disadvantage of doped cerias is the lattice expansion experienced in low oxygen partial pressure environments, which results from the ceria ion undergoing a valency state change from Ce^{4+} to Ce^{3+}.[30] This lattice expansion affects the mechanical integrity of the material, though the problem can be reduced by doping with Gd^{3+}, Sm^{3+} or Y^{3+}.[30]

2.3.4 Perovskite Oxides

Lanthanum chromite, $LaCrO_3$, has been considered as a potential anode material for SOFCs due to its excellent thermal and chemical stability in a reducing environment, but unfortunately it undergoes lattice expansion in this type of atmosphere (due to reduction of the Cr^{4+} ion to Cr^{3+}, and the larger radius of the latter ion) and is poor mechanically.[30,31] However, doping may improve the properties of this material. Pudmich et al[32] have looked at doping $LaCrO_3$ with calcium or strontium on the A-site and titanium, iron, vanadium or niobium on the B-site to form $La_{1-x}A_xCr_{1-y}B_yO_3$. Conductivities of 60 S/cm at 900°C in reducing atmospheres were recorded, though these values were significantly lower in air (by one to five orders of magnitude).[32] Unfortunately, these materials result in a lower performance than Ni-YSZ, which can be partially attributed to their poor adherence to the YSZ electrolyte.[30,32] However, it has been demonstrated that composites of these materials with YSZ may provide adequate performance. The composite material of LSCV-YSZ (LSCV = $La_{0.8}Sr_{0.2}Cr_{0.97}V_{0.03}O_3$) has been shown to have similar performance to that of Ni-YSZ.[30]

By substituting either strontium or barium for lanthanum and titanium for chromium, $SrTiO_3$ and $BaTiO_3$ materials are formed. $SrTiO_3$-based materials are found to undergo less dramatic lattice expansion in reducing atmospheres and demonstrate n-type conductivity.[30] In addition, their thermal expansion coefficients are in line with that of the electrolyte.[33] Hui and Petric[33] have found that cobalt, copper, gallium and aluminum are all effective dopants in enhancing the degree of reduction of $Sr_{0.85}Y_{0.10}Ti_{0.95}M_{0.05}O_{3-\delta}$ (M = Co, Cu, Ga, Al). For cobalt-doped materials, conductivity is found to be better for dense samples as opposed to porous samples. Of the materials tested, $Sr_{0.85}Y_{0.10}Ti_{0.95}Ga_{0.05}O_{3-\delta}$ and $Sr_{0.85}Y_{0.10}Ti_{0.95}Co_{0.05}O_{3-\delta}$ gave the best cell performance, though the power density was poor and "...partial delamination of the anode was evident."[33]

2.3.5 Tetragonal Tungsten Bronzes

Another type of anode material that has been tested for its ability to be used in a solid oxide fuel cell is the tetragonal tungsten bronzes. In earlier work where $SrTiO_3$ was doped with lanthanum or niobium, Slater and Irvine[34] came across the impurity with composition $Sr_{0.6}Ti_{0.2}Nb_{0.8}O_3$ that had the tetragonal tungsten bronze structure, which is formed "from the perovskite by rotation of some of the Ti/NbO_6 octahedra." A comparison of the perovskite structure to that of tetragonal tungsten bronze may be seen in Figure 2-1.

In their work looking at niobium-based tetragonal tungsten bronzes as potential SOFC anodes, Slater and Irvine[34] tested 15 different samples to determine their electrical conductivity and re-oxidation kinetics at 930°C, and stability for long-term operation in hydrogen at 1000°C. Overall, the samples showed good electrical conductivity at low oxygen partial pressures with a clear enhancement in the re-oxidation kinetics as compared to the perovskites.[34] Final conclusions reached indicate that $Ba_{0.6-x}A_xTi_{0.2}Nb_{0.8}O_3$ (A=Sr, Ca), and most specifically $Ba_{0.4}Sr_{0.2}Ti_{0.2}Nb_{0.8}O_3$, have the greatest potential to become anodes for SOFCs of all of the samples tested.[34] These materials have the advantage of both good electrical conductivity in low oxygen partial pressures and good re-oxidation kinetics, along with no evidence of decomposition when subjected to a hydrogen fuel environment.[34] Samples of the compositions $Sr_{0.6-x}La_xTi_{0.2+x}Nb_{0.8-x}O_3$, $Ba_{0.4-x}Sr_xNa_{0.2}NbO_3$, $Ba_{0.5-x}A_xNbO_3$ (A=Sr, Ca) and $Ba_{0.3}NbO_{2.8}$ were also tested and exhibited varying results as compared to those of composition $Ba_{0.6-x}A_xTi_{0.2}Nb_{0.8}O_3$ (A=Sr, Ca), with some having poorer conductivities or re-oxidation kinetics, or the occurrence of decomposition when subjected to a hydrogen fuel environment.[34] It was also noted that the re-oxidation kinetics depended on the density of the sample, with a higher density resulting in poorer kinetics.[34]

Slater and Irvine[35] have further investigated the possibility of using tetragonal tungsten bronze phases as anode materials by considering materials with a composition of $(Ba/Sr/Ca/La)_{0.6}M_xNb_{1-x}O_{3-\delta}$ where M=Mg, Ni, Mn, Cr, Fe, In, Sn. Again, a large number of samples (17) with varying compositions was investigated for electrical conductivity and re-oxidation kinetics at 930°C and stability for long-term operation in hydrogen at 1000°C.[35] As was the case for previously discussed samples (preceding paragraph), these samples also experienced the same dependency on density in terms of re-oxidation kinetics, although they had poorer kinetics when compared to $Sr_{0.6-x}Ba_xTi_{0.2}Nb_{0.8}O_3$ tungsten bronze type phases.[35] In the case of electrical conductivity at low oxygen partial pressures, performance was found to be similar.[35] Looking at the overall results

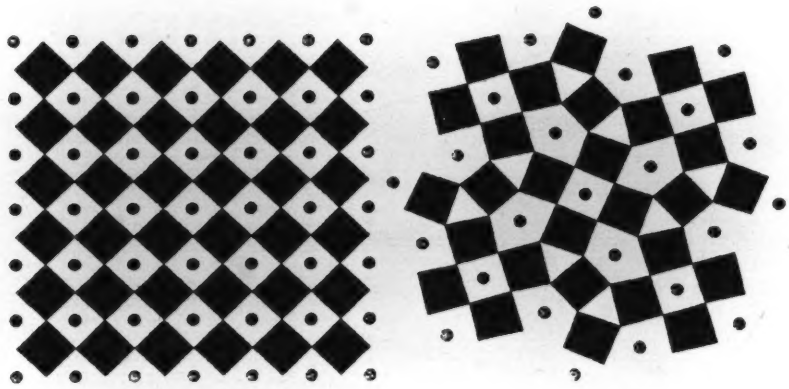

a. Cubic perovskite b. Tetragonal Tungsten Bronze

Figure 2-1: Comparison of the cubic perovskite and tetragonal tungsten bronze structures: (a)$SrTiO_3$ and (b)$Sr_{0.6}Ti_{0.2}Nb_{0.8}O_3$ viewed down the [001] axis[35]

shows anodes containing Mg, Cr or In were stable in both air and reducing (hydrogen) conditions, whereas samples containing the remaining metals (Mn, Ni, Fe and Sn) all demonstrated partial decomposition in the reducing atmosphere, with the sample containing Sn experiencing reduction in the air atmosphere.[35] For the cases of all samples, except Sn, the conductivity was reduced with increasing metal M content, in particular for Mg, Mn and In.[35] Overall results indicate that samples containing Mg and In may be possibilities for SOFC anode materials, but still do not have as good properties as found in $Ba_{0.6-x}A_xTi_{0.2}Nb_{0.8}O_3$ (A=Sr, Ca) materials, especially due to a decrease in the material conductivity with an increase in substitution level.[35]

The use of $(Sr_{1-x}Ba_x)_{0.6}Ti_{0.2}Nb_{0.8}O_{3-\delta}$, particularly $Sr_{0.2}Ba_{0.4}Ti_{0.2}Nb_{0.8}O_3$, as an anode material for a solid oxide fuel cell has been tested by Kaiser et al.[36] Good electrical conductivity at low oxygen partial pressures was again demonstrated but concern over the possible interaction of this anode with a YSZ-electrolyte was brought to light by aging mixtures of the anode and electrolyte at 1200°C and 1300°C.[36] Segregation of tetragonal zirconia occurred when the mixed particles were aged in both air and 5 vol% H_2/95 vol% Ar for 48 hours, with another potential problem being the fact that the thermal expansion coefficient for the anode is quite a bit lower than for the electrolyte.[36] Poor electrochemical performance was noted for an SOFC single cell using this material as the anode.[36]

2.4 Cathode

The material chosen as a solid oxide fuel cell cathode, the site of oxygen reduction in the cell, has

several criteria that it must meet. Obviously the material must be a catalyst for oxygen reduction, with a high catalytic activity.[37] It must also have a high electronic conductivity, in order to provide electrons from the external circuit for the reduction of oxygen.[37-39] A high ionic conductivity is also desirable.[37] Along with the requirements of conductivity and catalytic activity, the cathode material must be chemically stable with respect to other cell components and maintain morphological stability.[38]

2.4.1 Lanthanum Oxide Based

A popular choice for today's SOFC cathodes is lanthanum oxide (La_2O_3)-based materials. The compounds used are perovskites with the general formula ABO_3 (previously described in the electrolyte section), with a few different elements used on the B-site. Examples of these materials include lanthanum manganite ($LaMnO_3$), lanthanum cobaltite ($LaCoO_3$), lanthanum iron oxide ($LaFeO_3$) and lanthanum copper oxide ($LaCuO_3$). These compounds are usually doped in an effort to increase their electronic conductivity and bring their thermal expansion coefficient in line with that of the electrolyte.

2.4.1.1 Lanthanum Manganite

Currently, the most commonly used material for SOFC cathodes is doped lanthanum manganite. The conductivity of this material is due to the formation of cation vacancies.[40] Strontium (Sr^{2+}) and calcium (Ca^{2+}) are regularly used as A-site dopants, with strontium being used most frequently.[22,40] Strontium-doped lanthanum manganite, $La_{1-x}Sr_xMnO_3$, is known by the familiar acronym LSM. As the concentration of strontium is increased in $LaMnO_3$, the electronic conductivity is found to increase, as is the thermal expansion coefficient.[22,40] It has been reported that the conductivity of LSM reaches a maximum at an Sr concentration of $x=0.55$[18] with the highest reported values in oxidizing atmospheres.[40]

LSM is known to have good stability with zirconia-based electrolyte systems, typically yttria-stabilized zirconia, up to relatively high temperatures.[22,40,41] However, it is not without its potential difficulties. At temperatures greater than 1250-1300°C (even as low as 1200°C, reported by reference 40) the potential for the reaction of this material with YSZ is present.[22,40,41] Phases that may form are $La_2Zr_2O_7$ (a pyrochlore) and/or $SrZrO_3$, and the formation occurs at the boundary between the LSM cathode and YSZ electrolyte.[22,40,41] Both of these compounds are detrimental to the operation of the fuel cell because they have a lower conductivity than either the cathode or the electrolyte.[22] This results in the transfer of oxygen from the cathode to the

electrolyte being restricted, which increases the resistance voltage losses of the cell.[23] In order to remedy the problem of reaction products between LSM and YSZ, it has been found that LSM cathodes that are La^{3+}-deficient are less likely to form these phases.[22,40,42]

2.4.1.2 Lanthanum Cobaltite

The manganese in lanthanum manganite may be substituted by cobalt to form lanthanum cobaltite. Lanthanum cobaltite is a p-type conductor, with a large oxygen deficiency at high temperature.[40] It is often doped with strontium or calcium on the A-site to produce a compound of the formula $La_{1-x}A_xCoO_3$ (A=Sr, Ca) in order to enhance its conduction.[40,41] Many sources point out that while strontium-doped $LaCoO_3$ is a material with a high electronic conductivity (higher than that of $LaMnO_3$), its high thermal expansion coefficient and reactivity with YSZ to produce $La_2Zr_2O_7$ and/or $SrZrO_3$ in large quantities preclude its use as an SOFC cathode when YSZ is the electrolyte.[22,38,40,41,43] However, it can be used with ceria-based electrolytes, as there is no reaction between the materials to form pyrochlores or other phases.[22]

2.4.1.3 Lanthanum Iron Oxide

Another substitution for manganese in $LaMnO_3$ is iron. Lanthanum iron oxide, when doped with strontium, shows a higher electronic and oxygen-ion conductivity than the frequently used LSM.[38] The thermal expansion coefficient is found to decrease with increasing iron concentration and the material shows excellent compatibility with both YSZ and ceria-based electrolytes.[38] Maguire et al[38] have considered strontium-doped lanthanum iron oxide (LSF) which also contains cobalt, and compared the performance of iron-rich ($La_{0.84}Sr_{0.16}Co_{0.3}Fe_{0.7}O_3$, LSCFe7) and cobalt-rich ($La_{0.84}Sr_{0.16}Co_{0.7}Fe_{0.3}O_3$, LSCFe3) materials. Of the two, higher conductivity is demonstrated by the cobalt-rich material, but more current is passed by the iron-rich material.[38] In the case of gadolinia-doped ceria electrolytes, lanthanum iron oxide cathodes are commonly used, with LSCF ($La_{0.6}Sr_{0.4}Fe_{0.8}Co_{0.2}O_3$) being most prevalent.[44]

2.4.1.4 Lanthanum Copper Oxide

Finally, doped lanthanum copper oxide has shown promise as a potential SOFC cathode material. It is typically doped with strontium, with a higher doping level stabilizing the perovskite structure, while increasing the electronic conductivity and Cu^{3+} ion formation.[39] The conductivity is found to decrease as the temperature is increased, which indicates that metallic conduction is occurring.[39] The conductivity has been found to be greater than that for LSM, with the added advantage that no reaction is evident with YSZ.[39]

2.4.2 Other

While pyrochlores that may form between La_2O_3-based materials and YSZ can cause performance problems for SOFCs, research into other types of pyrochlores has revealed their potential as cathode materials. Takeda et al[41] have considered ruthenium pyrochlores of the formula $Pb_2Ru_2O_{6.5}$ and $Bi_2Ru_2O_7$, as the former shows "...excellent cathodic properties" based on cathode polarization curves. In addition, these pyrochlores have a thermal expansion coefficient very close to that of 8YSZ, as well as showing no reaction with this electrolyte material.[41] Their conductivity is higher than that of perovskites.[41]

Another material considered as a possibility for the cathode is praseodymium cobaltite, $PrCoO_3$. Due to the mobility of the cobalt ion, it diffuses into the YSZ electrolyte leaving the Pr^{3+} ion to react with the YSZ.[44] While this would normally be undesirable, the phase formed is conducting rather than insulating and is "...electrocatalytically active to oxygen reduction."[44] This material has been found to work well with a gadolinia-doped ceria electrolyte.[44]

2.4.3 Composites

As with electrolytes and anodes, the potential of composite materials being used for cathodes for solid oxide fuel cells has been and continues to be researched. Composites between LSM and a few different materials have been investigated. LSM-YSZ composites have been studied, as the combination of these two materials increases the number of reaction sites available and has a high catalytic activity.[22] The addition of platinum to the LSM also improves oxygen reduction rates.[22] It has been found that composites of LSM-GDC have better performance than composites of LSM-YSZ, directly due to the better oxygen ion conductivity of GDC as compared to YSZ.[45,46] LSM has also been paired with $Ce_{0.7}Bi_{0.3}O_2$ (CBO), and as the CBO content increases, the polarization resistance of the composite decreases, which indicates it could lead to good fuel cell performance.[45]

Other materials that may be used to form composites with GDC include LSCF-SSC ($La_{0.6}Sr_{0.4}Co_{0.2}Fe_{0.8}O_{3-\delta}$ - $Sm_{0.5}Sr_{0.5}CoO_{3-\delta}$), LSF and LSCF.[43,46]

2.5 Interconnect

The interconnect is the component that connects individual solid oxide fuel cells into a "stack". Each cell does not produce enough power on its own, so they are connected together to give a greater power output, similar to a traditional battery. As mentioned in the introduction, the

interconnect connects the cathode of one cell to the anode of a second electronically, while separating the reducing and oxidizing atmospheres of the anode and cathode, respectively.[22,47]

Since the interconnect material is in contact with both oxidizing and reducing atmospheres, it may have the most difficult requirements to fulfill of all SOFC components. Clearly, it has to be able to withstand both types of environments (reducing and oxidizing), while providing a high electronic conductivity (reference 48 reports a value of at least 1 S/cm is desirable).[47-49,50] The material must also have a good thermal conductivity and have a thermal expansion coefficient in line with the electrodes and electrolyte.[47,49,50] At the same time, it must not react with the anode and cathode materials to produce reaction products that could diminish the performance of the cell.[43,45,46] It is important that the interconnect material have good oxidation, sulphurization and carburization resistance, along with good high-temperature strength and creep resistance.[47] Finally, as with all SOFC components, it should be easy to fabricate at a reasonable cost.[47,49,50]

There are two broad categories that interconnect materials fall into: ceramic and metallic. Each type of material has its own benefits and disadvantages, which will be discussed.

2.5.1 Ceramic Interconnects

Ceramic interconnect materials are typically used for fuel cells operating at temperatures greater than 800°C, which are primarily SOFCs of tubular design.[47,49] The most common ceramic used is lanthanum chromite, $LaCrO_3$, which has a perovskite structure.[459] As has been noted for perovskites of the general formula ABO_3, lanthanum chromite can be doped with various elements in order to bring its properties in line with those required.[49]

Lanthanum chromite is often chosen because of its fulfillment of the majority of the requirements of an interconnect material, particularly in terms of stability and electronic conductivity requirements.[47] By doping with Sr^{2+} and Ca^{2+} for La^{3+}, and Mg^{2+}, Fe^{2+}, Ni^{2+}, Cu^{2+} and Co^{2+} for Cr^{3+}, the electronic conductivity can be increased, though it is generally found that the conductivity is much higher in an oxidizing atmosphere than a reducing one.[47]

However, $LaCrO_3$ is not an easy material to work with. It is fairly expensive and difficult to sinter to full density in an oxidizing atmosphere.[47,50] The interconnect is usually fabricated using a plasma-spraying technique.[47] Some reduction of the material has been observed at the interface between the interconnect and fuel gas.[50]

2.5.2 Metallic Interconnects

Metallic interconnects are used for fuel cells that are operated at temperatures below 800°C and have a planar configuration.[47] Metallic interconnects have several advantages over traditional ceramic interconnect materials, including higher electronic and thermal conductivities, small ohmic losses, greater ease of fabrication and lower fabrication cost.[47,49] Since they are a major structural component of the fuel cell stack, they should have good mechanical strength.[47]

There are several metallic materials that have been investigated as potential interconnects for SOFCs. These include chromium-based alloys, ferritic stainless steels and nickel/iron/cobalt-based superalloys.[50] All of these materials contain chromium and/or aluminum, which are important in the formation of oxide layers (Cr_2O_3 and Al_2O_3, respectively) on the interconnect.[49,50] The oxide layers are responsible for providing oxidation resistance for the interconnect, which is important since the material is exposed to an oxidizing atmosphere on the cathode side.[50] The amount of chromia or alumina formed is of importance, so it is necessary to have sufficient chromium levels in the material to form a continuous scale, while only a very thin layer of alumina is desired since it is an insulator.[50] Metallic interconnects that form an alumina layer tend to have a higher mechanical strength and be more stable to both oxidation and corrosion.[50] It is important that any oxide layer have good adhesion to the interconnect while at the same time not interacting with the material, and it should have low electronic resistance.[51]

2.5.2.1 Chromium-Based Interconnects

Chromium-based alloys have been researched for their potential as SOFC interconnect materials, and have demonstrated moderate promise with respect to their oxidation and reduction resistance.[47] These materials have a thermal expansion coefficient in line with the electrolyte, and have a low electronic resistance at high temperature - two desirable qualities.[47] A small amount of doping takes place using yttrium, cerium, lanthanum and zirconium in order to improve the oxidation resistance.[47] Unfortunately, chromium-based alloys present a problem because of the chromium ion. It has two valence states, Cr^{3+} and Cr^{4+}, and the latter state can interact with SOFC cathodes and cause degradation in their performance.[47]

2.5.2.2 Ferritic Stainless Steel Interconnects

Ferritic stainless steels are the most likely metallic interconnect material considered to date. These materials offer the advantages of having thermal expansion coefficients very close to that of the electrolyte, as well as being the most inexpensive and easy to work with.[47,50] The

chromium content of these materials is generally in the range of 17-26 wt%, in order to have the required corrosion resistance but still maintain the required TEC.[47,50] Iron-chromium-manganese and iron-chromium-tungsten alloys have been researched, with Fe18Cr9W showing promise.[47]

Unfortunately, as with chromia-based alloys, the chromium in ferritic stainless steels can lead to problems with the SOFC cathode.[22,52] The chromium is oxidized from Cr^{3+} to Cr^{4+} and interacts with water vapour to form $H_2Cr(VI)O_4$ which blocks the active sites at cathode/electrolyte interface.[52] Since fewer active sites are available, polarization at the cathode increases which leads to decomposition of the lanthanum manganite.[52] An additional problem encountered by ferritic stainless steel interconnects stems from the formation of oxide scales.[52] Though the oxide scales are typically insulators, their conductivity can be increased when manganese, lanthanum and titanium are added to the stainless steel.[52] Additionally, it is best to keep aluminum and silicon levels low.[52]

2.5.2.3 Other

Nickel-based and cobalt-based alloys have also been investigated for their potential, but have been found to have thermal expansion coefficients that do not match the electrolyte as well as those for ferritic stainless steels and chromium-based alloys.[50]

Another option for metallic interconnect materials involves applying a coating to the interconnect of choice in order to provide additional oxidation resistance. The coatings would prevent the oxide layer from growing too much, while at the same time controlling the degradation rate.[50] Perovskite coatings have been considered in the case of chromia-forming alloys and have been shown to reduce or even prevent the evaporation of chromium species.[50] Another effective solution is to improve the insulation on non-conductive sections (the channels that air passes through) and encourage the performance of the conductive sections (the ribs that directly contact the cathode) by applying appropriate coatings to each.[22] This has been accomplished using alumina and La-Sr-chromite, respectively.[22]

2.6 Solid Oxide Fuel Cell Configuration

The four most common stack configurations for the solid oxide fuel cell are sealless tubular, segmented-cell-in-series, monolithic and flat plate, which may be seen in Figure 2-2 on the following page. Tubular design is self-contained and does not require a sealant. While planar configurations offer a higher power density than tubular configurations, the difficulty in finding a

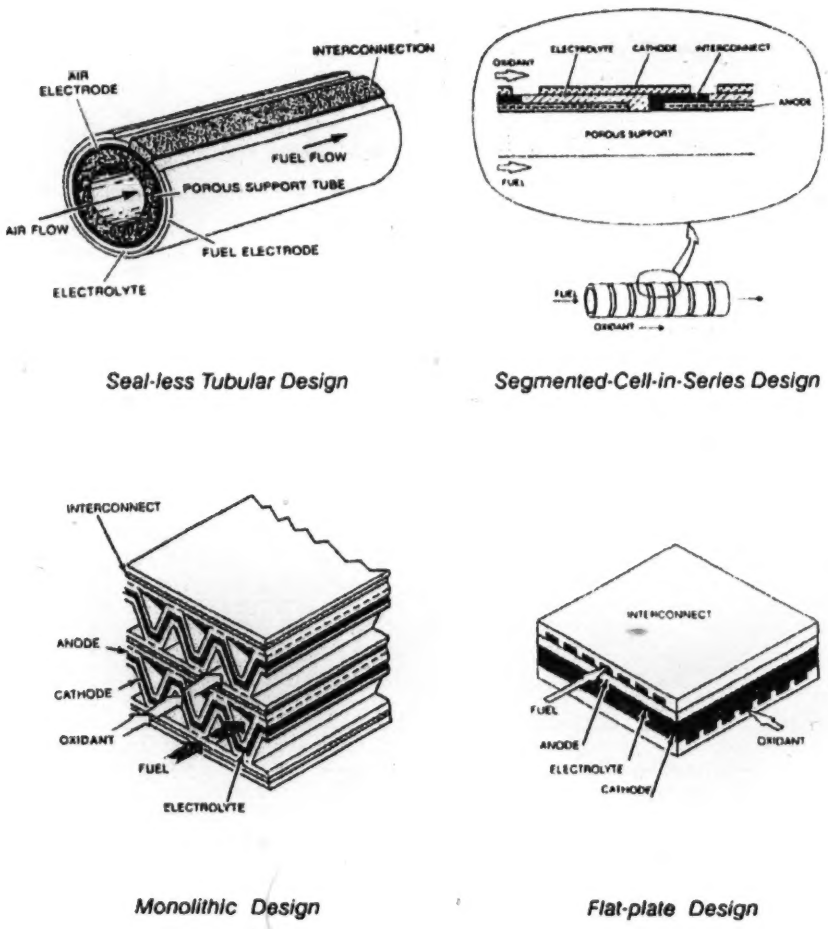

Figure 2-2: Solid oxide fuel cell configurations[18]

sealant material that does not crack or allow gas crossover is considerable. Glasses, ceramics and glass-ceramics are most commonly used today as sealants, with a specific example being SrO-La_2O_3-Al_2O_3-B_2O_3-SiO_2.[19] This material offers a thermal expansion similar to other SOFC materials, a viscosity tolerant to the thermal cycling of the cell and a sustained gas-tight seal.[19]

2.7 Advantages of the Solid Oxide Fuel Cell

Solid oxide fuel cells demonstrate several important and beneficial properties in comparison to other types of fuel cells, including (but not limited to)[19]:

- Ability to tolerate much higher impurity levels in fuels
- Multi-fuel capability

- Produce high quality, high temperature heat that may be used in cogeneration applications
- No electrolyte management problems due to the solid electrolyte

The multi-fuel capability of solid oxide fuel cells is one of the most attractive features of this type of cell. Due to the thermodynamic instability of hydrocarbons at the operating temperature of these fuel cells[18], their use as fuels is greatly desired as they are less expensive than using pure hydrogen and will speed up the introduction of fuel cells as a practical, everyday device. The most common fuel used as an alternative to hydrogen is natural gas, which is mostly made up of methane, but other possibilities include naphtha, gas oil and kerosene (all used as liquid fuels), and biogas or gas derived from biomass/landfill wastes and gasified coal.[18]

2.8 Solid Oxide Fuel Cell Applications

The most common application of solid oxide fuel cells is in stationary power generation. Due to their high operating temperature, the waste heat can be used in cogeneration applications, such as running turbines.[53] Solid oxide fuel cell power plants are being used in Tokyo, and research into microturbine cogeneration units is being conducted in the United States.[54] The possibility of using SOFCs for automobile applications is also being investigated.

3.0 Vapour Deposition Methods

Vapour deposition is a common method used to deposit a solid layer of material onto a solid substrate. Chemical vapour deposition (CVD) and electrochemical vapour deposition (EVD) are two well-known and commonly used methods. Both are similar in their use of gaseous reactants to form the layer on the substrate, but have differences that make them unique. A relatively new vapour deposition method, polarized electrochemical vapour deposition (PEVD), is based on the principles of EVD but with better control of the process. A brief introduction to both the CVD and EVD processes follows, as well as examples of how they are used in the fabrication of solid oxide fuel cells. A description of the PEVD process and its use in our laboratory completes this chapter.

3.1 Chemical Vapour Deposition (CVD)

Chemical vapour deposition involves the chemical reaction of reactants in the gaseous phase to form a solid layer on a heated substrate.[55-59] The reactants used may be atoms, molecules or a combination of the two and a variety of different chemical reactions may be carried out.[55-57] Thermal decomposition is one of the most basic CVD reactions and involves the decomposition of a substance into its individual elements or molecules.[55] Reduction and oxidation are also two straightforward reactions, involving the gain or loss of electrons, respectively, by an element.[55] Disproportionation also uses the reduction and oxidation reactions simultaneously to produce a deposit from two or more dissimilar substances.[55,60] Oxide layers may be formed by hydrolysis, which uses water vapour as a reactant.[55] Carburization and nitridation reactions result in layers of carbides or nitrides, respectively, with ammonia gas (NH_3) commonly used in the nitriding deposition.[55] Of these many types of reactions, thermal decomposition and reduction are the most frequently used for depositing solid layers.[55]

Most commonly, chemical vapour deposition is carried out at a substrate temperature between 600°C and 1000°C, under either atmospheric or reduced pressure.[57] Several steps are necessary for the formation of the layer on the substrate. The reactant gases are fed into the CVD reactor, where they diffuse to the surface of the substrate.[55,58,61] Once at the surface, the atoms or molecules of the reactant adsorb onto the surface and then undergo the specific chemical reaction to form the deposit.[55,58,61] Finally, the gaseous by-products desorb from the substrate surface and diffuse through the boundary layer to be removed from the CVD reactor.[55,58,61] As all of these steps are involved, the rate-limiting step of the reaction may be due to surface reaction kinetics or mass transport.[55,58] If surface kinetics are responsible for limiting the rate of the reaction, it is

due to the availability of the reactants, while mass transport becomes a rate-limiting factor when diffusion through the boundary layer is slow.[55] Though operation under mass transport control allows for the fastest deposition rate, generally surface kinetic control is more favourable to obtain the best deposited layer.[58]

Epitaxy, gas-phase precipitation and thermal expansion are three factors which control the nature of the CVD deposited layer.[55] Epitaxy refers to the substrate structure controlling the deposit structure by acting as a "seed crystal."[55] Two types of epitaxy exist: homoepitaxy and heteroepitaxy. In the case of the former, both the deposit and substrate are either the same material or have the same crystal structure.[55,58] For heteroepitaxy, the crystal structure of the deposit is different than that of the substrate.[55,58] Epitaxial films may grow by nucleation and growth or by monolayer formation.[58] These types of deposits are desired as they have superior properties.[55]

Supersaturation of the reactant gases may lead to gas-phase precipitation, which forms particles that "fall" into the deposited layer.[55] This is detrimental to the growing CVD layer, as the particles lead to non-uniformity and poor adhesion to the substrate surface.[55,58]

Finally, thermal expansion plays a role in the deposited CVD layer. The thermal expansion coefficient of both the substrate and the deposited layer should be as similar as possible.[55] If they are too different, the deposited layer can crack because of the thermal stresses induced.[55]

The structure produced by CVD is one of three different types, as may be seen by the diagram in Figure 3-1 on the following page. Two of these structures have grains that are columnar in nature, with one having a domelike cap on the column and the other being more faceted and angular.[55] Both are typical of metal deposits.[55] The third type of structure, common to ceramic materials, is fine accost grains.[55]

The basic components of a chemical vapour deposition system include the feed system, reaction chamber and exhaust system. The feed system is used to transport reactants, with the type of system used dependent on the physical state of the reactants.[55] Gaseous reactants are the easiest to feed to the CVD reactor and are fed by using various gas-flow control equipment.[55] Liquid reactants are also fairly straightforward. After being heated to their evaporation temperature, a carrier gas is used to transport them to the reactor.[55] Solids pose the greatest challenge, as they

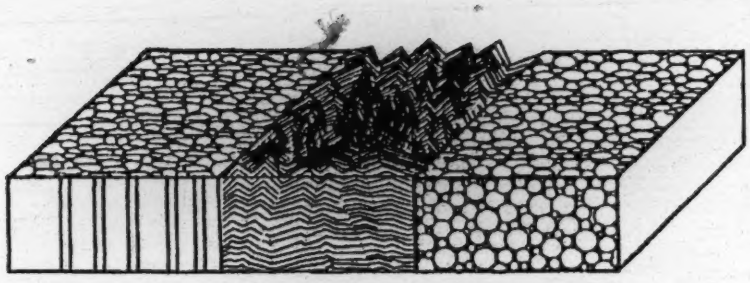

Figure 3-1: Chemical vapour deposition structures: (a) domed columnar grains, (b) faceted columnar grains, (c) fine accost grains[55]

need to be sublimed and vapourization temperatures can be very high.[55]

Two types of reactors are used: closed and open reactors. As the names imply, the former is sealed with the reactants inside, while the latter has reactants continuously supplied.[55] The closed reactor is most commonly used.[55] Reaction chambers used for CVD may be termed either hot-wall or cold-wall reactors. Hot-wall reactors have the reactor wall temperature the same as that of the substrate, while cold-wall reactors have a significantly lower wall temperature (usually ambient) than the temperature of the substrate.[55,58,59] Cold-wall reactors have the advantage that no layer is deposited on the wall, though it is easier to control the temperature using a hot-wall reactor.[58] For either type of reactor, its shape should be as close to that of the substrate as possible.[58]

The exhaust system needs to be tailored to the specific reactants being used, as not only by-product gases may require removal.[55] Generally, a particle trap, vane pump, oil demister and scrubber are employed to remove any dangerous or toxic by-products or unreacted reactants.[55]

CVD has several advantages including high depositions rates, high throwing power and it does not require a high vacuum.[55] However, it is limited in its application by the requirement that the substrate needs to be a temperature greater than or equal to 600°C and the vapour pressures of the reactants need to be fairly high.[55]

There are many variations on the traditional chemical vapour deposition process. Metal-organic CVD (MOCVD) is widely used when transition metals are deposited.[55,56] Plasma-enhanced CVD (PECVD) relies on plasma as a catalyst of sorts for the chemical reactions occurring and is

a low temperature deposition.[56] Laser CVD uses a laser to activate the chemical reaction and is carried out in a cold-wall reactor since the beam heats the substrate.[55] Photo CVD relies on UV radiation to break chemical bonds and has the advantage of room temperature operation.[55]

3.2 Electrochemical Vapour Deposition (EVD)

Electrochemical vapour deposition (EVD) is unique, although related, to the chemical vapour deposition process. However, the one fundamental difference between the two is that EVD relies on the effect of an electrochemical gradient to drive the growth of the deposited layer.[62-65] Through utilization of this process, thin, dense, gas-tight metal oxide layers are grown on a porous substrate.[62-65] These layers may be ionically or electronically conducting materials, or both.[64,65] The process was first developed by Isenberg while working on refractory oxide layers at Westinghouse in the 1970s.[66]

The EVD process is generally carried out under conditions of low pressure ($\leq 10^{-4}$ atm) and high temperature ($\geq$ 1273K).[63] Halides in the gaseous state are most commonly used as reactants to form the deposited layer, and are held (in sublimation boats) at a temperature that results in a sufficient reactant vapour pressure that allows it to be transported to the substrate using a carrier gas.[66] EVD is a two-step process to develop the deposit on the porous substrate.

The first step relies on a CVD-type reaction to close the pores in the substrate.[62-64,66] Metal chlorides are provided to one side of the substrate and a mixture of oxygen (or hydrogen) and steam is provided to the other side.[62-68] The species diffuse from each side of the substrate into its pores, where they react to form the metal oxide deposit on the pore walls.[62-68] The reaction that occurs (when metal chlorides are used, as denoted by "Me") is as follows:[62,64]

$$MeCl_4 + 2H_2O \rightarrow MeO_2 + 4HCl$$

The depositing of metal oxide into the pores of the substrate will continue until they are completely filled, thus separating the metal chloride from the oxygen (or hydrogen) and steam.[62-68] At this point, a gradient in oxygen partial pressure exists, as the metal chloride side has a very low oxygen partial pressure, while the oxygen (or hydrogen) and steam side has a high oxygen partial pressure.[62-68] As a result of this gradient, solid-state electrochemical transport occurs, with the oxygen anions traveling to the metal chloride/deposited oxide interface, where they react with chloride vapours to form more metal oxide.[62-68] At steady-state, no net current is present as electroneutrality is maintained by the return of electrons to the oxygen and steam side of the

substrate.[62,63,66] This second phase of the EVD process is known as scale growth and the reactions that occur are:[62,64]

$$MeCl_4 + 2O^{2-} \rightarrow MeO_2 + 2Cl_2 + 4e^-$$

$$2H_2O + 4e^- \rightarrow 2H_2 + 2O^{2-}$$

A diagram of these two steps may be seen in Figure 3-2, which assumes the deposit is a mixed ionic/p-type conductor.

There are four mass transport steps that take place in the second step of the electrochemical vapour deposition process (once the CVD reaction has closed the pores). The first three are related to the oxygen ions getting through the already deposited layer to react with the metal chlorides to produce more film.[68] Diffusion of oxygen and steam through the pores to the already deposited film is the first step, while the second and third steps are the reduction of oxygen and its transport through the already deposited film.[68] The fourth step is the reaction between the metal chloride and oxygen ions.[68] Rate-limiting steps for EVD include gas diffusion, surface kinetics and charge transport in the film.[62,64] Exactly which step is rate-limiting has not been unequivocally established. If the process is rate-limited by solid-state diffusion, the Wagner theory of oxidation of metals applies and the growth rate can be expected to be parabolic:[62-64,67,68]

$$L^2 = 2Kt + C_o$$

However, observation of a linear relationship with time for scale growth indicates that another rate-limiting step may be at work.[62,68] de Haart et al[68] have attributed the change from a linear to a parabolic relationship to a change in the rate-limiting step from pore diffusion to bulk electrochemical diffusion. The rate of growth experienced by a film deposited by EVD varies for

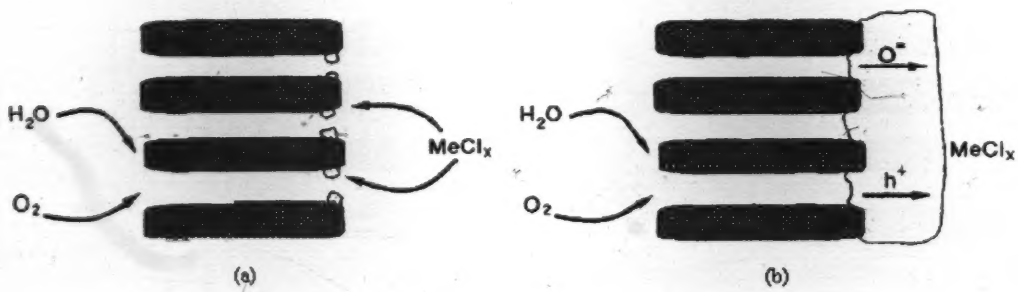

Figure 3-2: Diagrams of the (a) chemical vapour deposition and (b) scale growth steps of electrochemical vapour deposition on a porous substrate[64]

the particular oxide, but examples include rates of 6 μm/hr at 1300K for 10 mol% $Zr(Y)O_{2-x}$ and 3 μm/hr at 1600K for magnesium-doped $LaCrO_3$.[62]

The structure of the layer deposited by electrochemical vapour deposition is dependent upon the reactants used as well as the conditions under which the process is carried out. For mixed oxides, when the EVD process is rate-limited by solid-state diffusion, the ratio of the chloride (or halide) vapour pressures will produce an oxide layer that has a composition of the same ratio.[62] In terms of the EVD of yttria-stabilized zirconia, two surface morphologies are seen. At temperatures greater than 1300K, a surface likened to that of cauliflower is observed, while at temperatures less than 1300K, the surface is more faceted.[62,64] The reason for this change in surface structure may be due to different growth rates at the different temperatures or surface reconstruction.[62,64] Another possibility may be the change in kinetic contribution at different temperatures, with electrons and holes contributing at temperatures less than 1300K, but only electrons contributing at temperatures greater than 1300K.[62,64]

One advantage of EVD is due to the electrochemical potential gradient that induces a "self-leveling" effect.[64,66] If an area of the film has a greater thickness than the areas surrounding it, it will have a higher resistance to the anions and electrons, so the thinner areas surrounding it will grow more easily.[64,66] As with chemical vapour deposition, the high temperature operation of EVD is a disadvantage.[65] Due to the use of halides as reactants, corrosive gases are hazardous by-products.[65] The deposition rate is also fairly low when compared to other techniques.[65]

3.3 Polarized Electrochemical Vapour Deposition (PEVD)

Polarized electrochemical vapour deposition (PEVD) was first developed as a controlled method to deposit thin, ionically conducting layers on potentiometric sensors.[69] The deposition method is very similar to that of electrochemical vapour deposition, except that electrons are provided by an external dc source instead of traveling through the substrate.[70] There are two major differences that arise when PEVD and CVD are compared. The first is that not all of the reactants are in the vapour phase.[8] As with EVD, one of the reactants is ionically transported through the substrate due to an electrochemical potential gradient.[8] Coupling the fact that one reactant is in the deposit with external control of the gradient permits close control of the growth characteristics. Secondly, it is an electrochemical reaction that forms the product, rather than a chemical reaction.[8]

PEVD has been used to apply a ceramic layer over the metallic anode of a solid oxide fuel cell in an effort to realize the ideal anode microstructure, which consists of the grains of a metallic anode surrounded by a continuous ceramic phase in contact with the electrolyte.[8] PEVD accomplishes this microstructure for several reasons. Depositing an ionically conducting material increases the length of the ionic conduction path.[8] This also expands the three-phase region to the entirety of the anode, rather than just at the interfaces with the electrolyte.[8] Not only will the surrounding layer match the thermal expansion coefficient of the anode and electrolyte more closely, but the metallic phase remains continuous and is protected from evaporation, sintering and poisoning.[8]

Specifically, in our laboratory, polarized electrochemical vapour deposition has been used to deposit a yttria-stabilized zirconia (YSZ) layer onto the anode of a solid oxide fuel cell with an 8 mol% YSZ electrolyte and platinum electrodes. Air is provided to the cathode side of the fuel cell in order to produce oxygen anions (O^{2-}), which then travel through the YSZ electrolyte to the anode under the combination of an oxygen chemical potential gradient and an applied dc electric field:[8]

$$O_2 + 4e^- \rightarrow 2O^{2-}$$

On the anode side, YCl_3 and $ZrCl_4$ powders are sublimed to produce YCl_3 and $ZrCl_4$ vapours, which are carried to the anode using an argon carrier gas. Once they reach the anode, they react with the oxygen anions that have traveled through the electrolyte to the anode.[8] The reaction of the vapours and oxygen anions results in the formation of a YSZ ceramic layer on the platinum anode:[8]

$$ZrCl_4 + 2O^{2-} \rightarrow ZrO_2 + 2Cl_2 + 4e^-$$
$$2YCl_3 + 3O^{2-} \rightarrow Y_2O_3 + 3Cl_2 + 6e^-$$

The electrons are then released to the external circuit. The $ZrCl_4$ and YCl_3 powders are kept at an equilibrium vapour pressure ratio of 8:1, which gives a YSZ layer of composition 11 mol% $YO_{1.5}$–ZrO_2, or 5.5 mol% YSZ.[8] This is accomplished by placing the powders at different points in the furnace to keep them at temperatures that correspond to the correct vapour pressures: in the case of $ZrCl_4$, the powder is at a temperature of 160°C (vapour pressure of 0.2 torr) and the YCl_3 is at a temperature of 700°C (vapour pressure of 0.025 torr).[67] Chlorides are used because of their relatively high vapour pressure.[8]

The PEVD layer has two different directions in which growth may proceed, since the nature of

the electrical conductivity of the deposit controls its growth.[70] For a layer that has a low electrical conductivity (high ionic conductivity), the rate of its growth is limited by the rate at which ions travel through the layer.[8] However, for a layer that has high electrical conductivity, the rate of its growth is limited by the rate at which electrons travel through the layer.[8] Since the product layer being deposited, yttria-stabilized zirconia, has a much higher ionic conductivity than electronic conductivity, it is easier for the oxygen ions to travel through the layer and growth occurs preferentially along the electrode surface.[8,70]

Initial deposition of the PEVD layer occurs at the three-phase boundary, where the solid electrolyte, porous anode and gaseous phase containing $ZrCl_4$ and YCl_3 meet.[70] As deposition proceeds, the layer is thicker closer to the electrolyte/anode interface, which maintains the porosity of the anode at about the same level prior to deposition.[8] Since the ceramic layer is thickest closest to the electrolyte/anode interface, its thermal shock resistance is increased.[8] Also, having a ceramic layer surrounding the metallic electrode that is the same composition as the solid electrolyte brings the thermal expansion coefficients more in line with each other, thus reducing the stresses that may be induced at the operating temperature.

When the YSZ layer produced by polarized electrochemical vapour deposition is examined using the scanning electron microscope, it is quite evident how thin the layer formed is. The platinum grains may actually be seen through the PEVD layer, indicating that it is in the range of 1-3 μm thick.[8,70] X-ray diffraction (XRD) was used to analyze the PEVD layer, with the spectrum showing a cubic zirconia phase, a monoclinic zirconia phase and a metallic platinum phase.[8] The platinum phase shows up due to the x-rays being able to pass through the thin PEVD layer. The presence of cubic and monoclinic zirconia phases (which are stabilized and unstabilized phases, respectively) indicates that the zirconia is partially stabilized.[8] A comparison of the anode microstructure before and after deposition may be seen in Figure 3-3 on the following page.

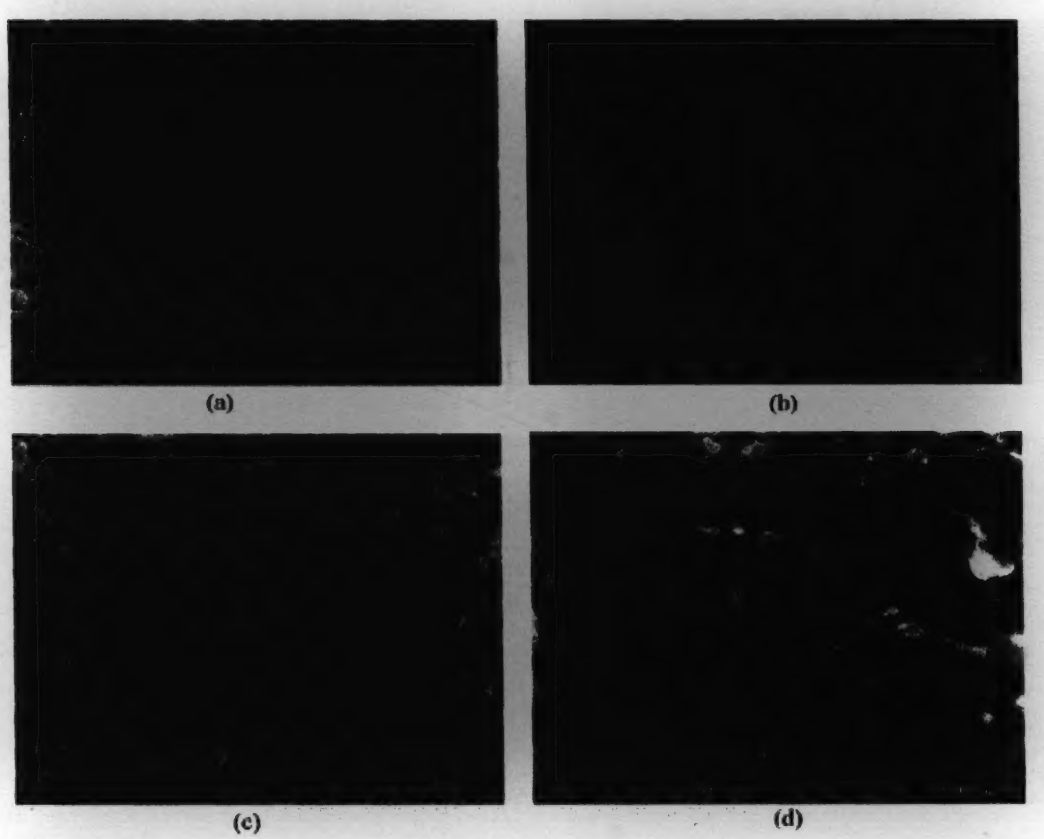

Figure 3-3: SEM micrographs of the platinum anode before (a,c) and after (b,d) deposition of 5.5YSZ by PEVD[70]

4.0 Effect of Anode Microstructure on Electrical Performance of Solid Oxide Fuel Cells

A significant amount of research has been conducted to optimize anode materials and their microstructure to obtain the best SOFC performance possible. Microstructural components, such as porosity, grain size and composition, may be altered by many different methods, including preparation methods, particle size and constituent amounts. The following sections aim to give a basic understanding of many of the different ways anode microstructure may be altered to improve overall performance of the SOFC. The majority of the information focuses on the nickel/yttria-stabilized zirconia cermet anode, simply because such a large amount of research has been conducted with this particular material. Other materials, such as doped cerias, have also been studied and a brief review of some work is included.

4.1 Nickel/Yttria-Stabilized Zirconia

4.1.1 Cermet Preparation

Many different methods for preparing nickel/yttria-stabilized zirconia (YSZ) anode cermets are available and a few of them, and their effect on the performance of a solid oxide fuel cell, will be discussed. The preparation methods to be discussed include methods for the formation of Ni-YSZ and how the cermet is either made into an anode substrate or applied to the electrolyte substrate.

Lee et al[71] have compared the resultant anode microstructure and electrochemical performance when the spray drying method (SDM) and the liquid condensation process (LCP) are used to prepare Ni-YSZ cermet anodes.[71] NiO, fine YSZ and coarse YSZ particles were used to fabricate the anode substrate. In the case of SDM, graphite was used as a pore former and the resulting microstructure shows anisotropy.[71] The microstructure produced using LCP does not show this anisotropy and instead has a uniform pore distribution.[71] The LCP cermet has a greater effective porosity, which means that the microstructure produced by LCP was better for gas permeation.[71] The electrical conductivity and power generating characteristics were both better for the LCP cermet, with maximum power densities almost three times higher for the LCP cermet, indicating a uniform distribution and good pore connections are more beneficial than a greater total porosity.[71]

Simwonis et al[72] have compared the performance of Ni-YSZ anode substrates when prepared by tape casting (TC) and the coat-mix® (CM) process. The resultant microstructures lead to a higher gas permeability (at equivalent porosities) and greater conductivity at lower gas permeability for

the CM cermet.[72] The microstructure of the CM cermet is finer and has a lower porosity (43 vol%) than the TC cermet (48 vol%).[72] Due to the structure of the green substrate, coarse pore channels develop upon reduction, leading to enhanced gas permeability.[72] The CM cermet demonstrates better electrical conductivity because of the agglomeration of nickel particles.[72]

Another Ni-YSZ cermet preparation process that has been studied is solution combustion. In their experiment, Aruna et al[73] prepared Ni-YSZ cermet anodes from the solution combustion of 15, 30 and 50 vol% Ni concentrations and 9 mol% YSZ using nanosize particles. Solution combustion is accomplished by mixing nitrates of the three cermet components with carbohydrazide fuel, which boils and forms a blue gel when heated to 350°C.[73] Once the gel is formed, a flame will move from one end to the other, and the NiO-YSZ product is produced.[73] As the nickel content of the cermet increases, the density achievable after sintering decreases.[73] Conductivity increased with increasing temperature in the case of the 15 and 30 vol% Ni cermets, with the 30 vol% Ni cermet having conductivity values three orders of magnitude greater.[73] In the case of the 50 vol% cermet, the conductivity decreased with increasing temperature, although it was two orders of magnitude greater than the 30 vol% Ni cermet and five orders of magnitude greater than the 15 vol% Ni cermet.[73] The 30 vol% cermet demonstrates better conductivity than the 15 vol% sample because both ionic (through YSZ particles) and electronic (through Ni particles) conduction paths are available.[73]

Fukui et al[74] have investigated the use of spray pyrolysis to form a composite NiO-YSZ powder that is used to make the cermet anode. The composite powder results in a cermet microstructure in which a fine dispersion of YSZ particles covers the nickel particles in order to reduce the sintering of nickel.[74] Figure 4-1 on the following page clearly shows the YSZ particles have a fine dispersion around the nickel particles. In 5500 hours of operation at 1000°C, an SOFC with this cermet as the anode gave stable performance, with a cell voltage of 0.8V.[74]

A relatively new method of forming SOFC electrodes comes in the form of mesoporous materials, as reported by Mamak et al.[75,76] These materials, which are fabricated using an aqueous co-assembly method, have intragranular porosity and contiguous networks of nanocrystalline YSZ and NiO phases.[75] When tested at 450°C, it was found that total conductivity increases and activation energy decreases with increasing NiO content.[75] When compared to traditional NiO-YSZ cermets tested at the same temperature, the activation energy of the meso-NiO-YSZ is significantly lower, which is indicative of a better connectivity between the

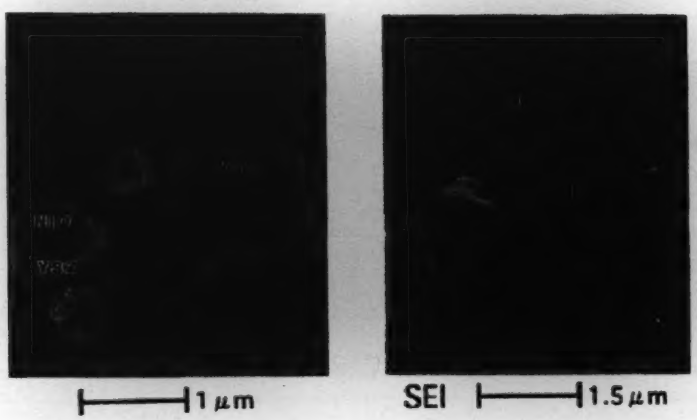

Figure 4-1: Comparison of the microstructure of Ni-YSZ anodes prepared by spray pyrolysis
(a) NiO-YSZ composite powder, (b) Ni-YSZ anode after reduction[74]

NiO nanocrystallites.[75] Further work by the authors investigated the difference in microstructure when the material was sintered at 1100°C or 1400°C.[76] A higher sintering temperature resulted in a denser, larger particle size microstructure as compared to the lower sintering temperature.[76] In comparison to a typical cermet anode with a NiO/YSZ ratio of 40/60 sintered at 1400°C, both mesoporous anodes perform better, and compared to one another, the anode sintered at 1400°C has the better performance.[76] A comparison of the performance of these two materials to the traditional Ni-YSZ cermet (sintered at 1400°C) when used as anodes for SOFCs shows maximum power densities almost three times greater for the mesoporous anode sintered at 1400°C.[76]

Bieberle and Gauckler[77] compared the microstructures and resulting electrochemical performance of four different Ni-based anodes. The four anodes made were: Ni gauze sandwiched between single crystalline YSZ, a pattern anode of sputtered Ni and YSZ, a Ni paste anode (10 wt% YSZ) and a screen-printed Ni-YSZ anode.[77] A comparison of the polarization resistances shows a decrease with increasing overpotential for the pattern, paste and screen-printed anodes, with the pattern anode having the greatest slope.[77] The current density of each of the four anodes increases with increasing anodic overpotential, with the screen-printed anode showing the highest density.[77]

Brown et al[78] also compared the performance of four different anodes: a fine cermet anode by spray painting, a coarse cermet anode by screen-printing, a Ni-paste anode and a Ni-felt anode.

The felt anode was made by pressing Ni felt into the surface of the electrolyte.[78] When the impedance spectra (collected with the four anodes operating at 1000°C) are compared, four very different spectra are evident.[78] With the exception of the fine cermet anode, structure dependence is very strong for the anodes.[78] Gas conversion plays the most significant role for the fine cermet anode while diffusion impedance seems to be minimal for all samples.[78] The activation energy for the different anodes was found to decrease as the anodes moved from point contacts (such as that produced by the Ni-felt anode) to fine cermets.[78]

Another anode preparation method involves the addition of a mixed-conducting interfacial layer between the Ni-YSZ anode and YSZ electrolyte. Tsai and Barnett[796] have studied the effect of adding a mixed-conducting layer of TiO_2-doped YSZ (YZT) or Y_2O_3-doped CeO_2 (YDC) with impedance spectroscopy. In both cases, the addition of an interlayer 0.5 μm in thickness decreased the interfacial resistance, r_i, (low frequency intercept with the x-axis) and the greater the roughness, the lower the r_i.[79] For the anodes with a YZT interlayer, increasing the interlayer thickness resulted in a decrease in the high frequency arc (HFA) while an increase in the low frequency arc (LFA) occurred.[79] The same effect was seen for the YDC interlayer, though the decrease in the interfacial resistance was more pronounced for this case than for the YZT interlayer.[79]

Studies into the effect of compaction pressure when fabricating nickel-YSZ cermets have been undertaken. Kim et al[80] and Lee et al[81] used a combination of fine and coarse YSZ particles (0.25 μm and 1.8 μm) and NiO (0.8 μm) to fabricate NiO-YSZ anodes, which were then reduced in hydrogen to Ni-YSZ. Compaction pressures of 2-7 MPa were used on the NiO-YSZ mixtures, and results show that an increasing compaction pressure leads to a finer pore structure, with no significant change in porosity and mean pore diameter at pressures greater than 5 MPa.[80,81] Along with the porosity and mean pore diameter, the gas permeability of the anode decreases with increasing compaction pressure, which demonstrates that interparticle pores between granules are responsible for gas permeability.[80,81] As the compaction pressure increases, the distribution of pore sizes becomes narrower and smaller.[80,81] In terms of electronic conductivity, the conductivity shows a gradual increase as the compaction pressure is increased until ~4 MPa, at which point a significant jump occurs, which is indicative of a structural transition of the pore structure.[80,81] This could be due to greater interparticle penetration, or a lower porosity and a more homogeneous distribution of conducting phases.[80] From these studies, it was shown that a balance needs to be struck to define an optimum compaction pressure.

4.1.2 Particle Size and Composition

The method of fabrication of the anode cermet is not the only aspect of SOFC anodes that affects their performance. The amount of each constituent phase in the particular cermet, along with the particles sizes plays a significant role, as seen by several studies.

Lee et al[82] have studied the effect of varying the ratio of nickel and YSZ from 20-80 vol% NiO in the anode cermet. The coarsening of Ni during heat treatment is the most likely cause for the measured porosity being less than the theoretical porosity (the latter is calculated from the difference between molar volumes of Ni and NiO[83]), which was more pronounced at higher NiO contents.[82] As Ni contents increased, the Ni grain size increased while the YSZ grain size decreased, and the pore perimeter increased.[82] The increase in pore perimeter is indicative of Ni coarsening playing a dominant role in the formation of the cermet microstructure.[82] For the cermets studied, a nickel content of 40 vol% is the critical content, due to significant increase in conductivity at this point, and above this conductivity is significantly higher.[82] However, the effect of nickel coarsening increases with increasing Ni content; thus the authors recommend a nickel content of 40-50 vol%.[82]

Koide et al[84] have also compared the electrochemical properties of anode cermets prepared from NiO and YSZ in varying ratios. The authors found the conductivity of the Ni-YSZ cermet to increase with increasing nickel content.[84] When used as the anode of an SOFC, power output increases with increasing nickel content.[84] The polarization resistance reached a minimum at 40 vol% Ni and then increased, while the IR resistance decreased with increasing nickel content.[84] Impedance spectra comparing two different cermet anodes clearly shows three impedance arcs, which is indicative of three electrode reactions occurring.[84] When the high frequency arc is examined in more detail for several different cermet anodes, the size of the arc decreases with decreasing nickel content from Ni/YSZ = 87/13 to Ni/YSZ = 40/60, which indicates an increase in the electrode reaction rate.[84]

Lee at al[85] have studied the effect of NiO and YSZ particle size on the electrochemical performance of the Ni-YSZ anode cermet. The first type of anode was fabricated from a mixture of NiO particles with an average diameter of 12.5 μm and YSZ particles with an average diameter of 0.21 μm, while the second type of anode subjected the particles to heat treatment and ball milling to bring the average size particle size to 3.1 μm.[85] Differences in the microstructures may be seen in Figure 4-2. For the first type of cermet, the microstructure shows poorly

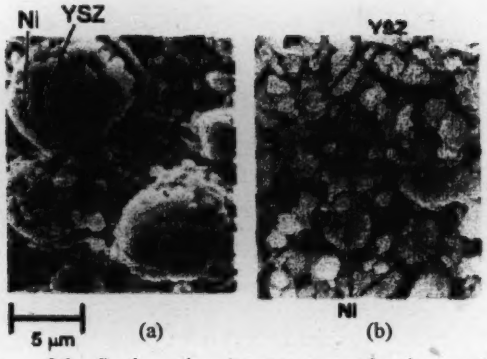

Figure 4-2: Comparison of the final anode microstructures for the two Ni-YSZ anode cermets (a) first type, (b) second type[85]

developed nickel channels and cracked surface-coated YSZ, while the microstructure of the second type of anode is a porous, evenly dispersed layer of YSZ-coated NiO particles.[85] A comparison of the impedance spectra for both types of anodes (45 vol% Ni) shows that the electrolyte resistance is quite different between the two types of cermets, with the second cermet having a resistance an order of magnitude lower.[85] This may be explained by the second type of anode having a larger effective nickel surface area.[85] When varying nickel contents were used in the second type of cermet, the total resistance and each component's (R_{bulk}, the electrolyte resistance; R_1 and R_2, related to the triple phase boundary) resistance decreased as the nickel content was increased from 25 to 45 vol%, but for contents higher than 45 vol% the resistances increased with increasing nickel content.[85]

Kawashima and Matsuzaki[86] have also studied the effect on electrochemical performance of Ni-YSZ cermets by varying the particle size of Ni (or NiO) and YSZ powders used for fabrication, using a composition of 44 vol% Ni. When either the Ni(NiO) diameter or YSZ diameter were varied, the polarization curves showed a minimum at a particular particle diameter.[86] When the ratio of the YSZ diameter to the nickel diameter was compared to the polarization, anodes with a constant YSZ diameter of 0.35 or 0.11 μm and those with a constant NiO diameter of 21 μm, a minimum in the polarization resistance was seen at a ratio of $\sim 2.0 \times 10^{-2}$.[86] This ratio is indicative of small diameter YSZ particles, which fit between the larger Ni(NiO) grains, and effectively reduce the amount of sintering of the nickel.[86]

Itoh et al[87] and Itoh et al[88] have investigated the use of both fine and coarse YSZ particles when fabricating Ni-YSZ cermet anodes. The coarse particles are important for inhibiting nickel

cohesion and providing micropores, while at the same time bringing the thermal expansion coefficient of the cermet in line with that of the electrolyte and reducing the shrinkage experienced by the anode layer.[87] The fine particles are important in ensuring a strong adhesion of the coarse particles.[84] Itoh et al[87] used a coarse YSZ particle size of ~50 μm, an NiO particle size of ~15 μm and a fine YSZ particle size of ~0.8 μm in a ratio of 4:6:1 by weight. The new anode cermet showed a significantly smaller volume change and a steady porosity with reduction time.[87] The steady porosity is due to the microstructural framework created by the fine and coarse YSZ particles and the fact that only the nickel particles sinter.[87] At a constant current, the voltage of the cell remained fairly steady for several hundred hours and when compared to a conventional cell, the anode material lifetime was two orders of magnitude greater.[87] When a current density of 0.2 A/cm^2 was applied, the conventional cell experienced a significant jump in the anodic overpotential after just 10 hours, while the new cell stayed at a low value for several thousand hours.[87]

Itoh et al[88] used an NiO content of 40 vol% and varying ratios of fine YSZ to coarse YSZ to fabricate their anodes. The anodes fabricated were designated AP*x*, where *x* is the weight ratio of coarse YSZ to the total amount of YSZ.[88] When the new anode was compared to an anode formed of just fine and coarse YSZ particles, both exhibited a decrease in shrinkage and an increase in porosity with increasing coarse YSZ content.[88] It was found that the new anode will densify more readily when the coarse YSZ content is increased.[88] In the case of porosity, increasing coarse YSZ content led to an increase in the porosity, which was fairly constant with time once NiO had been reduced to Ni.[88] Conductivity was found to be higher for new anodes containing a greater coarse YSZ content (AP5, AP7, AP9, AP11) as reduction time increased. When anodes were held for 24 or 144 hours in a hydrogen atmosphere, the conductivity increased with increasing coarse YSZ content.[88] The increase was more gradual for anodes held for 24 hours but a sharp increase was seen between AP1 and AP3 anodes held for 144 hours.[88]

In an attempt to clarify the role of YSZ in an Ni-YSZ cermet anode, de Boer et al[89] studied the effect of a dispersion of fine YSZ particles on a porous nickel electrode. A total of seven different nickel anodes were fabricated, three of which then had a fine dispersion of YSZ added to their surface.[89] From the appearance of the impedance arcs and subsequent determination of an appropriate equivalent circuit, there is no evidence to suggest a change in the reaction mechanism once YSZ is added to the surface of the nickel anodes.[89] For both types of anodes, the conductivity was found to increase with increasing nickel network perimeter length, although

the modified anodes showed almost twice the conductivity of their unmodified counterparts.[89]

Jiang et al[90] have studied the effect of various fabrication parameters on the development of a Ni-YSZ cermet anode made with 3 mol% Y_2O_3-ZrO_2 (TZ3Y), which is zirconia stabilized in the tetragonal phase. The performance of cells using Ni(70 vol%)/TZ3Y(30 vol%) anodes made from each of the three different NiO powders at two coarsening temperatures (900°C and 1000°C) was studied.[90] The anode fabricated with the smallest particle size, NiO-1, showed the best performance, particularly at a coarsening temperature of 900°C.[90] In terms of the TZ3Y particle size, overpotential losses increased with increasing particle diameter due to an increase in the electrode interfacial resistance, which resulted from poor contact between the TZ3Y particles.[90] The performance decreased with increasing nickel content. When the microstructures of Ni(70 vol%)/TZ3Y(30 vol%) and Ni(40 vol%)/TZ3Y(60 vol%) are compared, it is clearly seen that the lower nickel content anode has a less porous microstructure with a continuous network of TZ3Y particles surrounding the nickel particles.[90] This improves performance of the anode because the size of the TPB is increased.[90] As the firing temperature of the Ni/TZ3Y anode is increased, the electrode performance increases.[90]

Skarmoutsos et al[91] studied the effect of doping 8 mol% YSZ with 5 mol% TiO_2 on the electrical conductivity and thermal expansion coefficient (TEC) of Ni-YSZ cermet anodes. The thermal expansion coefficient increased with increasing nickel content, but TEC values were less for the doped cermets.[91] The reason given for this is that the nickel adheres better to the TiO_2-YSZ and thus its movement is restricted.[91] Conductivity increases with increasing nickel content for both cases, though the values for the TiO_2-doped YSZ samples are only slightly higher than the undoped samples.[91] In all cases, for both doped and undoped samples, the conductivity decreased as annealing time in hydrogen at 1000°C increased, although to a lesser extent for the doped samples.[91]

4.1.3 Sintering Temperature

The adherence of an anode cermet onto an electrolyte (or, conversely, adherence of an electrolyte onto an anode substrate if an anode-supported fuel cell is fabricated) plays an important role in the resulting performance of the fuel cell. The optimal sintering temperature used to adhere an Ni-YSZ cermet has been investigated by several researchers.

Primdahl et al[92] have investigated the effect of the sintering temperature (1100-1550°C) used to

attach NiO-YSZ anode cermets to YSZ electrolytes on the microstructure and electrochemical performance of the anode. Cracking occurred on all of the sintered cells, with lower-temperature sintering (1100°C) causing mud cracks and higher-temperature sintering (1300-1500°C) causing channel cracks, as may be see in Figure 4-3.[92] As the sintering temperature was increased, the resulting microstructure showed larger nickel and YSZ particles, with the nickel particles agglomerating.[92] The area-specific resistance (R_s) and polarization resistance (R_p) reach a minimum when the sample is sintered at temperatures between 1300 and 1400°C, and the addition of a current collector helps to reduce both R_s and R_p.[92]

Fukui et al[93] have investigated the effect of sintering temperature on the resulting morphology of the anode. The cells were sintered at 1200, 1300, 1350, 1400 and 1500°C.[93] The initial microstructure, before sintering, shows spherical particles.[93] The sample sintered at 1200°C is similar to the initial microstructure, although the particles show a weak connection to each other.[93] Morphologies at the higher sintering temperatures are clearly different, showing fine YSZ particles surrounding the nickel particles.[93] Anode polarization and internal resistance reach minimum values at a sintering temperature of 1350°C, which indicates samples sintered at this temperature had the best electrical performance.[93] The fuel cell with the anode sintered at 1350°C was tested at 1000°C with hydrogen as the fuel and had a stable cell voltage for several thousand hours.[93]

The effect of sintering temperature and sintering atmosphere on the morphology of Ni-TZ3Y cermet anodes were studied by Jiang.[94] Anodes composed of 100% Ni, Ni(70 vol%)/TZ3Y(30 vol%) and Ni(50 vol%)/TZ3Y(50 vol%) were sintered at a temperature of 1000°C for times of 1, 250, 750 and 2000 hours under both dry and moist hydrogen.[94] After sintering for 1 hour, the

Figure 4-3: Cracking of NiO-YSZ cermets sintered to YSZ electrolytes at temperatures of (a) 1100°C and (b) 1300°C[92]

cermets showed continuous nickel networks with small TZ3Y particles surrounding the nickel particles.[94] As the sintering time was increased, the nickel particles could grow and agglomerate, with the Ni(70 vol%)/TZ3Y(30 vol%) anode showing much more nickel growth than the Ni(50 vol%)/TZ3Y(50 vol%) anode.[94] In contrast, the TZ3Y particles did not appear to have a significant change in their size as the sintering time was increased.[94] The porosity of the anodes containing TZ3Y decreased with increasing sintering time.[94] When the same tests were carried out under dry hydrogen, the significant nickel growth experienced by the 70 vol% Ni sample was not observed.[94] The performance of a fuel cell made with an Ni(50 vol%)/TZ3Y(50 vol%) anode was tested under moist hydrogen at 1000°C and showed fairly stable performance over 2500 hours.[94]

4.2 Doped Ceria

Interest in the use of ceria and doped ceria as anode materials has increased as of late, due to the mixed electronic and ionic conduction (MEIC) ceria provides. By using ceria or doped-cerias, the triple phase boundary is essentially extended throughout the entire anode, rather than being confined to the area directly in contact with the electrolyte. Several different methods of enhancing the performance of ceria have been investigated.

4.2.1 Samaria-Doped Ceria

4.2.1.1 Metal Electrocatalysts

Wantanabe et al[95] used $(CeO_2)_{0.8}(SmO_{1.5})_{0.2}$ as the anode material and dispersed platinum, ruthenium, rhodium, palladium, nickel or iridium onto the particle surfaces. Ru had the highest electrocatalytic activity, but when compared in terms of surface area of catalyst, Pt showed the best performance.[95] The performance of cells made with varying sizes of SDC particles, both with and without a metal catalyst (in this case, Pt) was compared. Performance of the cell increased with decreasing SDC particle size, with the best performance occurring for a particle size of 1.5-2.0 μm.[95]

Uchida et al[96] further investigated the effect of nickel nanoparticles used as electrocatalysts on SDC anodes. A cell made with a cermet anode of nickel/samaria-doped ceria was used as a basis of comparison.[96] A higher loading of nickel reduced the overpotential even more.[96] The microstructure of the dispersion-type anode showed a much finer, uniform dispersion of nickel when compared to the microstructure of the Ni-SDC anode.[96] Although the dispersion-type anode had significantly less nickel than the cermet anode, the current density reached much

higher values and the ohmic resistance was significantly less.[96] Through the dispersion of nanosized nickel particles, more active sites are created, thus improving the performance of the anode and, consequently, the fuel cell.[96]

The effect of the microstructure of the SDC anode was investigated by Uchida et al.[97,98] In their earlier work, Uchida et al[97] investigated the effect of a four-layer SDC anode microstructure, which consists of a thin SDC film on the YSZ electrolyte and coarse SDC particles covered with fine SDC particles and Ru catalyst particles.[97] It is clear that these fine SDC particles decrease the overpotential experienced by the cell at both operating temperatures.[97] The area specific ohmic resistance was reduced with the addition of the thin SDC film and this reduction was greater as operating temperature increased.[97] The dispersion of ruthenium electrocatalysts (nanometer size) further reduced the overpotential experienced by the fuel cell.[97]

Further work by Uchida et al[98] investigated the effect of using polymer beads (d = 1.2 μm) to form pores in SDC anodes with and without dispersed Ru electrocatalysts. The addition of 1.0 wt% polymer beads resulted in a microstructure with large and uniform pores, as opposed to the dense layer formed without the polymer beads.[98] Two types of pores were found: primary pores located within the aggregates and secondary pores located in the space between the aggregates.[98] The volume of secondary pores increased with increasing sintering temperature.[98] At an operating temperature of 1000°C, the overpotential increased with an increasing amount of pore former, and at 800°C a minimum in the overpotential was found for 0.5 wt% pore former.[98] The addition of the dispersed Ru catalysts on an anode with 0.5 wt% pore former resulted in a lower overpotential than that shown by either the anode with no pore former sintered at 1050°C or the anode with 0.5 wt% pore former sintered at 1150°C.[98]

4.2.1.2 Nickel/Samaria-Doped Ceria

Studies into the performance of cermet anodes prepared by the doping of ceria with both nickel and samaria have been carried out by several researchers. Wang et al[99] prepared tubular Ni-SDC cermet anodes with varying nickel content. The BET surface area of the Ni-SDC anodes was significantly higher than the values for Ni-YSZ cermet anodes, and decreased with increasing nickel content, though a small spike was seen at 60 wt% nickel.[99] When these cells were tested using methane as the fuel, higher OCVs were seen for the Ni-SDC anodes, again with a peak occurring for the 60 wt% nickel sample.[99] The overpotential experienced by the cell at the varying nickel contents was plotted, and again the 60 wt% nickel sample clearly shows the best

performance.[99] When the 60 wt% Ni sample was tested under methane for an extended period of time, it was found that its performance was stable.[99] The microstructure consists of well-connected nickel particles surrounded by fine SDC particles, thus giving a good connection between the components.[99]

Maric et al[100] studied the effect of sintering temperature on the resulting microstructure of Ni-SDC cermet anodes. The anode powder was sintered onto the electrolyte at temperatures of 1200, 1300 and 1400°C for two hours.[100] SEM micrographs showed the initial powder to be composed of spherical particles and the resultant microstructures for the three sintering temperatures are varied.[100] At 1200°C, both types of particles are similar in size and at 1300°C, the nickel particles have increased in size with the SDC particles surrounding them.[100] At 1400°C, the microstructure is significantly different, with larger, more angular nickel particles that have SDC particles surrounding them.[100] The lowest polarization occurred for the sample sintered at 1300°C.[100]

Cheng et al[101] have investigated the performance of a NiO-SDC gradient anode, in which the concentration of nickel within the cermet anode gradually increases from one side to the other. An anode substrate of this type was made by laminating green tapes of NiO(75 wt%)/SDC(25 wt%) and NiO(55 wt%)/SDC(45 wt%) under pressure.[101] The higher NiO content side showed a coarse average pore size, while the lower NiO content side showed a finer pore size, with the average pore size of the gradient NiO/SDC almost the same as the lower content side.[101] Fuel cells were constructed and the results show that the gradient anode had the highest maximum power density, followed by the NiO(55 wt%)/SDC(45 wt%) anode and the NiO(75 wt%)/SDC(25 wt%) anode.[101]

4.2.2 Gadolinia-Doped Ceria

Xia and Liu[102] have studied the performance of cermet anodes made with gadolinia-doped ceria, $Ce_{0.9}Gd_{0.1}O_{1.95}$ (GDC), and NiO. The sintered Ni-GDC anodes (reduced in hydrogen at 700°C) showed an increase in porosity from their original state as NiO-GDC, and the porosity of the anodes decreased with increasing sintering temperature.[102] A sintering temperature of 1250°C shows the lowest anode resistance.[102] When the cells were tested at an operating temperature of 500°C in humidified hydrogen, the power density curve was best for the cell sintered at 1250°C, followed by 1350°C and 1450°C.[102] These results indicated that the anode sintered at 1250°C

had the desired properties of adequate porosity, good Ni-to-Ni particle connectivity and a solid skeleton of GDC particles which combined to produce an effective anode.[102]

Along with studying the effect of sintering temperature on the performance of nickel-GDC anodes, research has been undertaken to study the effect of impregnating nickel anodes with GDC particles. Jiang et al[103] looked at the impregnation of nickel anodes with nanosized GDC particles and the resultant electrochemical performance. The anodes had either 3.5 vol% GDC (one-time impregnation) or 8.5 vol% GDC (repeated impregnation), and showed a decreasing electrode resistance as the amount of GDC increased when tested in hydrogen.[103] When viewed using the SEM, the anode that had undergone repeated impregnation showed nickel grains covered with small (100-200 nm) GDC particles.[103] The impregnation of the Ni anodes with GDC may lead to a greater triple phase boundary and more active sites, while at the same time protecting the nickel from poisoning.[103]

Zha et al[104] have compared the performance of anodes formed from NiO and GDC coarse and fine powders, either commercially available or prepared by the glycine-nitrate process (GNP). Four Ni-GDC anodes were fabricated with a firing temperature of 1250°C and two more anodes of the same composition as two of them were fabricated with a firing temperature of 1350°C.[104] Of the four cells tested using the four anodes fabricated, the cell with an anode of GNP NiO and GDC powders had the highest performance and the cell with an anode of commercially available NiO and GNP GDC powders had the lowest performance.[104] Figure 4-4 on the following page compares the microstructures produced by each of the four mixtures of NiO and GDC powders. Clearly, the anode of GNP NiO and GNP GDC has a homogeneous microstructure with a small grain size, and sufficient porosity as compared to the other three anodes.[104] The microstructure of commercially available NiO and GDC powders also shows a reasonable microstructure with uniform distribution of the phases, though the performance is not as good as the previously mentioned cell.[104] When cells composed of anodes fired at 1350°C were tested, it was found that the microstructure had coarsened significantly, decreasing the porosity and thus the performance of the cells.[104]

4.3 Nickel/Titanium Dioxide

Meschke et al[105] have compared the performance of Ni-YSZ anode cermets with those fabricated from Ni-TiO_2. During sintering, the NiO-$NiTiO_3$ samples shrink faster than the NiO-8YSZ samples.[105] As the sintering temperature was increased the Ni-TiO_2 substrates showed a coarser

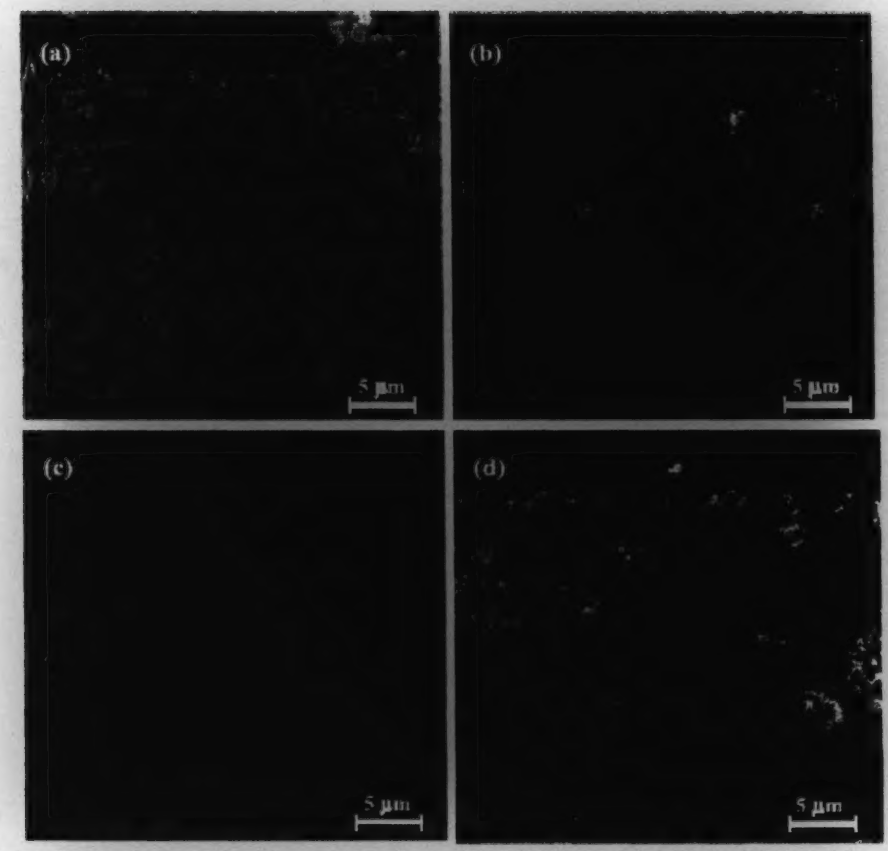

Figure 4-4: SEM micrographs of the cross-sections of the Ni-GDC anodes fabricated from (a) commercial NiO and commercial GDC, (b) GNP NiO and commercial GDC, (c) commercial NiO and GNP GDC and (d) GNP NiO and GNP GDC[104]

microstructure with larger grains and reduced porosity.[105] The TEC of the Ni-TiO_2 substrates is less than the Ni-YSZ substrates at equivalent volume fractions of nickel.[105] In terms of the electrical conductivity, the conductivity decreases with increasing porosity (or, equivalently, a lower sintering temperature) while the gas permeability increases, which is as expected.[105] From the current-voltage curves, it is seen that the Ni-TiO_2 anode will give the same performance as the standard anode when operated at a temperature ~100°C higher.[105] The cell resistance of fuel cells made with standard anodes was lower than that for the cells made with the Ni-TiO_2 anodes.[105]

5.0 Experimental Procedure

5.1 Polarized Electrochemical Vapour Deposition

To prepare the solid oxide fuel cells, platinum electrodes were screen printed onto 8 mol% yttria-stabilized zirconia discs (Intertec Southwest) using platinum conductor paste (Electro-Science Laboratories, 5542 and 5542-J-1). The YSZ discs are 2.54 cm (1.0 in) in diameter and 0.40 mm (0.016 in) thick. Circular electrodes of varying diameter, most commonly 13 mm (0.051 in), were made on the discs by screen printing three layers of the platinum paste onto each side of the disc. When reference electrodes were also made, they were applied at the same time as each circular electrode layer in a ring shape around the electrode (both anode and cathode). The discs were fired after each layer was applied in a Lindberg tube furnace at 93°C for 15 minutes and then at 950°C for 10 minutes. The cell was then allowed to furnace cool to room temperature. To act as a current collector for the cathode, 80 mesh platinum alloy gauze was used. It was pressed into the last layer of platinum screen printed onto the electrolyte disc, as well as into the reference cathode (if applicable) and secured into place with a small amount of platinum paste before being fired. A diagram of the fuel cell (with and without reference electrodes) may be seen in Figure 5-1.

In order to test the cell, it was mounted onto a closed end alumina tube. The closed end of the tube had a hole drilled into it with two small holes on either side of the larger hole, as seen in Figure 5-2. Platinum or platinum-rhodium wire of diameters 0.381 mm (0.015 in) or 0.508 mm (0.020 in) was used as the lead wires for the anode and cathode, as well as for the reference electrodes (when applicable). To attach the cathode lead wire, it was pulled through the platinum gauze, looped over and twisted to secure it. The anode wire was run through the alumina tube

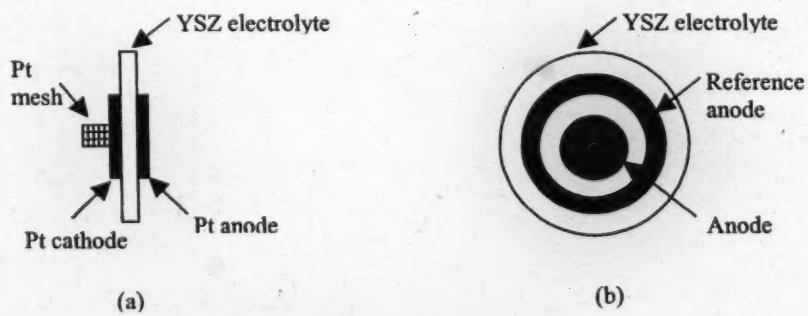

Figure 5-1: Diagram of Solid Oxide Fuel Cell
(a) side view of cell with no reference electrodes, (b) downward view of cell with reference anode

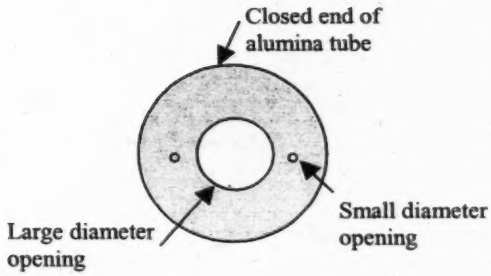

Figure 5-2: Downward View of Closed End of Alumina Tube

through one of the small diameter openings on the closed end of the tube. (If a reference anode and cathode were used, the same procedure for the lead wires was carried as described for the anode and cathode.) Ceramic sealant (Aremco, Ceramabond 503) was applied to the closed end of the tube to secure the anode lead wire in place. Once this step was completed, the cell (with the cathode wire attached) was placed onto the closed end and centered over the larger opening such that the cathode faced the inside of the tube and the anode faced the outside. The cell was gently pressed into the ceramic sealant already applied and more sealant was applied to cover the edge of the cell, which secured it in place and ensured no leaks. The alumina tube/fuel cell assembly may be seen in Figure 5-3. The lengths of wire that run through the alumina tube were covered with lengths of (most often) mullite refractory to protect the wire from the high operating/deposition temperatures. The assembly was placed into a drying oven at approximately 100°C for a minimum of two hours (most often overnight) to dry.

Once the ceramic sealant had dried, the alumina tube/fuel cell assembly was removed from the drying oven. A small amount of the 5542 (or 5542-J-1) platinum conductor paste was used to connect the anode lead wire to the anode (no gauze was applied to the anode during its preparation), with the same procedure used if a reference anode and reference anode lead wire were present. The assembly was then placed in to the PEVD reactor, as seen in Figure 5-4. The reactor consists of a Lindberg tube furnace controlled by an Omron E5CK temperature controller. One end of the tube protrudes from the furnace and is attached to a dry box. The other end is open and the alumina tube/fuel cell assembly was placed into the open end so that the fuel cell faced the dry box (see Figure 5-4). Also evident from Figure 5-4 is that part of the alumina tube/fuel cell assembly protrudes from the tube furnace. The open end of the tube furnace was first sealed using a rubber ring and metal ring that was screwed into place. The open end of the

(a)

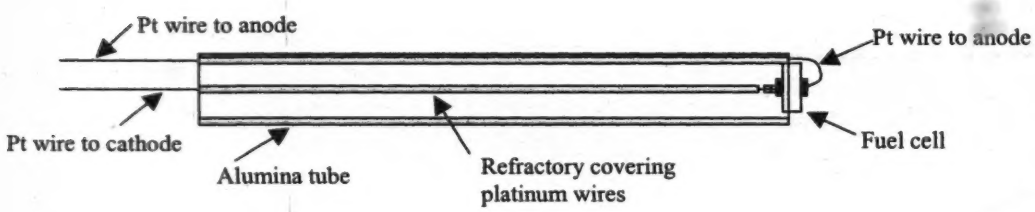

(b)

Figure 5-3: Diagram of Alumina Tube/Fuel Cell Assembly
(a) side view of assembly, (b) cut away view showing position of lead wires within tube

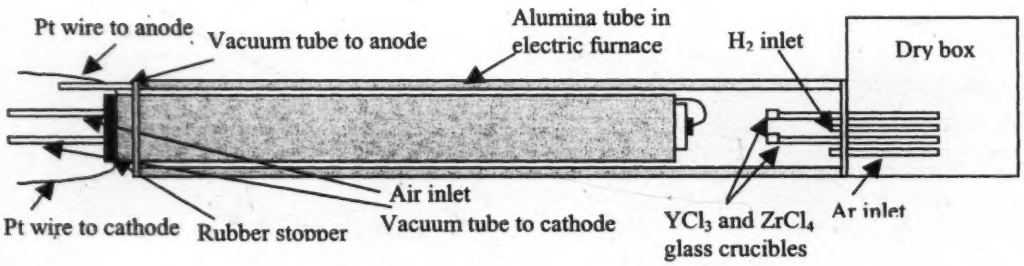

Figure 5-4: Cut away side view of PEVD reactor setup

alumina tube/fuel cell assembly was sealed by placing a rubber stopper in it. The rubber stopper has holes in it for the required air supply and vacuum tubes. Due to the small diameters of the anode and cathode lead wires, they did not present any difficulty when the rubber stopper was placed in the end of the tube and simply stayed to either side of the stopper. The end of the tube furnace attached to the dry box was sealed from within the dry box using a rubber ring and metal plate screwed into place. The metal plate has holes for the required glass tubes, hydrogen gas tube and argon gas tube (see Figure 5-4). The initial steps programmed into the temperature controller further dried the ceramic sealant at 96°C for 2 hours and 20 minutes, then cured it at

270°C for 2 hours and 370°C for 2 hours. The furnace was then heated to the desired operating temperature. During heating of the furnace, argon gas (Praxair, PP4.8), controlled by rotameters (Cole-Parmer), was flowed through the anode chamber and through the glass tubes at a rate of approximately 5 sccm through each.

For the yttria-stabilized zirconia deposition, reactant chlorides (Sigma-Aldrich, 99.99% YCl_3 and 99.9+% $ZrCl_4$) were placed into the glass crucibles at the end of the glass tubes. From the dry box, the crucibles were moved to the appropriate temperature zone in the furnace (as measured by thermocouples and an Omega HH22 microprocessor thermometer) so they would undergo sublimation. The temperatures required for each material was dependent upon the desired deposition ratio. In order to achieve a deposition ratio of 8:1 ($ZrCl_4$:YCl_3), temperatures of 160°C for $ZrCl_4$ and 700°C for YCl_3 were desired, which would give equilibrium vapour pressures of 0.2 torr for $ZrCl_4$ and 0.025 torr for YCl_3. For a deposition ratio of 5.25:1, the temperature of $ZrCl_4$ was reduced to 154°C, which would give a vapour pressure of 0.13 torr. In the case of ceria deposition, the reactant chloride (Alfa Aesar, 99.9% ultra dry $CeCl_3$) was placed into one of the glass crucibles. As for $ZrCl_4$ and YCl_3, the tube was moved to the appropriate temperature range in the furnace, which was 837°C. This was the melting temperature of the chloride, as provided by the supplier, and gave a vapour pressure of approximately 0.01 torr. The anode lead wire was connected to the working electrode and the cathode wire to the counter electrode of the potentiostat (Princeton Applied Research, Model 371), and air was admitted at 10-20 sccm (Omega FMA-5605 flow controller) to the cathode. The anode side was pumped down to less than 1 torr, as measured by a Pirani pressure gauge (Edwards), using a vacuum pump (Welch DuoSeal 1400). The cathode side was then pumped down. A chart recorder (Omega) measured the current.

5.2 Electrochemical Analysis

In order to see the effect of the deposition on fuel cell performance, polarization curves were measured before any deposition and after each subsequent deposition. In the majority of experiments, a total of four depositions were carried out. To obtain data for the polarization curves, a digital electrometer (Keithley 616) was used to measure voltage and a digital multimeter (Goodwill Instrument Company GDM-8034) was used to measure current while the resistance applied to the cell was manipulated with a decade resistor (General Radio 1433-X). To switch from deposition to fuel cell mode, it was only necessary to change the anode gas. For fuel cell operation, hydrogen (Praxair, pre-purified) was bubbled through room temperature water to

humidify it and then flowed with argon into the anode chamber. The flow of air to the cathode was increased to 70-100 sccm. The voltage was allowed to stabilize and this value was taken as the open circuit voltage (OCV). The circuit was then closed with resistance applied across the cell. The voltage and current were recorded as resistance was stepped down. Due to some concern over the internal resistance of the digital multimeter, a second polarization curve was also measured by changing the resistance and recording the responding voltage with no multimeter in the circuit. Power density curves were then calculated by multiplying the current density with voltage to obtain power density. In some experiments, complex impedance plots were measured using a second potentiostat (Princeton Applied Research, Model 273) and a frequency response analyzer (Solartron 1255) with Corrware and Z-Plot software.

5.3 Microstructural Examination

In order to observe and characterize the layer produced by PEVD, the anodes of selected cells were studied by scanning electron microscopy and energy-dispersive x-ray analysis using a Hitachi H-2700 SEM. The cells were coated with carbon to make them conductive. The majority of cells were viewed in plan view, though some were fractured by hand in an effort to see the layer.

5.4 Materials

Electrolyte dimensions and chloride analyses are listed in Tables 5-1 through 5-4.

Table 5-1 – Electrolyte Disc Specifications

Material	Outer Diameter (cm)	Thickness (mm)
8 mol% yttria-stabilized zirconia	2.54 +/- 1%	0.40 +/- 10%

Table 5-2 – Yttrium Chloride (YCl_3) Analysis

Element	ppm
Y	Major
Tb	13
Na	6
Dy	3
Er	0.8
Fe	0.7
Mg	0.7
Yb	0.4
Sc	0.2

Table 5-3 – Zirconium Chloride ($ZrCl_4$) Analysis

Element	ppm
Zr	Major
Sn	25
Mn	6.7
Fe	3.3
Na	1.8

Table 5-4 – Cerium (III) Chloride ($CeCl_3$) Analysis

Element	ppm	Element	ppm	Element	ppm
La	< 50	Nd	< 10	Ca	< 1
Dy	< 20	Tb	< 10	Cu	< 1
Gd	< 20	Tm	< 10	Lu	< 1
Pr	< 20	Y	< 10	Mn	< 1
Sm	< 20	Yb	< 10	Ni	< 1
Ca	10	Al	5	Pb	< 1
Si	10	Fe	5	Th	< 1
Er	< 10	P	5	Ti	< 1
Eu	< 10	S	5	U	< 1
Ho	<10	K	1	V	< 1
Mg	< 10	Ba	< 1	Zn	< 1
Na	< 10	Bi	< 1	Sc	< 0.1

6.0 Results and Discussion – Yttria-Stabilized Zirconia Depositions

6.1 Effect of Deposition Time

The first variable manipulated was the length of time that the depositions were carried out. All of the depositions were carried out at a temperature of 900°C with a potentiostat bias of -400 mV. The quartz tubes were kept at temperatures of 160°C and 700°C for the $ZrCl_4$ and YCl_3 powders, respectively, to give a vapour pressure ratio of 8:1. Setting the vapour pressures at this ratio should give a deposit that has 5.5 mol% yttria (Y_2O_3) and a balance of zirconia (ZrO_2).

Table 6-1 on the following page indicates the sample number and length of deposition time increments for the samples in this study. Four depositions, each of the length of time specified, were carried out on each sample. Polarization curves were measured for each of the samples before any deposition had taken place and after each of the four depositions, and may be seen in Figure 6-1. Since the electrolytes were relatively thick, the voltage values presented in the polarization curves have been corrected for the electrolyte resistance. The correction was calculated by using the formula for resistance:

$$R = \rho L/A$$

where ρ = resistivity = $1/\sigma$ (where σ is conductivity)

L = length (thickness of the electrolyte disc)

A = area of anode

to find the resistance of the electrolyte. The currents recorded were multiplied by this value and added to the recorded voltage to obtain the corrected voltage values. Supplemental to the polarization curves found in Figure 6-1 are those seen in Figure 6-2. The difference between these curves is that Figure 6-2 shows the corrected polarization curves for no deposition and after each of the four depositions for a specific sample, while Figure 6-1 compares the performance of all of the samples at a condition of no deposition, one deposition, etc. These additional polarization curves are included in order for the subsequent discussion to be easier to follow.

From Figure 6-1(a), the variation in performance among the cells before any deposition is performed is very evident. This is likely due to the variability in the anode microstructure that comes from the preparation technique. Every effort was made to keep the preparation methods as uniform as possible, but factors such as room temperature and humidity play a role, as does the pressure applied when pressing the platinum paste through the silk screen. Compared to the theoretical shape of a polarization curve, shown in Figure 6-3(a), the curves in Figure 6-1(a) show

Table 6-1: Fuel cell samples for YSZ deposition at 900°C and -400 mV

Fuel Cell Sample	Deposition Time Increment (hrs)
03-03	6
03-05	8
03-06	8
03-07	10
03-08	10
03-10	12
03-01	16

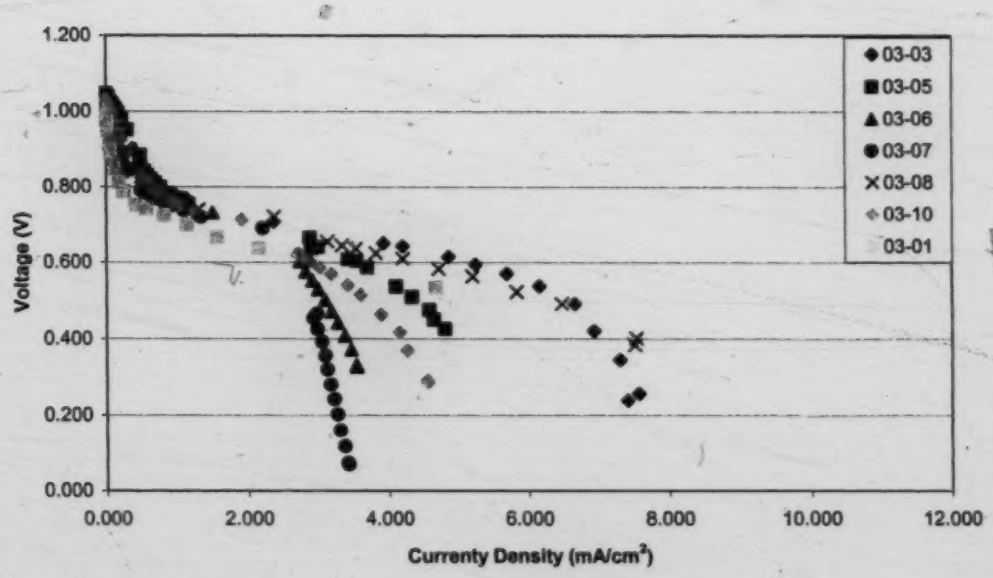

(a) no deposition

Figure 6-1: Corrected polarization curves for YSZ deposition at 900°C and -400 mV by number of depositions

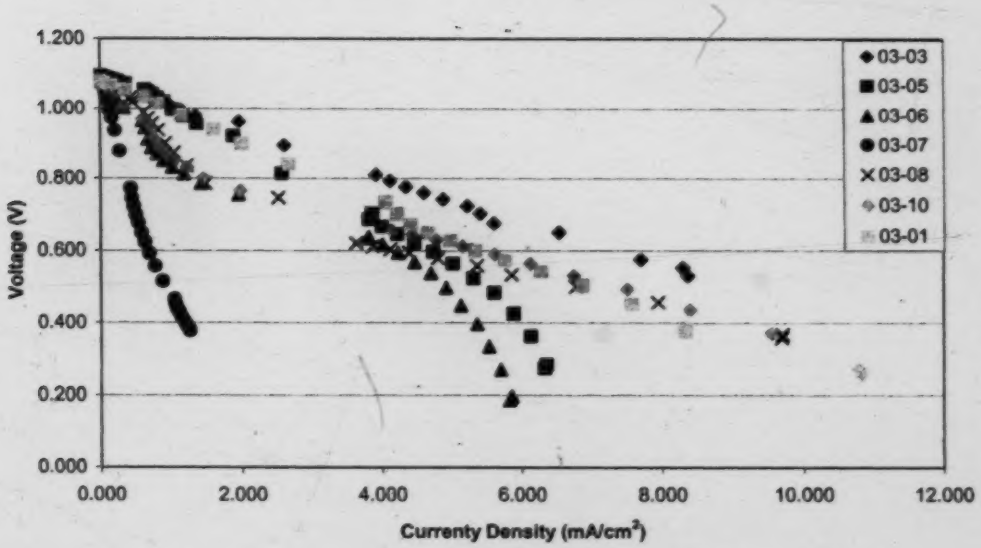

(b) 1 deposition

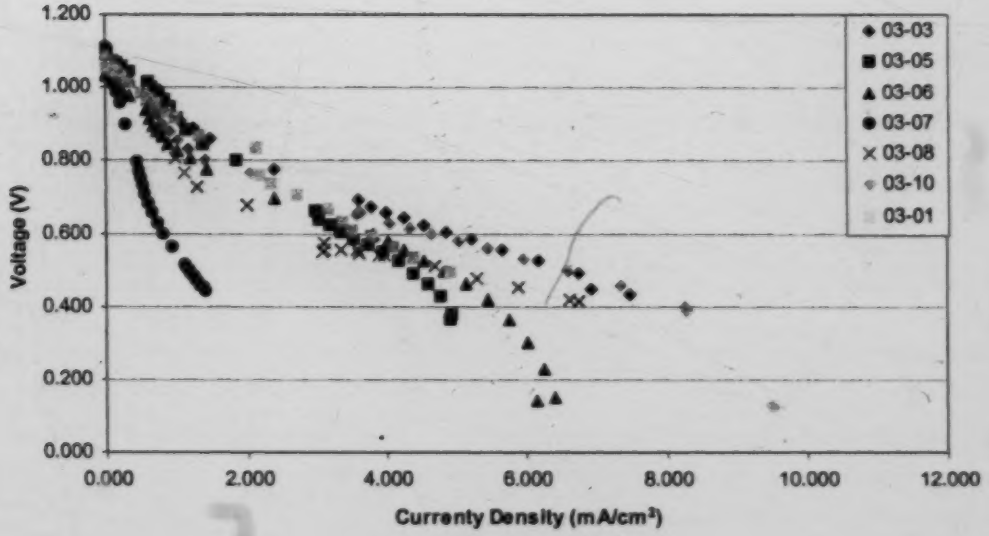

(c) 2 depositions

Figure 6-1 (con't): Corrected polarization curves for YSZ deposition at 900°C and -400 mV by number of depositions

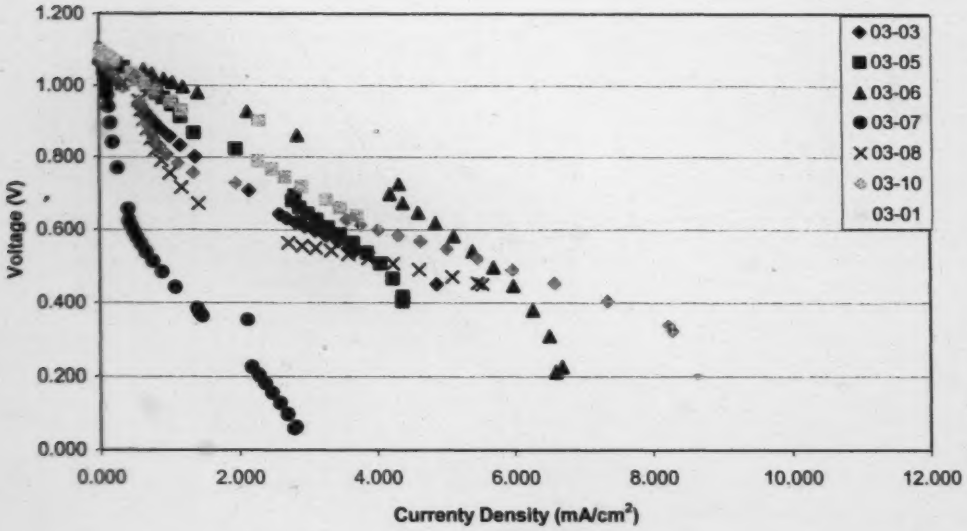

(d) 3 depositions

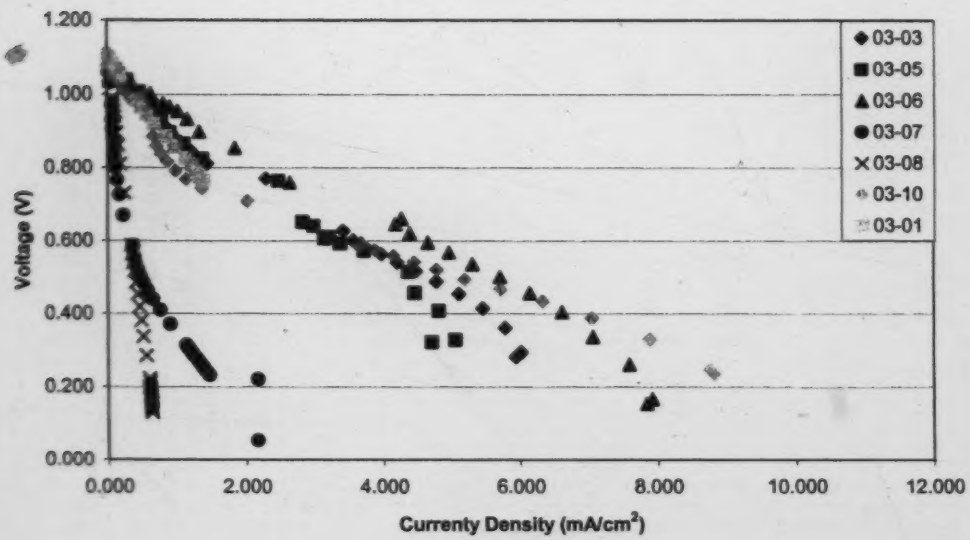

(e) 4 depositions

Figure 6-1 (con't): Corrected polarization curves for YSZ deposition at 900°C and -400 mV by number of depositions

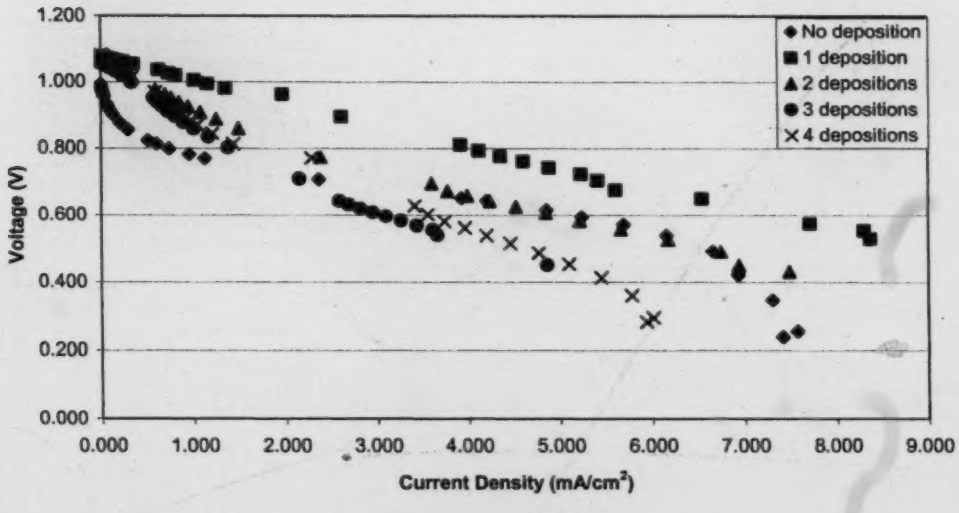

(a) sample 03-03

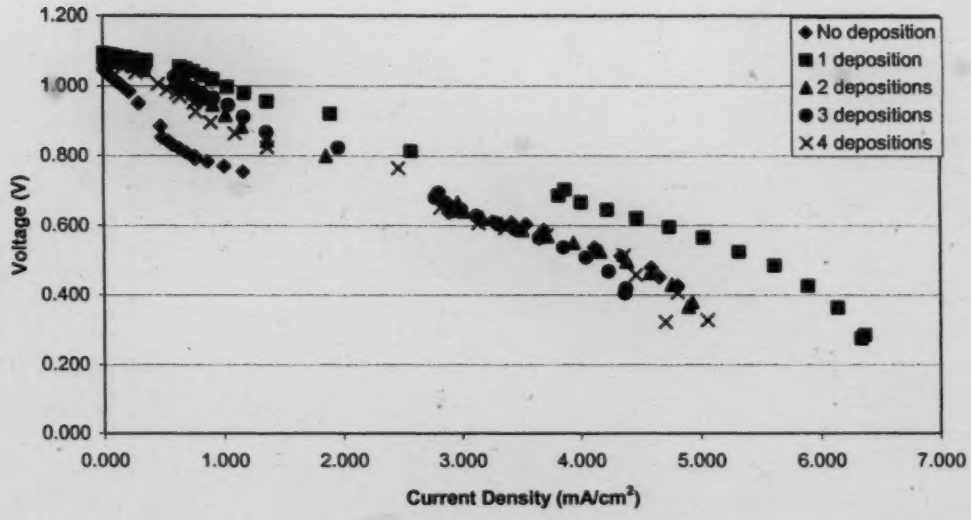

(b) sample 03-05

Figure 6-2: Corrected polarization curves for YSZ deposition at 900°C and -400 mV by sample

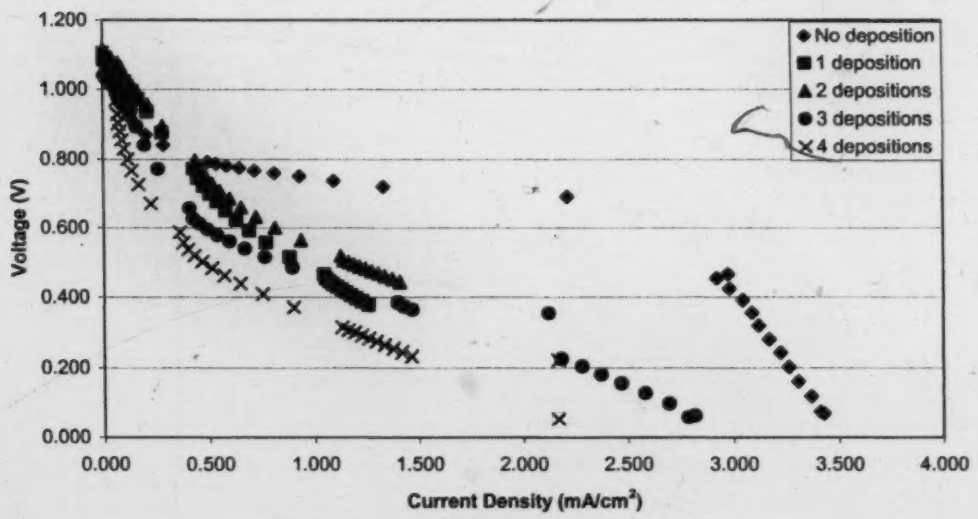

(c) sample 03-07

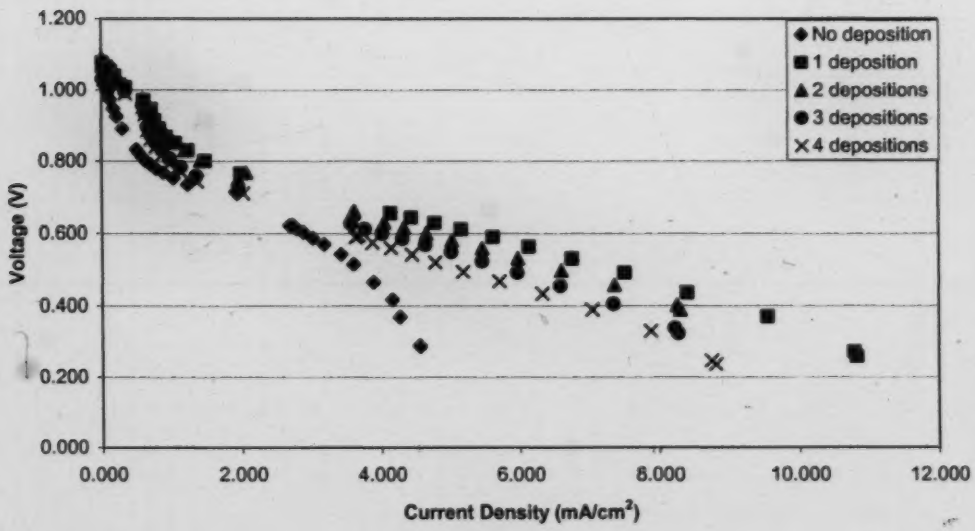

(d) sample 03-10

Figure 6-2 (con't): Corrected polarization curves for YSZ deposition at 900°C and -400 mV by sample

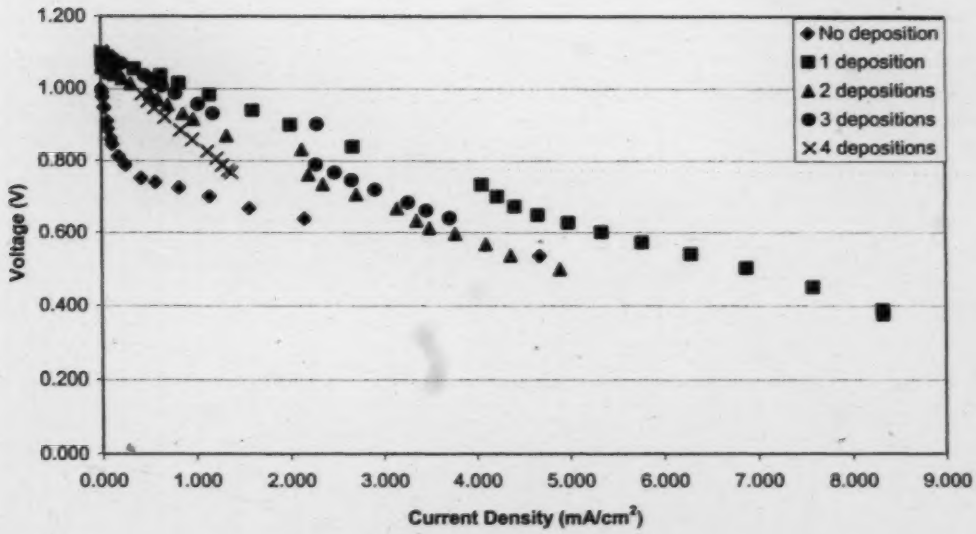

(e) sample 03-01

Figure 6-2 (con't): Corrected polarization curves for YSZ deposition at 900°C and -400 mV by sample

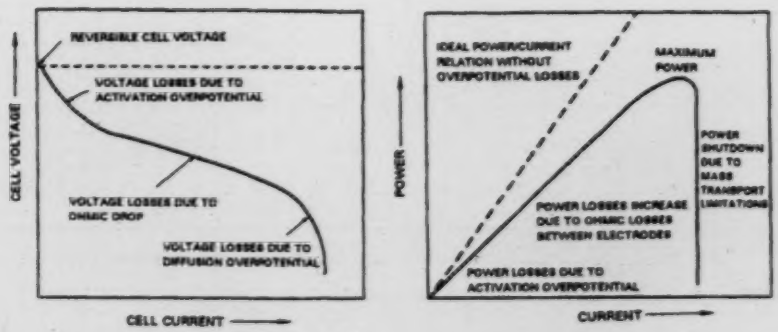
REVERSIBLE CELL VOLTAGE
VOLTAGE LOSSES DUE TO ACTIVATION OVERPOTENTIAL
VOLTAGE LOSSES DUE TO OHMIC DROP
VOLTAGE LOSSES DUE TO DIFFUSION OVERPOTENTIAL
CELL VOLTAGE
CELL CURRENT
IDEAL POWER/CURRENT RELATION WITHOUT OVERPOTENTIAL LOSSES
MAXIMUM POWER
POWER SHUTDOWN DUE TO MASS TRANSPORT LIMITATIONS
POWER LOSSES INCREASE DUE TO OHMIC LOSSES BETWEEN ELECTRODES
POWER LOSSES DUE TO ACTIVATION OVERPOTENTIAL
POWER
CURRENT

Figure 6-3: Effect of overvoltage on polarization and power curves[6]

some deviation. None of the samples clearly show a limiting current being reached. The dominant region of the curves is that produced by the effect of ohmic loss. Activation overpotential appears to play a small role a very low current densities, but is generally not expected to be significant to fuel cell performance because of the high operating temperature.[6]

Figures 6-1(b) to (e) show the polarization curves of the fuel cells after each of the four

depositions. By comparing these curves to those found for the cells in Figure 6-1(a), the effect of the deposited layer on the cell performance can be determined. Considering Figure 6-1(b), it is evident that all of the samples, except for 03-07, experience an increase in their performance after one deposition. This is evidenced by the shape and position of the curves, which are more ohmic and positioned higher on the plot, thus moving closer to the ideal reversible voltage. (The ideal reversible voltage is the voltage the cell would achieve if no voltage losses occurred and is a horizontal line on the current-voltage plot.) Samples 03-01, 03-03, 03-05 and 03-07 all show fairly linear curves, though sample 03-05 shows a slight bend downwards at high current densities, which is indicative of concentration overvoltage. The more linear plots show less effect of activation overpotential and ohmic loss, indicating a higher exchange current density and lower resistance to conduction of ions and electrons, respectively.[6,18]

Comparing the polarization curves of the cells after the second deposition, as seen in Figure 6-1(c), to those after the first deposition, a decline in performance is evident for all samples, except 03-07, which shows a slight increase. The positions of the curves have moved lower down on the plot, especially for samples 03-03, 03-05 and 03-08, meaning overpotential has increased. More of the samples show two distinct slopes, indicating activation overpotential and ohmic loss are playing more dominant roles. Concentration overpotential seems to be evident for samples 03-05 and 03-06.

From Figure 6-1(d), performance of the cells again shows a decrease after the third deposition, with the exception of sample 03-06. The samples still show better performance than with no deposition at all, except for samples 03-03 and 03-07. The shapes of the curves show activation overpotential and ohmic loss are the main sources of voltage loss for the samples, though samples 03-05 and 03-06 show some concentration polarization. The curve for sample 03-06 shows activation overpotential is much less significant for this sample.

Finally, Figure 6-1(e), detailing the performance of the cells after the fourth deposition, shows either no significant change (samples 03-03 and 03-05) or a decrease in performance of the cells as compared to the third deposition. A marked decrease in performance is visible for sample 03-08. When compared to no deposition, only cells 03-07 and 03-08 showed poorer performance. The overall conclusion to be drawn from these polarization curves is that the deposited layer generally does improve the performance of the fuel cell, with the greatest improvement evident after one deposition.

By multiplying the current density by the voltage, the power density of the cells was also calculated. Power curves were plotted for each of the samples before any deposition and after each of the four depositions, and may be seen in Figure 6-4. These curves also used the correction for electrolyte resistance used for the polarization curves. As for the polarization curves, additional power curve plots for specific samples detailing their performance before any deposition and after each subsequent deposition have been included. These may be seen in Figure 6-5. From the power curves, the maximum power density for each deposition was determined. These values may be seen in Table 6-2 below.

Since the data for the power curve plots are based on the data from the polarization curves, the same observations as to the effect of depositing a yttria-stabilized zirconia layer on the fuel cell anode can be made. After the first deposition, as seen in Figure 6-4(b), the position of the power curves, with the exception of sample 03-07, shows a lesser effect of activation overpotential and ohmic loss. The curves have greater slopes and move toward the ideal situation of no voltage loss, which is represented by a line emanating from the origin. Upon further depositions, seen in Figures 6-4(c) to (e), the fuel cells generally experience a decline in performance, as seen by the smaller slopes of the power curve and lower maximum power densities. Some samples, particularly 03-03, 03-07 and 03-08, show poorer performance after two or more depositions than when no deposited layer had been applied. The highest power densities achieved by the samples most often occurred after the first deposition, with the exceptions of samples 03-06 and 03-07, as seen in Table 6-2. The data also show that the maximum power density is comparable at the various deposition times except for samples 03-07, 03-08 and 03-01 after the final deposition.

In order to better understand what may be causing the observed trends, scanning electron microscope (SEM) images were taken. To have a basis for comparison, secondary electron

Table 6-2: Maximum power density for deposition time increment samples

Fuel Cell Sample	Maximum Power Density (mW/cm^2)				
	Deposition				
	0	1	2	3	4
03-03	3.32	4.59	3.32	2.20	2.33
03-05	2.22	2.84	2.19	2.07	2.24
03-06	1.67	2.54	2.4	3.14	2.86
03-07	1.53	0.48	0.62	0.75	0.48
03-08	3.20	3.63	2.80	2.50	0.20
03-10	1.86	3.69	3.37	3.00	2.74
03-01	2.50	3.46	2.45	2.38	1.06

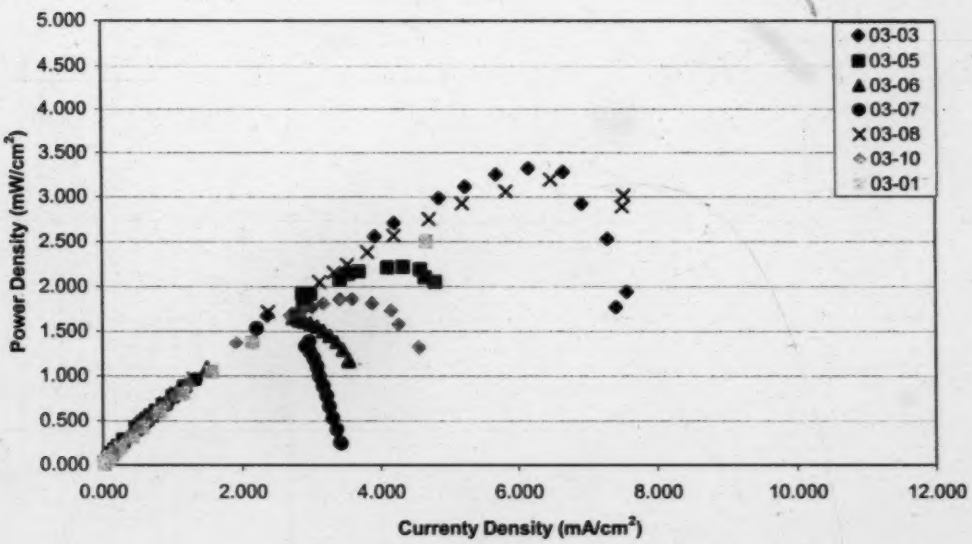

(a) no deposition

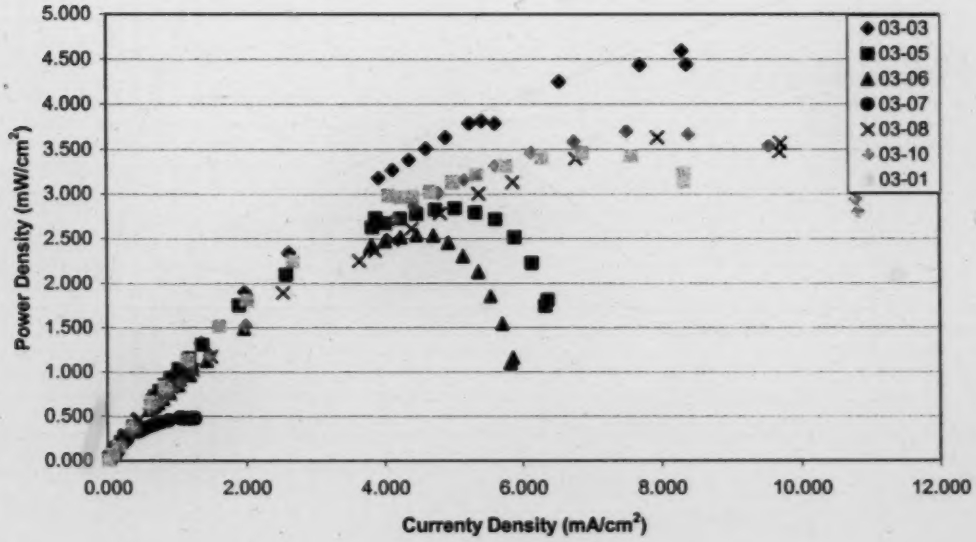

(b) 1 deposition

Figure 6-4: Corrected power curves for YSZ deposition at 900°C and -400 mV by number of depositions

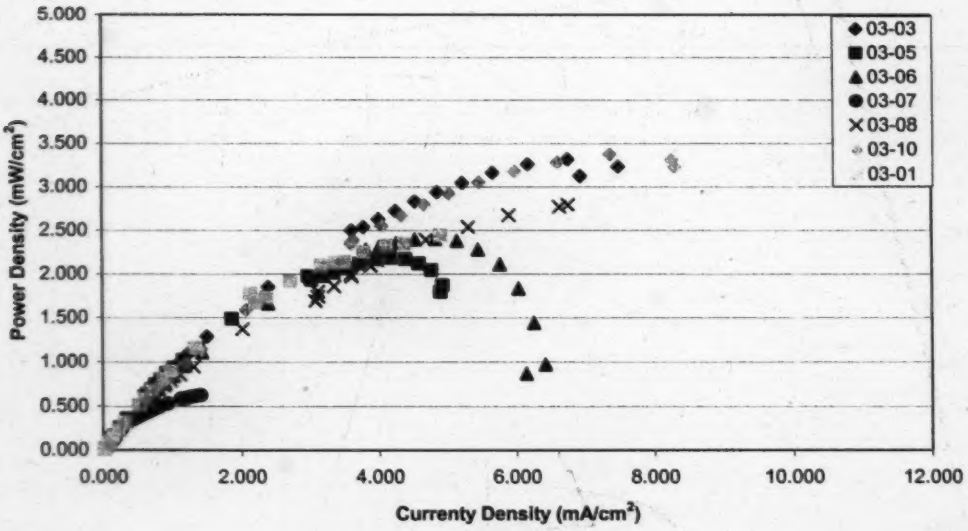

(c) 2 depositions

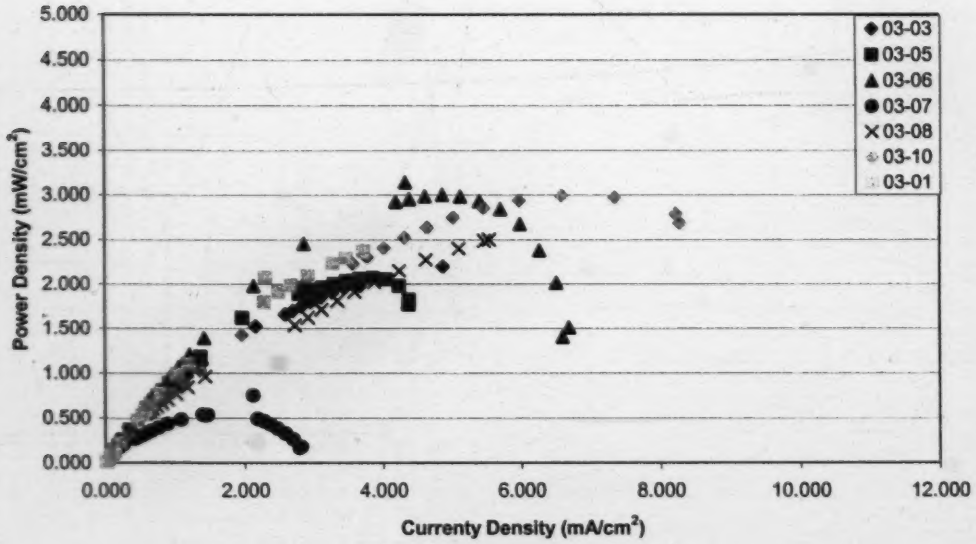

(d) 3 depositions

Figure 6-4 (con't): Corrected power curves for YSZ deposition at 900°C and -400 mV by number of depositions

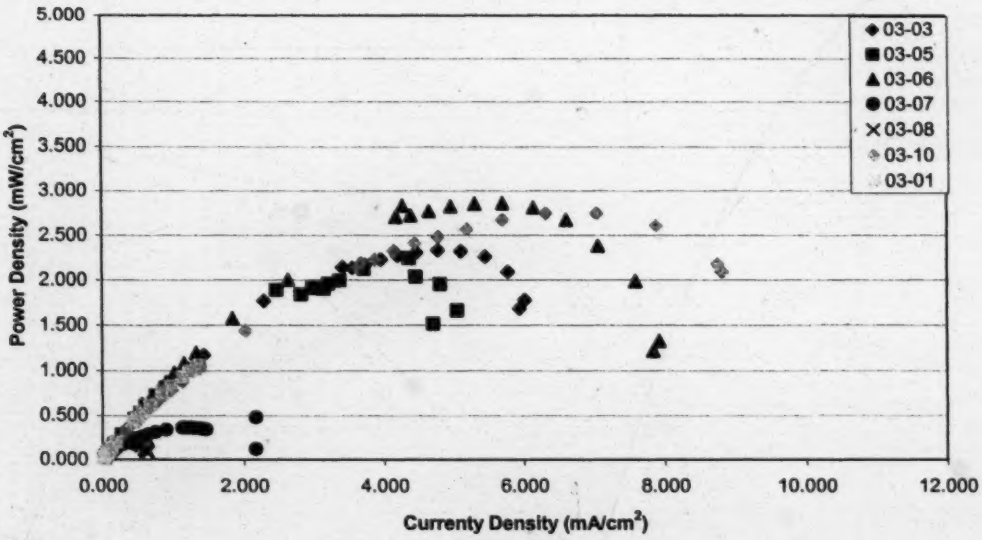

(e) 4 depositions

Figure 6-4 (con't): Corrected power curves for YSZ deposition at 900°C and -400 mV by number of depositions

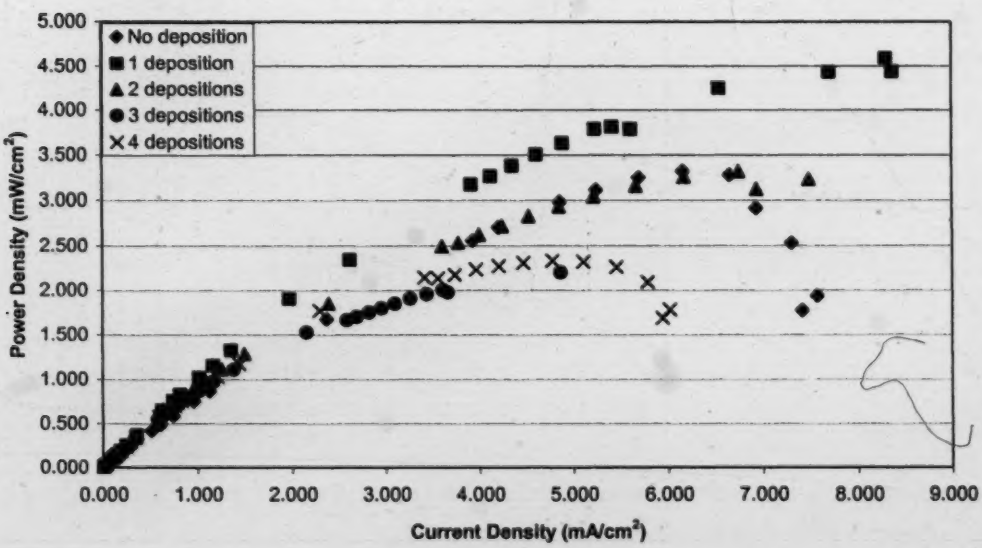

(a) sample 03-03

Figure 6-5: Corrected power curves for YSZ deposition at 900°C and -400 mV by sample

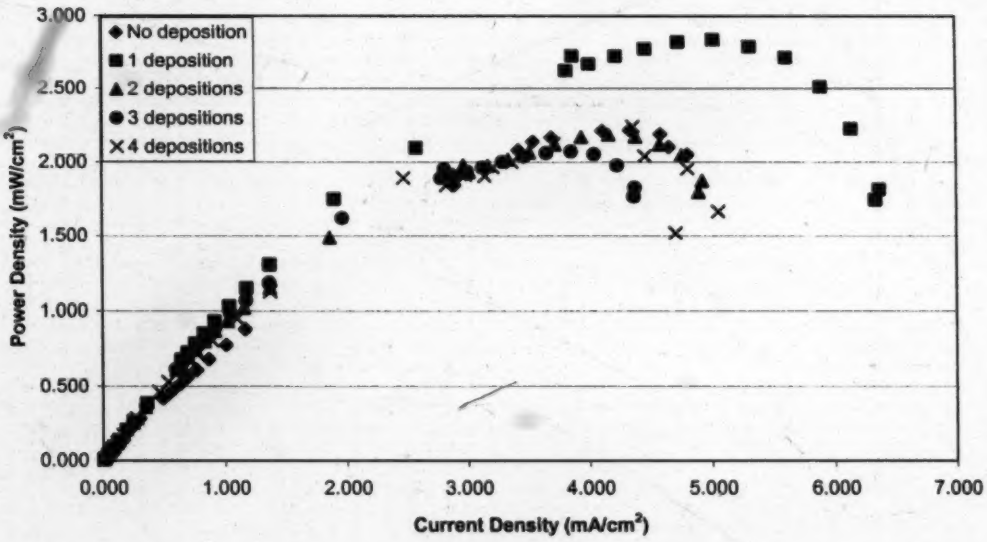

(b) sample 03-05

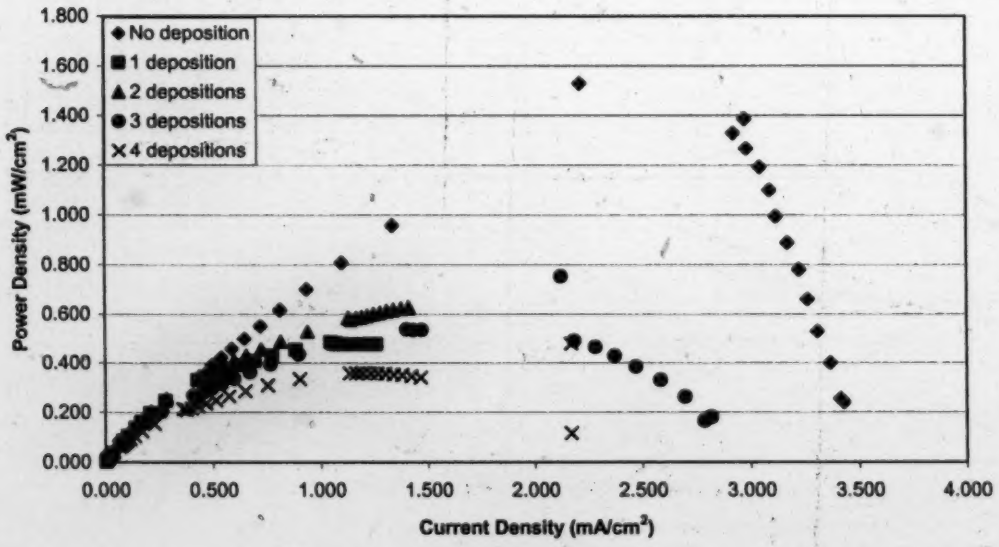

(c) sample 03-07

Figure 6-5 (con't): Corrected power curves for YSZ deposition at 900°C and -400 mV by sample

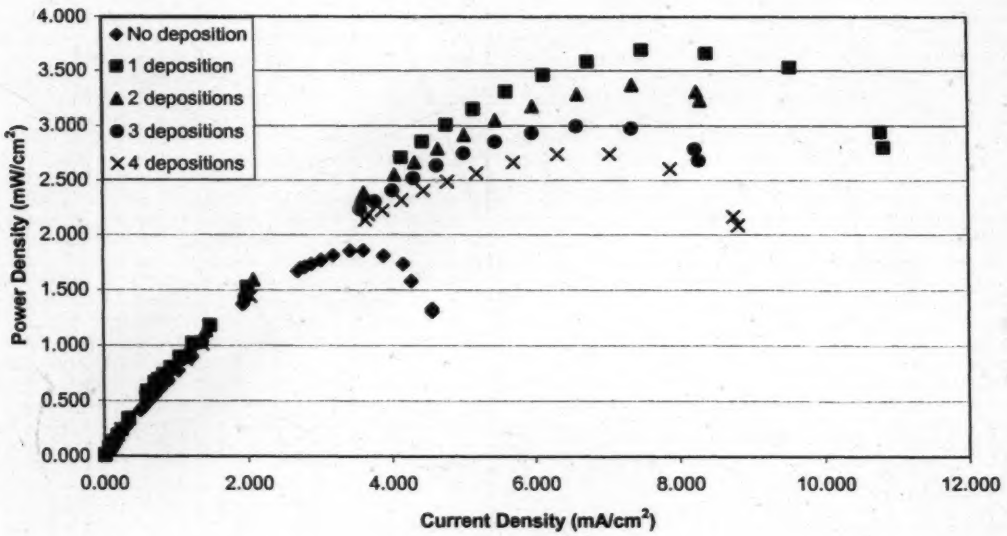

(d) sample 03-10

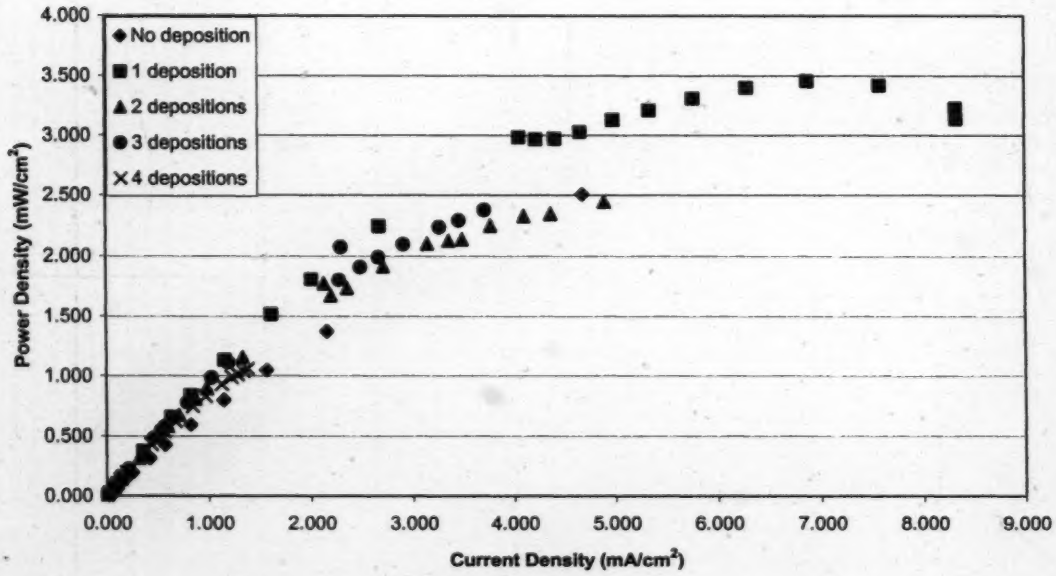

(e) sample 03-01

Figure 6-5 (con't): Corrected power curves for YSZ deposition at 900°C and -400 mV by sample

images of the platinum anode were taken and may be seen in Figures 6-6 and 6-7. The images show the anode structure after three layers of platinum paste have been screen-printed and fired, as described in the experimental procedure. The fuel cell used for these images was not heated to operating temperature nor exposed to hydrogen before observation. In considering the SEM images of the anode surface before depositions were carried out, the platinum grains are clearly visible. These grains are more apparent in Figure 6-6(b), which is at a higher magnification. From this image, the average grain size is 1-2 μm and the grains are well-connected. Figure 6-6(a), as well as Figure 6-7, allows one to the see the porous nature of the anode, which is necessary for the reactants to reach the three phase boundary, where the reactions take place. From these images, the porosity of the anode is estimated to be around 40%.

Secondary electron SEM images were taken for five of the seven samples considered, with each sample representative of a particular deposition time increment. The samples viewed were 03-03, 03-05, 03-08, 03-10 and 03-01; the images were quite similar and the best may be seen in Figures 6-8 to 6-11. In all cases, the images were taken after four depositions were carried out on the sample. The feature that immediately stands out from the sample images, as compared to the reference images of the anode, is a bright layer that has a crystal-like appearance. The brightness of this layer suggests that it is on the surface of the platinum grains, which is further evidenced by the cross-sectional view of sample 03-10 in Figure 6-10. Though the appearance of the layer in terms of its structure and uniformity on the anode surface is the same for all five samples, the relative amounts change. The layer appears to be most dense on samples 03-05 and 03-10, with the least amount present for sample 03-08. Samples 03-03 and 03-01 are comparable, with amounts between that of samples 03-05/03-10 and 03-08.

In addition to the crystal-like layer, one is also drawn to the change in appearance of the platinum framework of the anode. When the structure of the platinum is compared to the images in Figures 6-6 and 6-7, it is clear that the porosity of the anode has been reduced. The grain boundaries of the platinum are much less visible and from what can be seen, the platinum grains seem to have undergone some sintering. However, it appears the surface has experienced more sintering than the entirety of the anode. The combination of these two observations, platinum sintering and reduced porosity, is not a desirable outcome, since the electrochemically active area is reduced, leading to poorer cell performance.

From these SEM images, the appearance of the fuel cell's anode after deposition of stabilized

(a)

(b)

Figure 6-6: SEM secondary electron images of solid oxide fuel cell anode after preparation (plan view)

(a)

(b)

Figure 6-7: SEM secondary electron images of solid oxide fuel cell anode after preparation (cross section view)

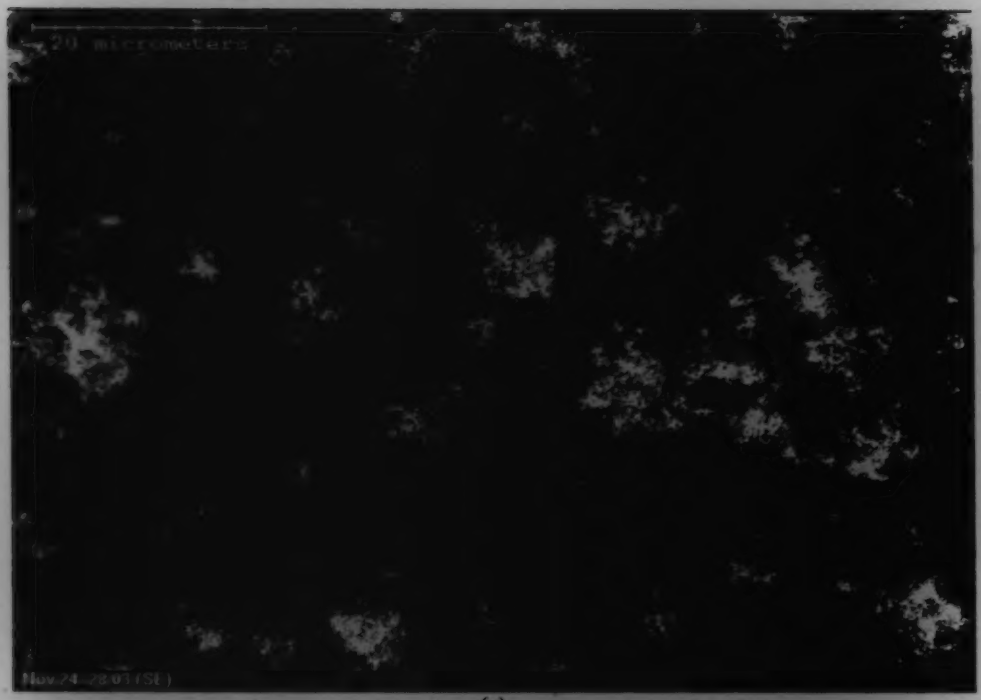

(a)

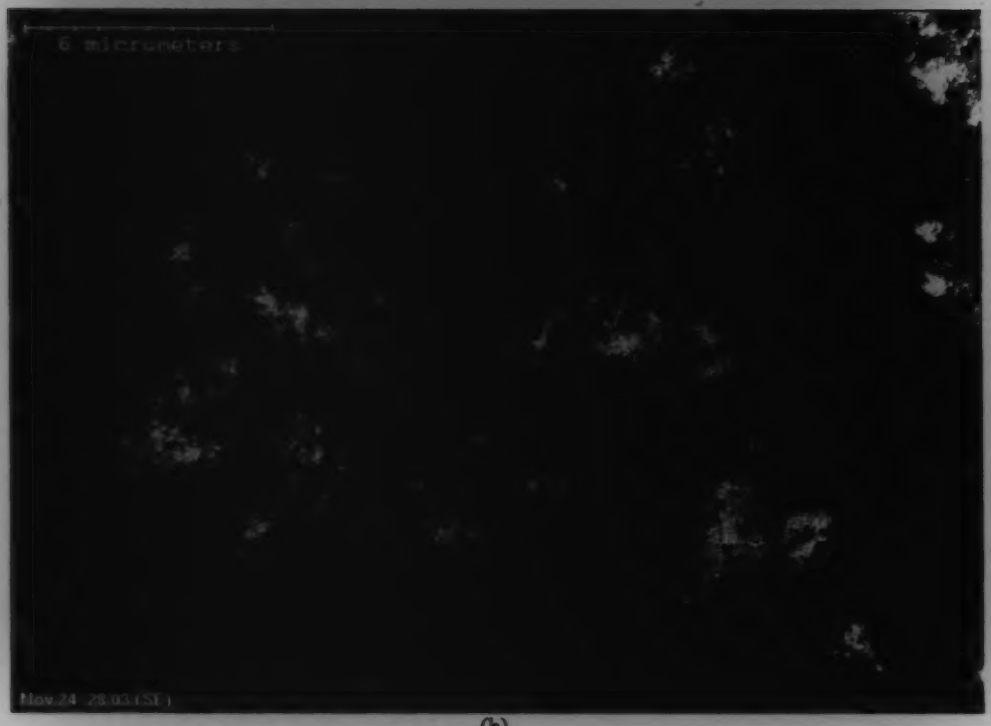

(b)

Figure 6-8: SEM secondary electron images of sample 03-08 (plan view)

(a)

(b)

Figure 6-9: SEM secondary electron images of sample 03-10 (plan view)

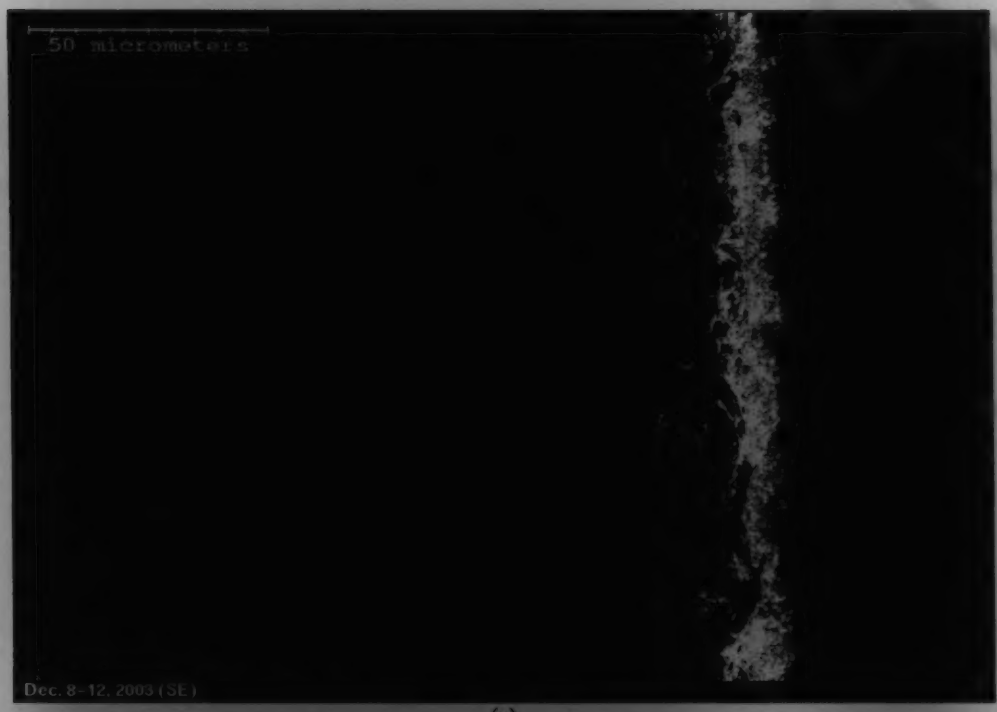

(a)

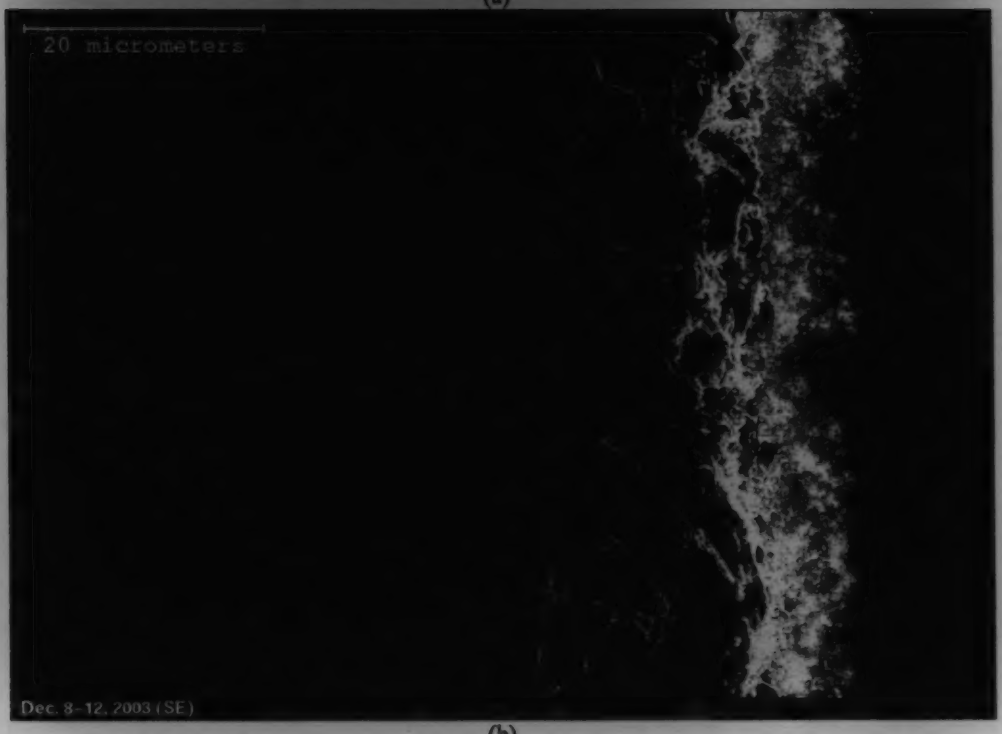

(b)

Figure 6-10: SEM secondary electron images of sample 03-10 (cross section view)

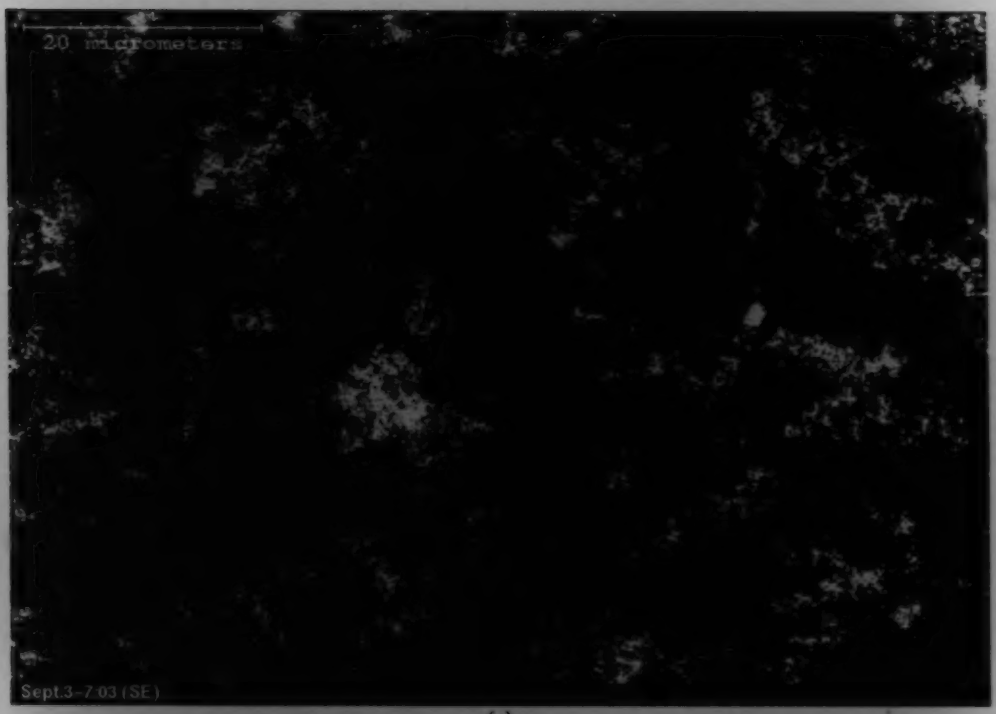

(a)

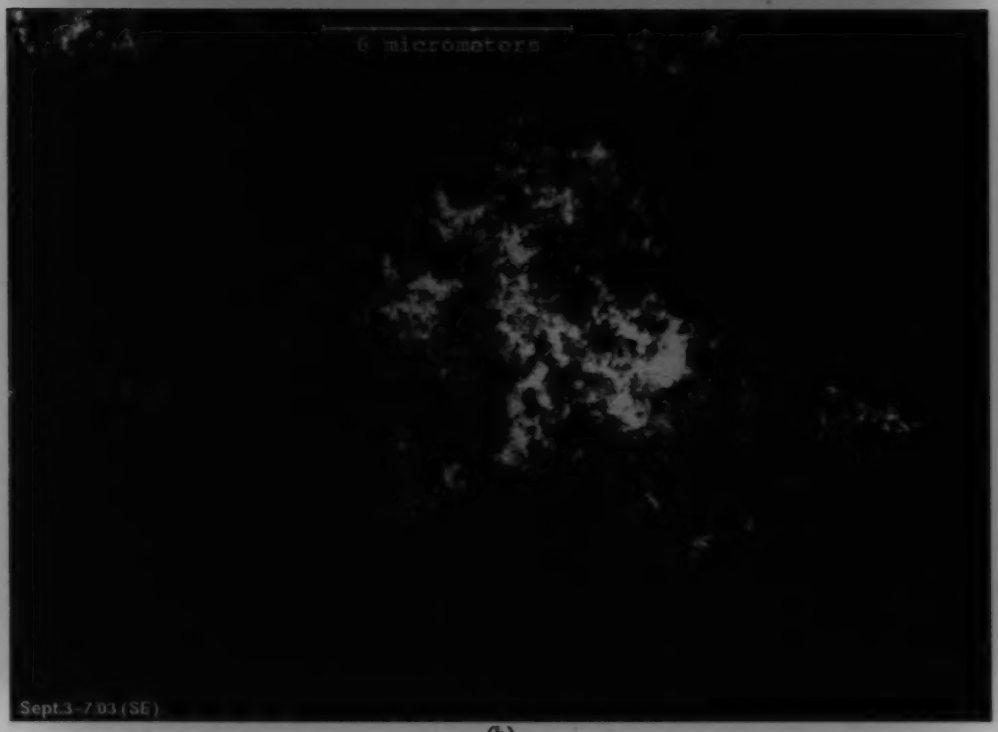

(b)

Figure 6-11: SEM secondary electron images of sample 03-01 (plan view)

zirconia is not as expected. From previous work done using polarized electrochemical vapour deposition to deposit a ceramic layer onto a metallic anode, the expected appearance of the layer is a very thin coating encapsulating the platinum grains that make up the anode. An example of this may be seen in Figure 3-3(d) in Chapter 3. From Figures 6-8 to 6-11, it appears that the deposit is concentrating in some areas and is effectively a solid deposit rather than a film. Energy-dispersive x-ray analysis was performed on the samples examined in the SEM in order to better understand what was being seen in the SEM photographs. An overall analysis was performed, along with analyses of particular points on each of the samples. Initially, an accelerating voltage of 20 kV was used for the analysis but, as reported by Haldane[103], it is difficult to resolve the overlapping low-energy peaks of platinum, zirconium and yttrium, and a higher accelerating voltage (30 kV) would allow for the high-energy peaks of these elements to be seen. However, when a higher accelerating voltage is used, the sample volume is increased, particularly in depth, and the results may not be definitive due to the expected thinness of the PEVD layer.[103]

EDX analysis was used to generate an overall spectrum for each of the five samples studied in the SEM, initially at an accelerating voltage of 20 kV, then using a higher voltage of 30 kV. The overall spectrum was collected at the lowest magnification (50X) and consists of an average of the data collected by a raster pattern scan across the anode surface. All of the spectra were quite similar in appearance, so those generated only for sample 03-10 may be seen in Figure 6-12. The most dominant feature seen in all of the spectra, both at 20 and 30 kV, is the presence of a platinum peak at ~2.0 keV. From this peak and the elemental analysis, seen in Table 6-3, it is clear that platinum is the major component of the anode, which is as expected. As discussed earlier, the higher accelerating voltage used to reduce peak overlap will lead to a larger and deeper sample area. This is evident in the amount of platinum found by the elemental analysis at the different accelerating voltages: 74-78 wt% at 20 kV versus 95-98 wt% at 30 kV.

Of the other two elements of interest, yttrium and zirconium, only zirconium was evident on all of the spectra, at both 20 and 30 kV, with the exception of the 30 kV spectrum of sample 03-01 which showed yttrium. From the elemental analysis in Table 6-3, 17-21 wt% zirconium is present in the samples when an accelerating voltage of 20 kV is used. The amount drops to 0-3 wt% at a voltage of 30 kV, which reinforces the assumption that the deposited layer is thin. For sample 03-01, 0.67 wt% of yttrium was detected at an accelerating voltage of 30 kV.

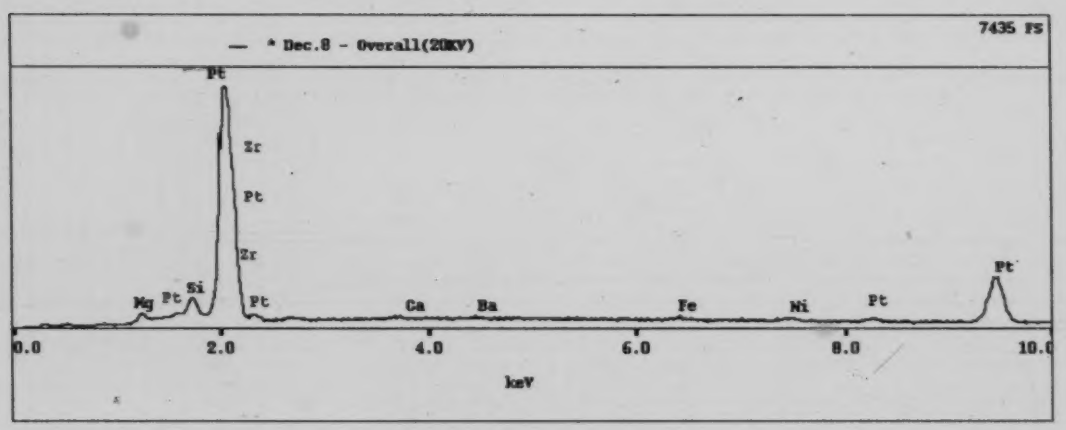

(a) accelerating voltage = 20 kV

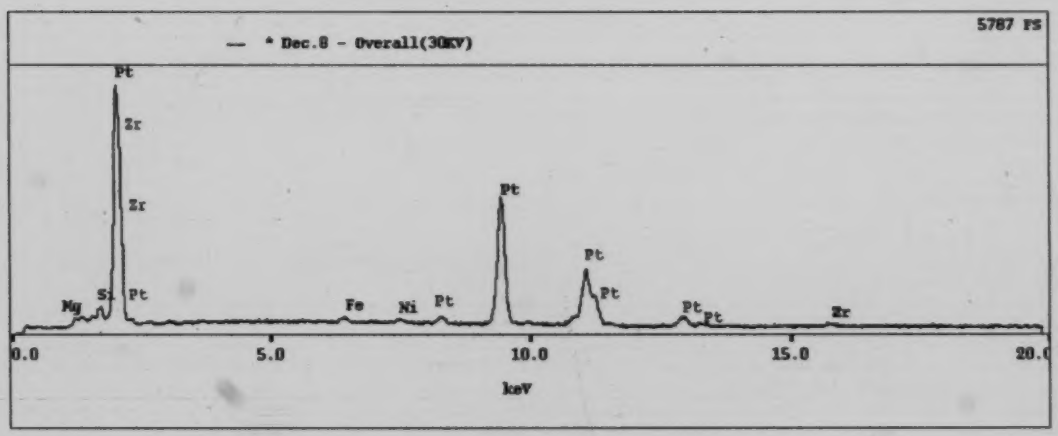

(b) accelerating voltage = 30 kV

Figure 6-12: EDX overall spectra for sample 03-10

Table 6-3: Elemental analysis from overall EDX analysis for 900°C and -400 mV samples viewed in the SEM

Fuel Cell Sample	Amount of Element (wt%)					
	Accelerating Voltage = 20 kV			Accelerating Voltage = 30 kV		
	Pt	Zr	Y	Pt	Zr	Y
03-03	76.31	19.89	-	98.43	-	-
03-05	74.15	21.51	-	95.07	3.32	-
03-08	78.03	17.42	-	98.21	-	-
03-10	77.32	16.96	-	95.01	2.70	-
03-01	76.71	19.93	-	93.84	3.63	0.67

In addition to the overall spectra, point analyses were also completed for each of the five samples to determine the composition of the crystalline-like layer visible on the anode surface. Again, these samples were studied using an accelerating voltage of 20 kV, followed by 30 kV. As for the overall spectra, an accelerating voltage of 20 kV showed a platinum and zirconium peak overlap, as seen in Figure 6-13 on the following page, with the exception of samples 03-08 and 03-01. From the elemental analysis in Table 6-4 below, no zirconium was detected for the layer on these two samples, despite the platinum peak for each appearing as broad as samples that did show zirconium. Once the accelerating voltage was increased to 30 kV, all of the samples show the presence of zirconium in the layer, though in lesser quantities than those found at 20 kV. In the case of yttrium, none showed up in the elemental analysis at either 20 or 30 kV. The reason for this is not quite clear, since the EDX is capable of detecting element amounts of 0.5 wt% or greater and it was expected that yttrium would be present in sufficient quantities to be detected.

6.1.1. Summary

The results presented by this set of experiments are a combination of expected and unexpected outcomes. The presence of a deposited layer was anticipated; however, the physical appearance presented itself as a solid deposit on the surface of the anode rather than a thin, encapsulating layer around the platinum grains. An increase in fuel cell performance was evident for the majority of the samples. Though the results of these experiments do not offer a definitive conclusion as to the best deposition time, it appears that the best results occur for sample 03-10. This cell achieved a high power density and, though the performance decreased somewhat as the number of depositions increased, the performance after deposition was consistently better than with no deposition at all. From this conclusion, a deposition time of 12 hours was used for the subsequent experiments investigating different operating/deposition temperatures, deposition voltages and equilibrium vapour pressure ratios.

Table 6-4: Elemental analysis from EDX point analysis of crystal-like layer

Fuel Cell Sample	Amount of Element (wt%)					
	Accelerating Voltage = 20 kV			Accelerating Voltage = 30 kV		
	Pt	Zr	Y	Pt	Zr	Y
03-03	67.13	22.58	-	83.86	10.10	-
03-05	63.56	31.83	-	90.77	7.21	-
03-08	85.46	-	-	87.86	5.89	-
03-10	65.43	27.08	-	91.48	6.81	-
03-01	80.52	-	-	88.07	5.81	-

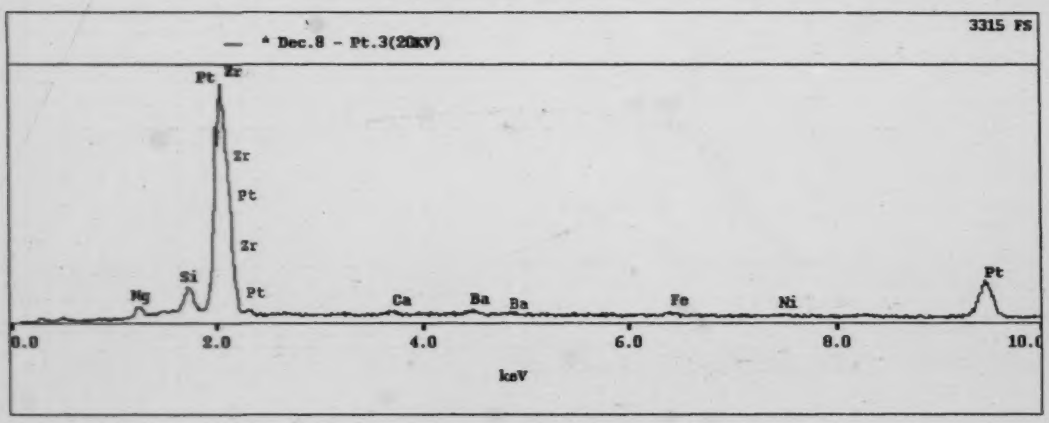

(a) accelerating voltage = 20 kV

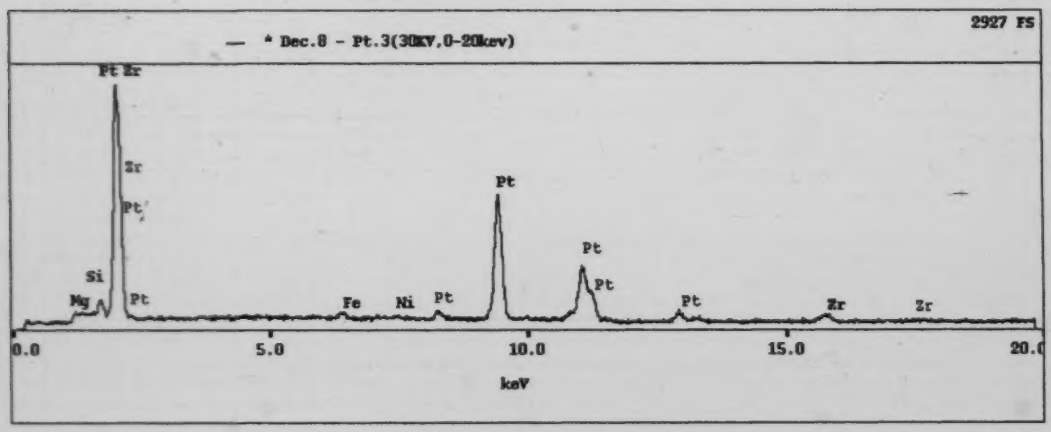

(b) accelerating voltage = 30 kV

Figure 6-13: EDX point analysis spectra for sample 03-10

6.2 Effect of Deposition Bias Voltage and Equilibrium Vapour Pressure Ratio

From earlier work studying the effect of deposition time on fuel cell performance, it was determined that a deposition time of 12 hours gave good overall results. Subsequent experiments have looked at the effect of the deposition bias voltage and of the equilibrium vapour pressure ratio between YCl_3 and $ZrCl_4$. The effects of these variables were investigated at operating/deposition temperatures of 750°C and 800°C. At each temperature, equilibrium vapour pressure ratios of 8:1 and 5.25:1 were used and at each ratio, deposition bias voltages of -500 mV and -800 mV were used. Additionally, the effect of temperature cycling on the performance of

the fuel cell was studied after the fourth deposition for each of the samples.

6.2.1 Experimental Difficulties

During the course of these experiments, an unexpected difficulty with the platinum wire used as lead wire to the anode occurred. The problem occurred after the fuel cell had been heated to its desired operating temperature in the tube furnace, and the hydrogen and air had been started in order to acquire current-voltage data. The open-circuit voltage would initially increase to values of approximately 0.9-1.0 V, and then suddenly drop to approximately 0.3-0.4 V. Upon removal of the cell assembly from the tube furnace, it was discovered that the wire coming through the cement and attached to the anode (see Figure 5-3 in Experimental Procedure) was no longer present. Inspection of the tube furnace led to the discovery of this piece of wire.

Initially, the problem was evident with new lengths of platinum wire, either 0.381 mm platinum or 0.508 mm platinum-rhodium wire. However, later experiments set up using lead wires from previous experiments where this problem had not occurred also experienced the same difficulty. The problem usually arose 1.5-2 hours after the hydrogen and air had been started, before any deposition had taken place. One theory of the cause of this problem was the use of "extra dry" air (for the previous experiments "hydrocarbon free" air had been used), but this was quickly ruled out due to the problem occurring on the anode side only. A second theory of the cause of this problem was the ceramic sealant, since the wire seemed to break off just above the ceramic. A new container of the ceramic had recently been purchased, but discussion with the supplier confirmed that no changes to the composition of the ceramic had been made. This fact, along with the fact that the "old" ceramic had been used for sealing the cell onto the alumina tube in a couple of experiments that experienced problems, ruled out this theory.

Finally, the hydrogen regulator was considered as the source of the problem. It had been used to test other cylinders in our laboratory for the amount of gas remaining in those cylinders. After discussion with the Praxair representative, it was clear that the regulator may have been contaminated and it was sent in for cleaning. Upon return of the regulator, the problem was not experienced again for about two months.

The problem does arise sporadically, though no major changes have been made to the furnace or cell assembly. When the problem does arise, the appearance of the wire changes from very smooth and shiny to somewhat dull, rough and pitted. SEM photographs of the change in wire

appearance may be seen in Figure 6-14 on the following page. On occasion, the presence of small spheres of what appear to be platinum is evident on the surface of the anode. Since this problem has occurred, the appearance of the anode after depositions has changed as well, with it looking shinier. Delamination of the anode has also occurred more frequently. Investigation into the root of this problem continues.

6.2.2 750°C Experiments

6.2.2.1 Equilibrium Vapour Pressure 8:1

A comparison between the corrected polarization curves of the depositions carried out at -500 mV and -800 mV, as detailed in Table 6-5, may be seen in Figure 6-15. Additionally, corrected polarization curves showing performance after each deposition for some samples are shown in Figure 6-16. The most apparent similarity is that all of the samples experienced a decrease in performance with an increasing number of depositions. This is clearly seen by the greater and greater deviation from the ideal discharge behaviour, which would be a horizontal line on the current-voltage plot.

Upon observation of the polarization curves in Figure 6-15, the dominant feature is the unexpected shape of the curves (with the exception of sample 04-06). The curves initially show a negative slope, likely due to the effects of activation polarization, followed by a region with a less negative slope, usually due to ohmic losses. However, after this point, the curves look to be moving into a vertical slope expected of concentration overpotential, but instead of staying vertical, they turn back towards lower current density values. This is readily visible for samples 04-02, 04-03 and 04-04 in Figure 6-15(a). When all of these cells, except sample 04-06, were being tested, it was observed that the current would initially increase upon application of the resistance, but then would decrease despite the voltage continuing to drop. From looking at Figures 6-15(b) to (e) after the subsequent depositions, it is clear that this behaviour continues,

Table 6-5: Fuel cell samples for YSZ deposition at 750°C and vapour pressure ratio 8:1

Fuel Cell Sample	Deposition Bias Voltage (mV)
04-01	-500
04-02	-500
04-03	-500
04-04	-800
04-05	-800
04-06	-800

(a) appearance before failure

(b) appearance after failure

Figure 6-14: SEM secondary electron images of 0.508 mm platinum wire

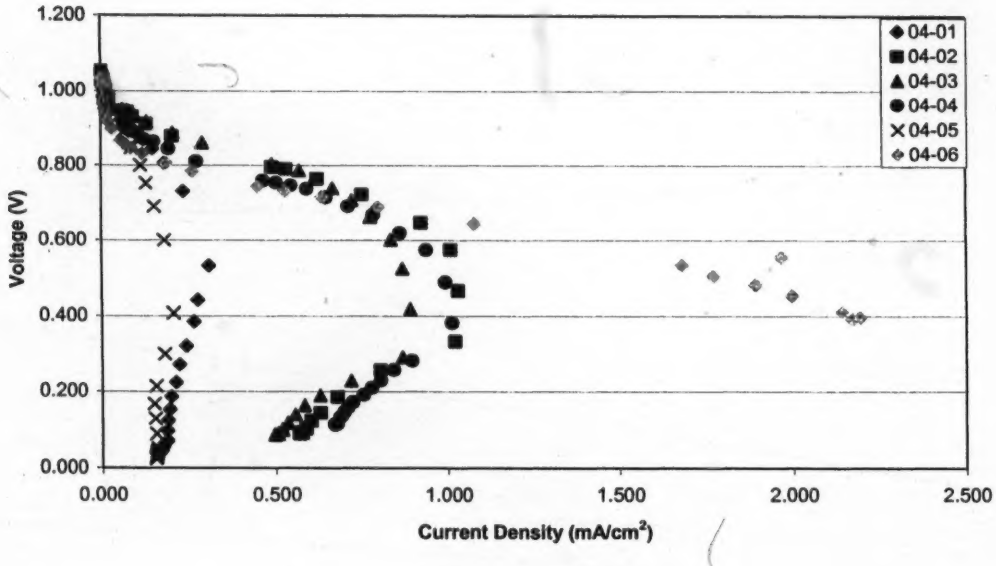

(a) no deposition

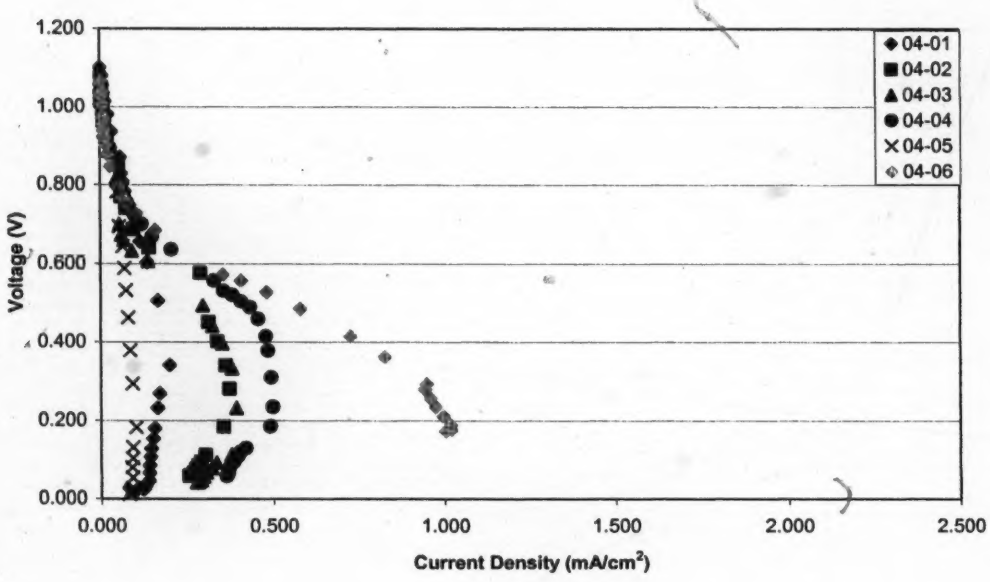

(b) 1 deposition

Figure 6-15: Corrected polarization curves for YSZ deposition at 750°C and vapour deposition ratio 8:1 by number of depositions

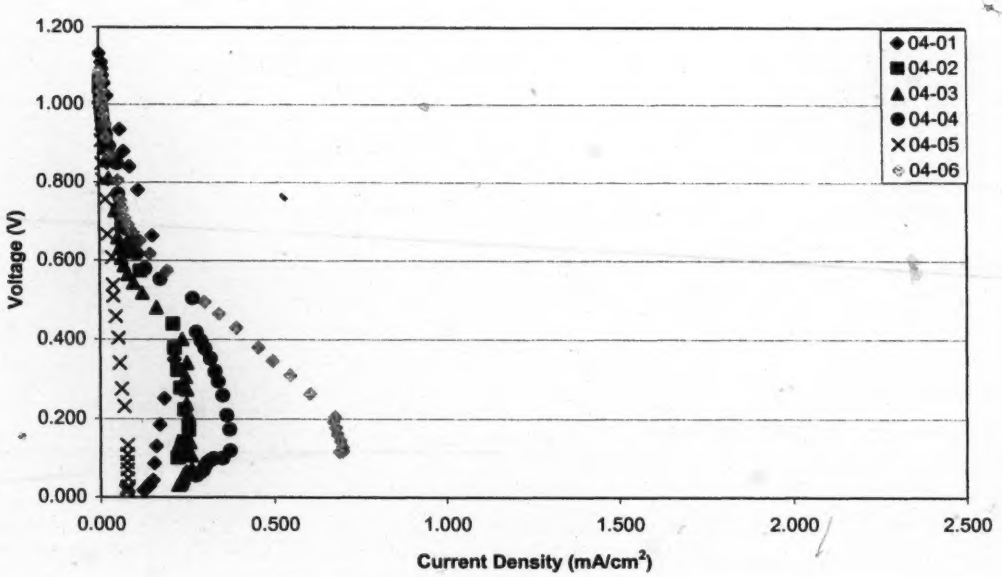

(c) 2 depositions

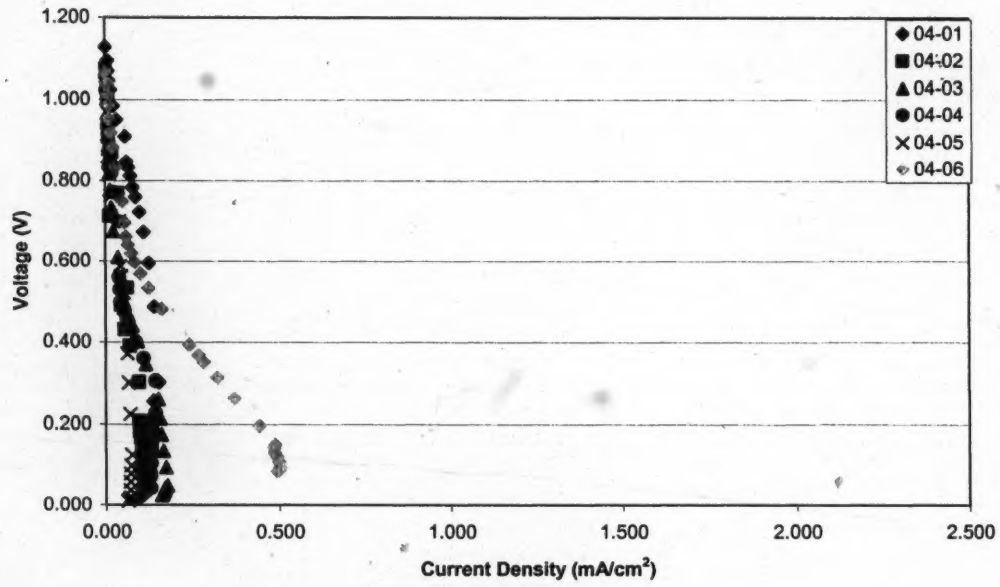

(d) 3 depositions

Figure 6-15 (con't): Corrected polarization curves for YSZ deposition at 750°C and vapour deposition ratio 8:1 by number of depositions

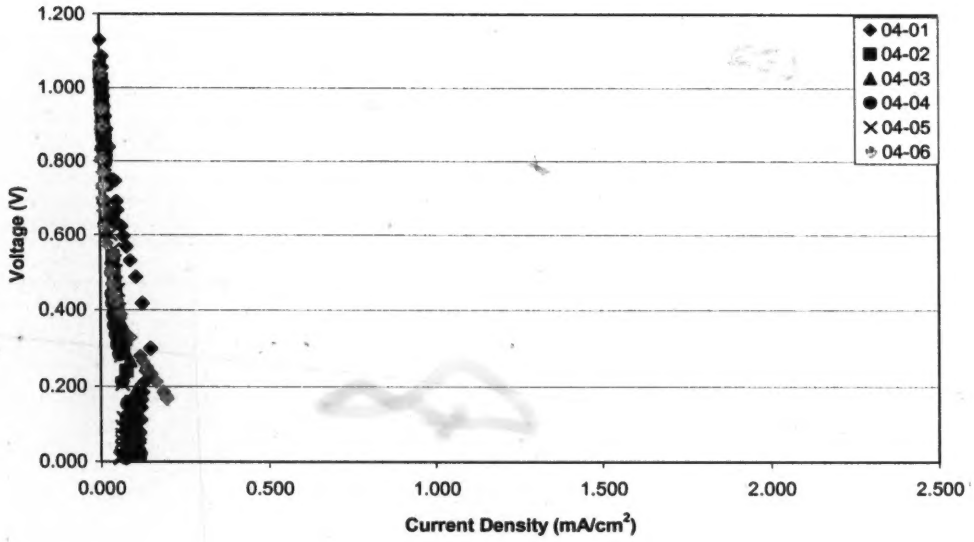

(e) 4 depositions

Figure 6-15 (con't): Corrected polarization curves for YSZ deposition at 750°C and vapour deposition ratio 8:1 by number of depositions

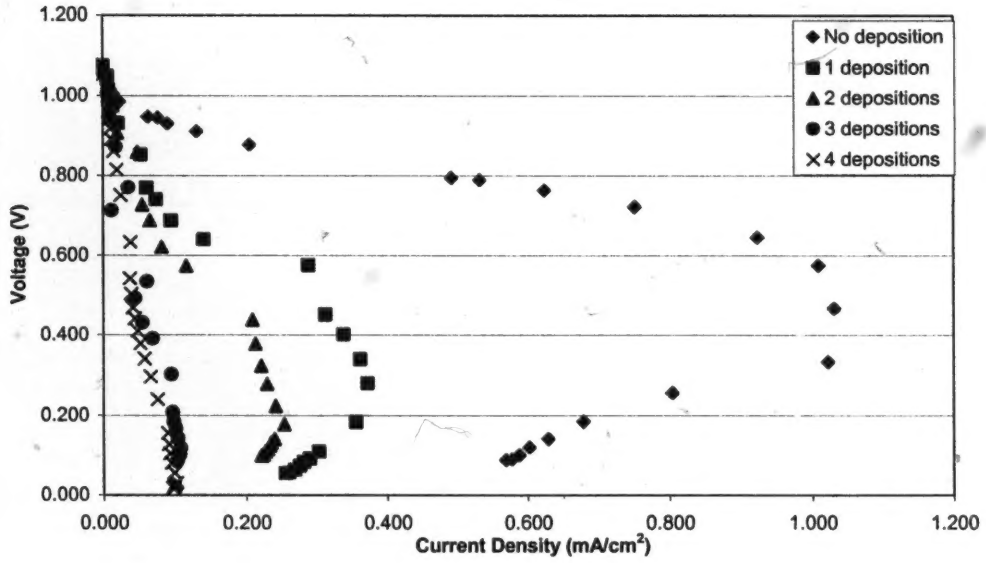

(a) sample 04-02

Figure 6-16: Corrected polarization curves for YSZ deposition at 750°C and vapour deposition ratio 8:1 by sample

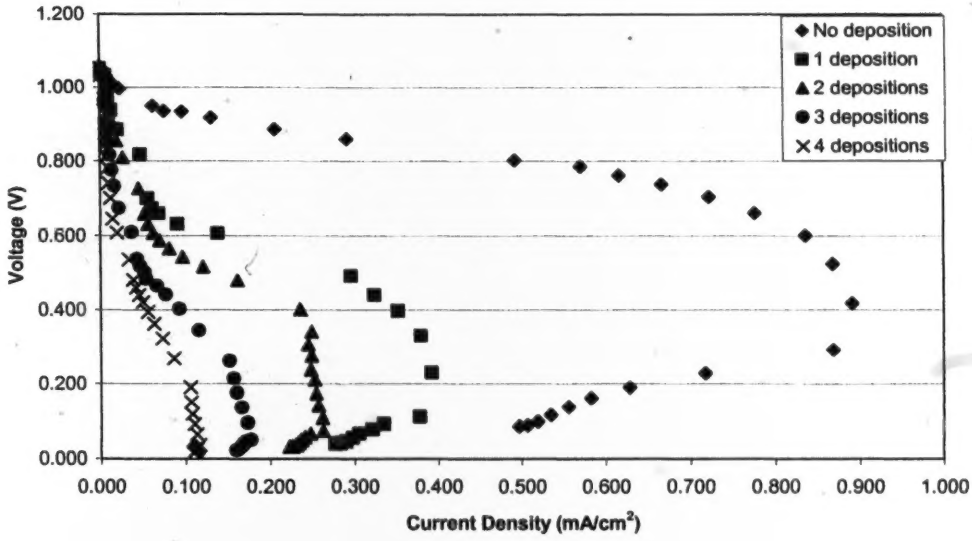

(b) sample 04-03

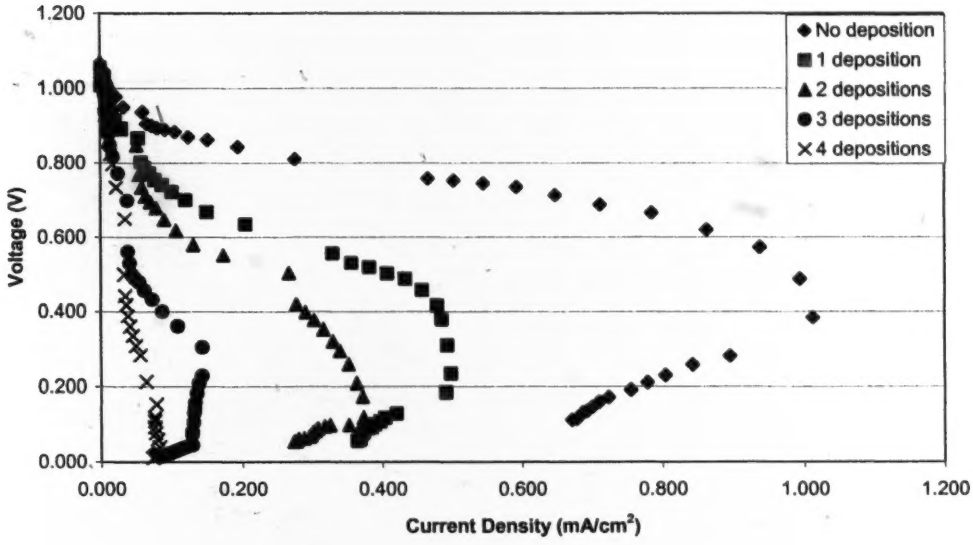

(c) sample 04-04

Figure 6-16 (con't): Corrected polarization curves for YSZ deposition at 750°C and vapour deposition ratio 8:1 by sample

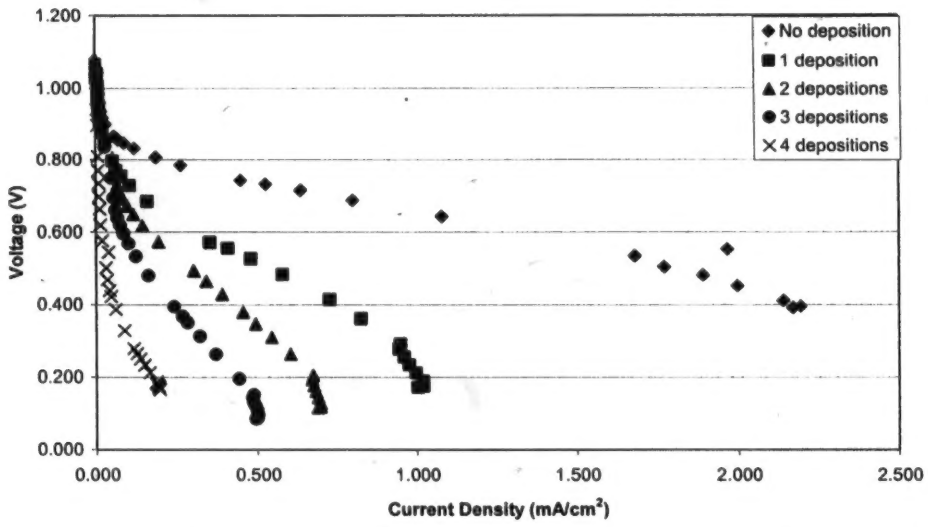

(d) sample 04-06

Figure 6-16 (con't): Corrected polarization curves for YSZ deposition at 750°C and vapour deposition ratio 8:1 by sample

though it is a bit more difficult to see due to the lower current densities. The reason for this behaviour is not clear and attempts to discover if this shape of polarization curve is indicative of some kind of electrochemical factor/reaction have not been successful.

As may be seen from the polarization curves in Figure 6-15, the performance of every cell decreased with each subsequent deposition. This is in contrast to the behaviour shown by the cells discussed in section 6.1, which had the general trend of an increase in performance after the first deposition, followed by a decrease in performance. As the number of depositions increase, activation overpotential seems to take on a more commanding role in the voltage loss of the fuel cells, as demonstrated by an increasingly negative initial slope. The evidence of a second and third region in the curves diminishes as the number of depositions increases, indicating ohmic loss and concentration overpotential play less of a role. Conversely, it may be greater ohmic loss that is causing the visibly steeper slope of the polarization curves, since it has been stated that activation overpotential is generally of less concern for SOFCs due to high operating temperature.[6]

Figure 6-17 shows the corrected power curves for the samples tested at an operating/deposition

temperature of 750°C and an equilibrium vapour pressure ratio of 8:1, with additional curves for specific samples in Figure 6-18. As expected from the polarization curves, the power curves show a decrease in the power densities achieved by the cells after each deposition. From Table 6-6, the maximum power density for all samples occurred when no deposition had been carried out. Once again, the unusual behaviour of the cells in regards to measured current manifests itself in the atypical shape of the power curves. Instead of reaching a maximum power density and then dropping after the power curve starts dropping, it then turns back to lower current densities.

In order to better understand why the samples showed poorer performance after depositions had been carried out, three samples were selected to be viewed using the SEM: 04-02, 04-03 and 04-06. The secondary electron images of these cells may be seen in Figures 6-19 to 6-21. Upon comparison of the anode microstructures of these samples with that of the anode before undergoing any deposition (Figure 6-6), a significantly different appearance is seen. As opposed to a porous structure with small, well-connected platinum grains, the samples show a large grain structure with very little porosity. The significantly less porous structure of the anodes is quire unexpected since the operating/deposition temperature of 750°C is much lower than the 950°C temperature the anode was subjected to during preparation. This notable change in anode microstructure is quite probably the reason for the poor performance of the cells. If the anode does not have sufficient porosity, less hydrogen will be able to reach the active sites, resulting in fewer electrochemical reactions and, consequently, lower current densities and power output by the cell. This theory is evidenced when the microstructure of sample 04-06 is compared to those of samples 04-02 and 04-03. Sample 04-06 shows significantly more porosity than the other two samples and it produced higher current and power densities.

Another consequence of the reduced porosity in the fuel cells would manifest itself in the

Table 6-6: Maximum power density for 750°C and 8:1 samples

Fuel Cell Sample	Maximum Power Density (mW/cm^2)				
	Deposition				
	0	1	2	3	4
04-01	0.10	0.08	0.10	0.07	0.05
04-02	0.60	0.17	0.09	0.03	0.02
04-03	0.51	0.15	0.09	0.04	0.02
04-04	0.54	0.21	0.13	0.04	0.02
04-05	0.11	0.04	0.02	0.03	0.02
04-06	1.09	0.30	0.17	0.10	0.04

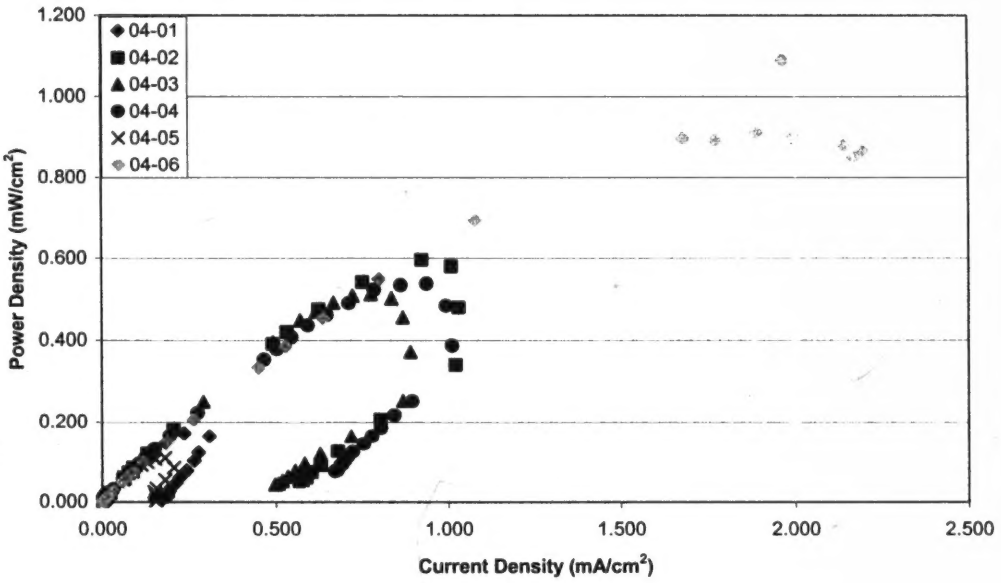

(a) no deposition

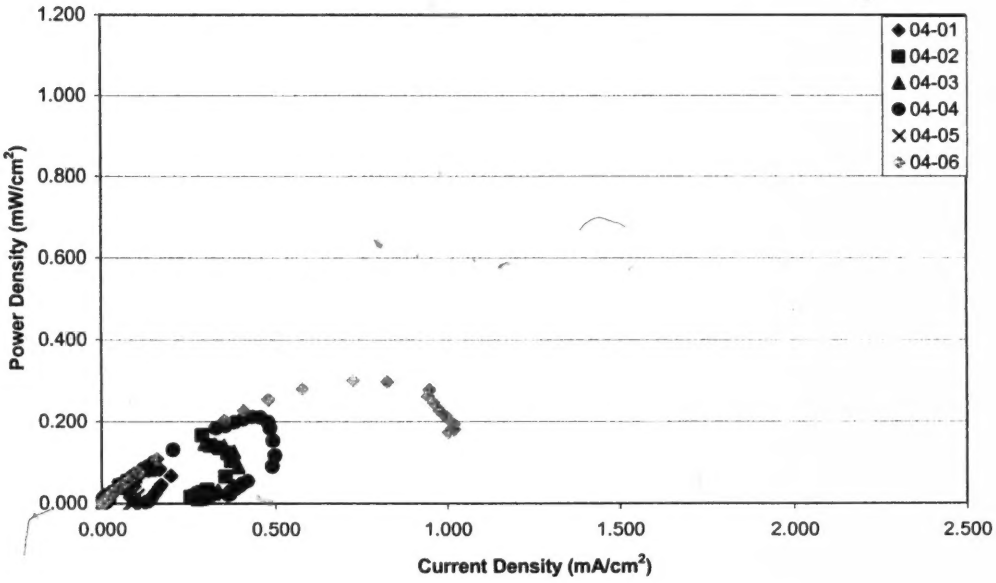

(b) 1 deposition

Figure 6-17: Corrected power curves for YSZ deposition at 750°C and vapour deposition ratio 8:1 by number of depositions

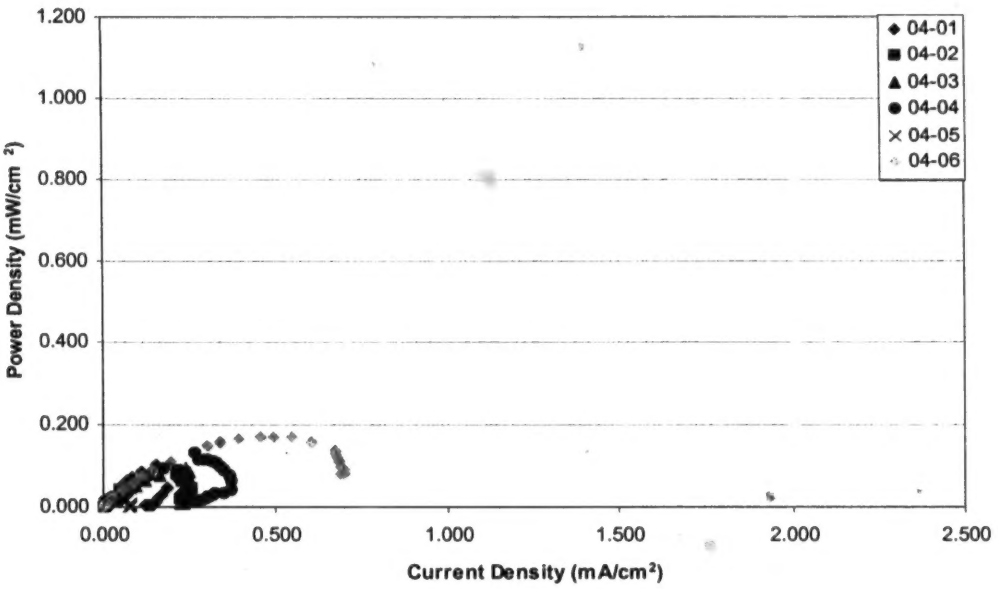

(c) 2 depositions

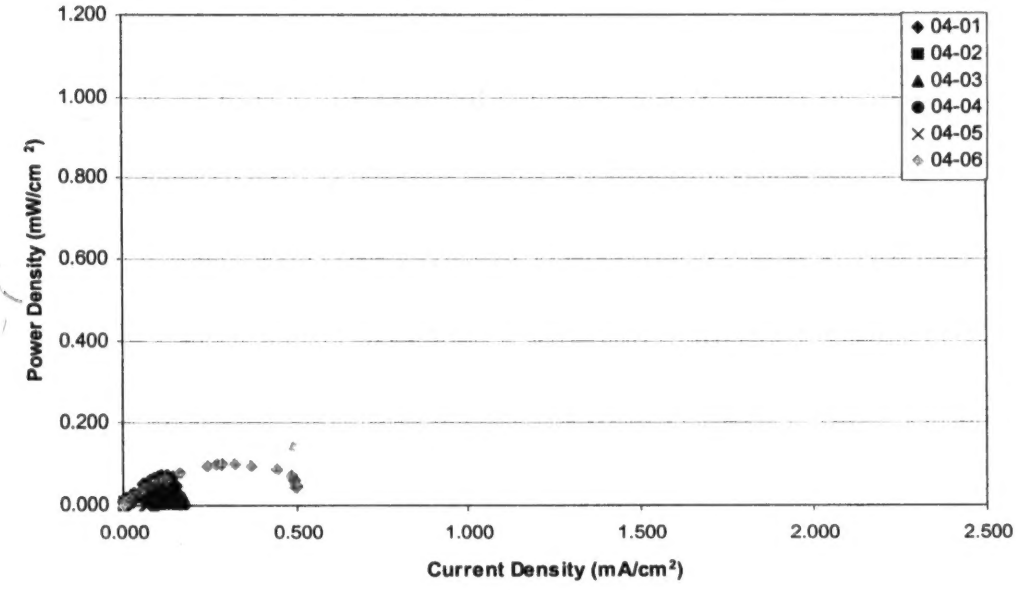

(d) 3 depositions

Figure 6-17 (con't): Corrected power curves for YSZ deposition at 750°C and vapour deposition ratio 8:1 by number of depositions

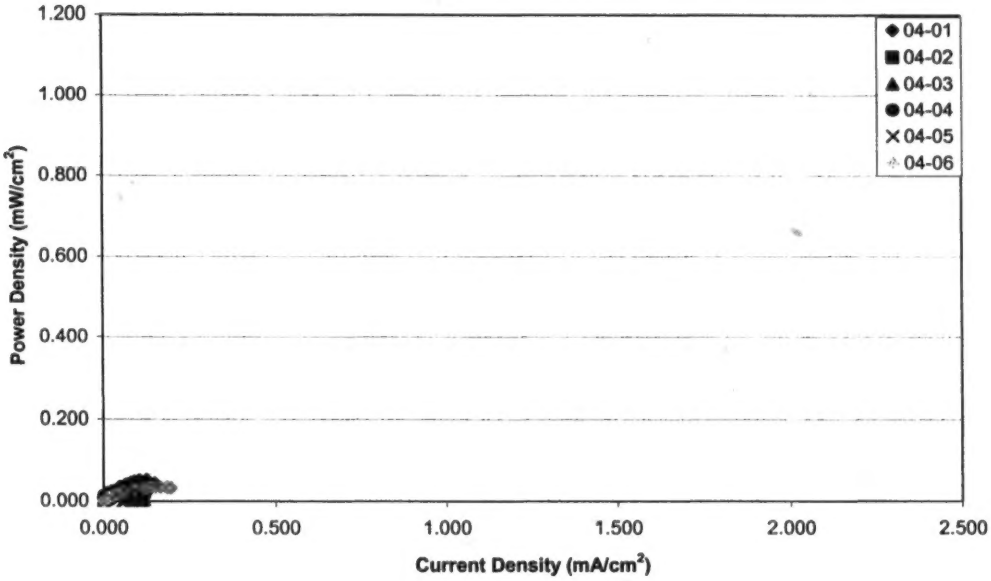

(e) 4 depositions

Figure 6-17 (con't): Corrected power curves for YSZ deposition at 750°C and vapour deposition ratio 8:1 by number of depositions

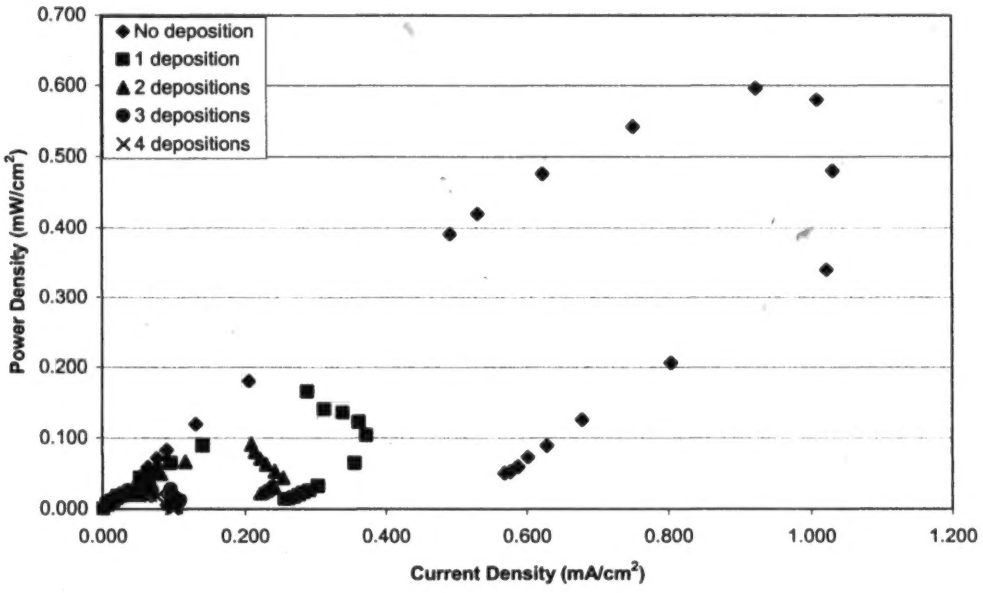

(a) sample 04-02

Figure 6-18: Corrected power curves for YSZ deposition at 750°C and vapour deposition ratio 8:1 by sample

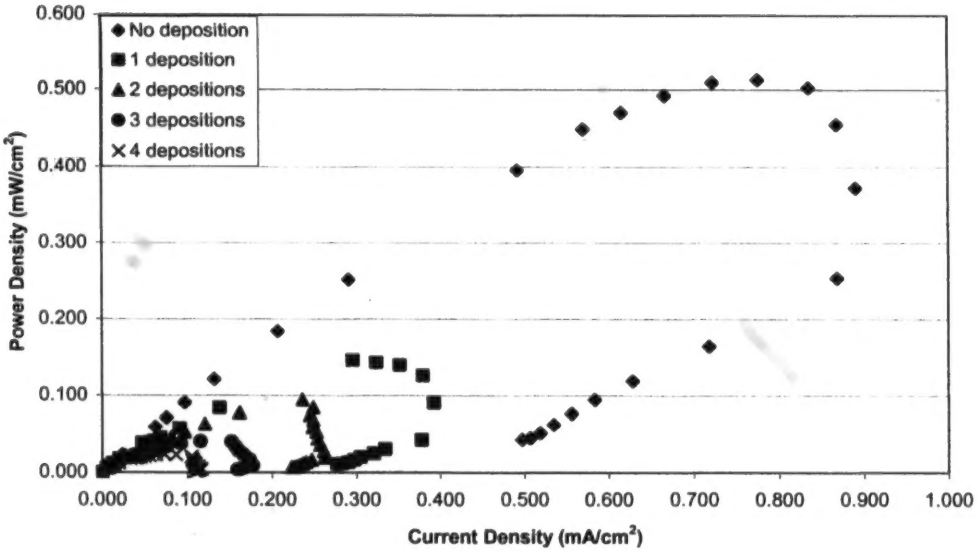

(b) sample 04-03

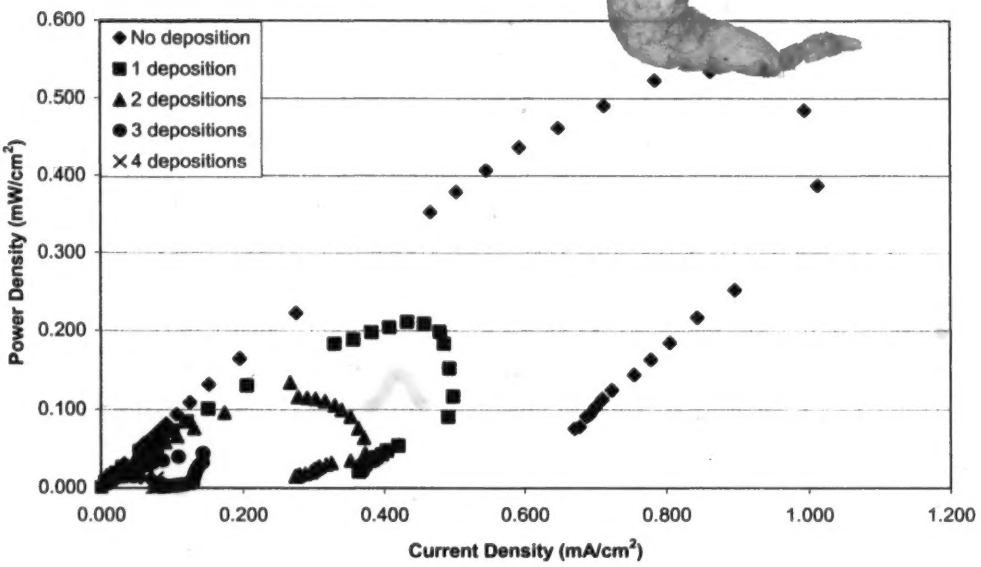

(c) sample 04-04

Figure 6-18 (con't): Corrected power curves for YSZ deposition at 750°C and vapour deposition ratio 8:1 by sample

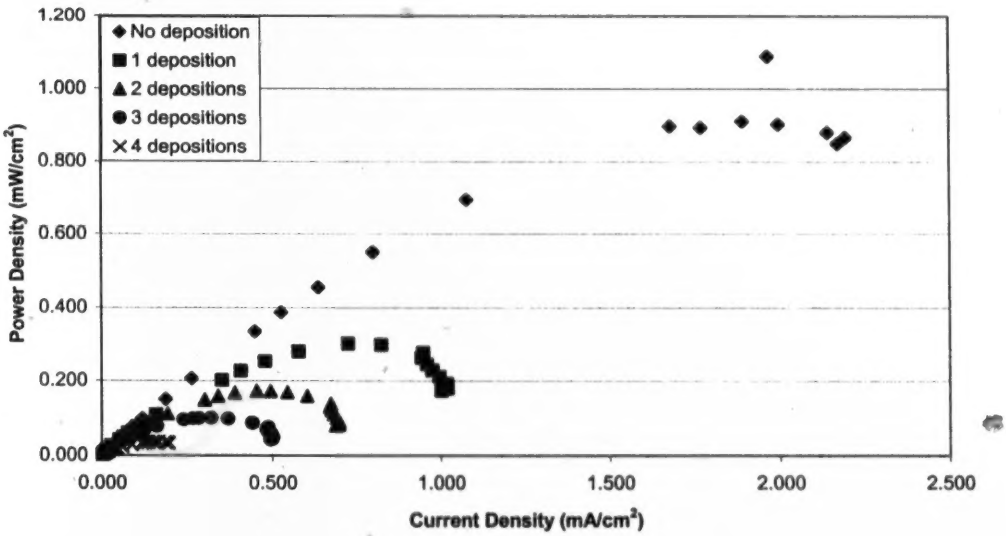

(d) sample 04-06

Figure 6-18 (con't): Corrected power curves for YSZ deposition at 750°C and vapour deposition ratio 8:1 by sample

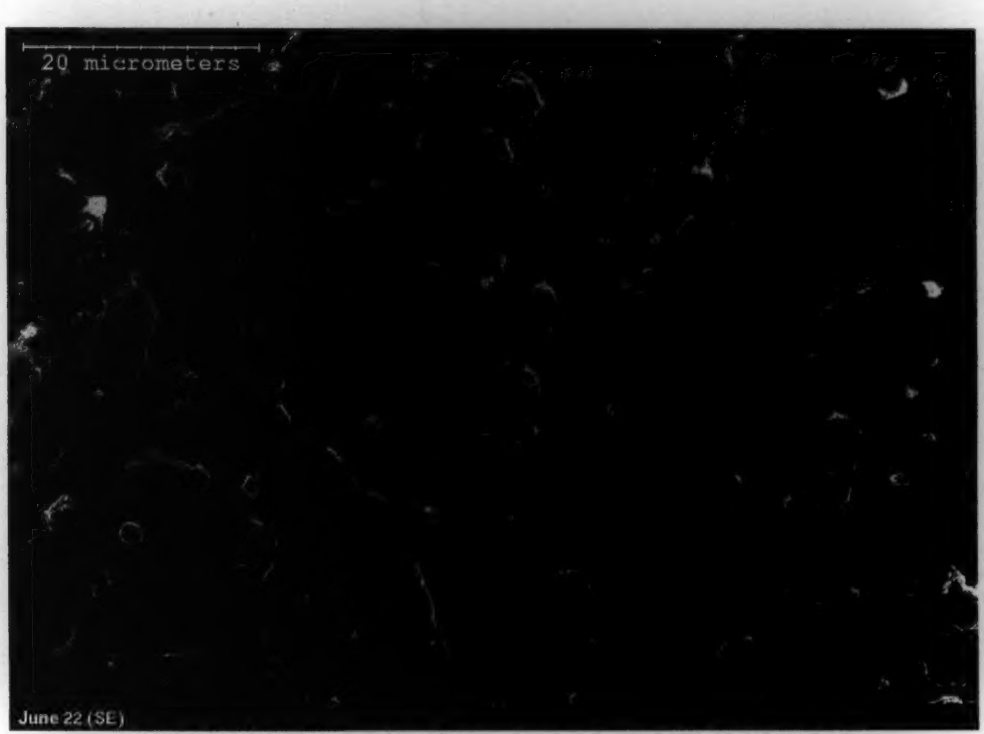

Figure 6-19: SEM secondary electron image of sample 04-02 (plan view)

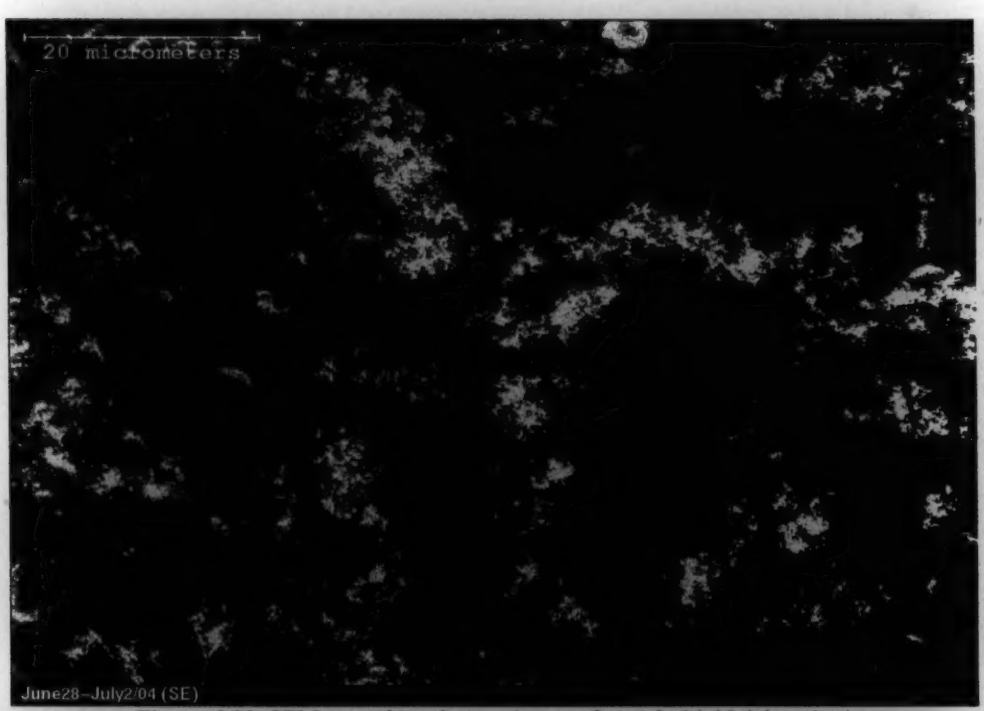

Figure 6-20: SEM secondary electron image of sample 04-03 (plan view)

Figure 6-21: SEM secondary electron image of sample 04-06 (plan view)

formation of the YSZ deposition layer. From the SEM images, only one sample, 04-03, has the crystal-like surface layer visible on the fuel anode discussed in section 6.1. If the porosity of the anode is insufficient, the yttrium and zirconium chloride vapours would not be able to reach the electrolyte to combine with oxygen ions to form the Y_2O_3-ZrO_2 deposit. In order to determine if any YSZ deposit had formed, EDX was again used to analyze the three samples observed in the SEM. As before, an overall spectrum at accelerating voltages of 20 kV and 30 kV was performed for each sample. However, due to the surface roughness of the samples and the peak overlap, the appearance of the spectra at both accelerating voltages is very similar for the three samples, so those for sample 04-02 are shown in Figure 6-22 on the following page. As with previous samples at 20 kV, low-energy peaks for platinum and zirconium are visible, though they are overlapping. A strong platinum peak is evident at ~9.5 keV. When an accelerating voltage of 30 kV is used, there is little change in the spectrum appearance, other than a stronger peak for platinum at ~9.5 keV. Sample 04-03 also shows a yttrium shoulder on the low-energy platinum peak. From the elemental analysis in Table 6-7, it is clear that less zirconium was found on the anode than earlier work, indicating that less deposition took place. For the crystal-like layer on sample 04-03, the elemental analysis showed ~87 wt% platinum and ~10 wt% zirconium at an accelerating voltage of 20 kV. Again, these values are less than those found for the samples studied in section 6.1.

In addition to studying the effect of the number of depositions on the performance of the fuel cell, it was also desired to see the effect of a change in cell operating temperature. For each cell, after the fourth deposition had been carried out and current-voltage data taken at 750°C, the operating temperature was decreased to 600°C, increased back to 750°C, further increased to 900°C and finally decreased back to 750°C. At each of these temperatures current-voltage data were measured. An example polarization curve and power curve (both corrected for electrolyte resistance) may be seen in Figure 6-23 on the page 111, which are both representative of the curves seen for the six samples. For all samples, an operating temperature of 900°C gave the

Table 6-7: Elemental analysis from overall EDX analysis for 750°C and vapour pressure ratio 8:1 samples viewed in the SEM

Fuel Cell Sample	Amount of Element (wt%)					
	Accelerating Voltage = 20 kV			Accelerating Voltage = 30 kV		
	Pt	Zr	Y	Pt	Zr	Y
04-02	92.96	5.45	-	98.93	-	-
04-03	86.53	9.97	-	96.39	0.73	0.82
04-06	96.46	-	-	98.53	-	-

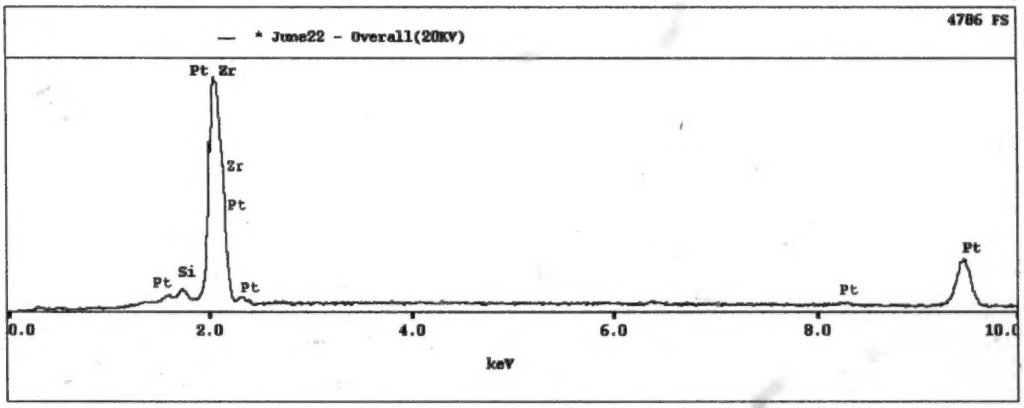

(a) accelerating voltage = 20 kV

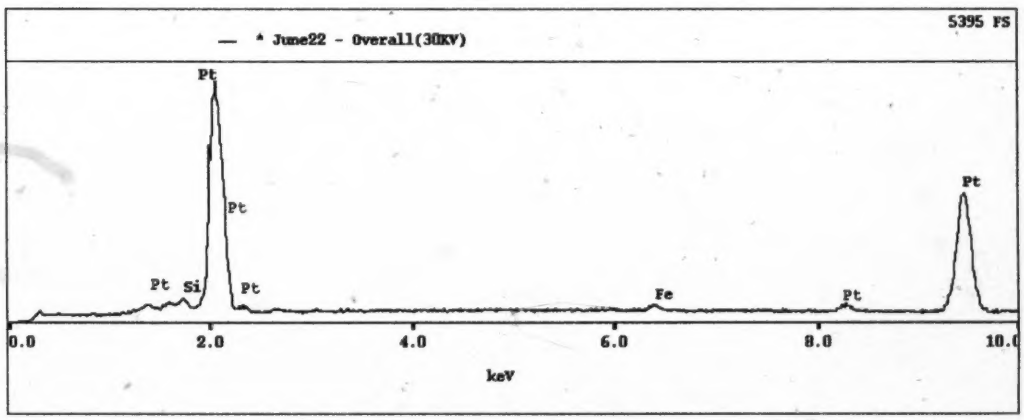

(b) accelerating voltage = 30 kV

Figure 6-22: EDX overall spectra for sample 04-02

best performance and an operating temperature of 600°C gave the poorest performance. These observations are not unexpected due to an increase in the ionic conductivity of the 8 mol% YSZ electrolyte as operating temperature is increased. A notable aspect of this investigation is the reproducibility of the cells each time the operating temperature was at 750°C, indicating that the cells were able to handle temperature cycling without significant loss of performance. The ability to thermally cycle fuel cells without significant loss in performance is highly desirable due to potential applications of the fuel cell stack that would require it to be shut down and restarted. However, the reason why the fuel cell experienced decreasing performance at 750°C after each

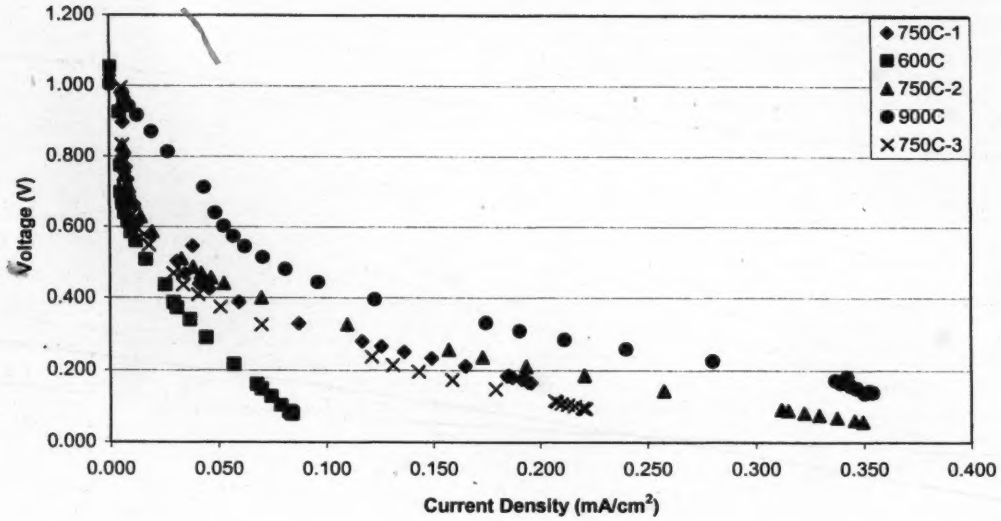

(a) corrected polarization curve

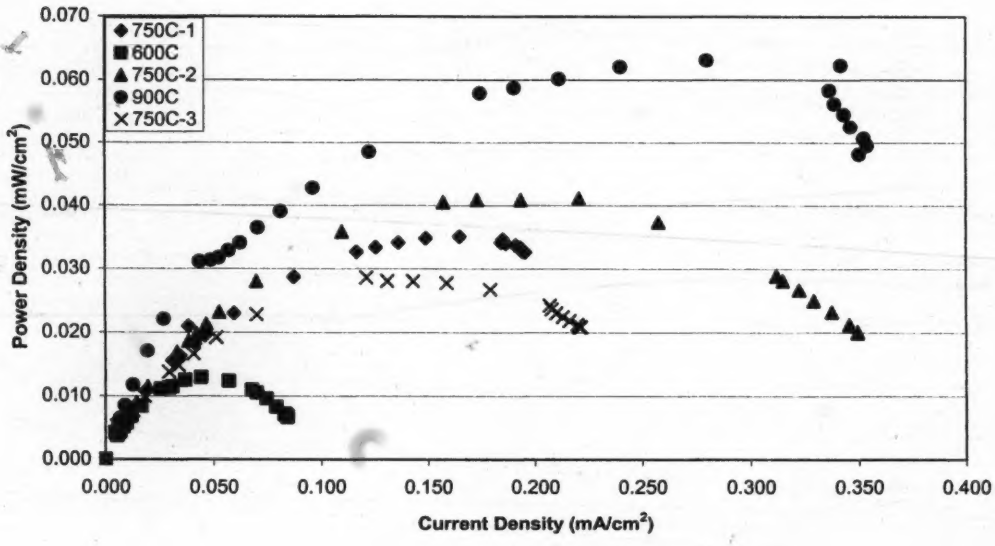

(b) corrected power curve

Figure 6-23: Corrected polarization and power curves for operating temperature cycling testing for sample 04-06

deposition while demonstrating consistent performance at this temperature during the temperature cycling test is unclear. Perhaps by this point in time, the anode had undergone as much sintering as possible leading to more consistent performance.

6.2.2.2 Equilibrium Vapour Pressure 5.25:1

In addition to studying the performance of cells deposited under an equilibrium vapour pressure ratio of 8:1, a ratio of 5.25:1 was also investigated. Using this ratio should give higher yttrium content in the final product of 8 mol%, as opposed to the 5.5 mol% when the first ratio is used. The reason for wanting a higher yttrium content in the YSZ layer being deposited is to allow comparison of a fully stabilized structure to a partially stabilized one.

As for the fuel cells tested at a ratio of 8:1, samples were tested at two different deposition bias voltages; details of the samples may be seen in Table 6-8. The polarization curves for these two samples may be seen in Figure 6-24. In a similar vein as the cells tested using an equilibrium vapour pressure ratio of 8:1, the cells tested at a ratio of 5.25:1 showed a dramatic decrease in performance after depositions were carried out. When Figures 6-24(b) to (e) are compared to Figure 6-24(a), the drop in current density from a maximum near 20 mA/cm^2 to less than 1.2 mA/cm^2 is seen. (Figures 6-24(b) to (e) are on a different current density scale than Figure 6-24(a) to allow for easier observation of the curve shape.) Unlike the curves in Figure 6-15, the curves for these samples show only a few points where the curve turns back to lower current densities at low voltage. After the first and subsequent depositions, the polarization curves take on an increasingly greater negative slope, indicating overpotential is increasing.

The corrected power curves for these two samples may be seen in Figure 6-25. These plots further reinforce the decrease in fuel cell performance after deposition, with specific maximum power densities after each deposition detailed in Table 6-9. As expected from the more typical shape of the polarization curves, the power curves also show a shape closer to that of theoretical than those seen in Figure 6-17. For comparison, the maximum power densities for these cells were compared against those tested at a ratio of 8:1 (see Table 6-6). The initial power densities

Table 6-8: Fuel cell samples for YSZ deposition at 750°C and vapour pressure ratio 5.25:1

Fuel Cell Sample	Deposition Bias Voltage (mV)
05-08	-800
05-09	-500

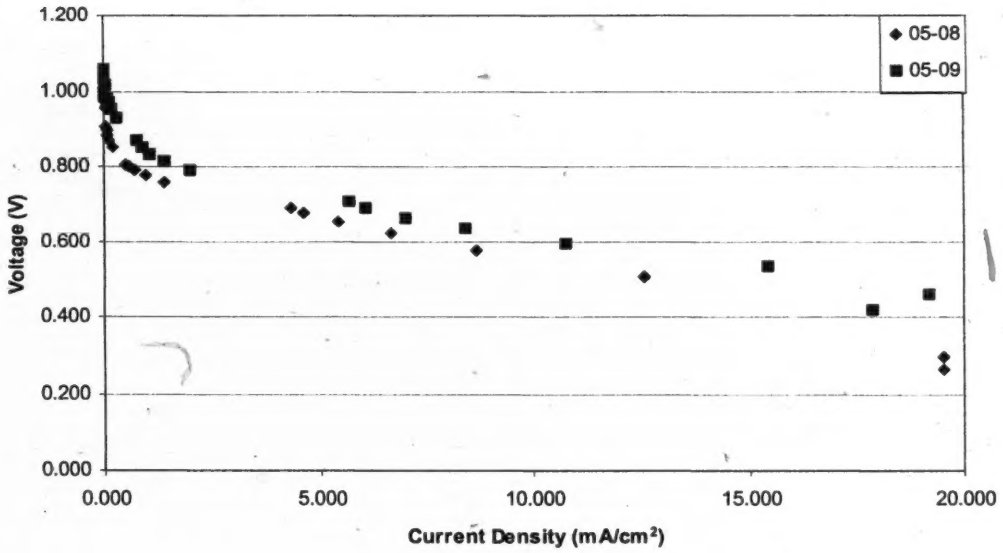

(a) no deposition

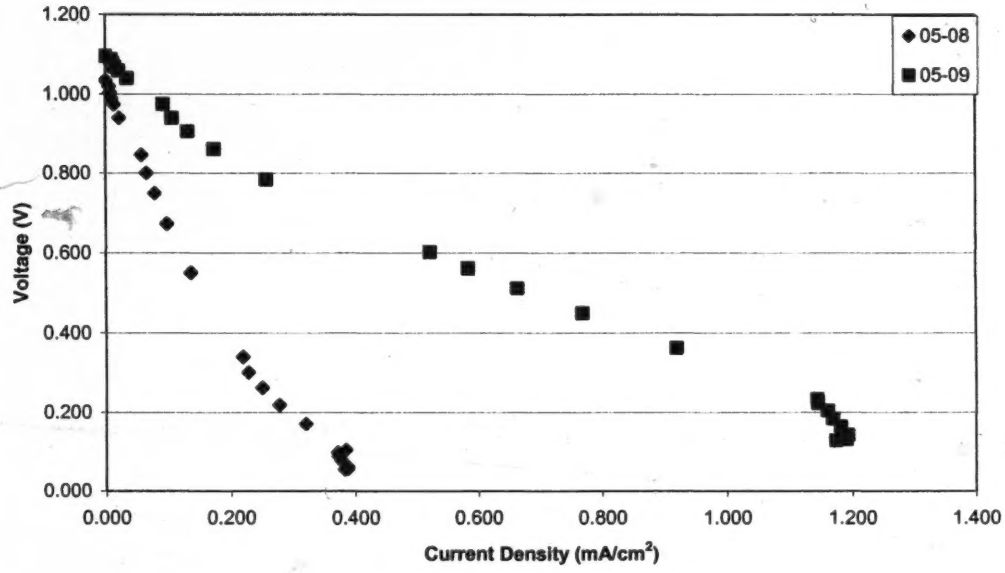

(b) 1 deposition

Figure 6-24: Corrected polarization curves for YSZ deposition at 750°C and vapour pressure ratio 5.25:1 by number of depositions

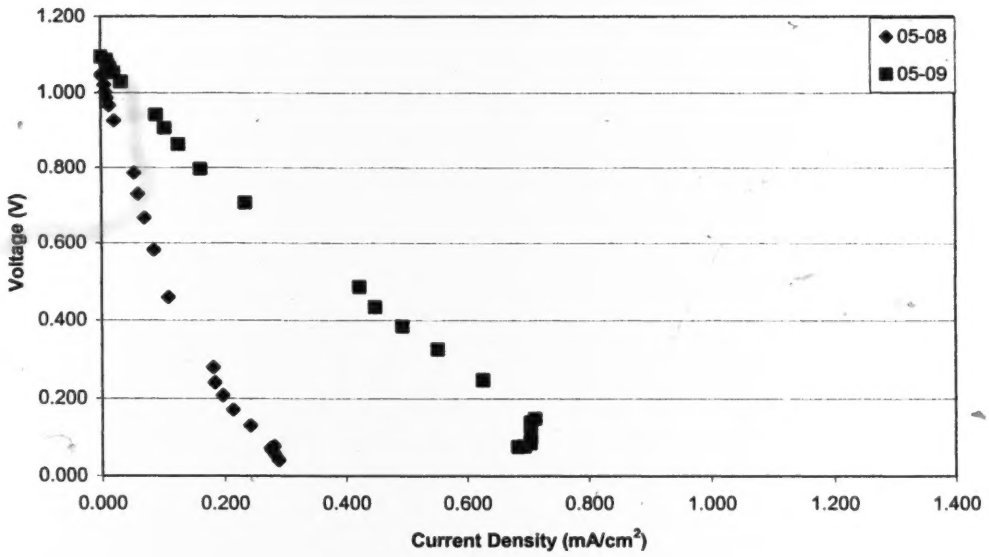

(c) 2 depositions

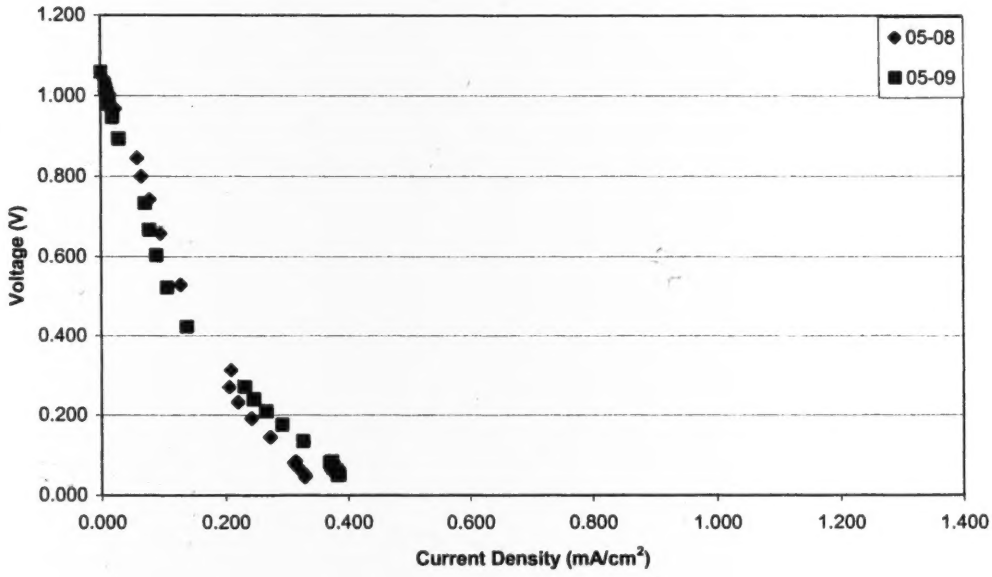

(d) 3 depositions

Figure 6-24 (con't): Corrected polarization curves for YSZ deposition at 750°C and vapour pressure ratio 5.25:1 by number of depositions

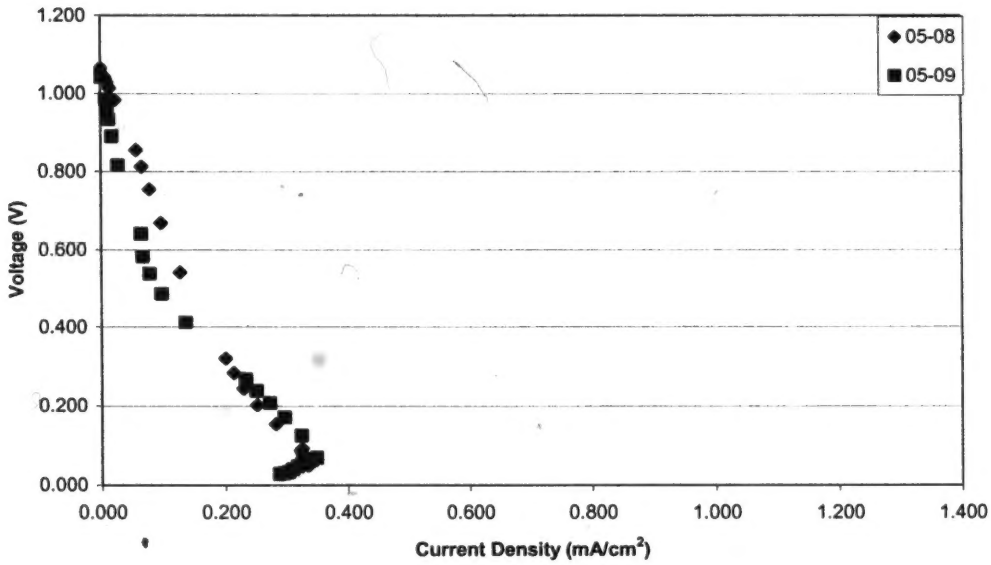

(e) 4 depositions

Figure 6-24 (con't): Corrected polarization curves for YSZ deposition at 750°C and vapour pressure ratio 5.25:1 by number of depositions

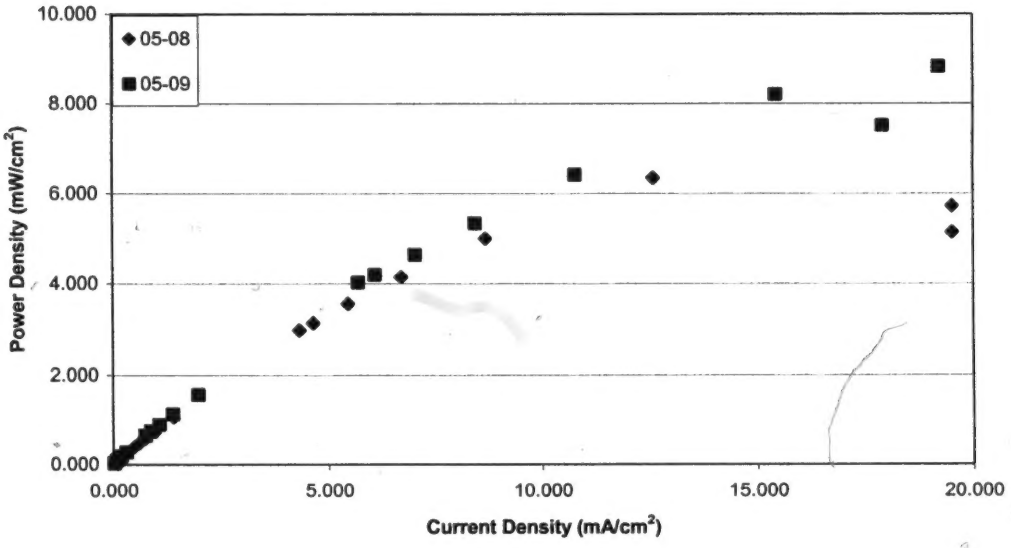

(a) no deposition

Figure 6-25: Corrected power curves for YSZ deposition at 750°C and vapour pressure ratio 5.25:1 by number of depositions

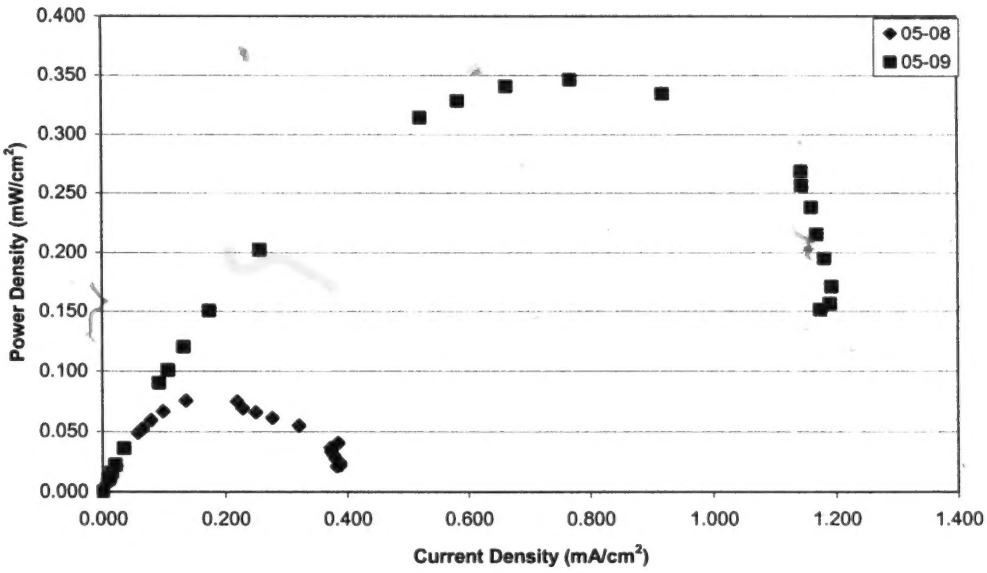

(b) 1 deposition

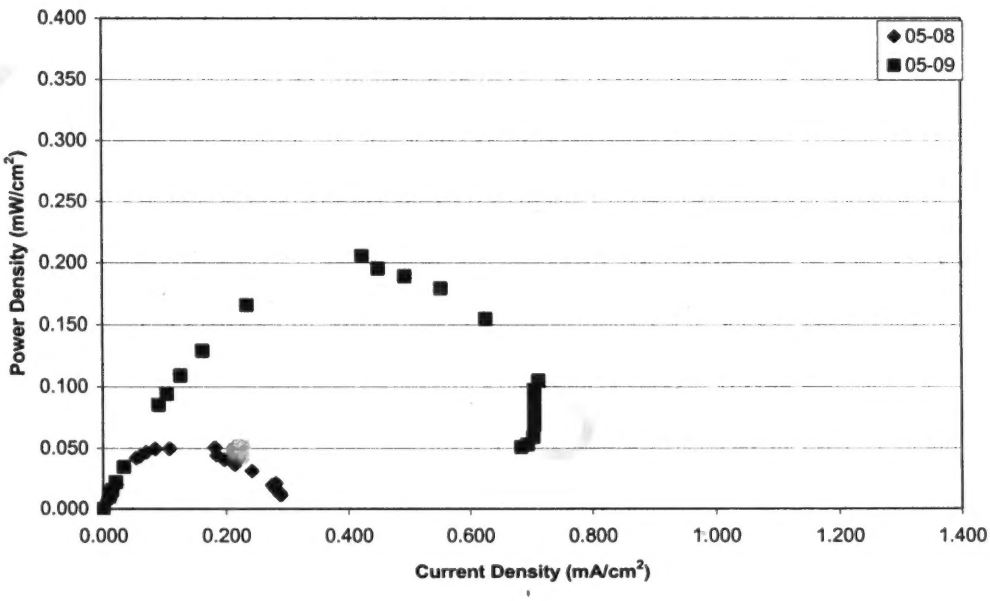

(c) 2 depositions

Figure 6-25 (con't): Corrected power curves for YSZ deposition at 750°C and vapour pressure ratio 5.25:1 by number of depositions

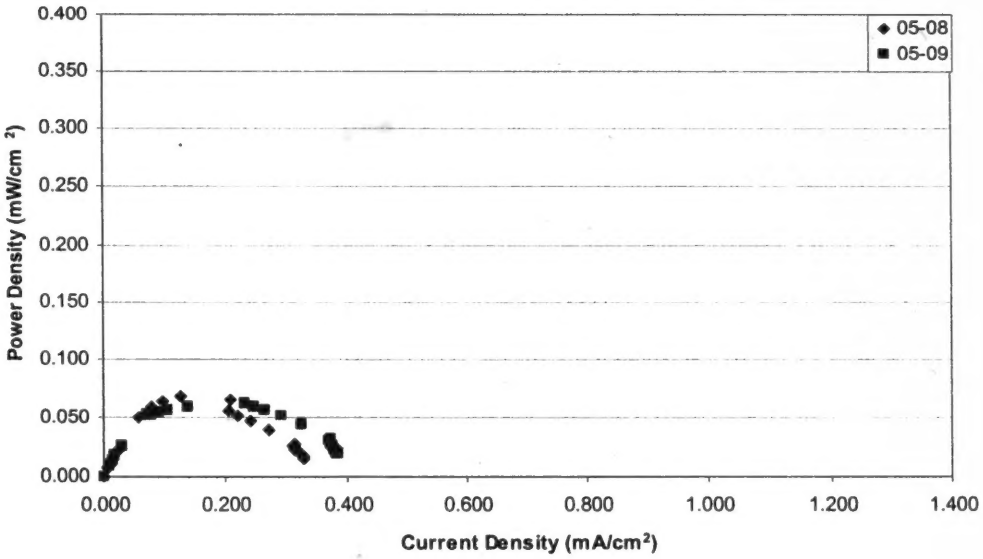

(d) 3 depositions

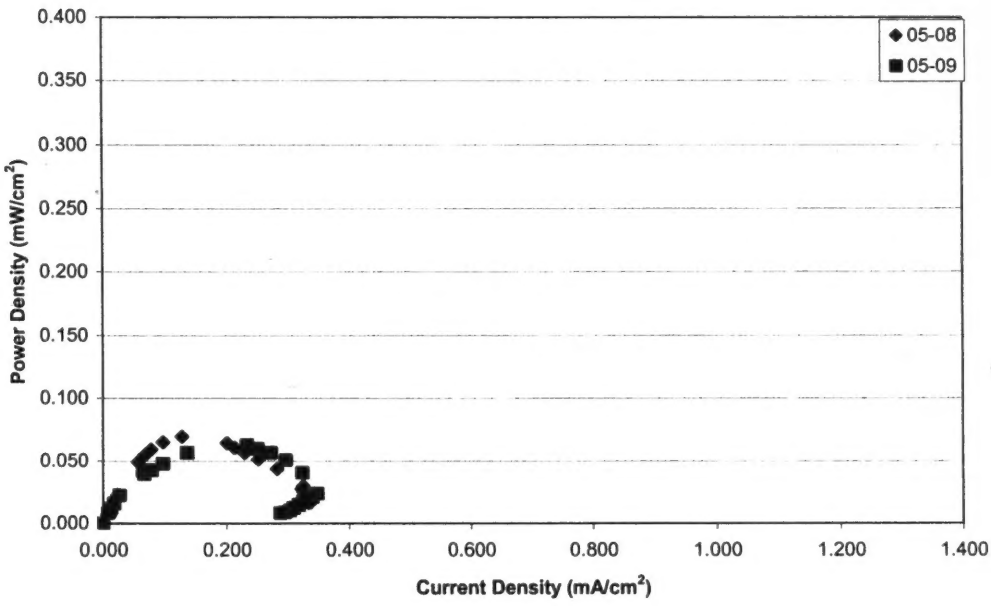

(e) 4 depositions

Figure 6-25 (con't): Corrected power curves for YSZ deposition at 750°C and vapour pressure ratio 5.25:1 by number of depositions

Table 6-9: Maximum power density for 750°C and 5.25:1 samples

Fuel Cell Sample	Maximum Power Density (mW/cm^2)				
	Deposition				
	0	1	2	3	4
05-08	6.35	0.08	0.05	0.07	0.07
05-09	8.84	0.35	0.21	0.06	0.06

(before any depositions had been carried out) were higher for these two samples than those in Table 6-6, but the power densities after depositions were comparable (i.e. same orders of magnitude) for all of the samples. Since the concern is in the performance of the cells after layers have been deposited, the better performance of samples 05-08 and 05-09 initially is not indicative of anything, other than perhaps better anode preparation.

Unfortunately, the anode of sample 05-08 experienced delamination when the cell was removed from the alumina tube, so only sample 05-09 could be observed using the SEM. The secondary electron image of this sample may be seen in Figure 6-26. Its appearance is similar to that for the samples tested at a vapour pressure ratio of 8:1; large grains with very little porosity between them are visible. Once again, the crystal-like layer seen for samples in section 6.1 is not present. The combination of these factors provides a strong explanation for the poor performance of the sample. Not only is hydrogen restricted from reaching the three-phase boundary to be a reactant, but yttrium and zirconium chloride are also prevented from reaching the electrolyte surface.

As predicted from the SEM images of sample 05-09, EDX analysis confirms that only small amounts of yttrium and zirconium are present, though again the results are semi-quantitative due to sample surface roughness. Only overall EDX spectra were collected for the sample at accelerating voltages of 20 kV and 30 kV, which may be seen in Figure 6-27. Once again, the spectrum at 20 kV shows a very strong platinum peak at ~2.0 keV overlapped with the zirconium peak. However, the amount of zirconium detected by elemental analysis is only ~4 wt%, which is significantly less than other samples studied. Platinum is clearly the dominant component, with 95 wt% measured at a voltage of 20 kV and nearly 100 wt% at a voltage of 30 kV. For interest's sake, EDX was also carried out on sample 05-08, which experienced anode delamination. From the results, it is clear that the anode has almost completely delaminated, since elemental analysis showed 67 wt% zirconium and 14 wt% yttrium, reasonably consistent with the electrolyte composition, with only 4 wt% platinum at an accelerating voltage of 30 kV.

Figure 6-26: SEM secondary electron image of sample 05-09 (plan view)

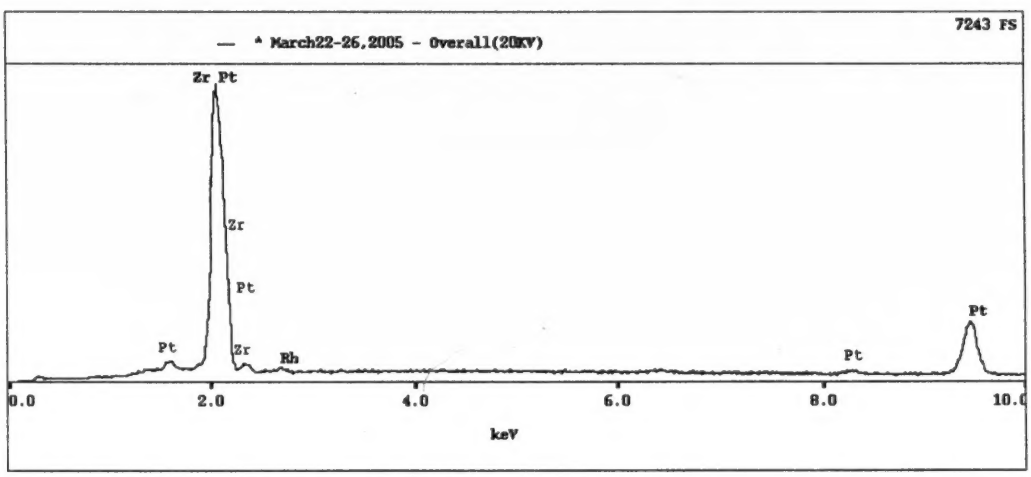

(a) accelerating voltage = 20 kV

Figure 6-27: EDX overall spectra for sample 05-09

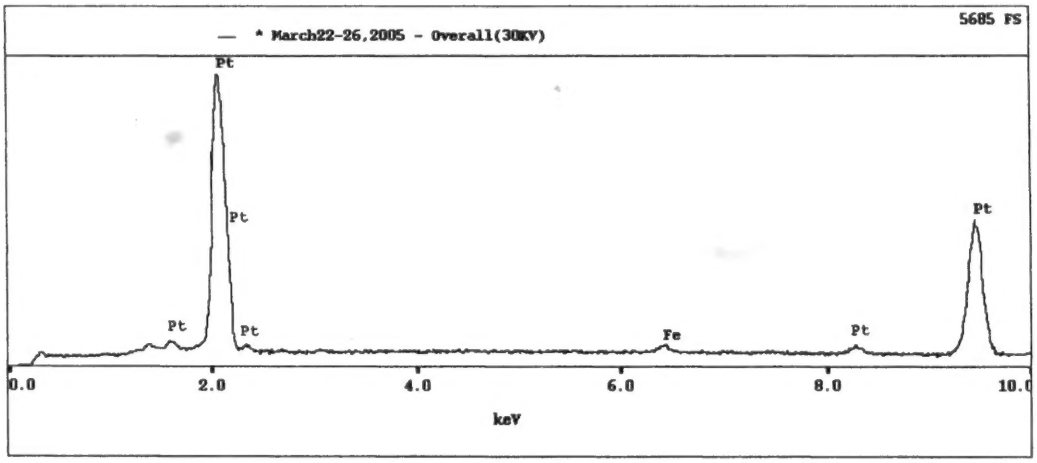

(b) accelerating voltage = 30 kV

Figure 6-27 (con't): EDX overall spectra for sample 05-09

Again, the performance of the cells under temperature cycling conditions was investigated, with quite similar results, as may be seen in Figure 6-28. The performance at an operating temperature of 900°C was again the best and the three tests at 750°C also showed very similar performance. In comparing the two samples, both showed maximum current and power densities that were very close to each other, within an order of magnitude.

6.2.3 800°C Experiments

6.2.3.1 Equilibrium Vapour Pressure Ratio 8:1

Consistent with the decrease in performance after deposition of cells tested at 750°C, the cells tested at 800°C also experienced poorer performance. Figure 6-29 shows the corrected polarization curves for the four samples tested using an equilibrium vapour pressure ratio of 8:1. The specifics of each sample may be seen in Table 6-10. It should be noted that the scale for

Table 6-10: Fuel cell samples for YSZ deposition at 800°C and vapour pressure ratio 8:1

Fuel Cell Sample	Deposition Bias Voltage (mV)
04-07	-800
05-01	-800
05-04	-500
05-05	-500

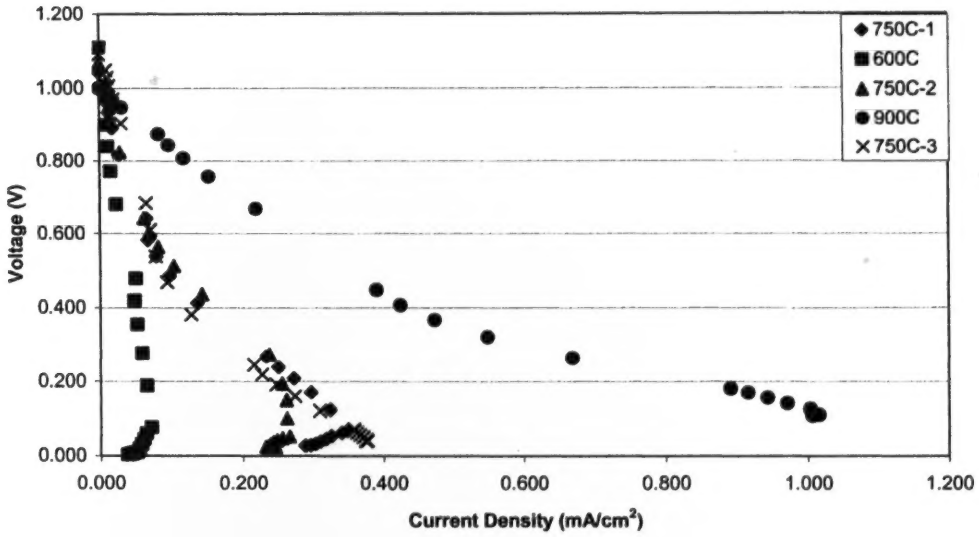

(a) corrected polarization curve

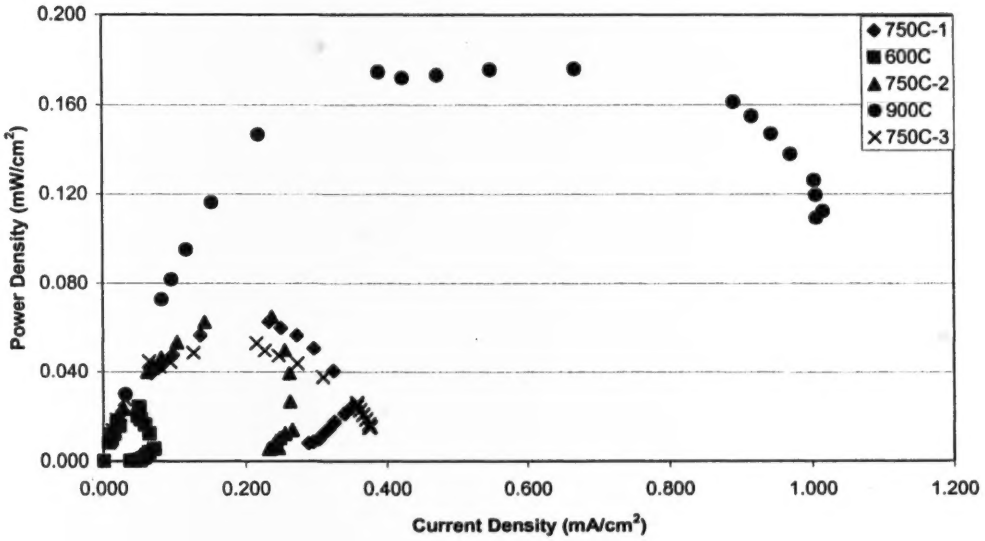

(b) corrected power curve

Figure 6-28: Corrected polarization and power curves for operating temperature cycling testing for sample 05-09

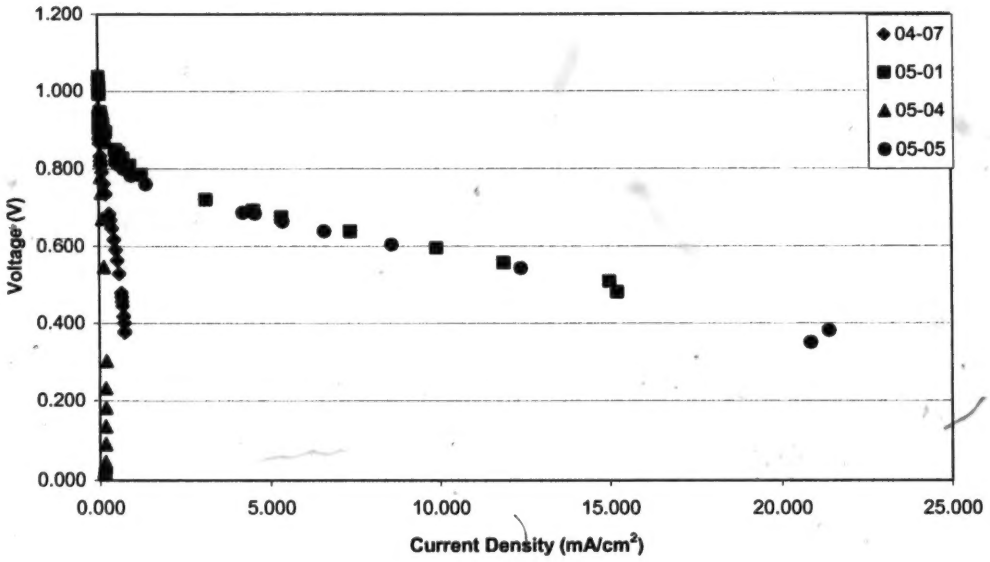

(a) no deposition

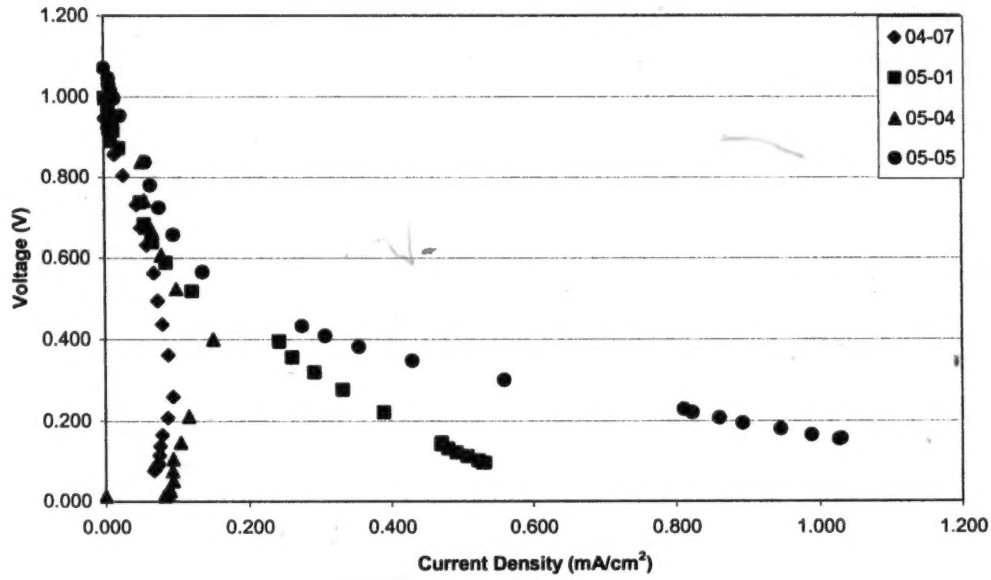

(b) 1 deposition

Figure 6-29: Corrected polarization curves for YSZ deposition at 800°C and vapour pressure ratio 8:1 by number of depositions

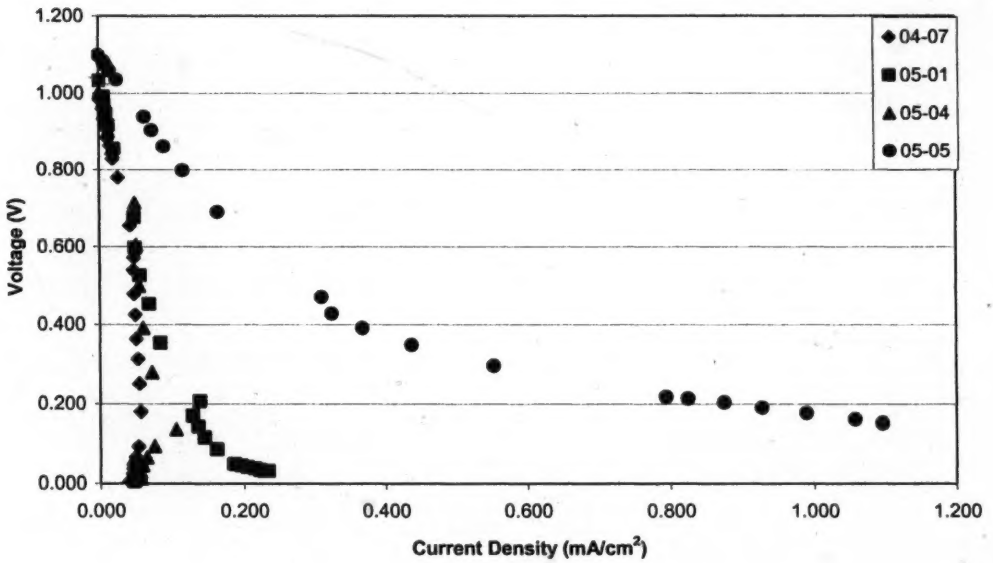

(c) 2 depositions

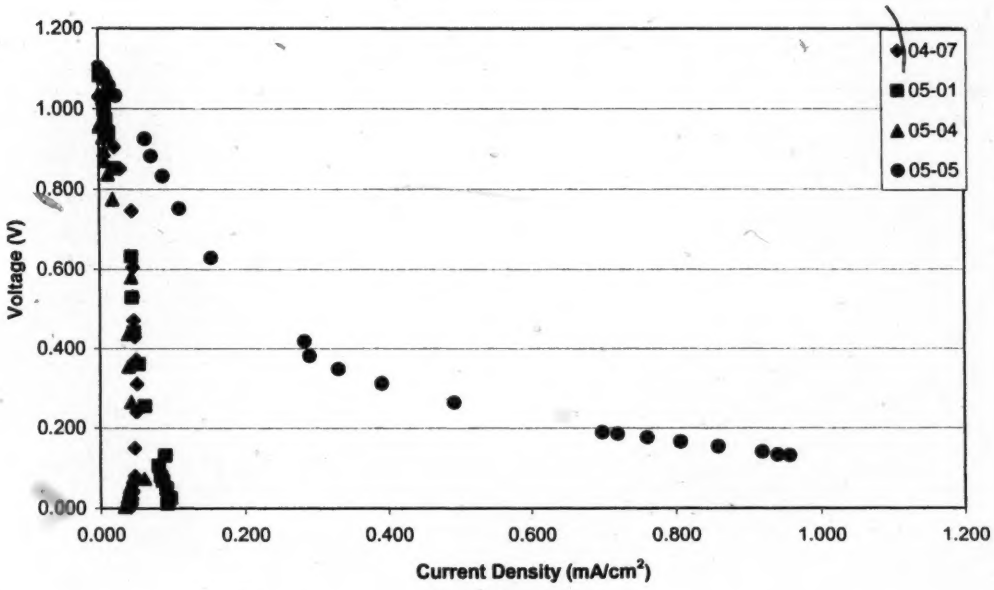

(d) 3 depositions

Figure 6-29 (con't): Corrected polarization curves for YSZ deposition at 800°C and vapour pressure ratio 8:1 by number of depositions

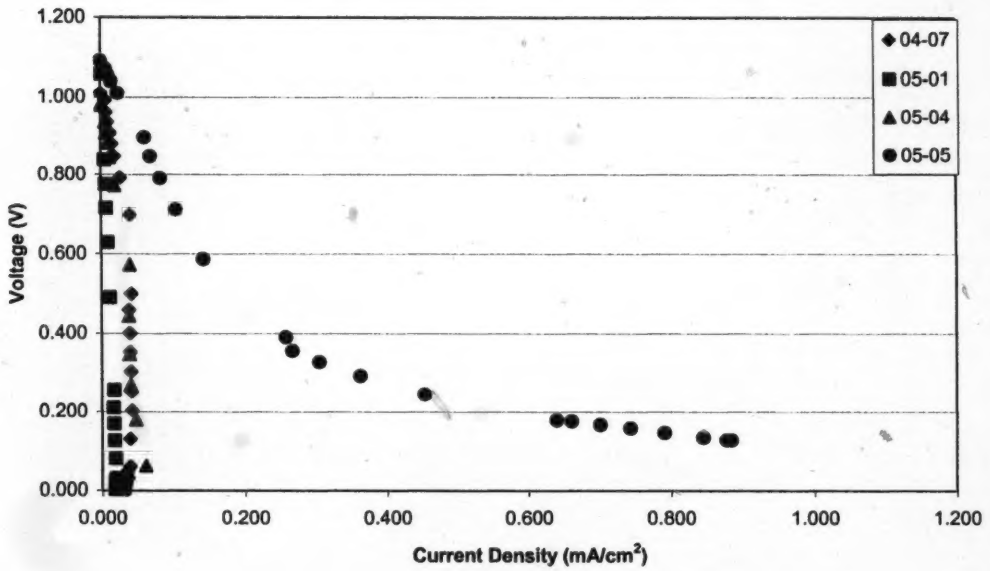

(e) 4 depositions

Figure 6-29 (con't): Corrected polarization curves for YSZ deposition at 800°C and vapour pressure ratio 8:1 by number of depositions

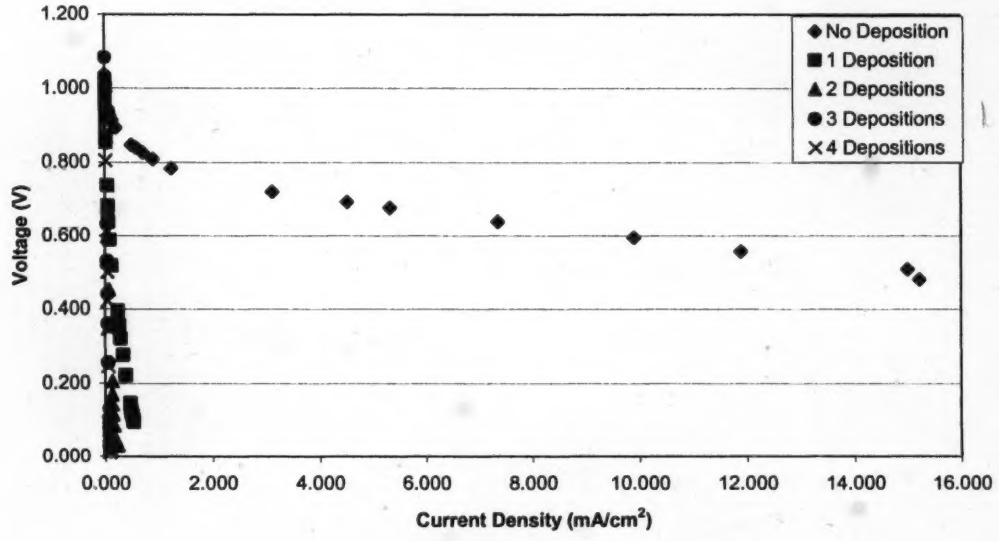

(a) sample 05-01

Figure 6-30: Corrected polarization curves for YSZ deposition at 800°C and vapour pressure ratio 8:1 by sample

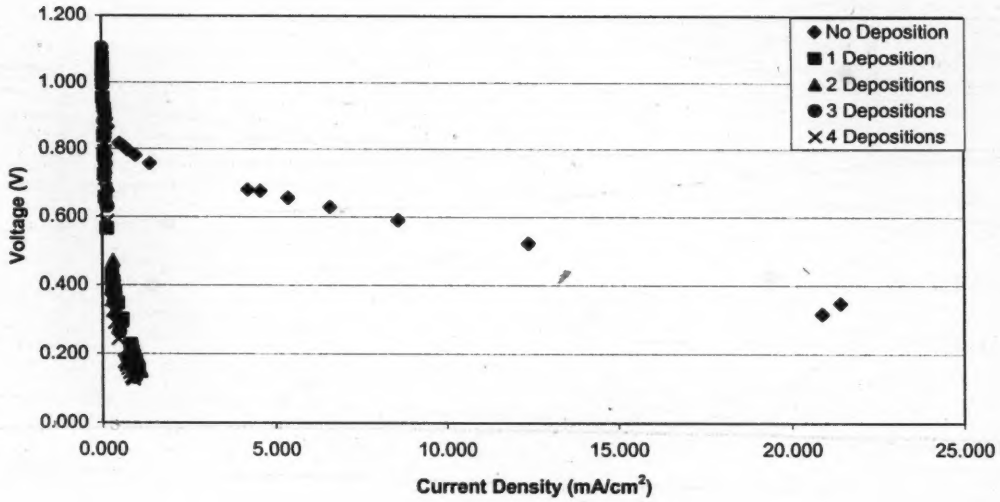

(b) sample 05-05

Figure 6-30 (con't): Corrected polarization curves for YSZ deposition at 800°C and vapour pressure ratio 8:1 by sample

current density changes after Figure 6-29(a). This is to make the shape of the polarization curve clearer. Figure 6-29(a) shows the variability of cell performance when no deposited layer had yet been applied, since samples 05-01 and 05-05 show much better performance than samples 04-07 and 05-04. Throughout the four depositions, sample 05-05 consistently outperforms the other three samples, but still undergoes a dramatic decrease in performance when compared to its initial behaviour, as seen in Figures 6-29(b) to (e). As the number of depositions increases, the shape of the polarization curves for all of the samples, except 05-05, becomes increasingly linear with a greater and greater slope. Sample 05-05 maintains a curve with two distinct slopes, which would seem to indicate that more than just ohmic loss is contributing to the voltage loss. To demonstrate the significance of the performance decrease, Figure 6-30 shows the polarization curves for two samples before any deposition and after each deposition.

The observations from the polarization curves of these samples repeat themselves in the corrected power curves seen in Figure 6-31, with specific plots for two samples seen in Figure 6-32. The power is greatly diminished after the four depositions, which may be noted by the decreased power density and current density scales in Figure 6-31(b) to (e). A detailed comparison of the maximum power densities achieved by the four samples after deposition is shown in Table 6-11 and again the maximum power density occurred before any deposition was carried out.

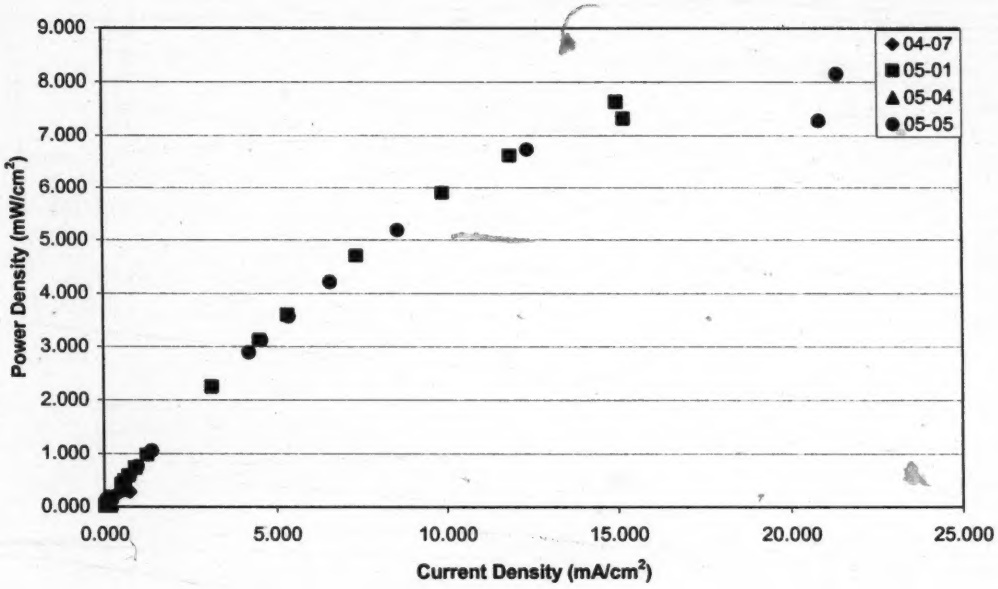

(a) no deposition

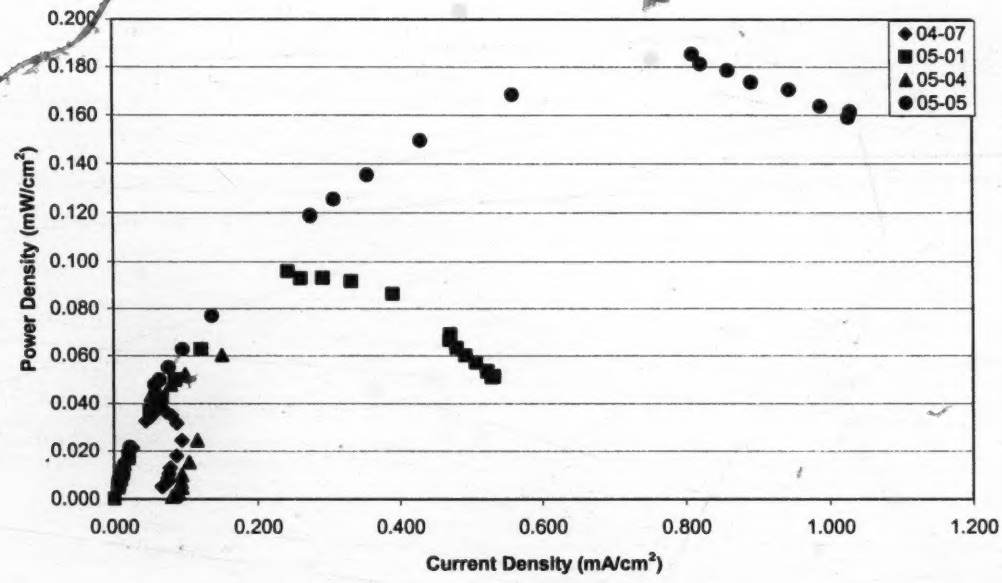

(b) 1 Deposition

Figure 6-31: Corrected power curves for YSZ deposition at 800°C and vapour pressure ratio 8:1 by number of depositions

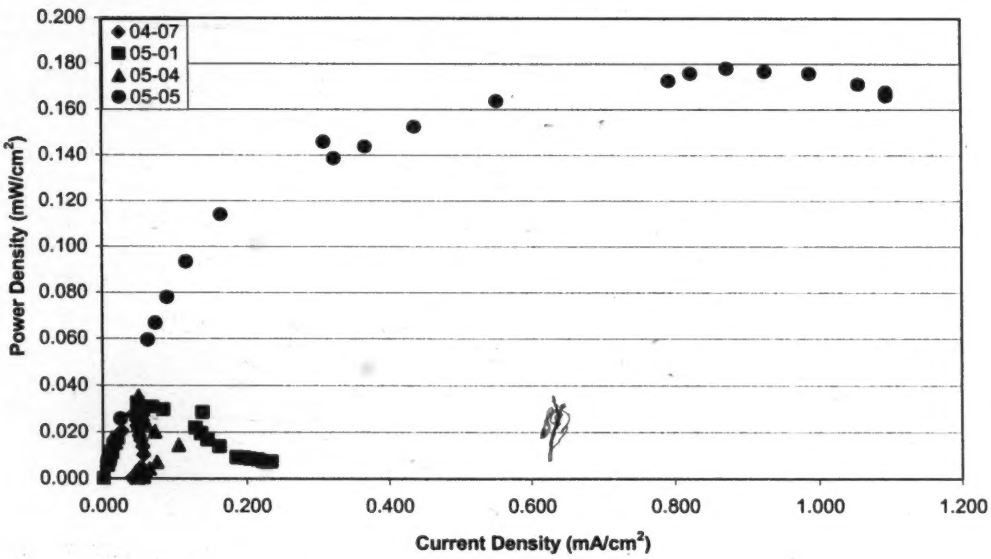

(c) 2 Depositions

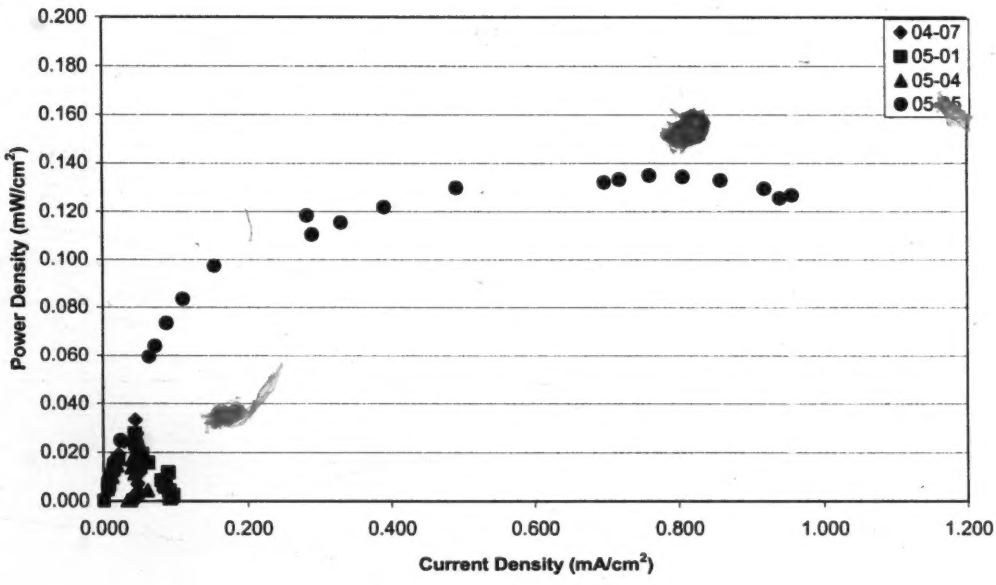

(d) 3 Depositions

Figure 6-31 (con't): Corrected power curves for YSZ deposition at 800°C and vapour pressure ratio 8:1 by number of depositions

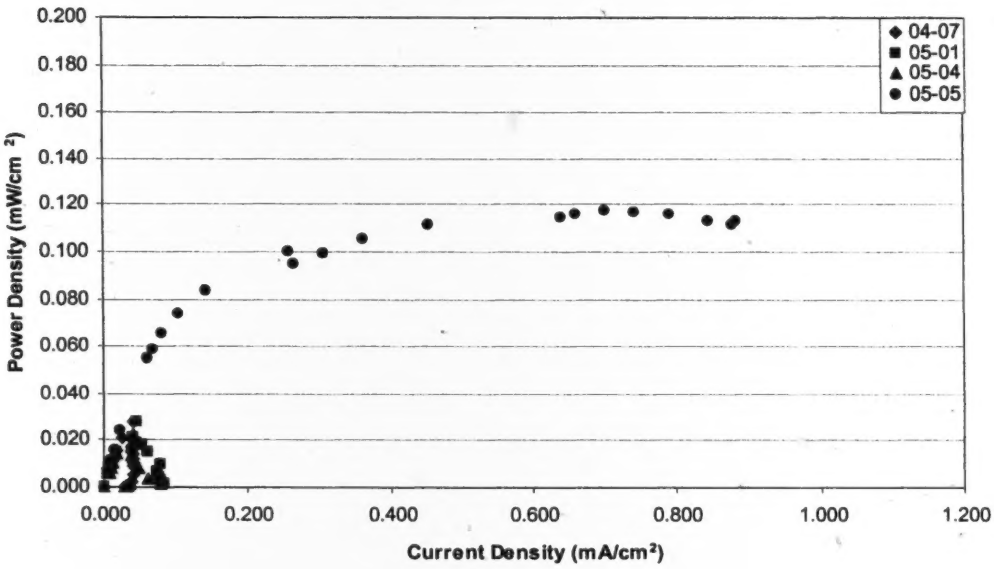

(c) 4 Depositions

Figure 6-31 (con't): Corrected power curves for YSZ deposition at 800°C and vapour pressure ratio 8:1 by number of depositions

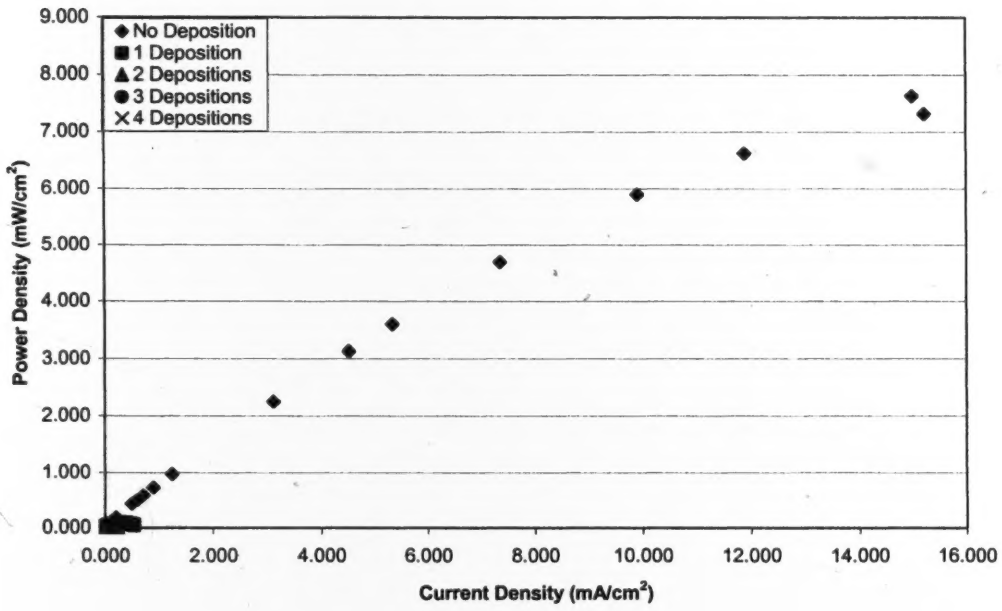

(a) Sample 05-01

Figure 6-32: Corrected power curves for YSZ deposition at 800°C and vapour pressure ratio 8:1 by sample

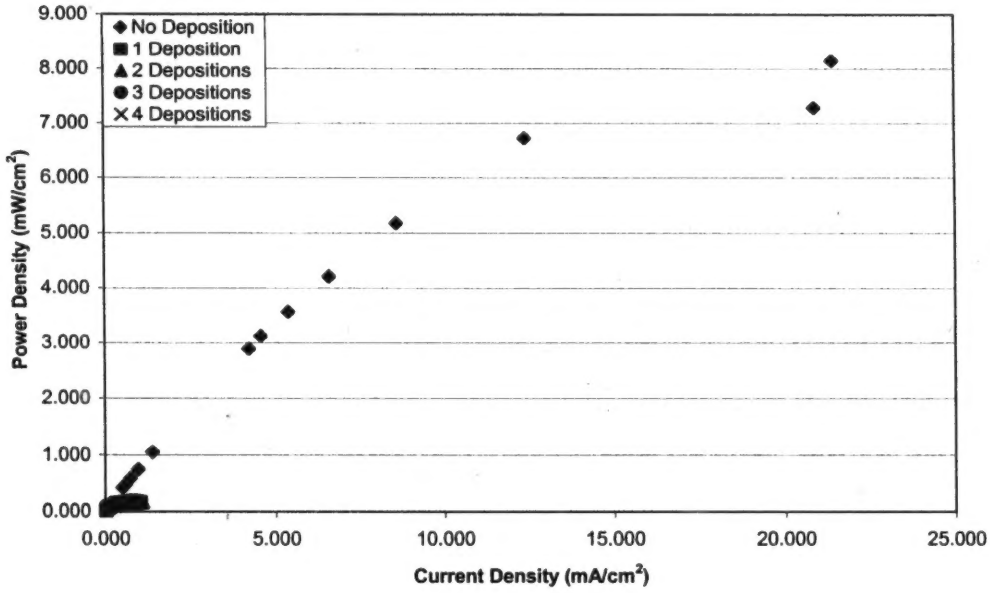

(b) Sample 05-05

Figure 6-32 (con't): Corrected power curves for YSZ deposition at 800°C and vapour pressure ratio 8:1 by sample

Table 6-11: Maximum power density for 800°C and 8:1 samples

Fuel Cell Sample	Maximum Power Density (mW/cm^2)				
	Deposition				
	0	1	2	3	4
04-07	0.31	0.04	0.03	0.03	0.03
05-01	7.63	0.10	0.03	0.03	0.03
05-04	0.07	0.06	0.04	0.03	0.02
05-05	8.14	0.19	0.18	0.13	0.12

The anode microstructure of two of the four samples tested was observed using the SEM, and the secondary electron images may be seen in Figures 6-33 and 6-34. As was anticipated from the poor performance and the similarities of these cells with the cells tested at 750°C, the anode microstructure of both cells shows large grains with very little porosity evident in the plan view. From the cross sectional view of sample 04-07 in Figure 6-33(b), it is clear that porosity still remains within the anode while the surface looks much less porous. In comparing the cells, sample 05-05 (Figure 6-34) appears to have larger and smoother grains than sample 04-07. The larger grains could lead one to infer that less porosity is present, thus meaning poorer cell performance, but sample 05-05 had much better performance than sample 04-07. While no thin, semi-transparent layer is evident on either sample, a small amount of the crystal-like layer seen

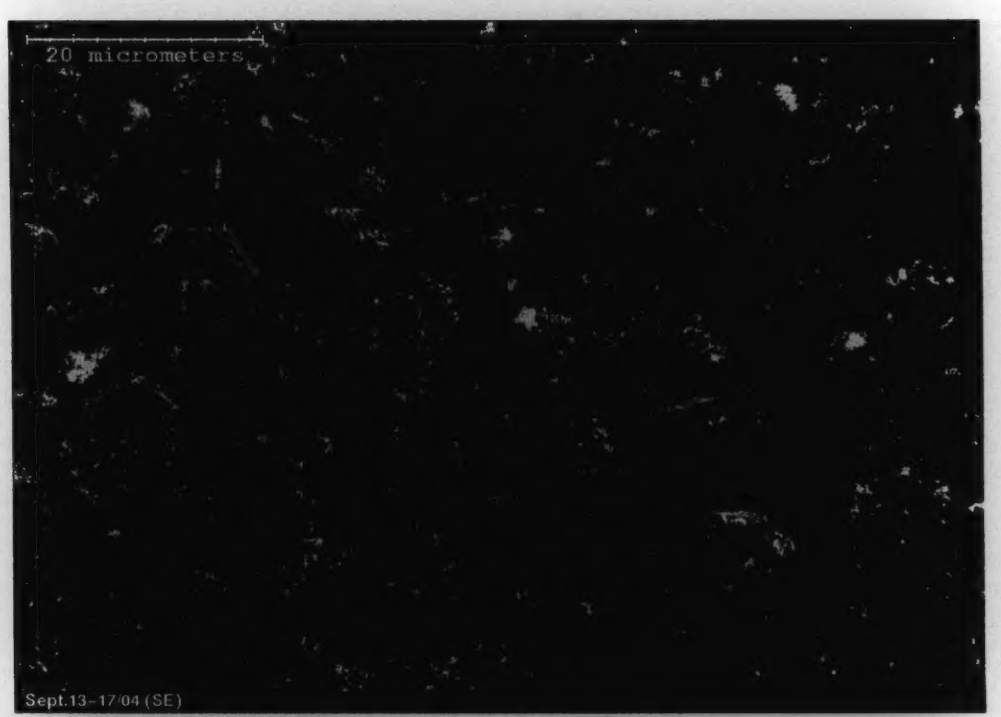

(a) plan view

(b) cross section view

Figure 6-33: SEM secondary electron image of sample 04-07

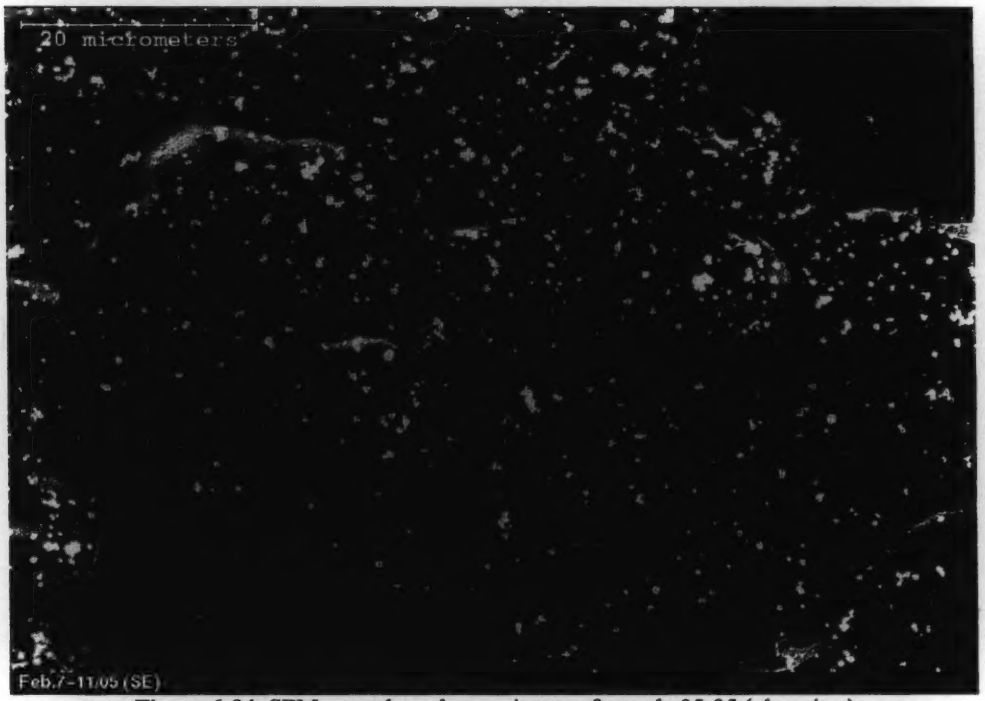

Figure 6-34: SEM secondary electron image of sample 05-05 (plan view)

on the samples in section 6.1 is present on sample 04-07. However, sample 05-05 shows only very small bright speckles on the anode surface.

From the apparent presence of the crystal-like layer on sample 04-07, it was expected that the sample would show less platinum than sample 05-05 when an overall EDX analysis was completed. However, this was not the case, as may be seen by the data presented in Table 6-12. (Once again, the data must be considered semi-quantitative.) Sample 05-05 actually showed less platinum in the overall elemental analysis at an accelerating voltage of 20 kV. The amount of zirconium detected in this sample was also greater than had been anticipated by the previous results seen at 750°C. When a higher accelerating voltage of 30 kV was used, a small amount of yttrium was detected in the sample, whereas sample 04-07 showed nearly 100 wt% platinum. The overall EDX spectra at 20 kV and 30 kV for sample 05-05 are shown in Figure 6-35. The only major difference between these spectra and those for sample 04-07 was the visibility of high-energy yttrium and zirconium peaks in Figure 6-35(b). No point analyses were carried out on either sample.

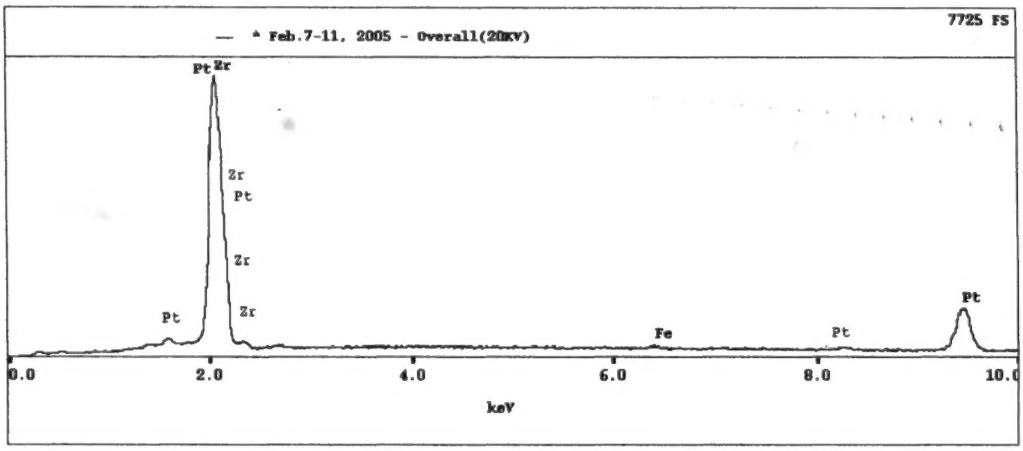

(a) accelerating voltage = 20 kV

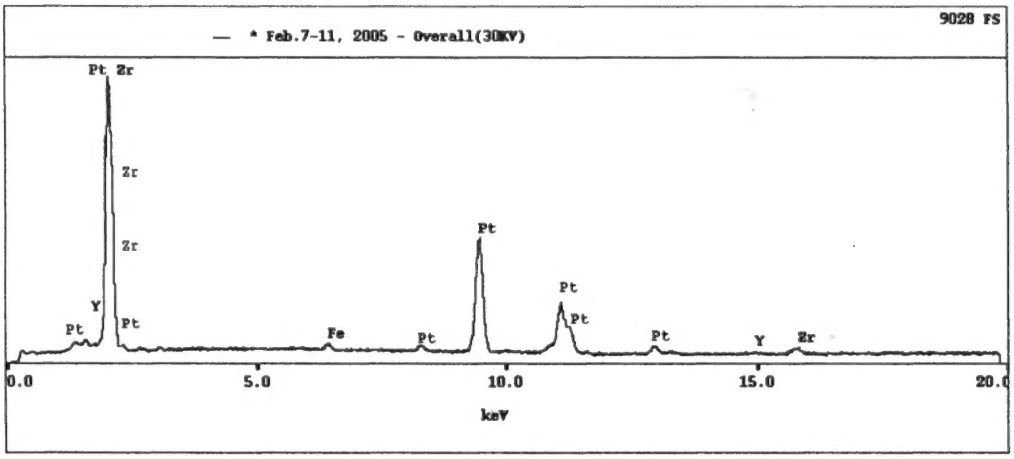

(b) accelerating voltage = 30 kV

Figure 6-35: EDX overall spectra for sample 05-05

Table 6-12: Elemental analysis from overall EDX analysis for 800°C and vapour pressure ratio 8:1 samples viewed in the SEM

Fuel Cell Sample	Amount of Element (wt%)					
	Accelerating Voltage = 20 kV			Accelerating Voltage = 30 kV		
	Pt	Zr	Y	Pt	Zr	Y
04-07	94.05	5.95	-	99.00	0.28	-
05-05	86.56	12.95	-	91.97	7.13	0.16

The effect of changing operating temperature was again studied. After the fourth deposition had been carried out and current-voltage data collected, the operating temperature was decreased to 650°C, increased back to 800°C, further increased to 950°C and finally decreased back to 750°C. For the most part, the same trend in cell performance as the operating temperature was varied that was seen for sample tested at 750°C was seen here. The best performance occurred at the highest temperature, 950°C, and the poorest performance occurred at the lowest temperature, 650°C, which was expected. As an example, the corrected polarization and power curves for sample 05-05 may be seen in Figure 6-36. However, contrary to the data for the 750°C experiments, the samples in this set did not experience as much reproducibility in the data acquired from the three tests at 800°C. Some samples (04-07 and 05-04) had similar data for the first two tests but then showed much better performance on the third test, while other samples (05-01 and 05-05) showed poorer performance on the third test. It is not known why these results occurred.

6.2.3.2 Equilibrium Vapour Pressure Ratio 5.25:1

The behaviour of decreasing cell performance after deposition seen for the samples under an equilibrium vapour pressure ratio of 8:1 was repeated for the samples under a ratio of 5.25:1. The corrected polarization curves for the samples, detailed in Table 6-13, may be seen in Figure 6-37. As before, the current density scale has been reduced in Figure 6-37(b) to (e) to improve clarity of the polarization curve shape, due to the significant drop in current density. Samples 05-06 and 05-07 show a fairly linear polarization curve shape, though sample 05-06 shows behaviour seen earlier with decreasing current densities at low voltages, causing the curve to bend back. This behaviour seems more pronounced after more depositions have been carried out, but it is uncertain why it shows up for some samples but not for others.

Figure 6-38 illustrates the corrected polarization power curves for the two samples and Table 6-14 details the maximum power density after each deposition for each sample. Both sources of information clearly show the dramatic decrease in maximum power density after each deposition, with power densities dropping more than an order of magnitude. When compared to the

Table 6-13: Fuel cell samples for YSZ deposition at 800°C and vapour pressure ratio 5.25:1

Fuel Cell Sample	Deposition Bias Voltage (mV)
05-06	-500
05-07	-800

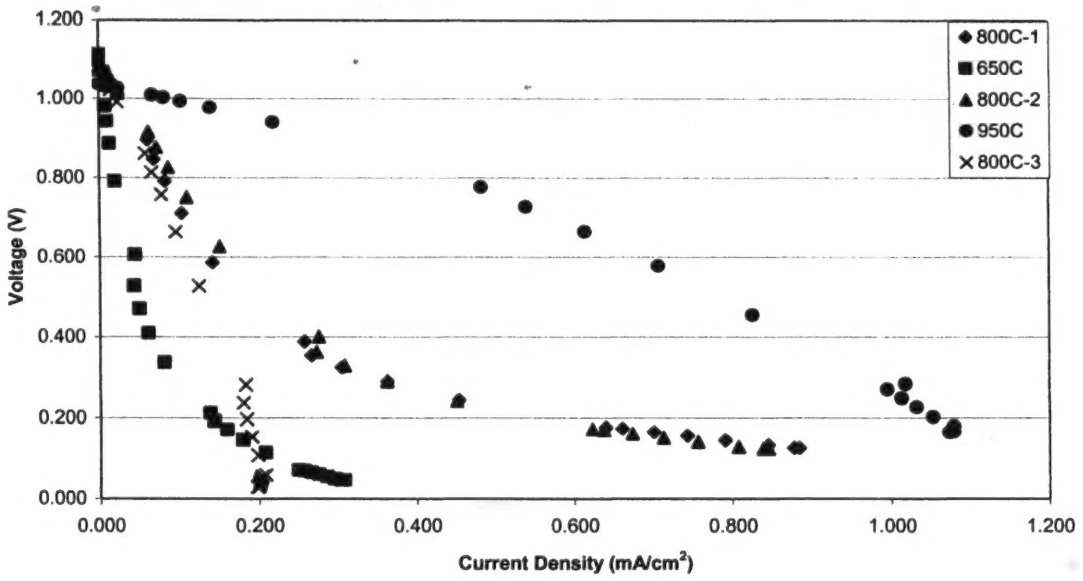

(a) corrected polarization curve

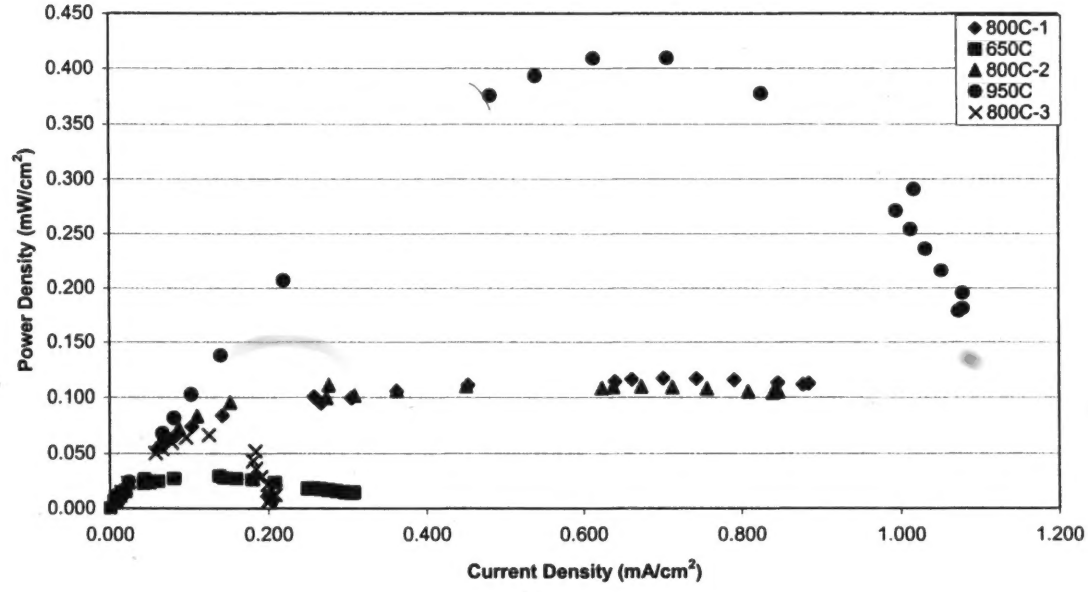

(b) corrected power curve

Figure 6-36: Corrected polarization and power curves for operating temperature cycling testing for sample 05-05

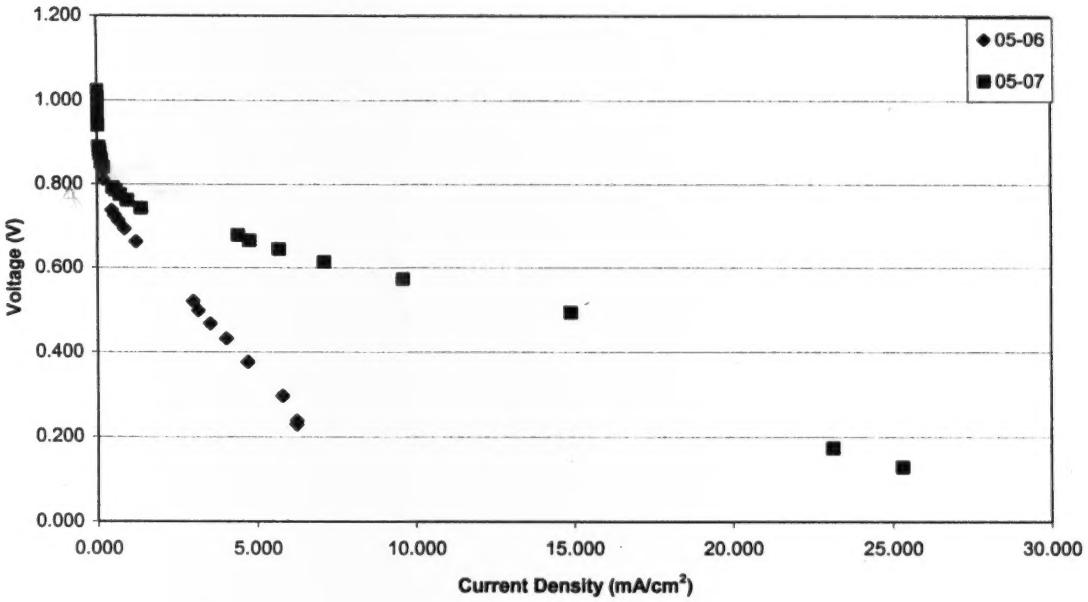

(a) no deposition

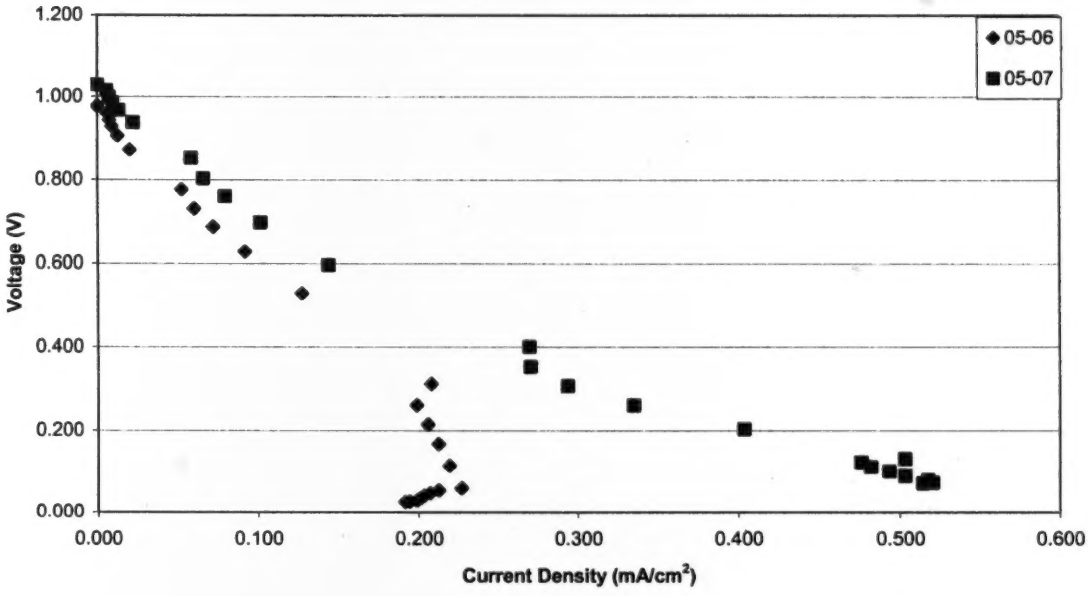

(b) 1 deposition

Figure 6-37: Corrected polarization curves for YSZ deposition at 800°C and vapour deposition ratio 5.25:1 by number of depositions

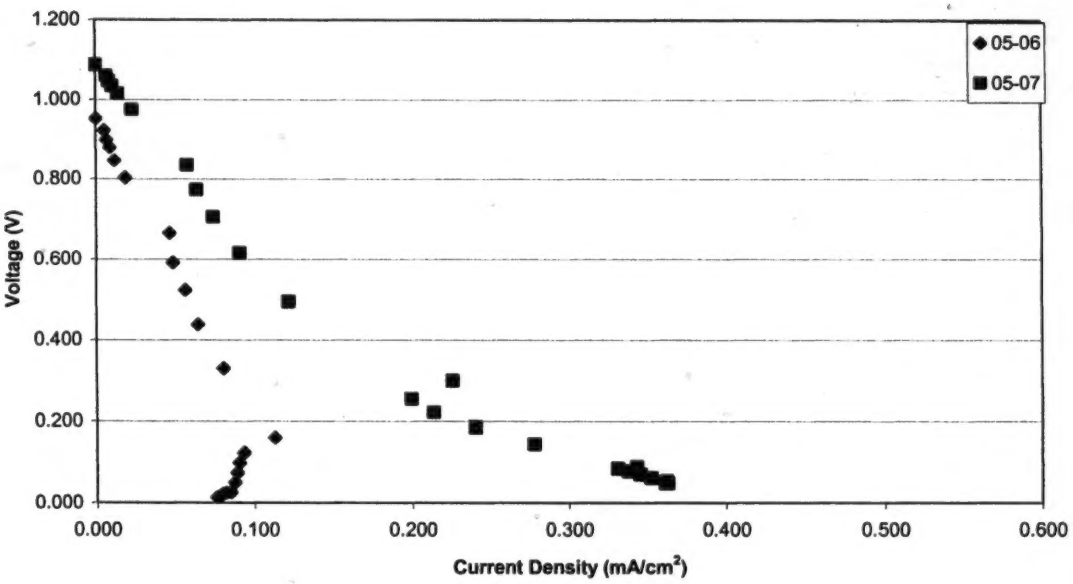

(c) 2 depositions

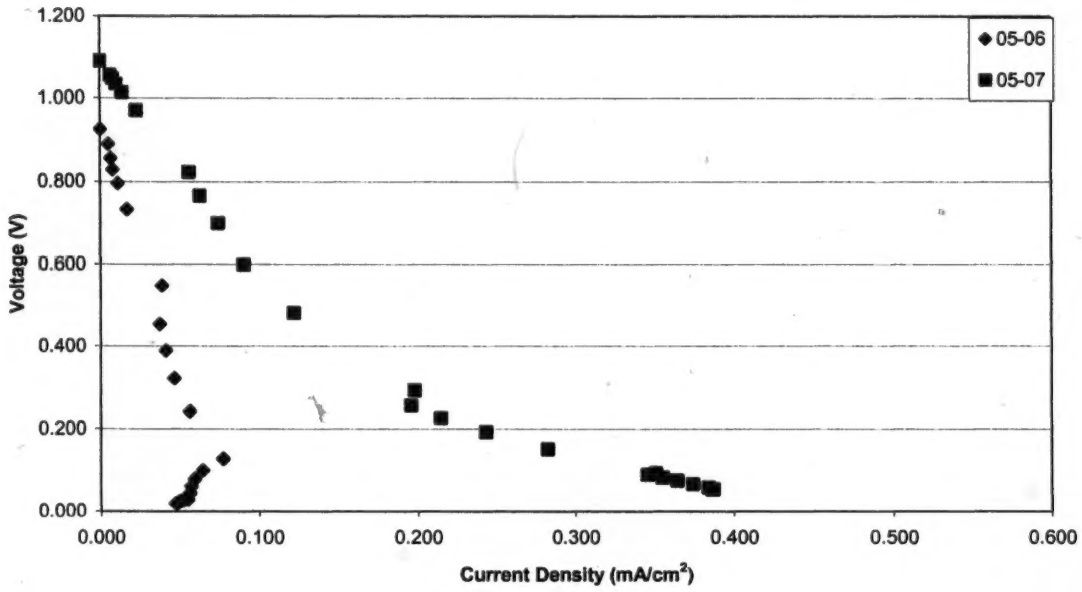

(d) 3 depositions

Figure 6-37 (con't): Corrected polarization curves for YSZ deposition at 800°C and vapour deposition ratio 5.25:1 by number of depositions

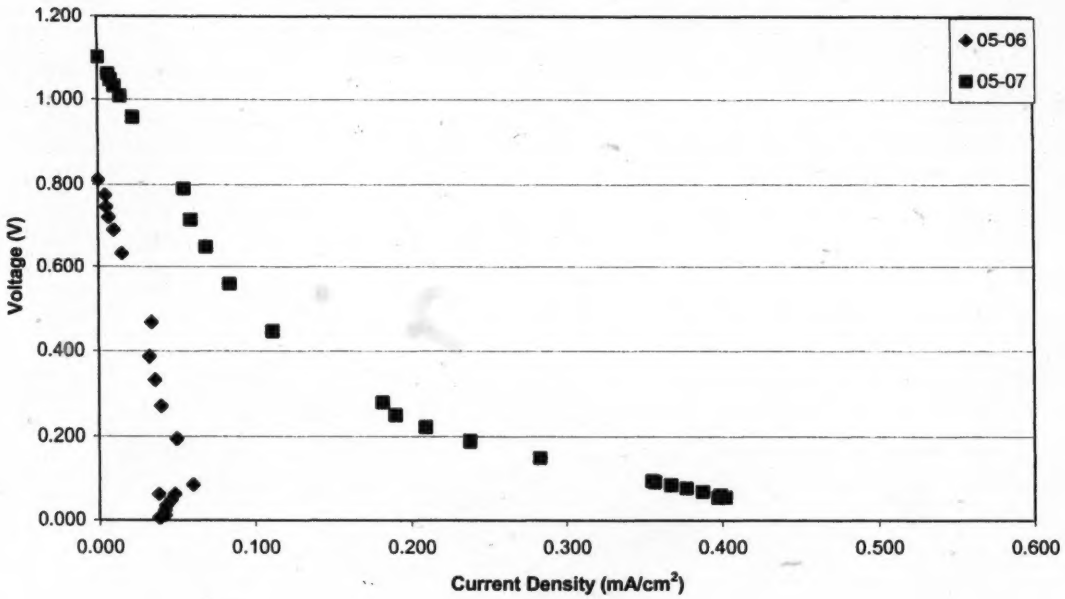

(e) 4 depositions

Figure 6-37 (con't): Corrected polarization curves for YSZ deposition at 800°C and vapour deposition ratio 5.25:1 by number of depositions

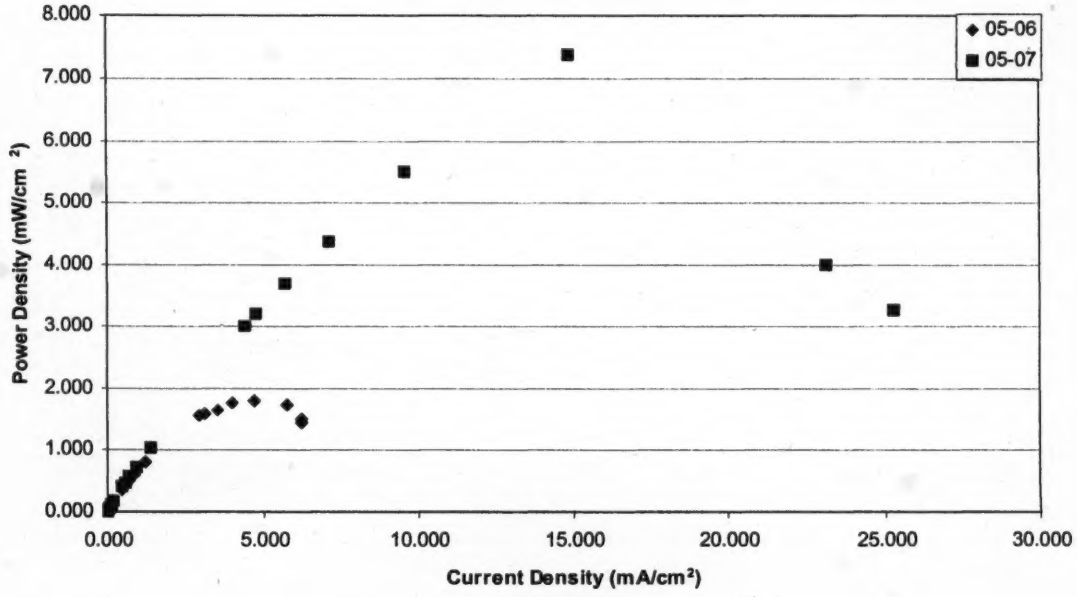

(a) no deposition

Figure 6-38: Corrected power curves for YSZ deposition at 800°C and vapour deposition ratio 5.25:1 by number of depositions

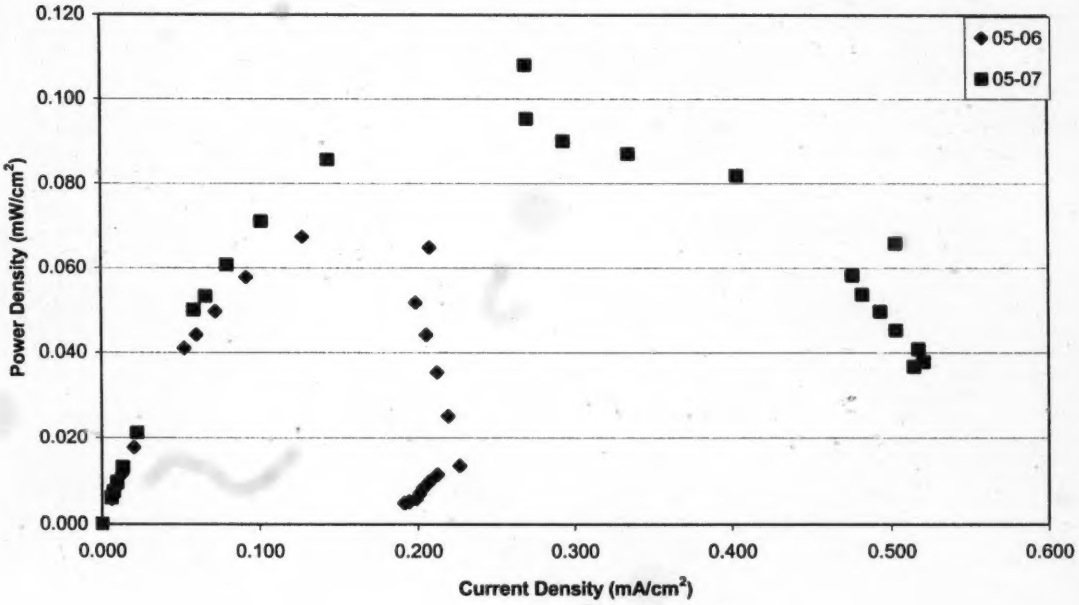

(b) 1 deposition

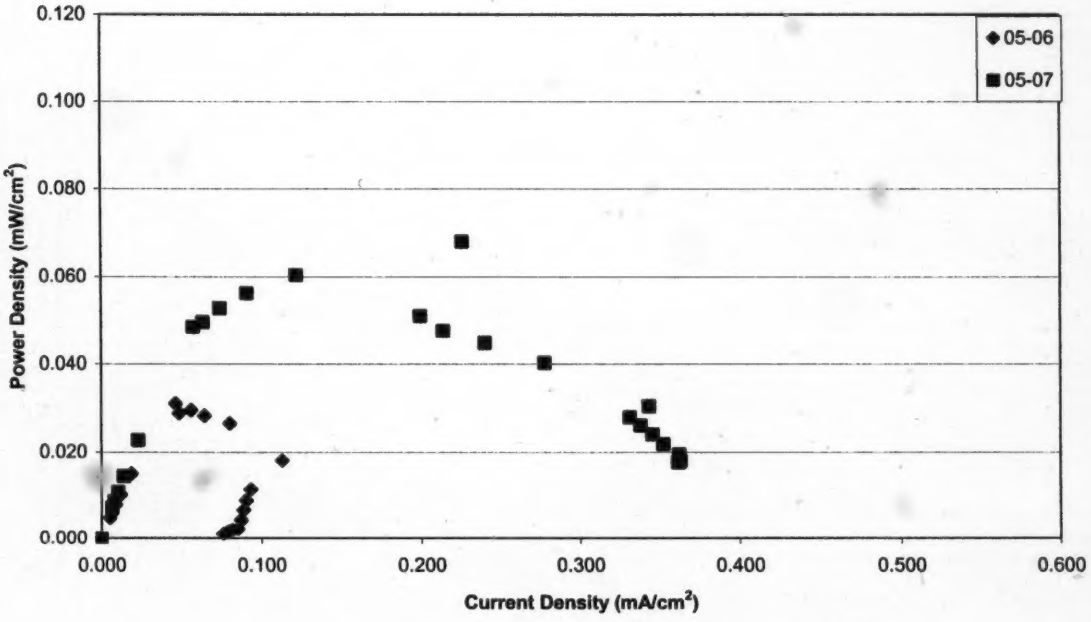

(c) 2 depositions

Figure 6-38 (con't): Corrected power curves for YSZ deposition at 800°C and vapour deposition ratio 5.25:1 by number of depositions

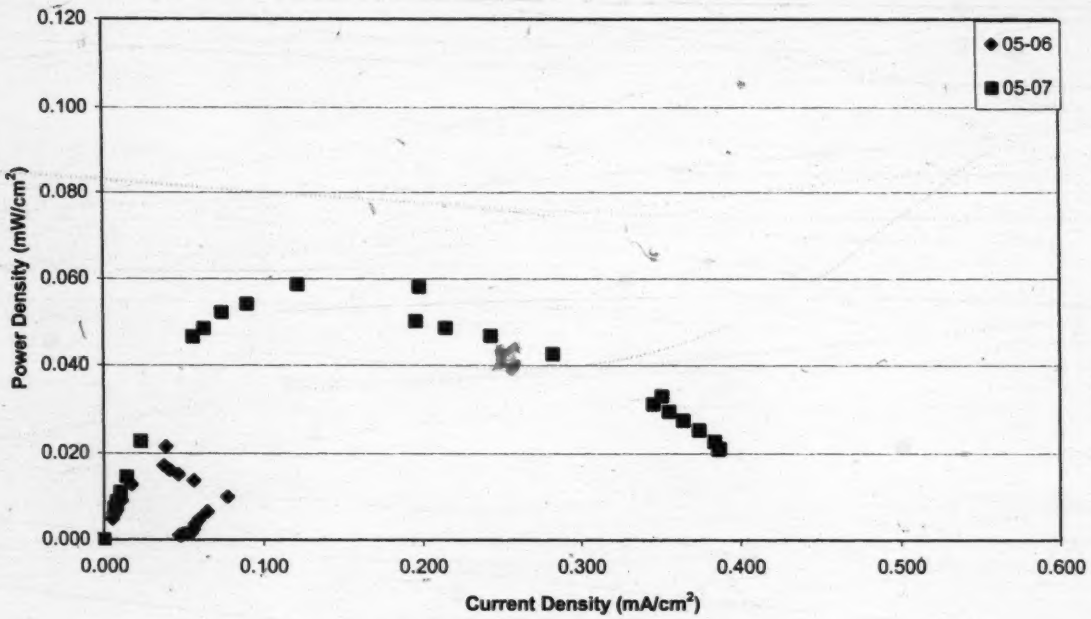

(d) 3 depositions

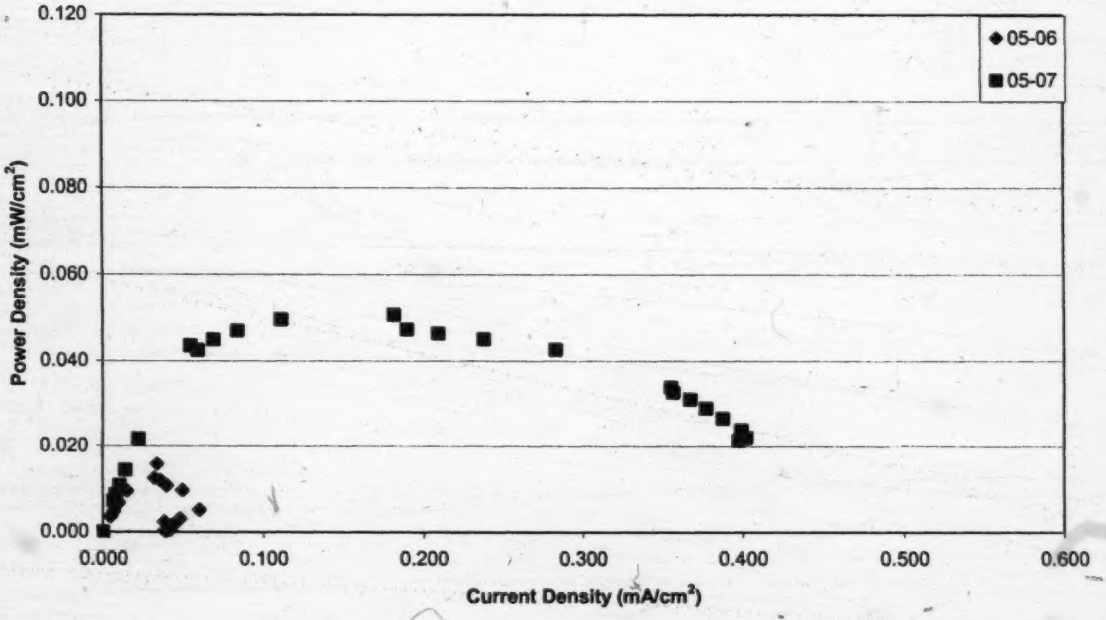

(e) 4 depositions

Figure 6-38 (con't): Corrected power curves for YSZ deposition at 800°C and vapour deposition ratio 5.25:1 by number of depositions

Table 6-14: Maximum power density for 800°C and 5.25:1 samples

Fuel Cell Sample	Maximum Power Density (mW/cm^2)				
	Deposition				
	0	1	2	3	4
05-06	1.77	0.07	0.03	0.02	0.02
05-07	7.36	0.11	0.07	0.06	0.02

maximum power densities for the samples tested under a ratio of 8:1 (see Table 6-11), it was found that the values were comparable before and after the depositions. As for the 750°C samples, since the power densities decrease after the depositions and are of the same order of magnitude, no real conclusion can be drawn to say which equilibrium vapour pressure ratio gives a better result.

In comparing the performance of the two samples to each other, it is clear that sample 05-07 outperforms sample 05-06. Secondary electron SEM images for each sample may be seen in Figures 6-39 and 6-40. Sample 05-07 clearly shows much more porosity than sample 05-06 in the anode microstructure, which would explain its better performance. With increased porosity, more hydrogen would be able to reach more active sites, promoting a greater reaction rate and better cell performance. However, the entire anode of sample 05-07 does not maintain the same amount of porosity as that seen in Figure 6-40. Also, from the image, it appears that this porous portion of the anode has begun to separate from the electrolyte. Common to both samples is the clear evidence of grain growth and the absence of any of the crystalline-like layer seen on previous samples.

EDX analysis was again performed on these samples to determine if any yttrium and/or zirconium were present to indicate the formation of a YSZ layer. Again, these results must be taken as semi-quantitative due to the surface roughness of the samples. The spectrum from the overall scans at accelerating voltages of 20 kV and 30 kV for sample 05-07 may be seen in Figure 6-41 and the elemental analysis for both samples in Table 6-15. The overall spectrums of sample 05-07 were included due to the presence of yttrium peaks, while the spectrums for sample 05-06 contained the typically seen platinum and zirconium low-energy peaks. From the data presented in Table 6-15, more zirconium and yttrium are present in sample 05-07 than sample 05-06, which, combined with greater porosity, could account for the better performance of the sample. However, without a deposited layer being visible, it is difficult to say this for certain.

Figure 6-39: SEM secondary electron image of sample 05-06

Figure 6-40: SEM secondary electron image of sample 05-07

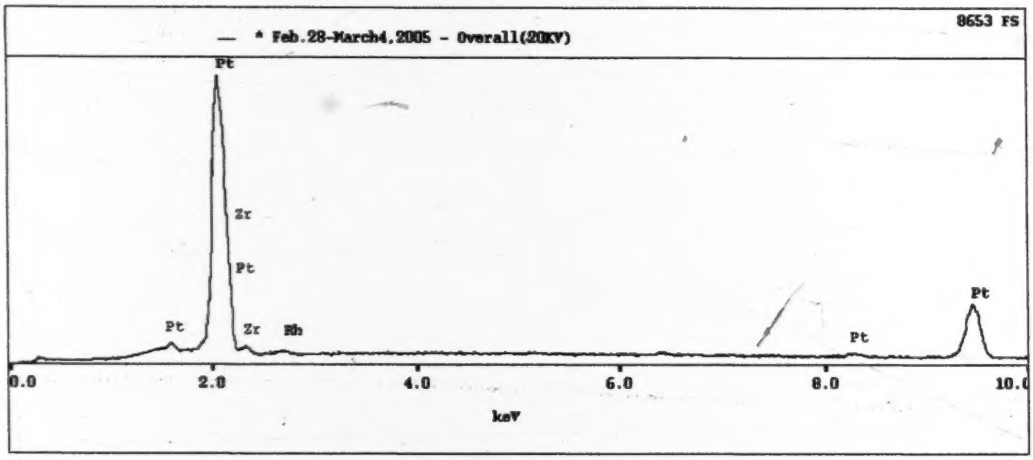

(a) accelerating voltage = 20 kV

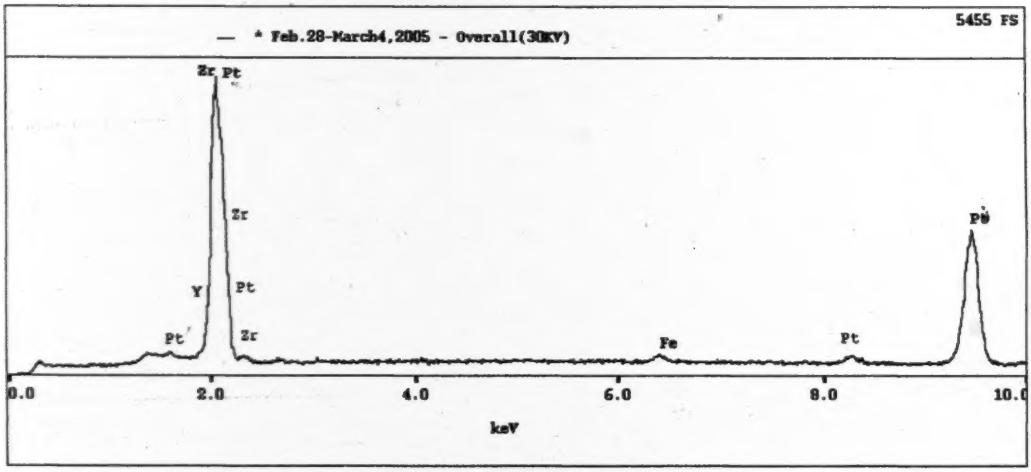

(b) accelerating voltage = 30 kV

Figure 6-41: EDX overall spectra for sample 05-07

Table 6-15: Elemental analysis from overall EDX analysis for 800°C and vapour pressure ratio 5.25:1 samples viewed in the SEM

Fuel Cell Sample	Amount of Element (wt%)					
	Accelerating Voltage = 20 kV			Accelerating Voltage = 30 kV		
	Pt	Zr	Y	Pt	Zr	Y
05-06	97.65	2.03	-	99.29	-	-
05-07	94.27	5.36	-	92.16	5.93	1.25

Similar results to those observed for the samples tested at a ratio of 8:1 were experienced for these samples when the operating temperature was varied after the fourth deposition. Figures 6-42 and 6-43 show the corrected polarization and power curves for the two samples. Once again, both cells experienced their best performance at an operating temperature of 950°C. However, the poorest performance for sample 05-06 was seen at 650°C, while for sample 05-07 it was seen on the third test at 800°C. Sample 05-06 also showed variability at 800°C with its third test at the temperature giving performance very close to that of 950°C. This variability in performance after the third test at 800°C was also evident for samples tested at a ratio of 8:1 and the reason for it is uncertain. The first and second tests at 800°C deliver very similar results.

6.2.4 Summary

Comparing the performance of the cells tested at the two different operating/deposition temperatures, 750°C and 800°C, does not show one having better performance than the other. For example, comparing the maximum power densities before and after deposition (see Tables 6-6, 6-9, 6-11 and 6-14) shows values of the same order of magnitude at both temperatures. When the results are further compared by deposition bias voltage and equilibrium vapour pressure ratio, the same observation is made. At an equivalent bias voltage and vapour pressure ratio, results at both temperatures show significant drops in the maximum power density over the course of the four depositions, with the most prominent occurring after the first deposition. A variation in the bias voltage (while temperature and vapour pressure ratio are held constant) seems to have no significant effect on maximum power density and the same observation is made when the vapour pressure ratio is varied (temperature and bias voltage are constant).

Another comparison to be made is in the amount of zirconium and yttrium found in the samples after deposition has been carried out, the results of which may be seen in Tables 6-7, 6-12 and 6-15. However, these comparisons may not be taken as completely accurate, due to the semi-quantitative nature of the data from the EDX elemental analysis. Overall, when the results are compared between the two test temperatures, very similar amounts of platinum, zirconium and yttrium are found in the anodes of each of the samples tested (with the exception of sample 05-08 which experienced anode delamination). At an equivalent bias voltage and vapour pressure ratio, the samples tested at 800°C seem to contain slightly more zirconium than those tested at 750°C. A variation in bias voltage (with temperature and vapour pressure ratio held constant) has inconsistent results. At a vapour pressure ratio of 8:1, the –500 mV sample tends to have more zirconium and yttrium than the –800 mV sample, though the opposite was true for the 5.25:1

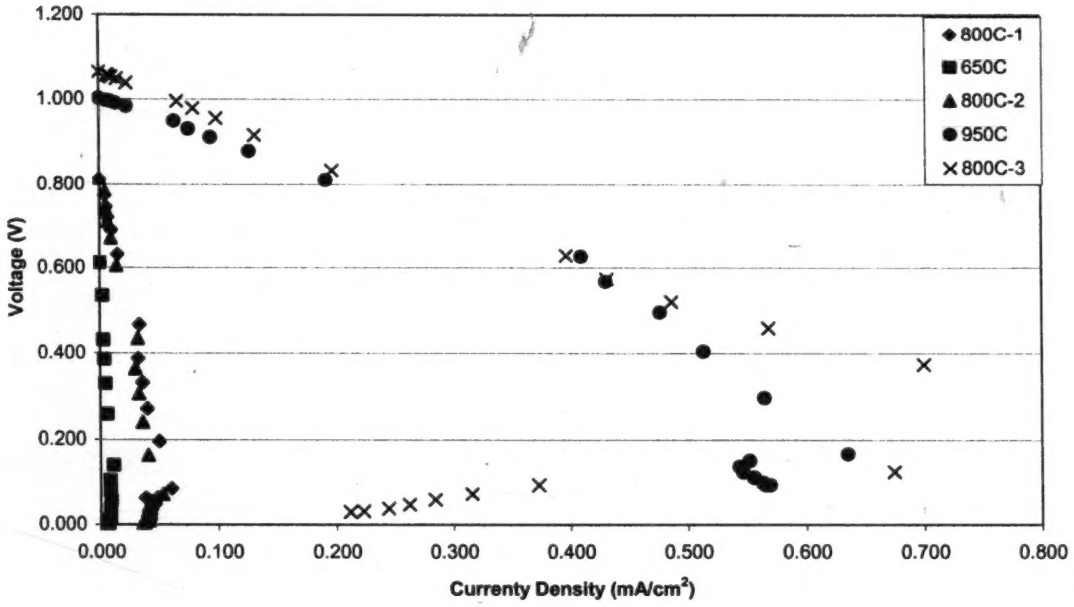

(a) corrected polarization curve

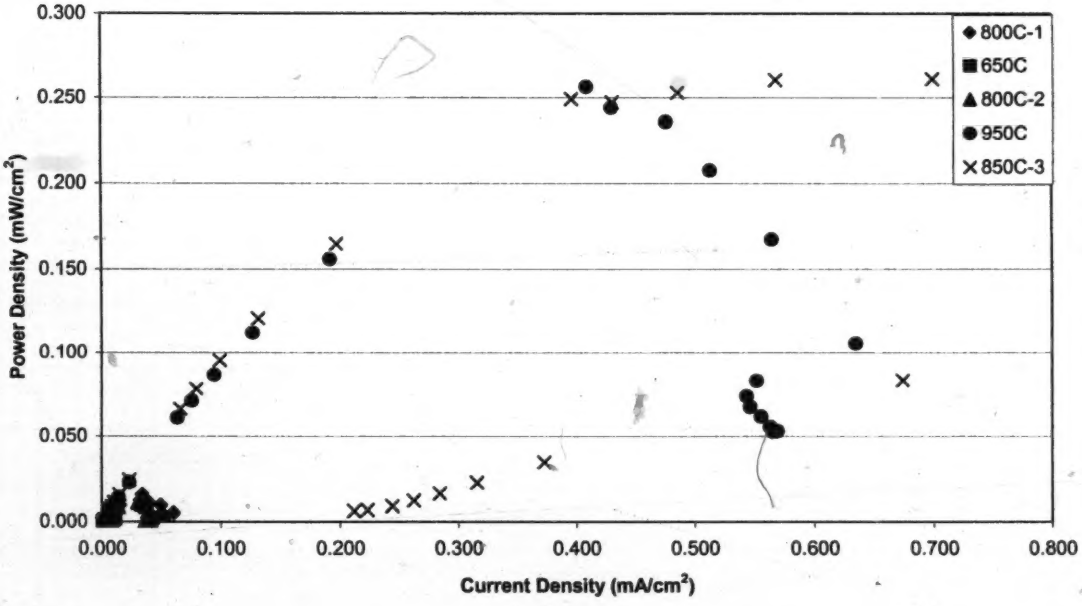

(b) corrected power curve

Figure 6-42: Corrected polarization and power curves for operating temperature cycling testing for sample 05-06

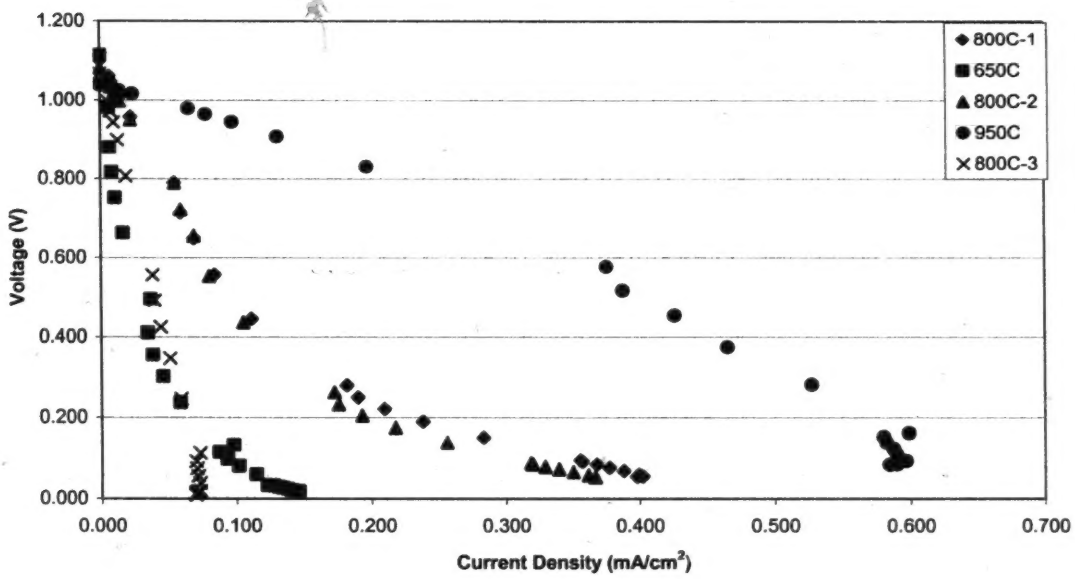

(a) corrected polarization curve

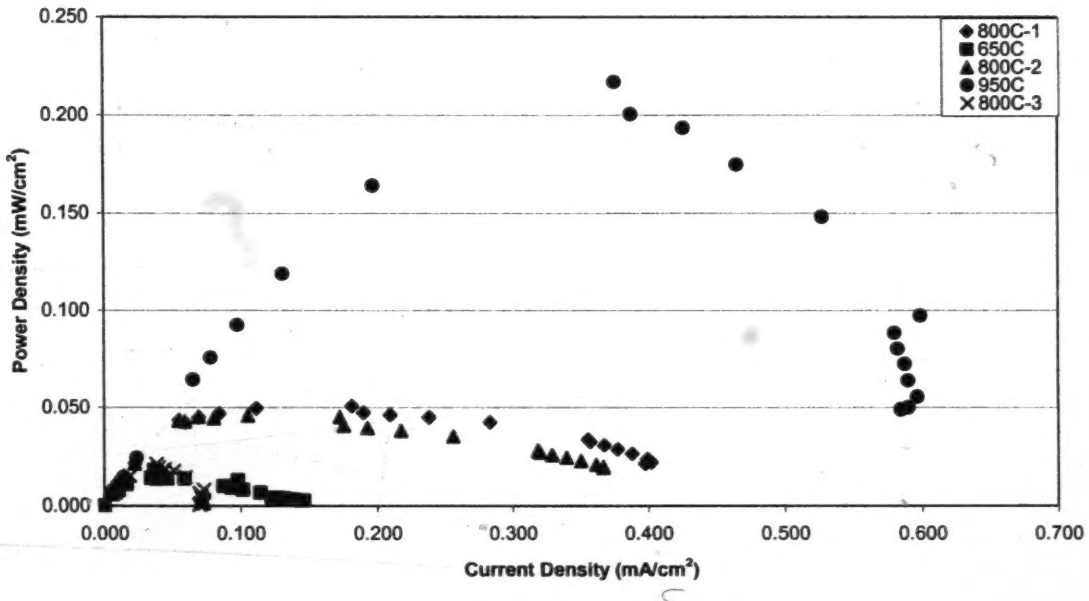

(b) corrected power curve

Figure 6-43: Corrected polarization and power curves for operating temperature cycling testing for sample 05-07

vapour pressure ratio samples (this comparison did not include the 750°C samples since sample 05-08 was inadmissible). When the vapour pressure ratio is varied (temperature and bias voltage are constant), the general trend is for very similar amounts of zirconium and yttrium to be present. An exception to this is for the samples at 800°C and a bias voltage of –500 mV, which show much less zirconium and yttrium in the 5.25:1 sample.

The study of the effect of deposition bias voltage and equilibrium vapour pressure ratio on the deposition of YSZ did not produce the results that were expected. Instead of forming a thin, deposited layer than encapsulates the platinum anode structure, it appears that little to no deposit was formed at all. The poor performance of the cells after each deposition, as seen by the polarization and power curves, was contrary to the results seen for the samples in section 6.1. Upon investigation in the SEM, no layer was visible and EDX elemental analysis showed very small amounts of zirconium and yttrium. From the poor electrochemical performance and lack of any strong evidence proving the presence of a deposited layer, it is difficult to draw any conclusion other than that the test conditions in this section do not produce an effective YSZ layer around the platinum anode.

7.0 Results and Discussion – Ceria Depositions

In addition to studying the deposition of YSZ onto the platinum anode of a solid oxide fuel cell under various conditions, preliminary tests were also completed using cerium (III) chloride ($CeCl_3$) to deposit a ceria (CeO_2) layer by PEVD. The desire to deposit a ceria layer was three-fold. Firstly, ceria is a mixed electronic and ionic conductor (MEIC), so by surrounding the platinum microstructure in ceria, it is theorized that even better cell performance could be realized due to the increased three-phase boundary area. Secondly, the use of only one reactant would simplify the PEVD process by eliminating the equilibrium vapour pressure ratio variable. Thirdly, ceria is generally a more effective catalyst than YSZ.

7.1 Effect of Deposition Time

In the first set of tests, the effect of deposition time on the performance of the fuel cells was tested. The operating/deposition temperature was held at 900°C and the deposition bias voltage was -100 mV. The operating temperature was chosen based on the equilibrium vapour pressure calculations for $CeCl_3$, which may be seen in Figure 7-1 on the following page. From the data found for solid $CeCl_3$, it has a very low vapour pressure, so a high temperature (~835°C) was selected in order to achieve what was thought to be a sufficient vapour pressure (~0.010 torr). A bias voltage of -100 mV was chosen as a starting point since previous work (section 6.2) with YSZ depositions did not show promise at high bias voltages. Deposition time increments of 1, 4 and 12 hours were chosen and four depositions were carried out for each sample. The specifics of each sample may be seen in Table 7-1.

The corrected polarization curves by number of depositions for these samples may be seen in Figure 7-2, with curves comparing the performance after each deposition for each sample presented in Figure 7-3. From Figure 7-2(a), it is clear that sample 05-11 reached much higher current densities than the other two cells, which may be due to better sample preparation. After the first deposition, performance of sample 05-10 improved, while performance for samples 05-11 and 05-13 both improved and declined. It is clear that the OCV of samples 05-11 and 05-13

Table 7-1: Fuel cell samples for ceria deposition at 900°C and -100 mV

Fuel Cell Sample	Deposition Time Increment (hr)
05-10	1
05-11	4
05-13	12

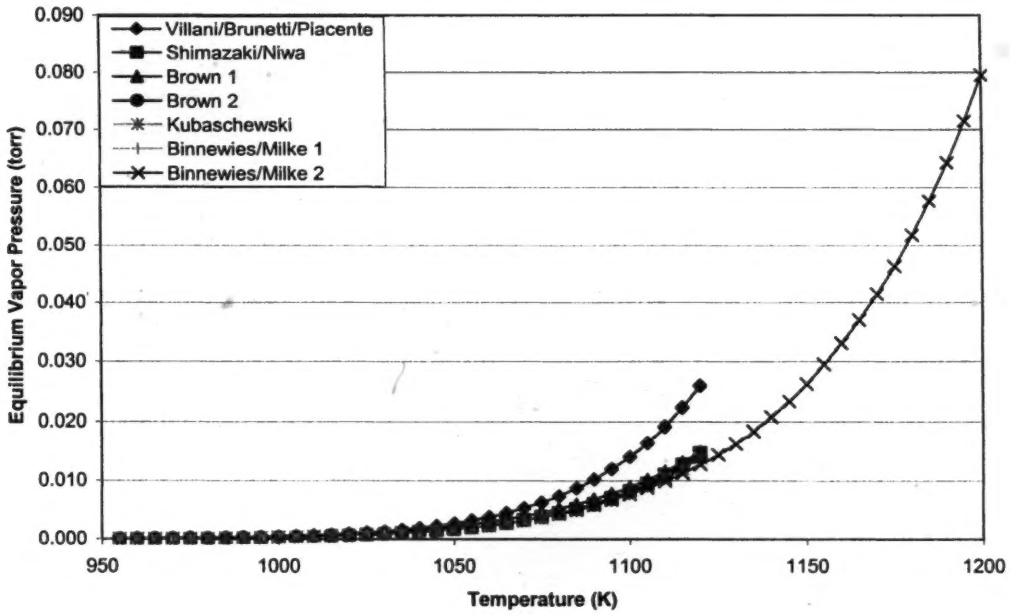

Figure 7-1: Cerium (III) chloride equilibrium vapour pressure from various sources[106-110]

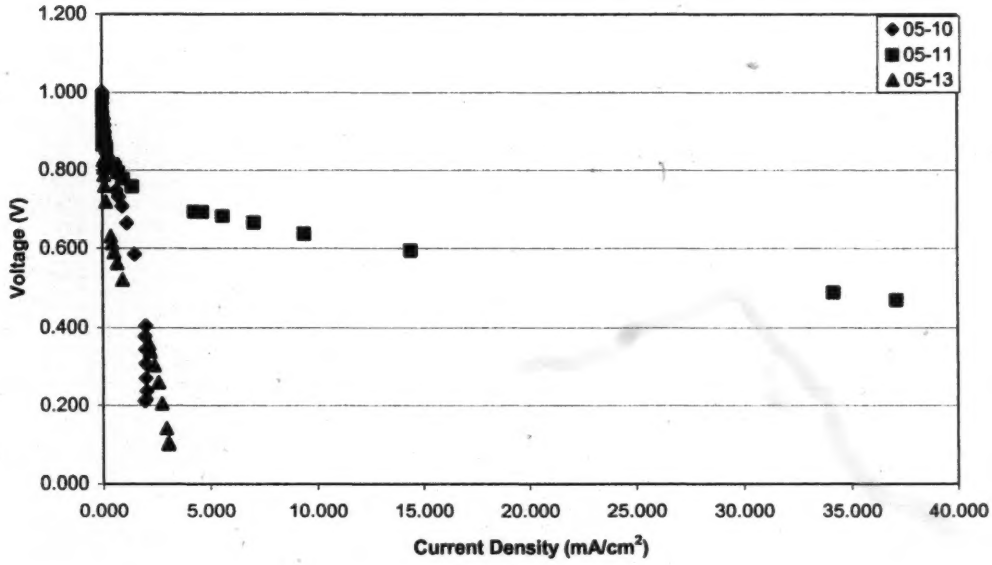

(a) no deposition

Figure 7-2: Corrected polarization curves for ceria deposition at 900°C and -100 mV by number of depositions

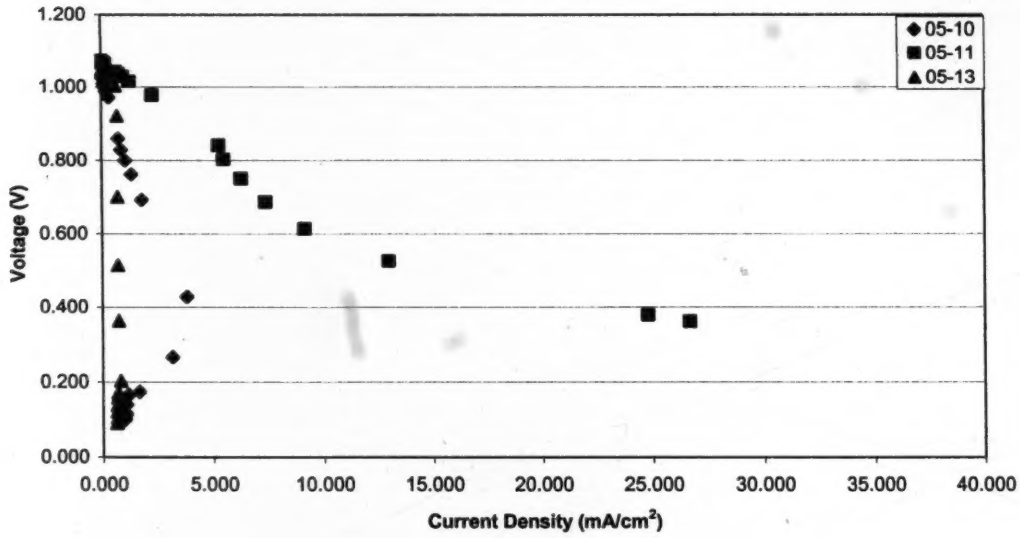

(b) 1 deposition

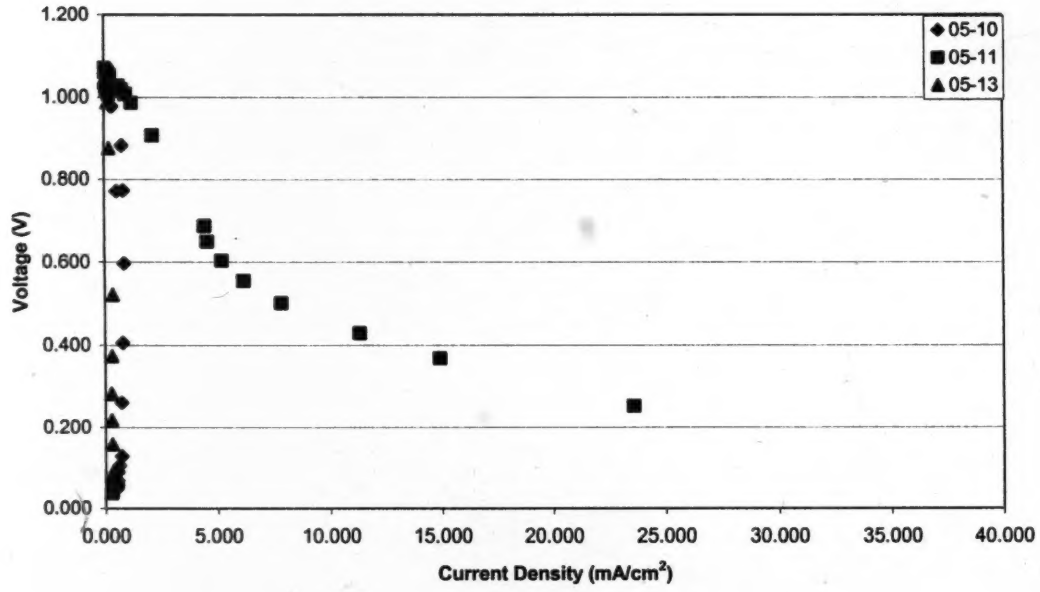

(c) 2 depositions

Figure 7-2 (con't): Corrected polarization curves for ceria deposition at 900°C and -100 mV by number of depositions

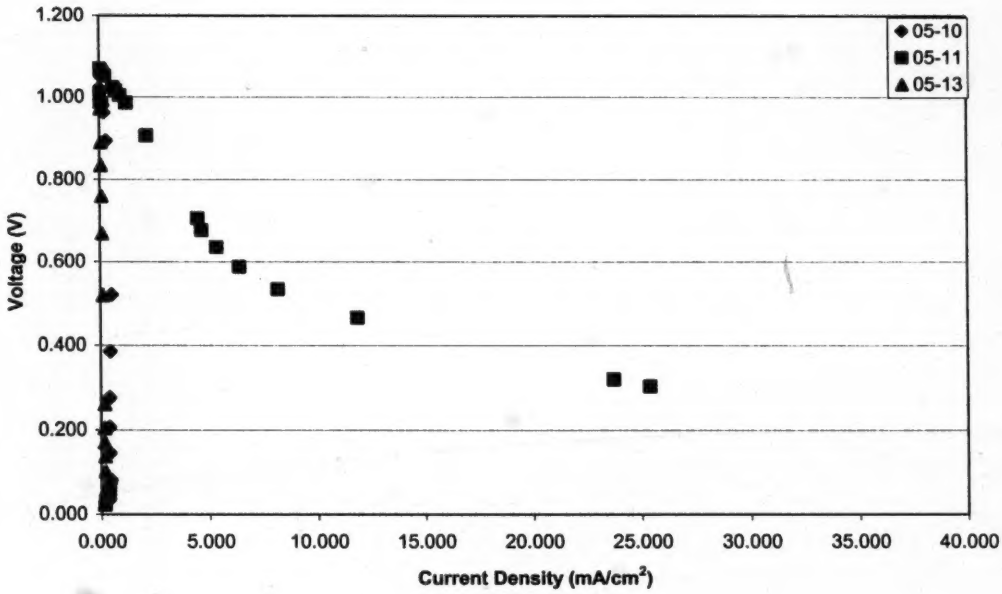

(d) 3 depositions

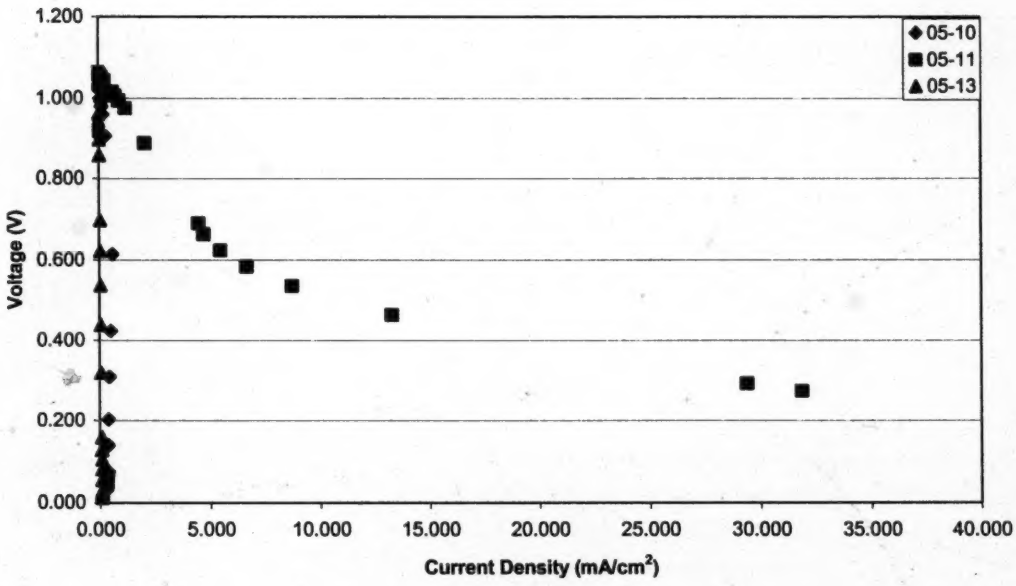

(e) 4 depositions

Figure 7-2 (con't): Corrected polarization curves for ceria deposition at 900°C and -100 mV by number of depositions

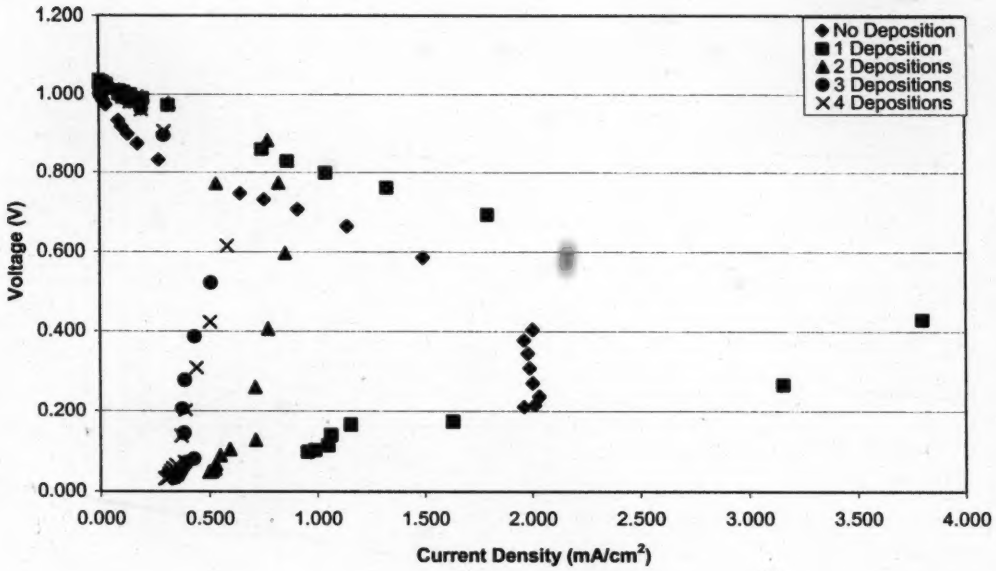

(a) sample 05-10

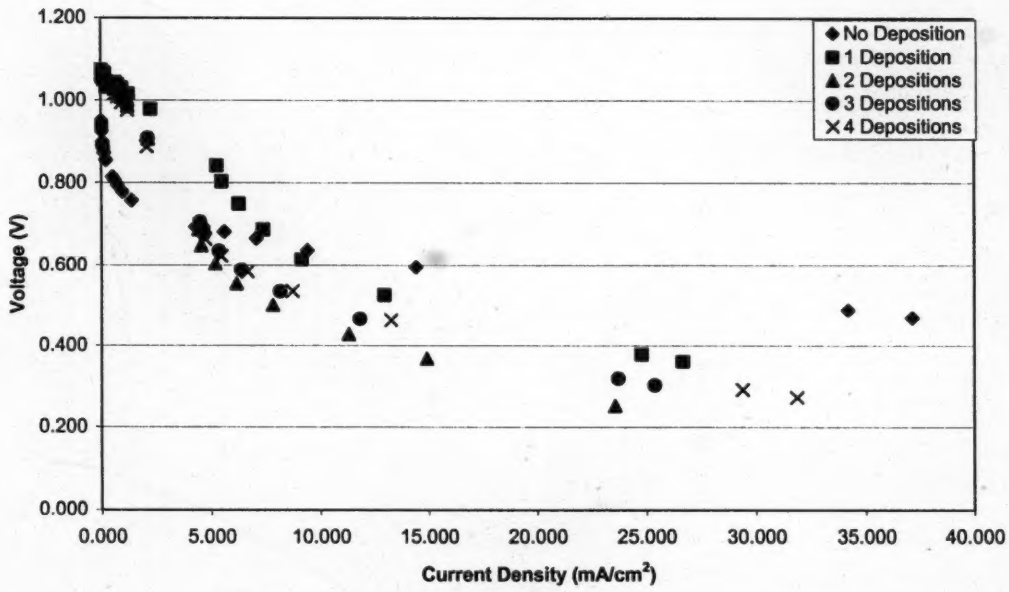

(b) sample 05-11

Figure 7-3: Corrected polarization curves for ceria deposition at 900°C and -100 mV by sample

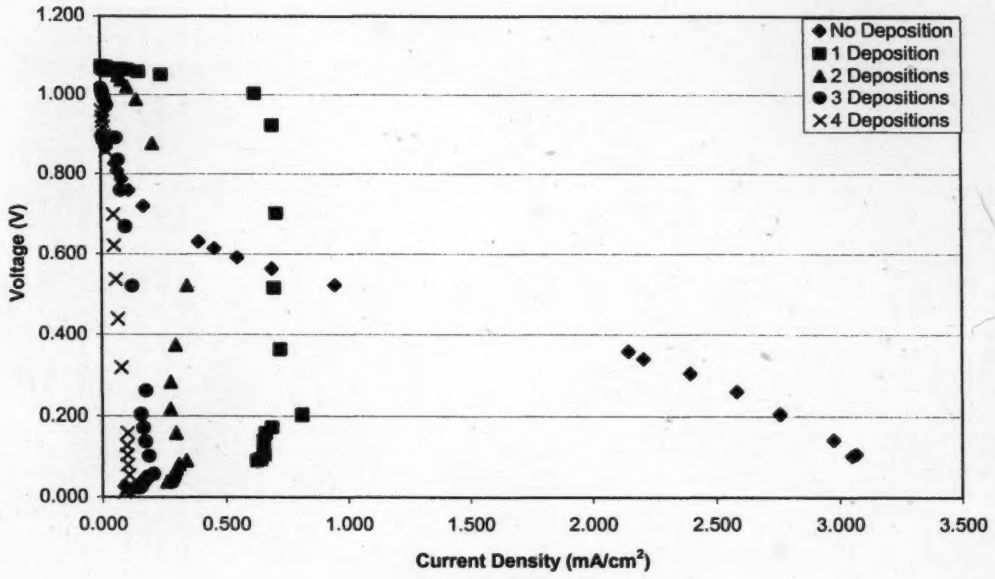

(c) sample 05-13

Figure 7-3 (con't): Corrected polarization curves for ceria deposition at 900°C and -100 mV by sample

increased and performance at low current densities was better than that before deposition. However, as higher current densities were reached, the performance of these two cells declined to levels lower than before deposition. This is most visible in Figures 7-3(b) and (c), particularly for the latter figure (sample 05-13). Sample 05-10, after reaching higher current densities, demonstrates the behaviour seen in section 6.2 with a shift to lower current densities at low voltages. As the number of depositions increases, all of the cells show a continual decline in performance. This is evidenced by the polarization curves tending towards a more vertical shape and moving further away from the theoretical ideal of a horizontal line emanating from the OCV. This is perhaps best demonstrated by the curves plotted in Figure 7-3.

From the polarization curve data, power curves (again corrected for electrolyte resistance) were plotted and may be seen in Figure 7-4 (by deposition) and 7-5 (by sample). The maximum power densities for each sample after each deposition may be seen in Table 7-2. From the data presented and the figures, it is clear that only sample 05-10 showed improvement after the first deposition. Though the other two samples showed greater OCVs after the first deposition, their maximum power densities were less. As more depositions were carried out, the power densities continued to decrease, except for slight increases after the third deposition for sample 05-11 and

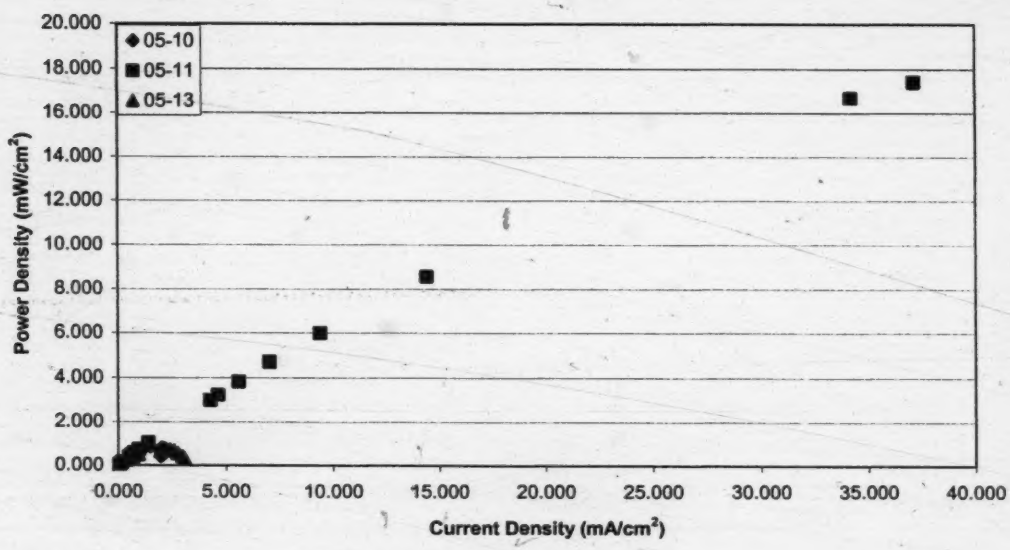

(a) no deposition

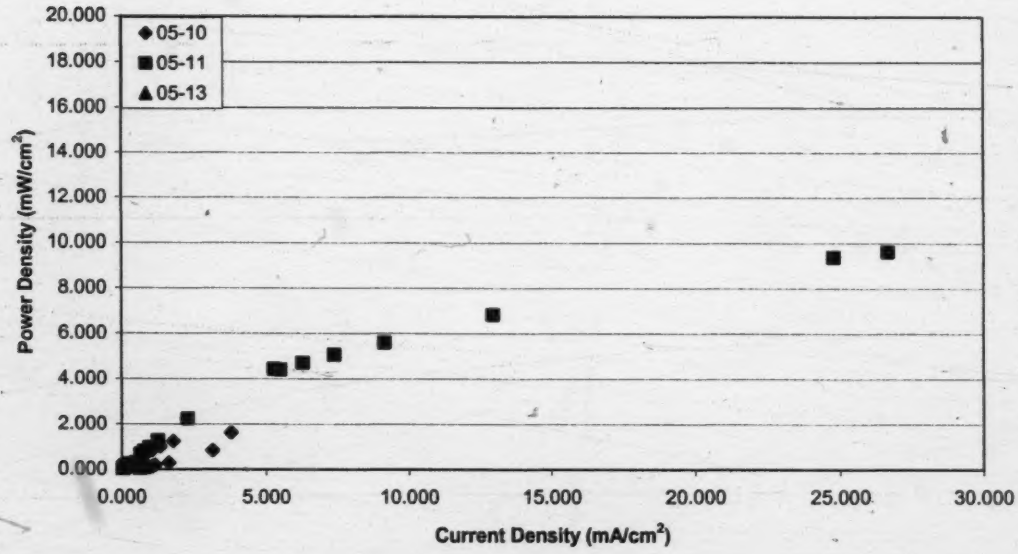

(b) 1 deposition

Figure 7-4: Corrected power curves for ceria deposition at 900°C and -100 mV by number of depositions

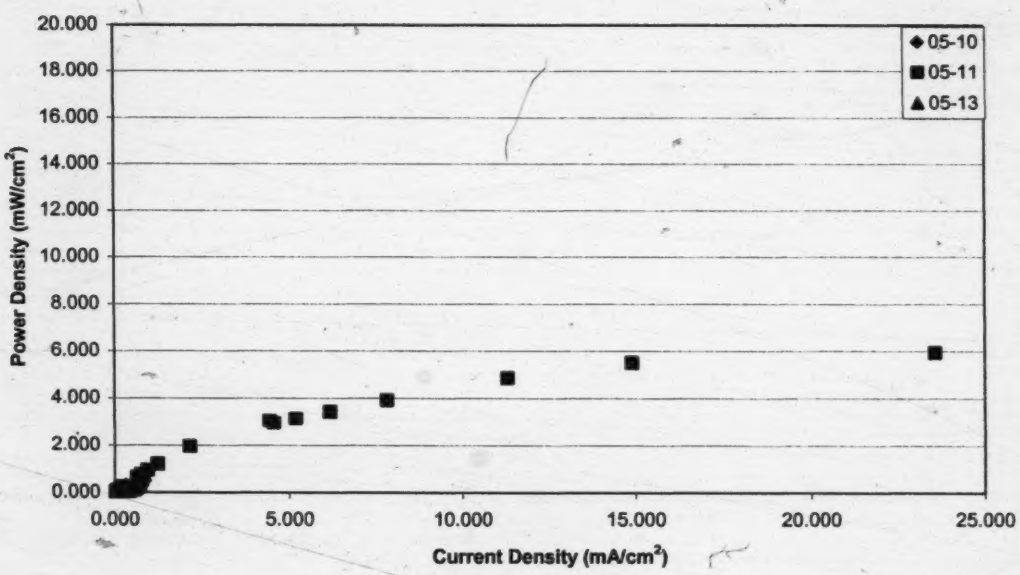

(c) 2 depositions

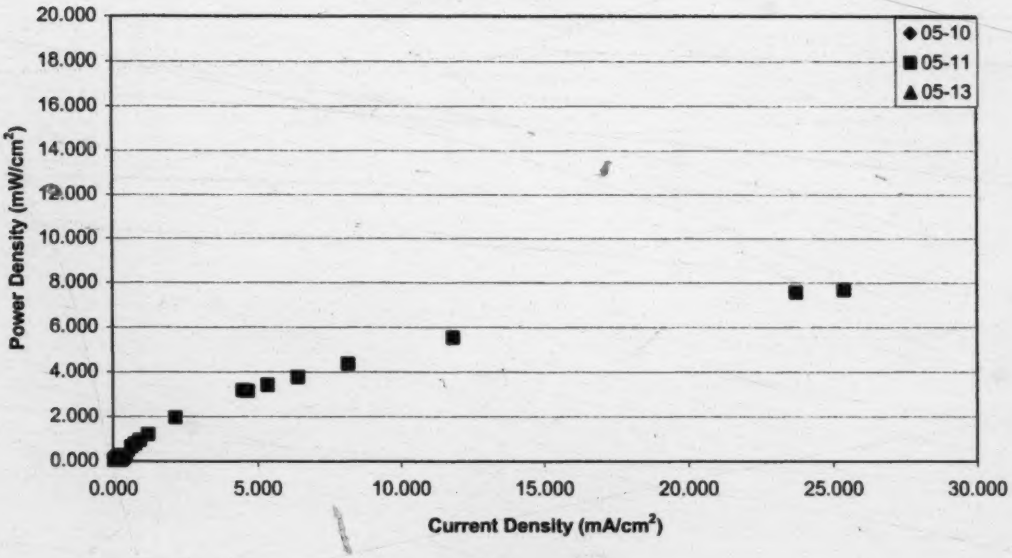

(d) 3 depositions

Figure 7-4 (con't): Corrected power curves for ceria deposition at 900°C and -100 mV by number of depositions

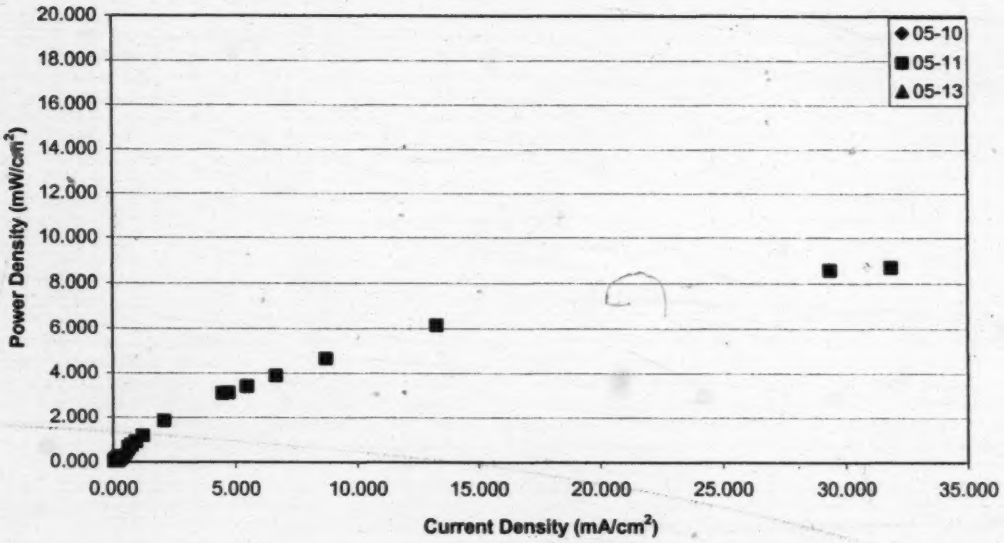

(e) 4 depositions

Figure 7-4 (con't): Corrected power curves for ceria deposition at 900°C and -100 mV by number of depositions

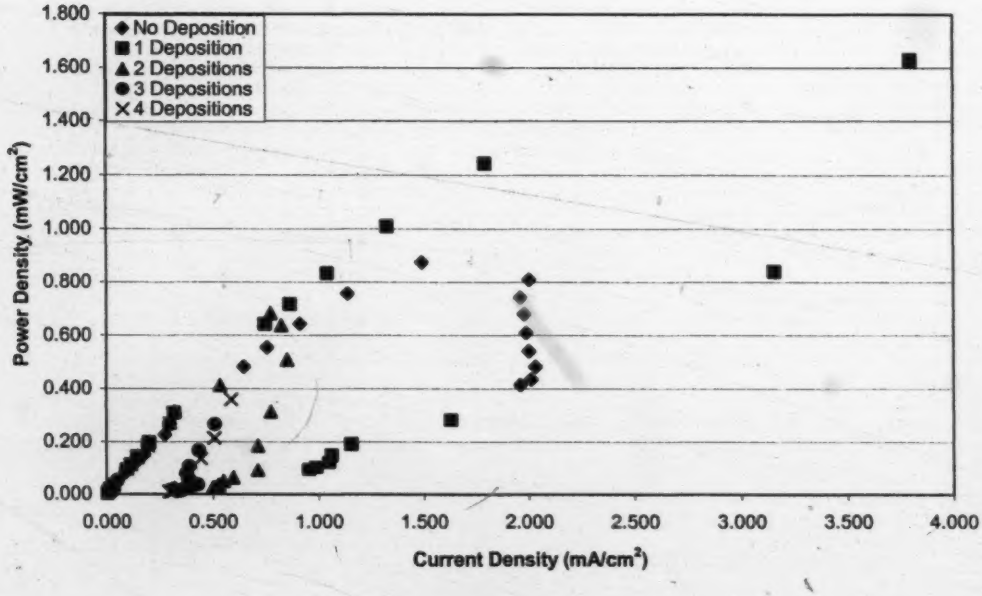

(a) sample 05-10

Figure 7-5: Corrected power curves for ceria deposition at 900°C and -100 mV by sample

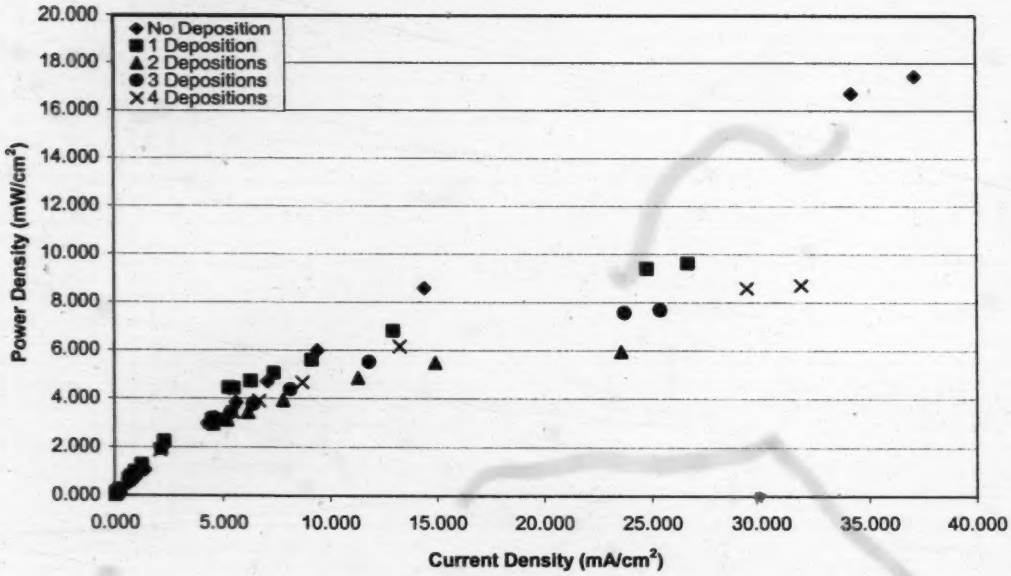

(b) sample 05-11

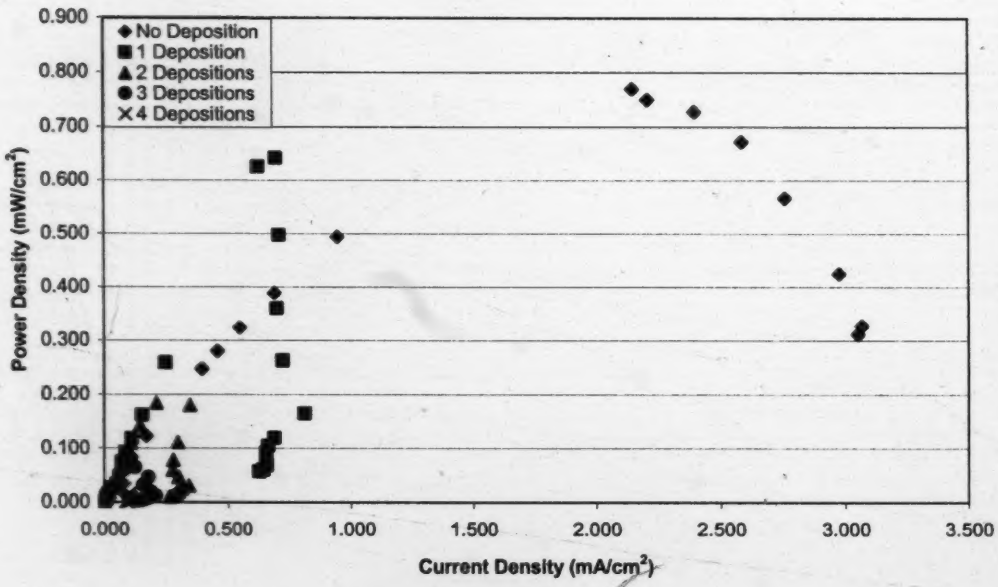

(c) sample 05-13

Figure 7-5 (con't): Corrected power curves for ceria deposition at 900°C and -100 mV by sample

Table 7-2: Maximum power density for 900°C and -100 mV samples

Fuel Cell Sample	Maximum Power Density (mW/cm^2)				
	Deposition				
	0	1	2	3	4
05-10	0.87	1.63	0.68	0.27	0.36
05-11	17.43	9.62	5.94	7.69	8.70
05-12	0.77	0.64	0.18	0.06	0.03

after the fourth deposition for sample 05-10. The shapes of the power curves are varied, as was seen with the polarization curves. From Figure 7-5(a), sample 05-10 shows the shape seen when current density starts decreasing as voltage does for all depositions, while Figure 7-5(c) shows the initially expected increase in power density followed by a sudden drop for all depositions. Figure 7-5(b) shows the most uniform shape between varying depositions. In all cases, the shape of the curve moves further from theoretical as the number of depositions increases.

For more insight into the behaviour of these fuel cells, they were once again viewed using the SEM. The secondary electron images of the anode may be seen in Figures 7-6 to 7-8. As before, these images were compared to the images of the platinum anode after preparation, seen in Figures 6-6 and 6-7. It is clear from the plan views that all three samples show a microstructure with much larger grains and less porosity than the original microstructure. The cross sectional view of sample 05-11 in Figure 7-8(b) has a much more dense appearance than that of the cross section of the as-prepared sample in Figure 6-7. When the samples are compared to each other, it is clear that sample 05-11 has more porosity than the other two. The grains also appear smoother in this sample. The greater porosity in sample 05-11 is probably a strong factor in its much better performance as compared to the other two. It is also observed from these images that there does not appear to be a deposited layer present on any of the samples. No visible evidence of the crystal-like layer seen on samples in section 6.1 is present; the only things visible are specks of material on the surface of varying brightness. There is a potential that a layer may be present, but so thin that it is not clearly visible.

In order to determine if any ceria had been deposited, EDX was used to verify what elements were present on the anode. The overall spectra at accelerating voltages at 20 kV and 30 kV were very similar for all three samples, so those generated for sample 05-10 are shown in Figure 7-9. The clear feature from these two spectra and those of the other two samples is the very strong platinum peaks and absence of any cerium peaks. While this result may have been expected for sample 05-10 (since the deposition time increment was only one hour), it was expected that some

Figure 7-6: SEM secondary electron image of sample 05-10 (plan view)

Figure 7-7: SEM secondary electron image of sample 05-13 (plan view)

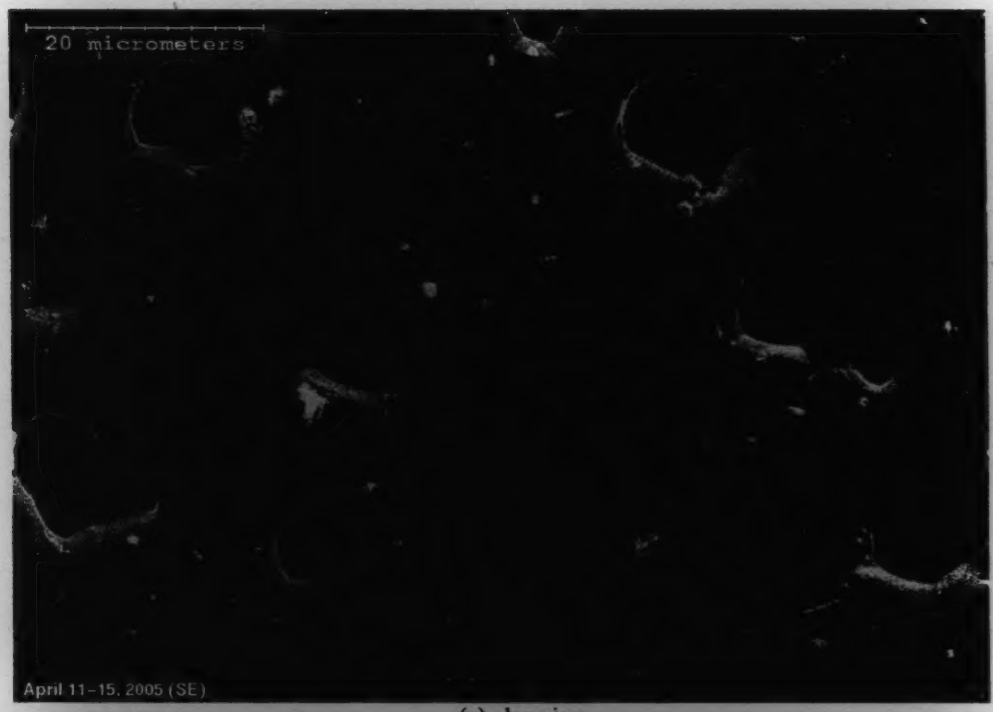

(a) plan view

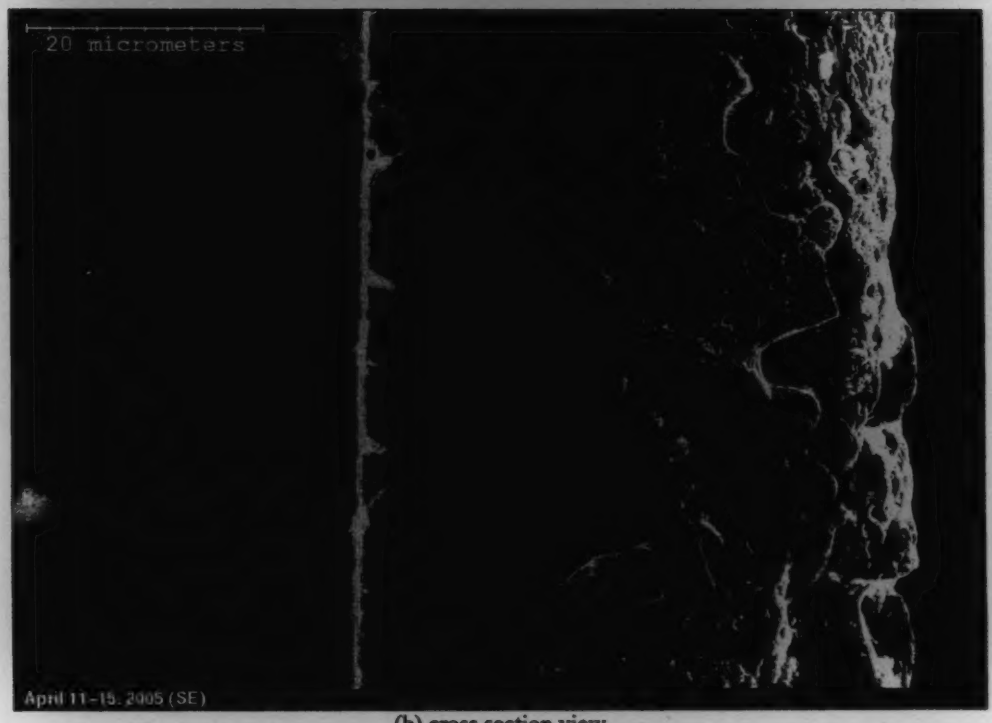

(b) cross section view

Figure 7-8: SEM secondary electron image of sample 05-11

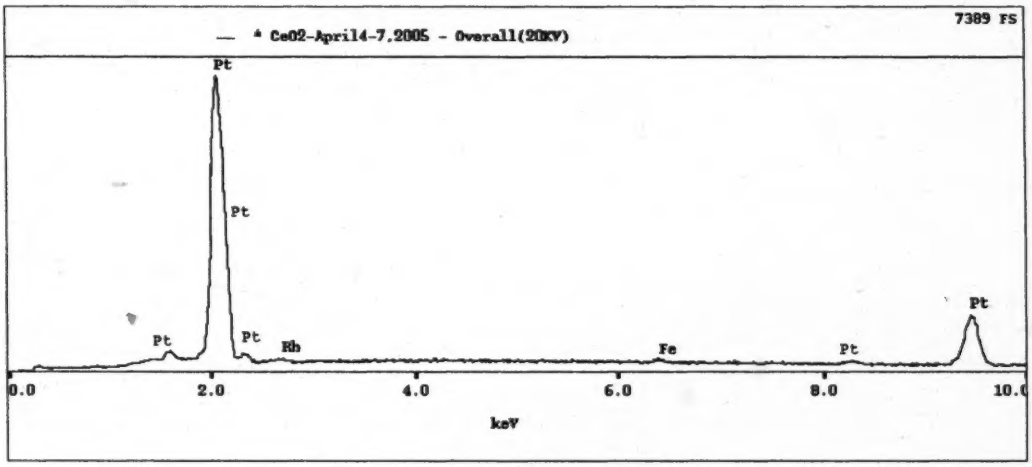

(a) accelerating voltage = 20 kV

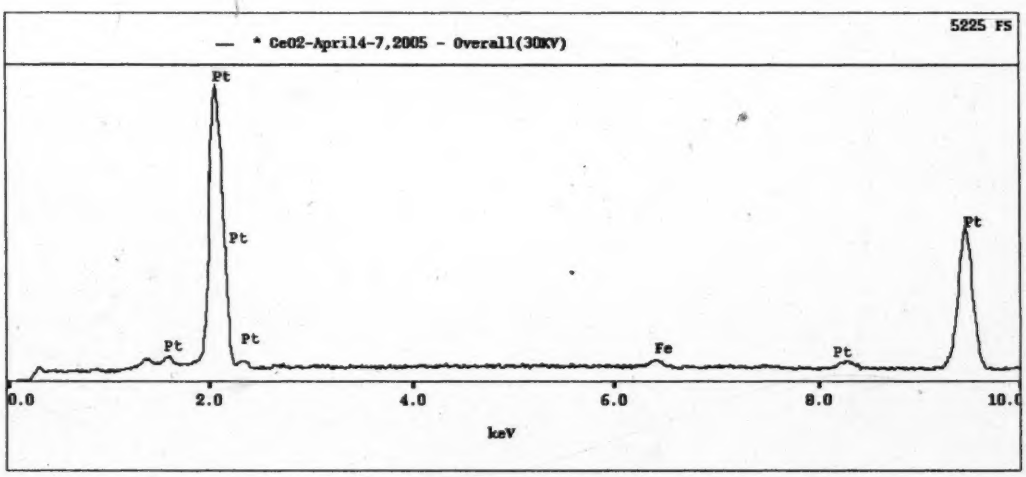

(b) accelerating voltage = 30 kV

Figure 7-9: EDX overall spectra for sample 05-10

Table 7-3: Elemental analysis from overall EDX analysis for samples viewed in the SEM

Fuel Cell Sample	Amount of Element (wt%)			
	Accelerating Voltage = 20 kV		Accelerating Voltage = 30 kV	
	Pt	Ce	Pt	Ce
05-10	98.98	-	99.32	-
05-11	100.00	-	98.07	-
05-13	100.00	-	100.00	-

cerium should be present in the other two samples. From the elemental analysis (considered semi-quantitative) seen in Table 7-3, it is clear that the main element present is platinum, since it is nearly 100 wt% in all cases.

In addition to the overall EDX analyses carried out on the samples, point analysis were carried out on some of the specks of material on the surfaces of samples 05-11 and 05-13. From these analyses, the presence of phosphorous, calcium, aluminum and silicon was identified, but no cerium was detected. These elements have appeared in previous EDX spectra for YSZ depositions. As discussed by Haldane[105], the phosphorous and aluminum may be attributed to the alumina cement and its phosphate binder system. The calcium and silicon may be attributed to the glass crucibles used for holding the reactant chlorides.[105]

From these three initial tests, it does not appear that ceria was deposited on the platinum anode surface. The reason for this may be cerium (III) chloride's very low vapour pressure, so it was placed at a temperature above the melting point to increase the vapour pressure. In order to do this, the operating/deposition temperature was increased to 1000°C. Since a deposition time increment of four hours gave the best results for the previous set of data, this time was selected for further work.

7.2 Effect of $CeCl_3$ Temperature

Since the deposition of ceria by PEVD did not work out as hoped when varying deposition time increments were studied, it was decided to try placing the reactant chloride at a higher temperature in the furnace. An operating/deposition temperature of 1000°C was selected while the deposition bias voltage of -100 mV was maintained. A deposition time of four hours was chosen based on the results in section 7.1, but for these tests only one deposition was carried out, since previous work (both with YSZ and ceria depositions) showed that the best results were usually obtained after one deposition. The sample specifications may be seen in Table 7-4.

The polarization curves (corrected for electrolyte resistance) for these two samples appear in

Table 7-4: Fuel cell samples for ceria deposition at 1000°C and -100 mV

Fuel Cell Sample	$CeCl_3$ Temperature (°C)	Vapour Pressure (torr)
05-14	~835	~0.01
05-15	~910	~0.05

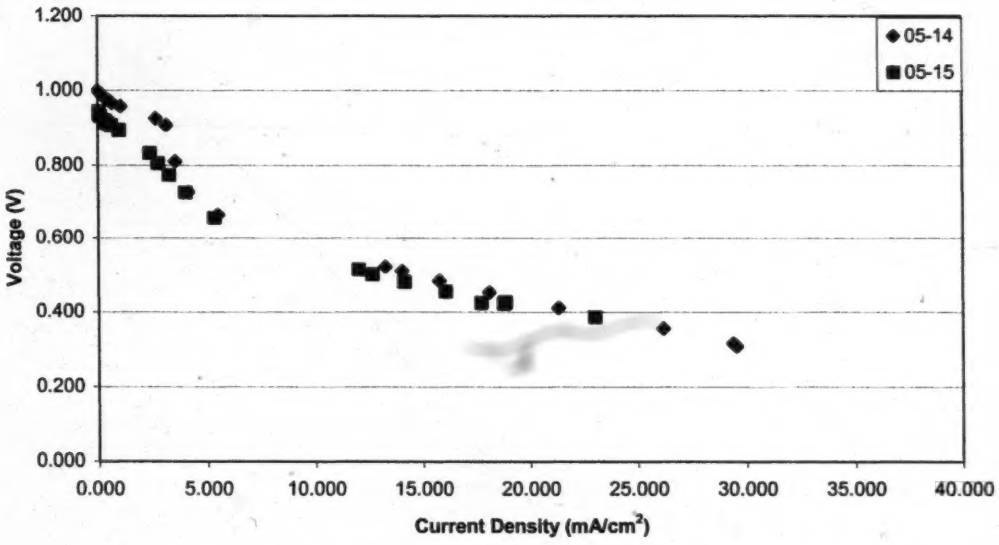

(a) no deposition

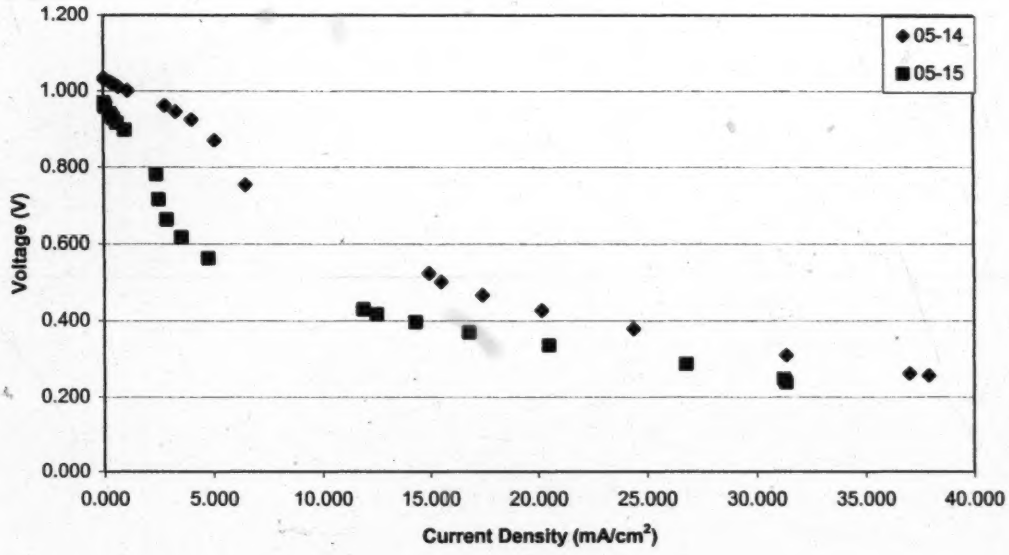

(b) 1 deposition

Figure 7-10: Corrected polarization curves for ceria deposition at 1000°C and -100 mV by number of depositions

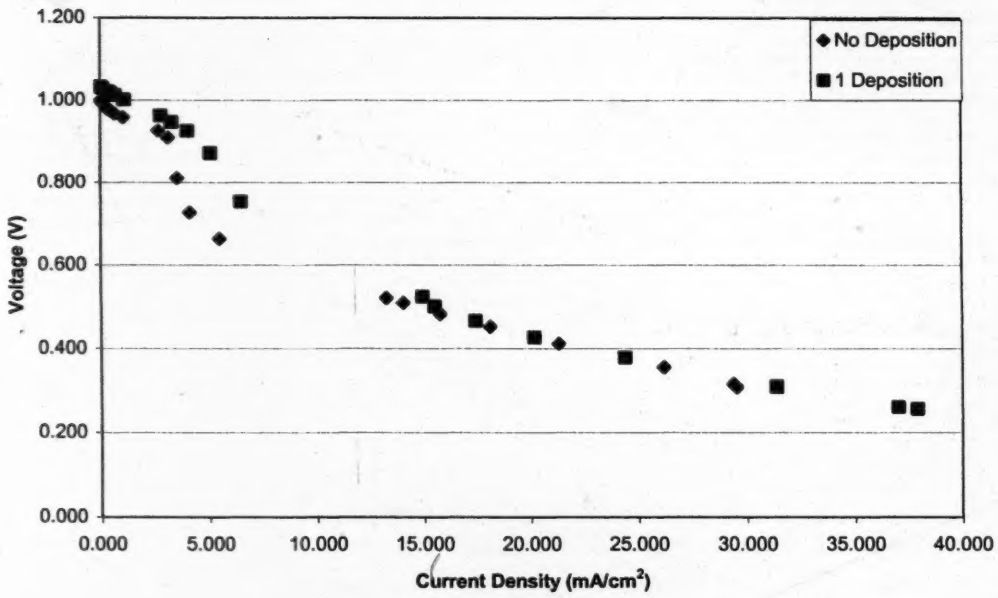

(a) sample 05-14

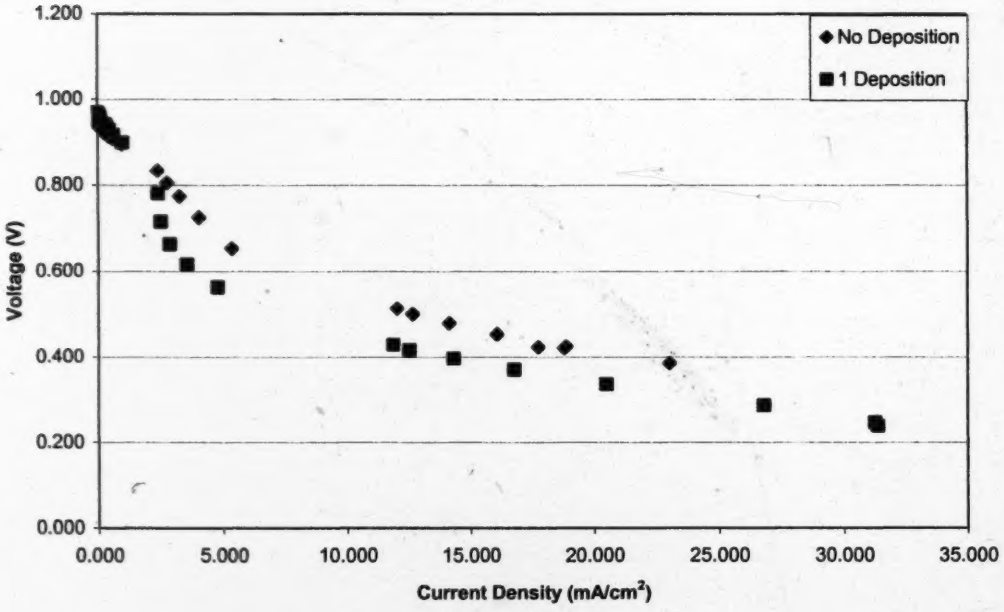

(b) sample 05-15

Figure 7-11: Corrected polarization curves for ceria deposition at 1000°C and -100 mV by sample

Figure 7-10 (by deposition) and 7-11 (by sample). Both figures show that cells reached high current densities before deposition was carried out and maintained these densities after deposition. Sample 05-14 appears to have slightly better performance than sample 05-15 by its position on the plot, mostly because sample 05-15 had lower OCV values. The shapes of the curves for both samples are as expected, with fairly uniform slopes. When looking at each sample individually, sample 05-14 seems to maintain its level of performance as compared to no deposition, though the OCV improved slightly. On the contrary, sample 05-15 appears to have decreased somewhat in its performance, despite a marginal improvement in its OCV.

The corrected power curves for these samples may be seen in Figure 7-12 (by deposition) and 7-13 (by sample), with the maximum power density values in Table 7-5. The improvement in performance for sample 05-14 is again clear, since the curve for data collected after the deposition is slightly higher than that for no deposition. The contrary is true for sample 05-15.

In addition to current-voltage tests, these cells were also studied using impedance analysis. Since impedance analysis is used to help identify the steps occurring in an electrochemical reaction, it should indicate if the deposition results in any changes to these steps. By setting the reference anode as the reference electrode, it can be observed if any change occurs in the impedance curve, thus indicating a change in the reaction steps occurring at the anode. Since the only modification being made to the cell is that of the deposited layer on the anode, the changes in the curve would be due to the deposition. Figure 7-14 shows the impedance plots for each of the samples before and after deposition. From both plots, it is immediately clear that some change must have taken place after the deposition was carried out. The semi-circles in the plot for sample 05-14, which are indicative of the number of reaction steps, are overlapped but decrease in size after deposition. A decrease in semi-circle size indicates that the resistance to a particular step has been decreased. From the high-frequency intercept ($Z' \rightarrow 0$), it is seen that the electrolyte resistance increased slightly. In the case of sample 05-15, the impedance plots before and after deposition look quite different. Before deposition there appears to be an extremely small semi-

Table 7-5: Maximum power density for 1000°C and -100 mV samples

Fuel Cell Sample	Maximum Power Density (mW/cm^2)	
	Deposition	
	0	1
05-14	9.29	9.70
05-15	8.87	7.72

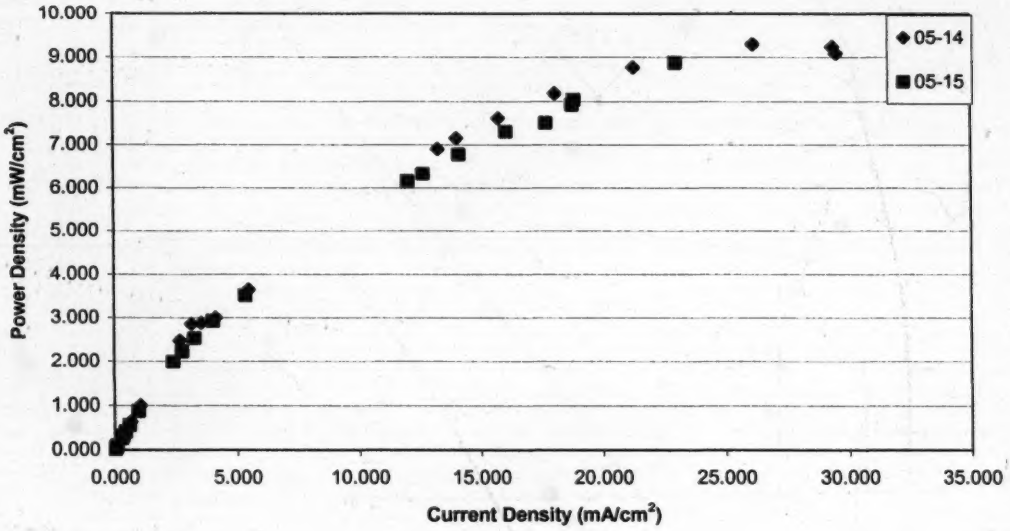

(a) no deposition

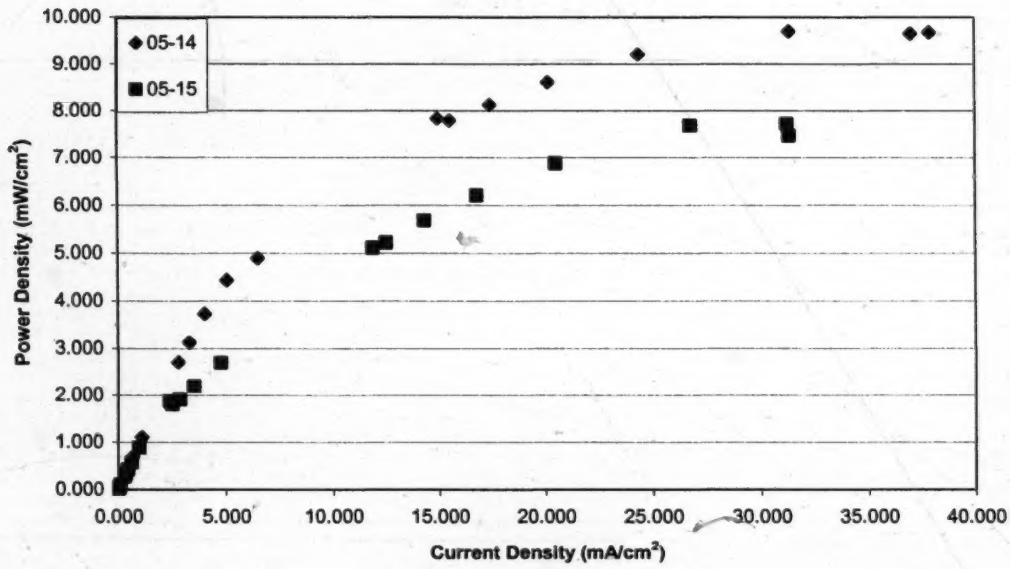

(b) 1 deposition

Figure 7-12: Corrected power curves for ceria deposition at 1000°C and -100 mV by number of depositions

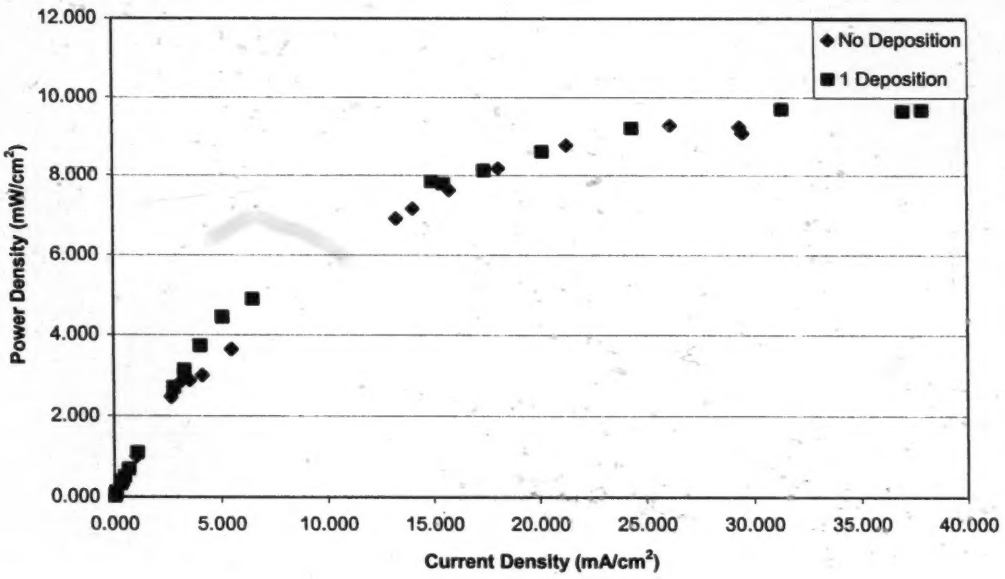

(a) sample 05-14

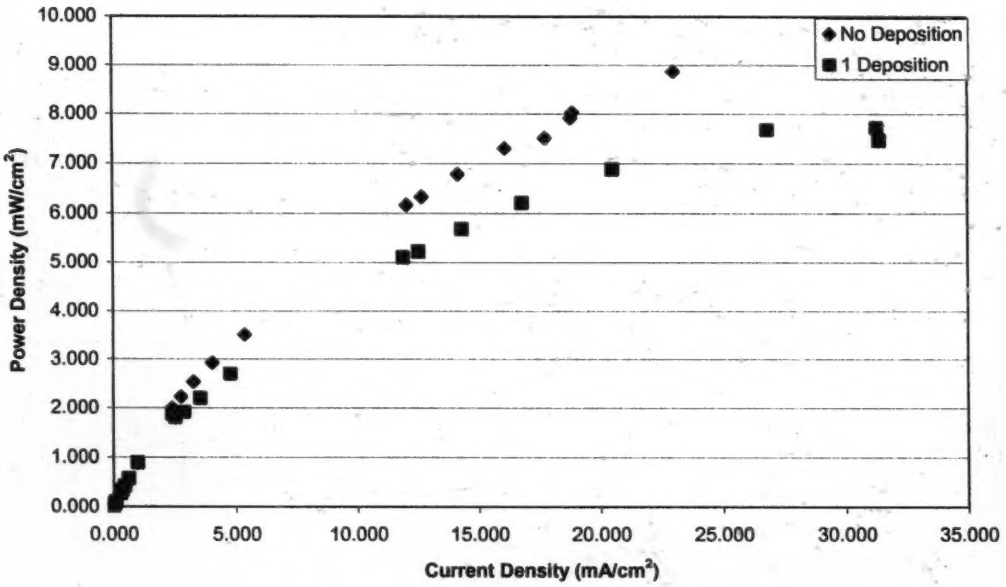

(b) sample 05-15

Figure 7-13: Corrected power curves for ceria deposition at 1000°C and -100 mV by sample

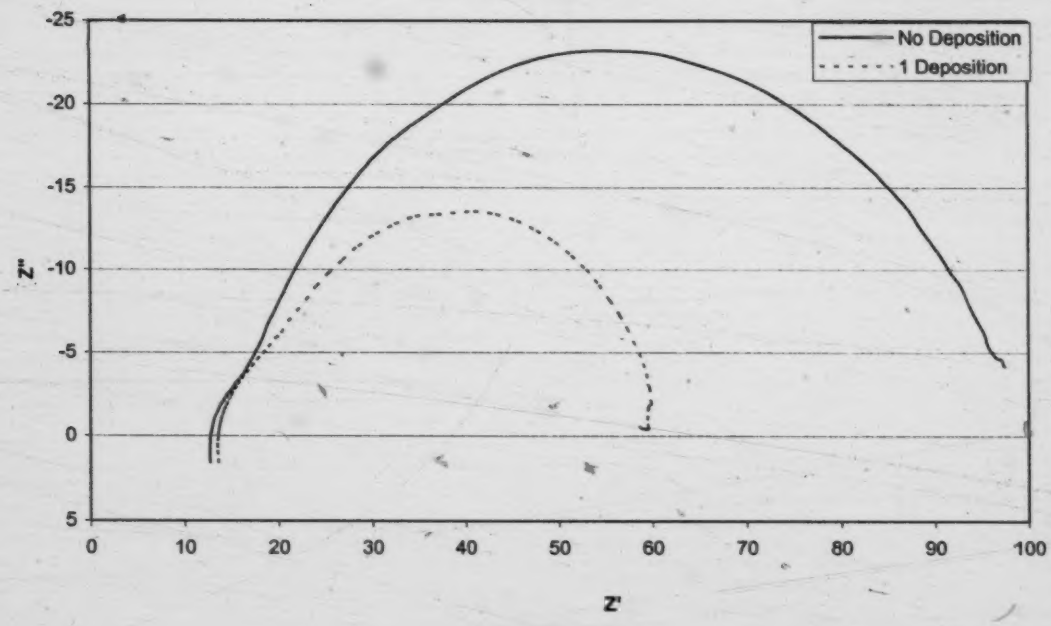

(a) sample 05-14

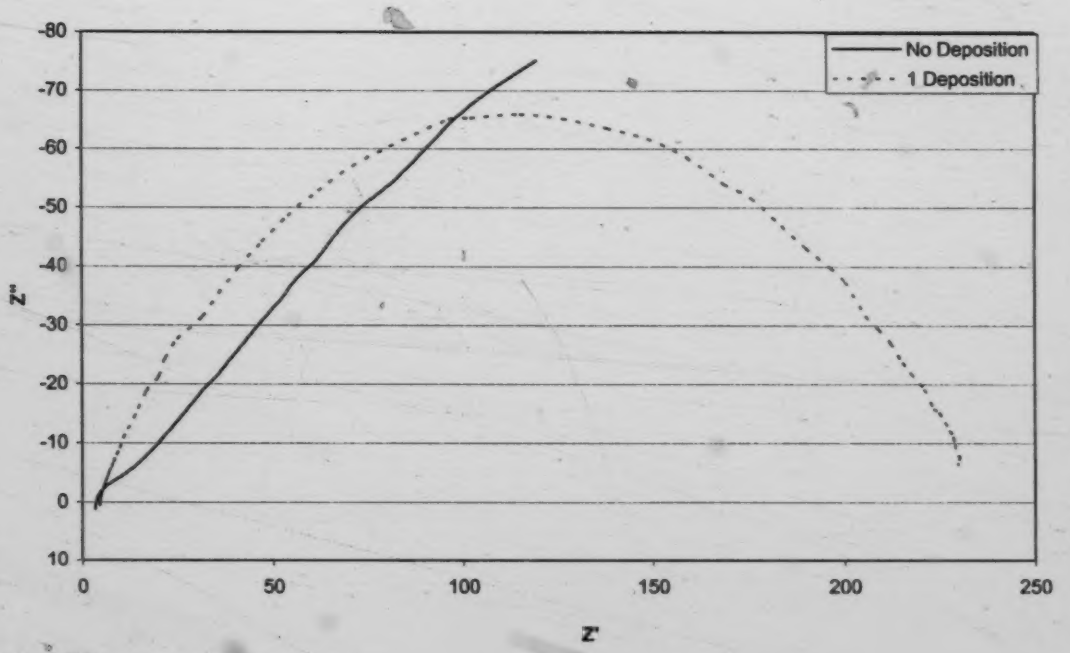

(b) sample 05-15

Figure 7-14: Impedance analysis for ceria deposition at 1000°C and -100 mV by sample

circle followed by a continually increasing slope. After deposition, one large semi-circle is present. Again, this would seem to indicate some improvement, but it should be noted that that Z' and Z" values are much larger for sample 05-15 than 05-14.

Once again, the samples were studied using the SEM. Secondary electron images of the anodes of both samples may be seen in Figure 7-15 and 7-16. As compared to previous samples examined, both of these samples have considerably more porosity, though the porosity does seem to be less relative to the as-prepared sample (Figure 6-6). Between the two samples, 05-14 appears more porous than 05-15. The porosity does not seem to be consistent throughout the anode though, as seen by two very different cross section views in Figures 7-15(b) and (c). Figure 7-15(b) seems to show some delamination of the anode while 7-15(c) shows good connection between the anode and the electrolyte. Its structure does appear a bit denser when compared to Figure 6-7. This factor would strongly account for the better performance of the cell. From these images, however, it does not appear that any deposited layer is present. Some larger particles are present on the surface, but they are not of the form of the crystal-like layer seen on the samples in section 6.1.

EDX was used to determine if any cerium was present that would indicate that ceria had been deposited. Figure 7-17 shows the EDX overall spectra that were obtained for sample 05-14 (similar results were obtained for sample 05-15). Yet again, the presence of cerium was not visible on either of the spectra at either of the accelerating voltages. Platinum was detected in abundance and some zirconium and yttrium were visible on the 30 kV spectrum. Their presence is most likely due to the higher accelerating voltage resulting in a larger (i.e., deeper) sample area. From the elemental analysis in Table 7-6, it is clear that cerium is not present in any detectable quantity. This result is not completely unexpected, since there was no significant change in cell performance after the deposition was carried out on each sample. However, the impedance analysis results would seem to indicate some change had taken place. Perhaps this is due to the change in microstructure due to sintering, as opposed to deposition as inferred. Point analyses

Table 7-6: Elemental analysis from everall EDX analysis for 1000°C and -100 mV samples viewed in the SEM

Fuel Cell Sample	Amount of Element (wt%)			
	Accelerating Voltage = 20 kV		Accelerating Voltage = 30 kV	
	Pt	Ce	Pt	Ce
05-14	100.00	-	94.26	-
05-15	99.65	-	100.00	-

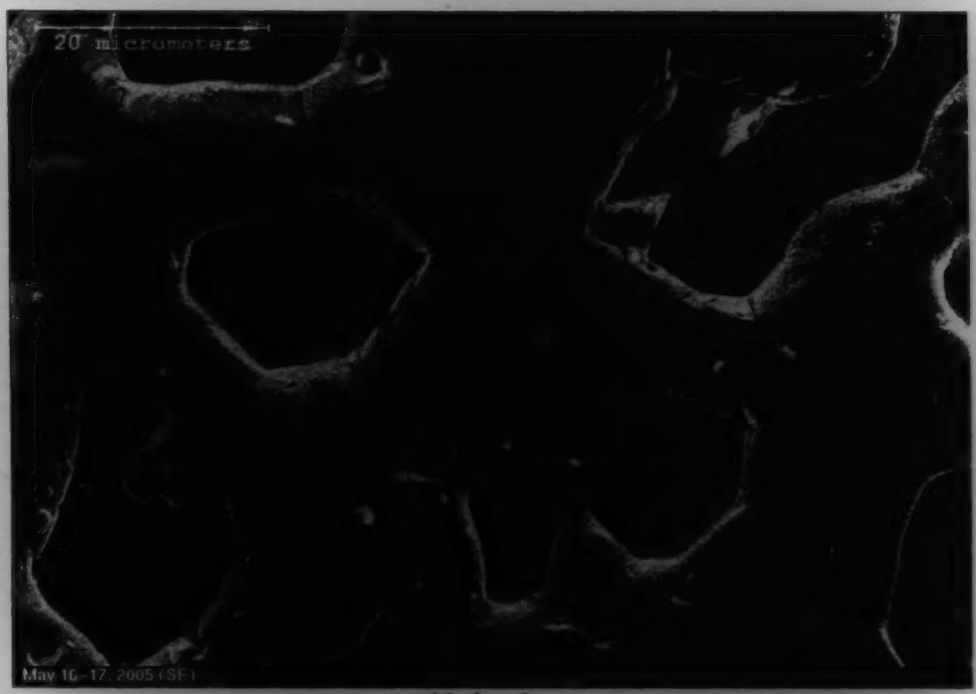

(a) plan view

(b) cross section view

Figure 7-15: SEM Secondary Electron Image of Sample 05-14

(c) cross section view

Figure 7-15 (con't): SEM secondary electron image of sample 05-14

Figure 7-16: SEM secondary electron image of sample 05-15 (plan view)

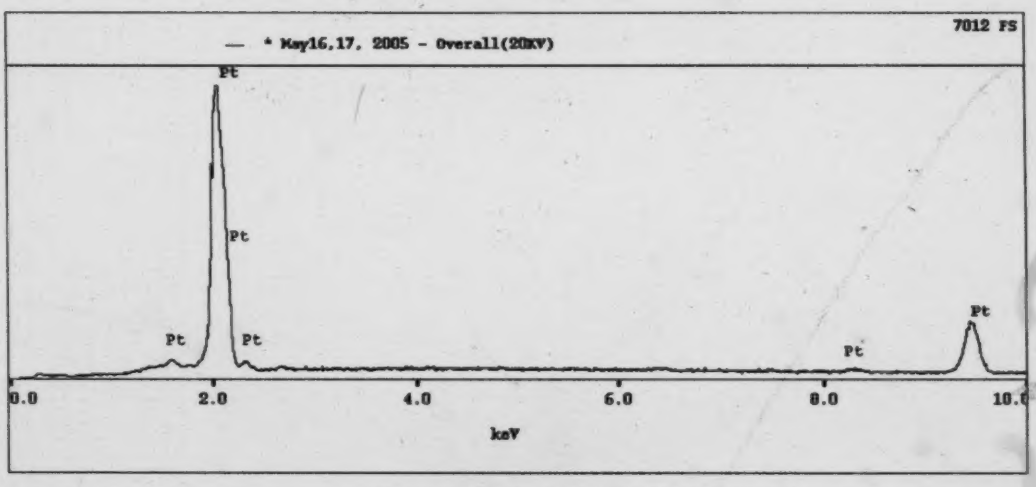

(a) accelerating voltage = 20 kV

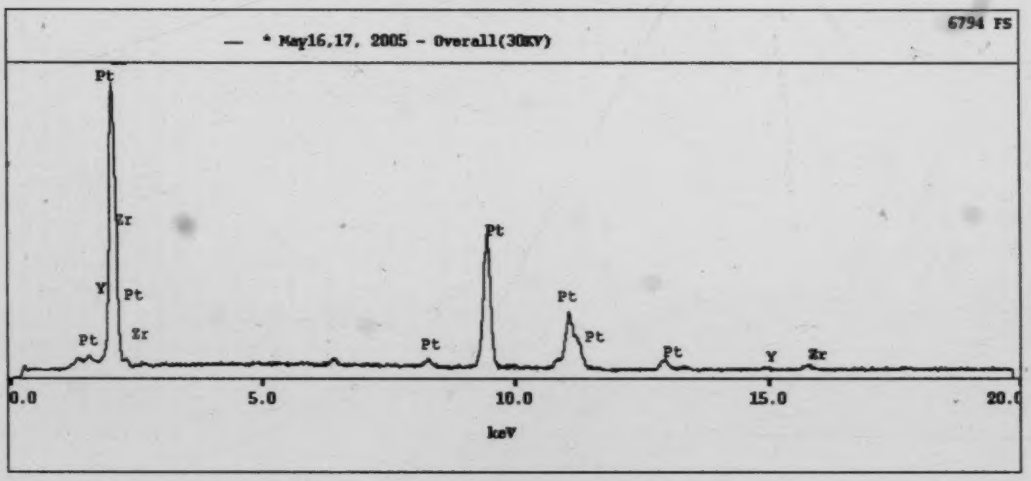

(b) accelerating voltage = 30kV

Figure 7-17: EDX overall spectra for sample 05-14

were carried out on some of the larger surface particles and similar results to previous tests were returned; phosphorous and aluminum were present in the particles and a small amount of calcium was detected as well.

7.3 Summary

From this preliminary investigation of the use of $CeCl_3$ as a reactant in the PEVD process to deposit a ceria layer around the platinum anode, no definite conclusions can be drawn. Some of

the electrochemical test results would indicate that an improvement occurred, but no layer was visible nor any cerium detected. The reason for this may be due to the very low vapour pressure of $CeCl_3$ that is insufficient for the PEVD process. The potential of ceria for this application is still very promising and further research should be carried out to fully determine its viability.

8.0 Conclusions

8.1 Yttria-Stabilized Zirconia Depositions

The results presented in regards to the deposition of yttria-stabilized zirconia onto a metallic anode by PEVD demonstrate the necessity for determining the optimal process conditions. Data collected at an operating/deposition temperature of 900°C, a bias voltage of –400 mV and an equilibrium vapour pressure ratio of 8:1 showed a deposition time increment of 12 hours gave good electrochemical results in terms of current and power density. However, the appearance of the deposit was not a film as expected, but rather a solid deposit of YSZ concentrated at various points on the anode surface.

A decrease in operating/deposition temperature (750°C or 800°C) combined with an increase in bias voltage (-500 mV or -800 mV) does not improve the deposition. On the contrary, cell performance is decreased under these conditions, seen by the lower current and power density values when compared to the as-prepared cell. When these cells were microstructurally examined, virtually no evidence of a deposited layer was found. Varying the equilibrium vapour pressure ratio from 8:1 to 5.25:1 to increase the amount of yttria in the final deposit did not have a beneficial effect at either temperature or bias voltage.

For all test conditions, the anodes of the cells had less porosity after depositions had been carried, though those tested at 900°C and –400 mV had more porosity than those tested at 750°C or 800°C which is not anticipated behaviour. Analysis for the presence of a YSZ layer by EDX was difficult due to the surface roughness of the samples and the overlapping nature of the platinum, zirconium and yttrium peaks.

From these results, it can be concluded that a higher operating/deposition temperature with an intermediate bias voltage gives better results than a lower operating/deposition temperature with a higher bias voltage. However, the unusual nature of the deposit indicates more work must be done to find the optimal process conditions.

8.2 Ceria Depositions

In terms of the deposition of ceria onto a metallic anode by PEVD, the preliminary results were not as expected. Though the electrochemical test results from the study into the effect of deposition time and $CeCl_3$ temperature seemed to indicate that some deposition took place, this was not supported by the microstructural examination. SEM images did not show the presence of

a deposited layer and EDX analysis did not indicate the presence of cerium on any of the sample anodes.

It would seem that the results from this series of testing are inconclusive, since some tests indicated a change in performance after ceria deposition had been carried out while other tests indicated no change.

8.3 Suggestions for Future Work

Based on the experimental results of YSZ deposition obtained in this work, along with the successful results obtained by Tang[9] and Young[10], further investigation into the process conditions of higher operating/deposition temperature (greater than 900°C) and intermediate bias voltage (-200 to -400 mV) is recommended. Due to the difference in the nature of the deposit in this work, a solid deposit rather than a thin film encapsulating the platinum grains of the anode, it would be beneficial to determine if there a threshold for the temperature and/or bias voltage that results in this change. Additionally, it is recommended to begin testing the cell using hydrocarbon fuel to see the effectiveness of the PEVD layer under these conditions. Using alternative anode materials, such as nickel, would be advantageous due to reduced cost.

In the area of ceria deposition, it is recommended to continue investigating the viability of using $CeCl_3$ as a reactant to deposit a ceria layer. Perhaps a higher operating/deposition temperature is required and the reactant chloride must be placed very close to the anode surface. If a film can be deposited, it is recommended that the use of hydrocarbon fuel be investigated.

References

1. http://yosemite.epa.gov/oar/globalwarming.nsf/content/climate.html
2. A.J. Appleby and F.R. Foulkes, *Fuel Cell Handbook*, Van Nostrand Reinhold, New York, 1989.
3. http://americanhistory.si.edu/csr/fuelcells/origins/origins.htm
4. A.W. Quade, *Energy Eng.* 98 (2001) 40.
5. http://americanhistory.si.edu/fuelcells/basics.htm
6. K. Kordesch, G. Simader, *Fuel Cells and Their Applications*, VCH Publishing, Weinheim, 1996.
7. W.Z. Zhu, S.C. Deevi, *Mater. Sci. Eng. A* 348 (2003) 227.
8. E.Z. Tang, T.H. Etsell, D.G. Ivey, *J. Am. Ceram. Soc.* 83 (2000) 1626.
9. Z. Tang, *Polarized Electrochemical Vapor Deposition (PEVD) and its Applications*, Ph.D. Thesis, University of Alberta, Edmonton, AB, 1998.
10. J.L. Young, *Two-Layer Cermet Anodes for Solid Oxide Fuel Cells*, M.Sc. Thesis, University of Alberta, Edmonton, AB, 2001.
11. M. Haldane, *Ceramic Fuel Cell Anode Enhancement by Polarized Electrochemical Vapour Deposition*, M.Sc. Thesis, University of Alberta, Edmonton, AB, 2004.
12. http://www.fuelcells.org/fchandbook.pdf
13. B.C.H. Steele, *J. Mater. Sci.* 36 (2001) 1053.
14. C. Yuh, R. Johsen, M. Farooque, H. Maru, *J. Power Sources* 56 (1995) 1.
15. http://americanhistory.si.edu/fuelcells/pem/pemmain.htm
16. http://americanhistory.si.edu/fuelcells/phos/pafcmain.htm
17. http://americanhistory.si.edu/fuelcells/mc/mcfcmain.htm
18. N.Q. Minh, T. Takahashi, *Science and Technology of Ceramic Fuel Cells*, Elsevier Science, Amsterdam, 1995.
19. J.M. Ralph, A.C. Schoeler, M. Krumplet, *J. Mater. Sci.* 36 (2001) 1161.
20. J.B. Goodenough, *Annu. Rev. Mater. Res.* 33 (2003) 91.
21. J.Luo, R.J. Ball, R. Stevens, *J. Mater. Sci.* 39 (2004) 235.
22. S.P.S. Badwal, K. Foger, *Materials Forum* 21 (1997) 187.
23. B. Zhu, X. Liu, M. Sun, S. Ji, J. Sun, *Solid State Sciences* 5 (2003) 1127.
24. M. Barsoum, *Fundamentals of Ceramics*, McGraw-Hill, New York, 1997.
25. C. Milliken, S. Guruswamy, *J. Am. Ceram. Soc.* 85 (2002) 2479.
26. R.J. Ball, R. Stevens, *Ceram. Eng. Sci. Proc.* 23 (2002) 751.
27. K. Eguchi, T. Setoguchi, T. Inoue, H. Arai, *Solid State Ionics* 52 (1992) 165.

28. B. Zhu, X.T. Yang, J. Xu, Z.G. Zhu, S.J. Ji, M.T. Sun, J.C. Sun, *J. Power Sources* 118 (2003) 47.
29. A.S. Nesaraj, I.A. Raj, R. Pattabiraman, *Transactions of the SAEST* 36 (2001) 89.
30. W.Z. Zhu, S.C. Deevi, *Mater. Sci. Eng. A* 362 (2003) 228.
31. http://www.netl.doe.gov/publications/proceedings/97/97fc/FC5-2.PDF
32. G. Pudmich, B.A. Boukamp, M. Gonzalez-Cuenca, W. Jungen, W. Zipprich, F. Tietz, *Solid State Ionics* 135 (2000) 433.
33. S. Hui, A. Petric, *J. Eur. Ceram. Soc.* 22 (2002) 1673.
34. P.R. Slater, J.T.S. Irvine, *Solid State Ionics* 120 (1999) 125.
35. P.R. Slater, J.T.S. Irvine, *Solid State Ionics* 124 (1999) 61.
36. A. Kaiser, J.L. Bradley, P.R. Slater, J.T.S. Irvine, *Solid State Ionics* 135 (2000) 519.
37. S.P. Simner, J.F. Bonnett, N.L. Canfield, K.D. Meinhardt, V.L. Sprenkle, J.W. Stevenson, *Electrochem. Solid-State Lett.* 5 (2002) A173.
38. E. Maguire, B. Gharbage, F.M.B. Marques, J.A. Labrincha, *Solid State Ionics* 127 (2000) 329.
39. H.-C. Yu, K.-Z. Fung, *Mater. Res. Bull.* 38 (2003) 231.
40. N.Q. Minh, *J. Am. Ceram. Soc.* 76 (1993) 563.
41. T. Takeda, R. Kanno, Y. Kawamoto, Y. Takeda, O. Yamamoto, *J. Electrochem. Soc.* 147 (2000) 1730.
42. S.P. Jiang, *J. Power Sources* 124 (2003) 390.
43. M.M. Seabaugh, S.L. Swartz, R.B. Cooley, K. Hasinska, C.T. Holt, J.L. Jayjohn, W.J. Dawson, *Ceram. Eng. Sci. Proc.* 24 (2003) 311.
44. J.M. Ralph, C. Rossignol, R. Kumar, *J. Electrochem. Soc.* 150 (2003) A1518.
45. H. Zhao, L. Huo, S. Gao, *J. Power Sources* 125 (2004) 149.
46. C. Xia, M. Liu, *Adv. Mater.* 14 (2002) 521.
47. W.Z. Zhu, S.C. Deevi, *Mater. Sci. Eng. A* 348 (2003) 227.
48. http://abulafia.mt.ic.ac.uk/publications/theses/stanek/intorduction.pdf
49. F. Tietz, H.-P. Buchkremer, D. Stöver, *Solid State Ionics* 152-153 (2002) 373.
50. Z.G. Yang, J.W. Stevenson, P. Singh, *Adv. Mater. Process.* 161 (2003) 34.
51. S. Linderoth, P.V. Hendriksen, M. Mogensen, N. Angvad, *J. Mater. Sci.* 31 (1996) 5077.
52. F. Tietz, *Mater. Sci. Forum* 426-432 (2003) 4465.
53. http://www.fe.doe.gov/coal_power/fuelcells/fuelcells_sofc.shtml
54. http://americanhistory.si.edu/csr/fuelcells/so/sofcmain.htm

55. H.O Pearson. *Handbook of Chemical Vapor Deposition (CVD): Principles, Technology and Applications 2nd Edition,* Noyes Publications, Norwich, NY, 1999.
56. http://en.wikipedia.org/wiki/Chemical_vapor_depositions
57. J. Edwards, *Trans. Inst. Met. Finish.* 64 (1986) 17.
58. W.A. Bryant, *J. Mater. Sci.* 12 (1977) 1285.
59. M.L. Hammond, *Solid State Technol.* 22 (1979) 61.
60. http://www.m-w.com/cgi-bin/dictionary
61. http://chiuserv.ac.nctu.edu.tw/~htchiu/cvd/home.html
62. N.J. Kiwiet, J. Schoonman, *Proc. 25th Intern. Soc. Energy Conv. Eng. Conf.* Eds. P.A. Nelson, W.W. Schertz, R.H. Till, Vol. 3 (AIChE, New York, 1990) 240.
63. U.B. Pal, *Solid State Ionics* 52 (1992) 227.
64. J. Schoonman, J.P. Dekker, J.W. Broers, *Solid State Ionics* 46 (1991) 299.
65. V.E.J. van Dieten, J. Schoonman, *Solid State Ionics* 57 (1992) 141.
66. A.O. Isenberg, in *Proc. Symp. Electrode Materials and Processes for Energy Conversion and Storage,* Proc. Vol. 77-6 (The Electrochem. Soc. Inc., Pennington NJ, 1977) 572.
67. M.F. Carolan, J.N. Michaels, *Solid State Ionics* 37 (1990) 189.
68. L.G.J. de Haart, Y.S. Lin, K.J. de Vries, A.J. Burggraaf, *Solid State Ionics* 47 (1991) 331.
69. E.Z. Tang, T.H. Etsell, *Solid State Ionics* 91 (1996) 213.
70. J.L. Young, T.H. Etsell, *Solid State Ionics* 135 (2000) 457.
71. J.H. Lee, J.-W. Heo, D.-S. Lee, J. Kim, G.-H. Kim, H.-W. Lee, H.S. Song, J.-H. Moon, *Solid State Ionics* 158 (2003) 225.
72. D. Simwonis, H. Thulen, F.J. Dias, A. Naoumidis, D. Stover, *J. Mater. Process. Technol.* 92-93 (1999) 107.
73. S.T. Aruna, M. Muthuraman, K.C. Patil, *Solid State Ionics* 111 (1998) 45.
74. T. Fukui, S. Ohara, K. Mukai, *Electrochem. Solid-State Lett.* 1 (1998) 120.
75. M. Manak, N. Coombs, G.A. Ozin, *Adv. Funct. Mater.* 11 (2001) 59.
76. M. Manak, N. Coombs, G.A. Ozin, *Chem. Comm.* 20 (2002) 2300.
77. A. Bieberle, L.J. Gauckler, *Z. Metallkd.* 92 (2001) 796.
78. M. Brown, S. Primdahl, M. Mogensen, *J. Electrochem. Soc.* 147 (2000) 475.
79. T. Tsai, S.A. Barnett, *J. Electrochem. Soc.* 145 (1998) 1696.
80. S.-W. Kim, J.-H. Lee, H.-S. Song, J.-S. Kim, H.-W. Lee, *Mater. Sci. Forum* 439 (2003) 125.
81. D.-S. Lee, J.-H. Lee, J. Kim, H.-W. Lee, H.S. Song, *Solid State Ionics* 166 (2004) 13.
82. J.-H. Lee, H. Moon, H.-W. Lee, J. Kim, J.-D. Kim, K.-H. Yoon, *Solid State Ionics* 148 (2002) 15.

83. J.-H. Lee, Korea Institute of Science and Technology, personal communication.
84. H. Koide, Y. Someya, T. Yoshida, T. Maruyama, *Solid State Ionics* 132 (2000) 253.
85. C.-H. Lee, C.-H. Lee, H.-Y. Lee, S.M. Oh, *Solid State Ionics* 98 (1997) 39.
86. T. Kawashima, Y. Matsuzaki, *Journal of the Ceramic Society of Japan, International Edition* 104 (1995) 304.
87. H. Itoh, T. Yamamoto, M. Mori, T. Watanabe, T. Abe, *Denki Kagaku* 64 (1996) 549.
88. H. Itoh, T. Yamamoto, M. Mori, T. Horita, N. Sakai, H. Yokokawa, M. Dokiya, *J. Electrochem. Soc.* 144 (1997) 641.
89. B. de Boer, M. Gonzalez, H.J.M. Bouwmeester, H. Verweij, *Solid State Ionics* 127 (2000) 269.
90. S.P. Jiang, P.J. Callus, S.P.S. Badwal, *Solid State Ionics* 132 (2000) 1.
91. D. Skarmoutsos, A. Tsoga, A. Naoumidis, P. Nikolopoulos, *Solid State Ionics* 135 (2000) 439.
92. S. Primdahl, B.F. Sørensen, M. Mogensen, *J. Am. Ceram. Soc.* 83 (2000) 489.
93. T. Fukui, S. Ohara, M. Naito, K. Nogi, *J. Power Sources* 110 (2002) 91.
94. S.P. Jiang, *J. Mater. Sci.* 38 (2003) 3775.
95. M. Watanabe, H. Uchida, M. Shibata, N. Mochizuki, K. Amikura, *J. Electrochem. Soc.* 141 (1994) 342.
96. H. Uchida, S. Suzuki, M. Watanabe, *Electrochem. Solid-State Lett.* 6 (2003) A174.
97. H. Uchida, S. Suzuki, M. Watanabe, *J. Electrochem. Soc.* 145 (1998) 615.
98. H. Uchida, T. Osuga, M. Watanabe, *J. Electrochem. Soc.* 146 (1999) 1677.
99. J.B. Wang, J.-C. Jang, T.-J. Huang, *J. Power Sources* 122 (2003) 122.
100. R. Maric, S. Ohara, T. Fukui, T. Inagaki, J.-I. Fujita, *Electrochem. Solid-State Lett.* 1 (1998) 201.
101. J. Cheng, H. Li, X. Liu, G. Meng, *Mater. Sci. Forum* 423-425 (2003) 449.
102. C. Xia, M. Liu, *Solid State Ionics* 152-153 (2002) 423.
103. S.P. Jiang, S. Zhang, Y.D. Zhen, A.P. Koh, *Electrochem. Solid-State Lett.* 7 (2004) A282.
104. S. Zha, W. Rauch, M. Liu, *Solid State Ionics* 166 (2004) 241.
105. F. Meschke, F.J. Dias, F. Tietz, *J. Mater. Sci.* 36 (2001) 5719.
106. A.R. Villani, B. Brunetti, V. Piacente, *J. Chem. Eng. Data* 45 (2000) 823.
107. E. Shimazaki, K. Niwa, *Z. Anorg. Allg. Chem.* 314 (1962) 21.
108. D. Brown. *Halides of the Lanthanides and Actinides*, John Wiley & Sons, London, 1968.
109. O. Kubaschewski. *Metallurgical Thermochemistry 5th Edition*, Pergamon Press, New York, 1979.

110. M. Binnewies, E. Milke, *Thermochemical Data of Elements and Compounds, 2nd ed*, Wiley-VCH, Weinheim, 2002.